

# Solar flare studies with the LYRA instrument onboard PROBA2

**Marie Dominique**

Supervisors:

Prof. Dr. Ing. G. Lapenta

Dr. A. N. Zhukov

(Royal Observatory of Belgium)

Dissertation presented in partial  
fulfillment of the requirements for the  
degree of Doctor of Science (PhD):  
Astronomy and Astrophysics

February 2019





# **Solar flare studies with the LYRA instrument onboard PROBA2**

**Marie DOMINIQUE**

Examination committee:

Prof. Dr. H. Sana, chair

Prof. Dr. Ing. G. Lapenta, supervisor

Dr. A. N. Zhukov, supervisor  
(Royal Observatory of Belgium)

Prof. Dr. S. Poedts

Prof. Dr. H. Van Winckel

Dr. D. Berghmans  
(Royal Observatory of Belgium)

Dr. M. Kretzschmar  
(University of Orléans)

Prof. Dr. P. Heinzel  
(Astronomical Institute /  
Czech Academy of Sciences)

Dissertation presented in partial fulfillment of the requirements for the degree of Doctor of Science (PhD):  
Astronomy and Astrophysics

February 2019

© 2019 KU Leuven – Faculty of Science  
Uitgegeven in eigen beheer, Marie Dominique, 3, Circular Avenue, B-1180 Uccle (Belgium)

Alle rechten voorbehouden. Niets uit deze uitgave mag worden vermenigvuldigd en/of openbaar gemaakt worden door middel van druk, fotokopie, microfilm, elektronisch of op welke andere wijze ook zonder voorafgaande schriftelijke toestemming van de uitgever.

All rights reserved. No part of the publication may be reproduced in any form by print, photoprint, microfilm, electronic or any other means without written permission from the publisher.

# Acknowledgments

Before you start reading this thesis, I would like to have the opportunity to thank all the people who, one way or another, supported me and helped me materialize it:

My supervisor, Giovanni Lapenta, who accepted me as a PhD student, knowing that I would be torn apart between this PhD work and my activities at the Royal Observatory of Belgium.

My co-supervisor, Andrei Zhukov, who had the hard task to follow me in my daily work and whose advices and guidance have always proven to be very valuable.

My supervising committee: Stefaan Poedts, Hans Van Winckel and David Berghmans for their helpful suggestions... and for their patience.

H. Sana, P. Heinzel and M. Kretzschmar who accepted to complete the jury despite the tight schedule and for taking the time to read this PhD work.

L. Dolla and T. Van Doorselaere for the very constructive discussions about QPPs.

Ingolf Dammasch for his huge contribution to the calibration of LYRA.

T. Katsiyannis for his help with the IDL routines and for the investigation of the auroral perturbations on LYRA.

E. D'Huys for helping me many times finding my way though the PhD administrative maze - a special thought to her and her newly-born Roos.

Hartelijke dank aan David Berghmans, Peter De Cat, Cis Verbeeck en Robbe Vansintjan voor hun collectieve hulp met de vertaling van de samenvatting.

I would also like to thank my colleagues and former colleagues from the LYRA team and from the Solar Physics Department of the ROB for their help and

support, and for the nice environment that they create at the Observatory. Working with you has always been highly motivating.

Finally, I would like address a special thanks to my family and my partner, Emmanuel Gamby. Nothing would have been possible without you.

\*\*\*\*\*

This research was mainly funded by the Belgian Science Policy Office (BELSPO) via successive ESA-PRODEX programmes (PEA 4000103240 and 4000120800) and via the Interuniversity Attraction Poles Programme (IAP P7/08 CHARM). I also acknowledge the contribution of the European Union's Seventh Framework Programme for Research, Technological Development and Demonstration under grant agreement No. 284461 (Project eHeroes, [www.eheroes.eu](http://www.eheroes.eu)), of the Solar-Terrestrial Center of Excellence (STCE) and of the ESA - PROBA2 guest investigator programme for specific investigations, organisation of workshops and collaborations.

I have used images and data from a number of space missions and data analysis tools that I would like to acknowledge here:

- LYRA, a project of the Centre Spatial de Liège, the Physikalisch-Meteorologisches Observatorium Davos and the Royal Observatory of Belgium funded by BELSPO and by the Swiss Bundesamt für Bildung und Wissenschaft.
- GOES satellite data, which are provided by the Space Weather Prediction Center (SWPC) at NOAA.
- SDO data, which are courtesy of NASA and the AIA, EVE, and HMI science teams.
- MAVEN time series, which are courtesy of NASA and the EUVM science team.
- SWAP, a project of the Centre Spatial de Liège and the Royal Observatory of Belgium funded by the Belgian Federal Science Policy Office (BELSPO).
- The Solar-Soft library.
- The CHIANTI atomic database.
- The Torrence and Compo wavelet library.

# Abbreviations

AIA	Atmospheric Imaging Assembly
BELSPO	Belgian Science Policy Office
CME	Coronal Mass Ejection
CmPA	Centre for mathematical Plasma-Astrophysics
ESA	European Space Agency
EUV	Extreme Ultraviolet
EVE	Extreme Ultraviolet Variability Experiment
FUV	Far Ultraviolet
FITS	Flexible Image Transport System
FOV	Field-Of-View
GOES	Geostationary Operational Environmental Satellite
HXR	Hard X-Rays
IR	Infrared
IRIS	Interface Region Imaging Spectrograph
ISS	International Space Station
LED	Light Emitting Diode
LTE	Local Thermodynamic Equilibrium
LYRA	Large Yield Radiometer
MAVEN	Mars Atmosphere and Volatile EvolutionN
MHD	Magnetohydrodynamics
MSM	Metal–Semiconductor–Metal (type of photodetector)
MUV	Middle-Ultraviolet
NLFFF	Non-Linear Force-Free Field
NUV	Near-Ultraviolet
PI	Principal Investigator
PiN	P-type Intrinsic N-type (kind of diode)
PFSS	Potential Field Source Surface model
PI	Principal Investigator
PMOD/WRC	Physikalisch-Meteorologisches Observatorium / World Radiation Center

PROBA2	Project for On Board Autonomy 2
QPP	Quasi-Periodic Pulsations
RHESSI	Reuven Ramaty High Energy Solar Spectroscopic Imager
ROB	Royal Observatory of Belgium
RTV	Room-Temperature-Vulcanizing silicone
SDO	Solar Dynamics Observatory
SOLSPEC	SOLar SPECtrometer
SSI	Solar Spectral Irradiance
SWAP	Sun Watcher using APS detectors and image Processing
SXR	Soft X-Rays
TSI	Total Solar Irradiance
UARS	Upper Atmosphere Research Satellite
UV	Ultraviolet
VIS	Visible

# Contents

<b>Contents</b>	<b>v</b>
<b>List of Figures</b>	<b>ix</b>
<b>List of Tables</b>	<b>xxi</b>
<b>1 Introduction</b>	<b>3</b>
1.1 The Sun: a Few Reminders...	3
1.2 Solar Radiation	6
1.3 The Solar Activity Cycle	13
1.4 A Manifestation of Solar Activity: Solar Flares	14
1.5 Zooming on a Flare Curve: the Quasi-Periodic Pulsations (QPPs)	19
1.5.1 MHD Waves as a Source of QPPs	22
1.5.2 Fluctuating Particle Acceleration as a Source of QPPs	26
1.6 Observing the Solar Irradiance from Soft X-Rays to Ultraviolet	28
1.7 Objectives of this Thesis	31
<b>2 PROBA2/LYRA: Instrument Description</b>	<b>33</b>
2.1 Design of the Instrument	33
2.2 LYRA Data Description	37

2.2.1	Data Products . . . . .	37
2.2.2	Calibration of LYRA Data . . . . .	41
2.2.3	Non-Solar Features in the LYRA Data . . . . .	50
2.2.4	Radiometric Accuracy . . . . .	53
2.3	Conclusion . . . . .	57
<b>3</b>	<b>Analysis of the Spectral Degradation of LYRA</b>	<b>59</b>
3.1	Identification of the Source of Degradation . . . . .	59
3.2	Model of Contamination . . . . .	60
3.3	Effect of the Contamination on the Spectral Response of the Instrument . . . . .	66
3.3.1	Using Occultation Data to Determine the Evolution of the Spectral Response. . . . .	67
3.3.2	Spectral Degradation . . . . .	73
3.4	Conclusion . . . . .	73
<b>4</b>	<b>Multi-Wavelength Analysis of the Strongest Solar Flare of Solar Cycle 24</b>	<b>77</b>
4.1	Introduction . . . . .	77
4.2	Data description . . . . .	78
4.3	Observations . . . . .	82
4.4	Spectral Modeling . . . . .	83
4.5	Impact of Degradation . . . . .	87
4.6	Summary and Discussion . . . . .	88
<b>5</b>	<b>Quasi-Periodic Pulsations in Solar Flares</b>	<b>91</b>
5.1	Introduction . . . . .	91
5.2	Wavelet Detection: the Wavelet Transform - Ideal Case Studies	95
5.2.1	Period Detection by Wavelet Transform . . . . .	96



5.2.2	Wavelet Coherence . . . . .	103
5.2.3	Detection Criteria . . . . .	103
5.3	Examples of Real Case Studies: Solar Flares . . . . .	107
5.3.1	X2.2 Flare SOL20110215 . . . . .	108
5.3.2	X1.1 Flare SOL20120706 . . . . .	108
5.4	Statistical Survey . . . . .	109
5.5	Correlation with the Alfvén Speed . . . . .	121
5.5.1	Estimation of the Magnetic Field and of the Length of the Loop . . . . .	123
5.5.2	Estimation of the Coronal Mass Density . . . . .	125
5.5.3	Comparison Between the Observed and Predicted Periods	126
5.6	Quasi-Periodic Pulsations in the Two Strongest Flares of Solar Cycle 24 . . . . .	129
5.7	Conclusions . . . . .	133
<b>6</b>	<b>Conclusions</b>	<b>137</b>
6.1	Summary . . . . .	137
6.2	Lessons Learned . . . . .	141
6.3	Future Prospects . . . . .	142
	<b>Beknopte Samenvatting</b>	<b>145</b>
	<b>Bibliography</b>	<b>151</b>
	<b>Short Curriculum Vitae</b>	<b>167</b>
	<b>Peer-Reviewed Publications</b>	<b>169</b>



# List of Figures

1.1	The Hertzsprung-Russell diagram (credit: ESO). . . . .	4
1.2	The various layers of the Sun (credit: NASA/Goddard). . . . .	5
1.3	Structure of the temperature and density throughout the solar atmosphere (credit: E. Avrett, Smithsonian Astrophysical Observatory). . . . .	5
1.4	Top panel: The full reference solar spectrum based on ISS/SOLSPEC data. Credit: Meftah et al. (2018). Bottom panel: UARS observations of the wavelengths around 2000 Å, where the spectral lines change from absorption to emission. Credit: Woods et al. (1996) . . . . .	8
1.5	The quiet-Sun formation height for various spectral lines. The difference in the emission altitude corresponding to the core and the wings of a spectral line is well illustrated for the Lyman- $\alpha$ line. Credit: Vernazza et al. (1981). . . . .	10
1.6	Ionization equilibria for Fe XXIV-XXVII as computed by Dere et al. (2009) (solid lines) in comparison with the previous work of Mazzotta et al. (1998) (dashed lines). Credit: Dere et al. (2009). . . . .	11
1.7	The sunspot number evolution since the beginning of the observations. The 11-year solar cycle is clearly visible. Credit: SILSO / Royal Observatory of Belgium . . . . .	13

1.8	Evolution of the global internal magnetic field along the solar cycle. Panels a to c show the progressive winding of the internal field as it is stretched by the differential rotation of the Sun. Panel d shows the formation of a magnetic loop. Panel e shows the emergence of the magnetic loop above the photosphere. The positive and negative magnetic regions correspond to the footpoints of the emerged loop. Credit: Paterno (1998). . . . .	14
1.9	Observations of the X2.2 flare on 15 February 2011 in multiple bandpasses, in the radio (Nobeyama), SXR (GOES), and EUV (EVE and LYRA) ranges. The sequence in which the various wavelengths peak is clearly visible. Credit: Dolla et al. (2012). . . . .	15
1.10	The standard model of a flare. Credit: Shibata et al. (1995). . . . .	16
1.11	Transport of the energy from the reconnection site in the corona to the chromosphere by Alfvén waves. Credit: Fletcher and Hudson (2008). . . . .	18
1.12	Various scenarii of reconnection. Top-left panel: the Sweet-Parker reconnection. Bottom-left panel: The Petschek reconnection. Both left panels are from (Aschwanden, 2005). Right panel: plasmoid-induced reconnection from (Shibata and Takasao, 2016) . . . . .	19
1.13	QPPs detected during the X4.9 flare of 25 February 2014. Top panel: the normalized irradiance from GOES 0.1–0.8 nm (black), LYRA 1–20 nm (blue), RHESSI 50–100 keV (red) and Nobeyama 17 GHz (green). Second, third and fourth panels: the same time series for respectively RHESSI, Nobeyama and LYRA, detrended with a 50 s window. The oscillating pattern was clearly visible in the HXR and radio time series, without the need to detrend the data. This is no longer the case when looking at SXR or EUV data, for which a detrending is required to highlight the oscillations. Credit: McLaughlin et al. (2018) . . . . .	21
1.14	Velocity and magnetic field perturbations for Alfvén (left panel) and magneto-acoustic (right panel) waves, obtained from Equation 1.16. Credit: (Goedbloed and Poedts, 2004). . . . .	25
1.15	Illustration of different types of MHD oscillations in a plasma cylinder: sausage mode (Panel a), kink mode (Panel b), Torsional mode (Panel c). Credit: MPS . . . . .	26
1.16	Illustration of possible mechanisms at the origin of QPPs. . . . .	27

1.17	The average solar spectrum before (dark blue) and after (light blue) absorption by the Earth atmosphere. The variability of the solar spectrum over the solar cycle is shown with the green line. Credit: J. Lean, NRL . . . . .	29
1.18	Overview of the main instruments measuring the EUV/SXR solar spectral irradiance. Note that LYRA observations continue up to now (2019). Credit: F.Eparvier, LASP . . . . .	30
1.19	Panel (a): LYRA ( $315 \times 92.5 \times 222 \text{ mm}^3$ ) during its integration on PROBA2. Panel (b): the open cover of unit 2 reveals the four observation channels. . . . .	31
2.1	Schematic representation of one LYRA channel: 1 and 2 are respectively the view-limiting and precision apertures, together forming the collimator, 3 is the filter, 4 are the two LEDs at 375 and 470 nm located behind the filter, and 5 is the detector. . .	34
2.2	Two examples of diamond detectors: MSM (a) and PIN (b). In both cases, we note the position of an electrode (central bar for the MSM, off-center circle for the PIN). Those electrodes strongly affect the flat-field of the detectors, as shown in the plots of relative responsivity along two perpendicular directions in (c) and (d). . . . .	36
2.3	Slow stabilization of MSM detectors: the signal has not yet reached its stabilization level three hours after the detector was switched on. This figure also shows the perturbation in the Si-detector signal when the SAA is crossed. Compared to silicon, diamond technology has proven to be more resilient to the impact of high-energy protons (and their secondary electrons), which cause this noisy behavior. Gray bands indicate the South Atlantic Anomaly (SAA) and dashed vertical lines the wide-angle rotations of the spacecraft. Time series have been rescaled to fit the same range and appear in the same order as in the legend. Scaling coefficients are indicated in the legend. . . . .	37
2.4	Simulated combined spectral (detector + filter) responsivities for LYRA unit 1 between 1 and 1000 nm, from (BenMoussa et al., 2009). . . . .	38
2.5	Percentage contribution of each continuum/line composing the bandpass of LYRA channels 1 (top panel) and 2 (bottom panel) to the total measured signal. . . . .	39

- 2.6 (a) Dark current in channel 1 of unit 2 *versus* temperature, as a function of time. Diamonds show pre-launch measurements and solid lines the dark current relation obtained after fitting the parameters  $a$ ,  $b$ , and  $c$  from Equation 2.1 for different times of the mission (dark/light lines respectively correspond to the beginning/end of the mission). (b) An example of quiet-day uncalibrated measurements by channel 1. The effect of orbital and daily temperature variations is clearly visible. After subtraction of dark current, the same time series turns into a flat line. . . . . 43
- 2.7 Loss of signal in the four channels of unit 2 from the beginning of the mission. The dark current is subtracted from the signal. . . . . 45
- 2.8 Unit 2 measurements from the beginning of the mission, after correcting for degradation (and subtracting dark current). During the season of occultations (days 0 to 40 and 300 to 400), the signal drops to the dark-current level during every orbit. As an unintended side effect of the additive correction for degradation, the level of the dark current – which is also the level reached during occultations – gives the impression of a progressive increase with time, while it is actually stable in general. . . . . 46
- 2.9 Reference solar spectrum reconstructed from TIMED/SEE and SORCE/SOLSTICE level-3 data on 6 January 2010, used as a reference to infer LYRA radiometric calibration. Wavelength coverage of different LYRA channels is marked with red lines. . . . . 49
- 2.10 Flat-field campaign of 26 August 2010: the spacecraft is off-pointed from  $0^\circ$  to  $3^\circ$  in steps of  $0.5^\circ$  in the S, E, N, W, SE, NE, NW, and SW directions. Results are plotted for unit 2 channels. Time series have been rescaled to fit the same range and appear in the same order as in the legend. Scaling coefficients are indicated in the legend. . . . . 51
- 2.11 Drop of signal when the spacecraft transits the Earth shadow (highlighted with gray). Vertical dashed lines indicate the wide-angle rotations of the spacecraft. Time series have been rescaled to fit the same range and appear in the same order as in the legend. Scaling coefficients are indicated in the legend. . . . . 52

2.12 Perturbations that appear when the auroral zone is crossed during or after a geomagnetic storm. Each horizontal line corresponds to one orbit. Four zones of perturbations are identified for each orbit (highlighted with red). They occur systematically in the same range of latitudes (north and south auroral ovals are each crossed twice during an orbit). Dashed vertical lines indicate the wide-angle rotations of the spacecraft. . . . . 54

2.13 Alternative spectra used to calibrate LYRA data. The full black line represents the TIMED/SEE-SORCE/SOLSTICE reference spectrum. Alternative spectra that were tested are overplotted and correspond to NRLSSI (blue), SRPM (green), SATIRE (orange), and EVE (olive). . . . . 58

3.1 Spectral dependancy of the absorption cross-section of the carbon (black line) and silicon (blue line). The data were obtained from the Centre for X-Ray Optics (<https://www.cxro.lbl.gov/>). . . . 61

3.2 Normalized spectral transmission of 5.764 nm of silicon + 143.4 nm of carbon (solid line) and comparison with the proportion of remaining signal in each channel of LYRA after 200 days of mission as compared to the first light (red dashed lines). The proportion of remaining signal in the SXR spectral range has been represented separately from channels 3 and 4 (while being actually part of their bandpasses) as this part of the spectrum is believed to be little affected by degradation. . . . . 62

3.3 Top panel: evolution over time of the thickness of the silicon (blue symbols) and carbon (red symbols) layers obtained by fitting the model of degradation to the loss of signal observed in the four channels of the unit 2 of LYRA. Bottom panel:  $\chi^2$  residuals of the fitting procedure. . . . . 63

3.4 Spectral transmission of 13.82 nm of silicon + 5.63 nm of carbon (solid line) and comparison with the proportion of remaining signal in each channel of LYRA after 200 days of mission as compared to the first light (red dashed lines). The proportion of the remaining signal in the SXR spectral range has been represented separately from channels 3 and 4 (while being actually part of their bandpasses) as this part of the spectrum is believed to be little affected by degradation. . . . . 64

- 3.5 Top panel: evolution over time of the thickness of the silicon (blue symbols) and carbon (red symbols) layers obtained by fitting the model of degradation to the loss of signal observed in channels 1, 2, and 4 of the unit 2 of LYRA (*i.e.* excluding the measurements of channel 3 from the fitting procedure). Bottom panel:  $\chi^2$  residuals of the fitting procedure. . . . . 65
- 3.6 Measured (red stars) and modelled (black lines) evolution of the transmission of the four channels of unit 2. The modelled curve is based on a contamination that is dominated by carbon (see Figure 3.3). . . . . 67
- 3.7 Top panel: evolution over time of the thickness of the silicon (blue symbols) and carbon (red symbols) layers obtained by fitting the model of degradation to the loss of signals observed in the four channels of the unit 3 of LYRA. Bottom panel:  $\chi^2$  residuals of the fitting procedure. . . . . 68
- 3.8 Top panel: evolution over time of the thickness of the carbon layer obtained by fitting the pure-carbon model of degradation to the loss of signal observed in the four channels of the unit 1 of LYRA. Bottom panel:  $\chi^2$  residuals of the fitting procedure. . . . . 69
- 3.9 Illustration of an occultation. The part of the orbit in green corresponds to the one during which the spacecraft is in the Earth shadow, while the parts in red are the ones during which the satellite observes the Sun through the Earth atmosphere, *i.e.* the occultation. . . . . 70
- 3.10 Measured (top panel) and modeled (bottom panel) occultation profile of the channel 1 of unit 3. The measured extinction shows a two-step drop, the one at the highest altitudes corresponding to the absorption of the wavelengths around the Lyman- $\alpha$  line, while the one at lower altitude corresponding to the absorption of wavelengths longer than 135 nm. The relative importance of each drops clearly evolves with time, which can be reproduced in the bottom panel by reducing the purity of the instrument. . . . . 71
- 3.11 Evolution of the spectral response of each channel of the unit 2. The different colours represent different times of the mission: Black: 6 January 2010 (first-light acquisition, no degradation), brown: 24 March 2010, red: 15 May 2013, orange: 15 May 2014, green: 25 February 2015 . . . . . 74



4.1	Solar radiance corresponding to typical quiet-Sun conditions and the increase (without the quiet-Sun background) of radiance produced by the flare. The spectrum $I_\lambda$ (red line) of the flare of 2017 September 6 has been calculated following the procedure described in Section 4.4. The jump observed at 3646Å is caused by the transition from the Balmer to the Paschen continua. The quiet-Sun spectrum (blue line) obtained by concatenating the measurements by SDO/EVE, SORCE/SOLSTICE and TIMED/SEE on 2010 January 7, is shown for comparison. The effective areas of the LYRA channels 1 (solid line) and 2 (dashed line) of the spare unit used during the flare campaign are overplotted in black. . . . .	79
4.2	Solar irradiance during the X9.3 flare of 2017 September 6 (with the pre-flare irradiance subtracted), observed by GOES (orange line) and LYRA channels 1, 2, and 4 (respectively the purple, green, and black lines for $E_1$ , $E_2$ , and $E_4$ ), as well as the Ly- $\alpha$ residual irradiance $E'_1$ (red line) extracted from $E_1$ . The LYRA data were rebinned to the cadence of 1 s. The time derivative of GOES 1–8 Å data is also shown (blue line) as a proxy of the non-thermal flare emission. Different scales were used for the various time series for the sake of clarity. . . . .	83
4.3	Left panel: difference between the SDO/HMI continuum images taken on 6 September 2017 at 11:59 and 11:50 UT. Right panel: SDO/AIA 1700 Å image (Lemen et al., 2012) at 11:59 UT. . .	85
4.4	Effect of the absorption by a layer of carbon on the spectral sensitivity of LYRA channels 1 (left panel) and 2 (right panel). The colours black, brown, red, yellow, green, and blue correspond to thicknesses of C of 0 nm (no contamination), 10 nm, 50 nm, 100 nm, 300 nm, and 500 nm respectively. Note the units of the X-axis in Å. . . . .	87
5.1	Time series $S_1$ ( <i>top panel</i> ), its wavelet power spectrum ( <i>bottom left panel</i> ), and the power spectrum averaged over time ( <i>bottom right panel</i> ) for the case with $p_1 = 5$ s, $p'_1 = 50$ s, $\phi_1 = 0$ , $A_1 = 1$ . The <i>hashed area</i> in the bottom left plot represents the cone of influence, where the border effects affect the detected periodicities, which are therefore not reliable. <i>Green lines</i> in the bottom right panel mark the local peaks in the average wavelet power spectra, and the <i>green numbers</i> show corresponding periods in seconds. . . . .	97

- 5.2 Periods detected in series  $S_1$  for  $p_1 = 15$  s and  $p'_1 = 20$  s (*top panel*) and for  $p_1 = 16$  s and  $p'_1 = 20$  s (*bottom panel*). The other parameters are  $\phi_1 = 0$ ,  $A_1 = 1$ . Because of the intrinsic uncertainty that affects the detection of periods, the wavelets fail to separate periods that are too closely to each other. . . . . 98
- 5.3 Time-series  $S_3$  (*top panel*), its wavelet power spectrum (*bottom left panel*), and the power spectrum averaged over time (*bottom right panel*) for the case with  $p_1 = 15$  s,  $p'_1 = 40$  s,  $\phi_1 = 0$ ,  $A_1 = 1$ ,  $\alpha = 0.995$ , and  $A_N = 0.01$ . The 95% confidence level is shown in the two bottom panels. . . . . 99
- 5.4 Same as Figure 5.3, but with  $A_N = 0.1$ . . . . . 100
- 5.5 *Left panels*: Periods corresponding to peaks in wavelet power spectrum of a synthetic sinusoidal signal depending on the size of the detrending window (all peaks are shown here, not only the ones reaching the 95% level of confidence). The signal is noiseless (*top panels*, corresponding to  $S_2$  with  $p_2 = 15$  s) or affected by a red noise with a 10% standard deviation (*bottom panels*, corresponding to  $S_4$  with  $p_2 = 80$  s). The parameters of the series are  $\alpha = 0.995$ , and  $A_N = 0.1$ . The *black line* represents the periods corresponding to the size of the detrending window  $l$ , while its successive harmonics  $l/2$ ,  $l/4$ ,  $l/8$ , and  $l/16$  are represented by the *blue lines*. *Middle panels*: Examples of wavelet power spectra for the noiseless series  $S_2$  and noisy series  $S_4$  respectively, obtained for the detrending window of 305 s. *Right panels*: the averaged spectra. . . . . 102
- 5.6 Periods detected by cross-coherence between series  $S_3$  and  $S_4$ , where  $p_1 = 15$  s,  $p'_1 = 40$  s,  $p_2 = 15$  s,  $\phi_1 = \phi_2 = 0$ ,  $A_1 = A_2 = 1$ ,  $\alpha = 0.995$ , and  $A_{noise} = 0.01$ . . . . . 104
- 5.7 Same as in Figure 5.6, but for  $A_{noise} = 0.1$ . . . . . 105
- 5.8 Solar flux measured in the zirconium channel of LYRA (*top panel*), detrended flux (*middle panel*) and wavelet power spectrum of the detrended flux (*bottom panel*) during the rising phase of the X2.2 flare on 15 February 2011, for the width of the detrending window of 50 s. . . . . 111

- 5.9 Effect of the detrending window size  $l$  on the periods detected for the X2.2 flare on 15 February 2011. The periods shown with *red lines* correspond to the periods found in the LYRA Zr data that reach (*solid lines*) and do not reach (*dashed lines*) the 95% level of confidence in the power spectrum during a time interval that is at least twice longer than the period. Similarly, the periods shown with *blue lines* were found in the ESP-Q data. Only the periods to the *right of the black diagonal line* (corresponding to the detected period equal to  $l$ ) are reliably detected. The periods found in ESP-Q have been shifted up by 0.5 s for clarity. . . . . 112
- 5.10 Solar flux measured in the zirconium channel of LYRA (*top panel*), detrended flux (*middle panel*) and wavelet power spectrum of the detrended flux (*bottom panel*) during the rising phase of the X1.1 flare on 06 July 2012, for the width of the detrending window of 50 s . . . . . 113
- 5.11 Effect of the detrending window on the periods detected for the X1.1 flare on 6 July 2012. The periods shown with *red lines* correspond to the periods found in the LYRA Zr data that reach (*solid lines*) and do not reach (*dashed lines*) the 95% level of confidence in the power spectrum during a time interval at least twice longer than the period. Similarly, the periods shown with *blue lines* were found in the ESP-Q data. Only the periods to the *right of the black diagonal line* (corresponding to the detected period equal to  $l$ ) are considered reliably detected. The periods found in ESP-Q have been shifted up by 0.5 s for clarity. . . . . 114
- 5.12 *Left panel*: Correlation of the periods detected in the ESP-Q and LYRA Zr data for all flares of Solar Cycle 24 with the GOES class above M5. *Right panel*: Histogram of all periods detected in these flares that were observed by LYRA (*blue*) and ESP-Q (*red*). . . . . 115
- 5.13 Periods detected in the ESP-Q (*blue*) and LYRA Zr (*green*) data for all flares of Cycle 24 with the GOES class above M5 as a function of the flare longitude. *Green vertical bars* connect periods in the LYRA and ESP-Q data that differ by less than 25%. According to the criterion (7), these bars are considered to represent the probable interval of the true period(s) in the flare data. . . . . 115

- 5.14 Periods detected in the ESP-Q (*blue*) and LYRA Zr (*green*) data as a function of the flare peak irradiance detected by GOES in the 1–8 Å channel. *Green vertical bars* connect periods in the LYRA and ESP-Q data that differ by less than 25%. According to the criterion (7), these bars are considered to represent the probable interval of the true period(s) in the flare data. . . . . 116
- 5.15 Correlation between the periods detected in the GOES (*blue*) and Fermi (*magenta*) data by Inglis et al. (2016) on the one hand, and those found in our study of the LYRA Zr data on the other hand, for flares of Solar Cycle 24 with GOES class M5 or higher. When more than one period was detected in the LYRA data, the plotted period is the one closest to the period detected in the GOES or *Fermi* data. The *grey lines* represent the  $\pm 25\%$  uncertainty on the period detection. . . . . 121
- 5.16 Comparison between the periods detected in the GOES data (*green intervals*) by Simões et al. (2015) and those found in the LYRA data for the same flares (*red triangles*). In 66% of the cases, one of the periods detected in our study is within the interval detected by Simões et al. (2015) in the GOES data. . . 122
- 5.17 Comparison between the observed loop structures (left panel: an image taken by SDO/AIA in the 171 Å passband) and the ones provided by the PFSS model (right panel: the background image taken by SDO/HMI) for the X1.5 flare on 9 March 2011. . . . . 124
- 5.18 The flare spectrum (*i.e.* after subtraction of the pre-flare spectrum) measured by SDO/EVE/MEGS-A during the X4.9 flare on 25 February 2014 (black line), with the fitted spectrum overplotted (red line). The fitted background and the lines involved in the density-sensitive ratios are shown in green. . . . 126
- 5.19 Theoretical relationships between the selected line ratios and density from CHIANTI. The lines involved in the ratios are expressed in nm. . . . . 127
- 5.20 Comparison between the periods of observed QPPs and the ones predicted considering the fundamental mode of a standing Alfvén wave. . . . . 128
- 5.21 Value of the magnetic field that corresponds to the main observed QPP period, considering the fundamental mode of a standing Alfvén wave. . . . . 128

5.22	Comparison between the magnetic field deduced from the observed QPP periods considering the fundamental mode of a standing Alfvén wave and the magnetic field calculated using the PFSS extrapolation. . . . .	129
5.23	Wavelet power spectra (left panels) and time-averaged spectra (right panels) of the 6 September 2017 flare measured by LYRA in channel 1 (top), channel 2 (middle), and channel 4 (bottom). The power spectra were normalized to the 95% significance. The channel 4 observations were detrended using the size of the detrending window of 60 s prior to applying the wavelet transform. The observations in channels 1 and 2 were not detrended. The red curve in the right panels corresponds to the 95% confidence level. It takes into account that the data are detrended when applicable, see Section 5.2. The peaks (in seconds) reaching the 95% confidence level are marked in green in the right panels. . . .	131
5.24	Effect of the detrending window on the periods detected in the LYRA data for the X8.2 flare on 10 September 2017. The periods shown with <i>red lines</i> correspond to the periods found in the LYRA unit 1 Zr data that reach ( <i>solid lines</i> ) and do not reach ( <i>dashed lines</i> ) the 95% level of confidence in the power spectrum during a time interval at least twice longer than the period. Similarly, the periods shown with <i>blue lines</i> were found in the ESP-Q data. Only the periods to the <i>right of the black diagonal line</i> (corresponding to the detected period equal to the size of the detrending window) are considered to be reliably detected. The periods found in ESP-Q have been shifted up by 0.5 s for clarity. . . . .	132
5.25	Respective positions of the Sun, Earth and Mars at the time of the X8.2 flare on 10 September 2017. From the perspective of the Earth, and therefore from PROBA2, the flare marked with the arrow was visible at the west limb, while from the perspective of Mars and from MAVEN, it was located on the disk in the eastern hemisphere of the Sun. The sizes of the Sun, Earth, and Mars are shown not to scale. . . . .	133

5.26	The X8.2 flare on 10 September 2017, as observed by MAVEN Lyman- $\alpha$ ( <i>black line</i> ), MAVEN SXR ( <i>brown line</i> ), GOES 0.1–0.8 nm ( <i>gold line</i> ) and LYRA channel 3 ( <i>blue line</i> ). Note that the MAVEN time series have been shifted by 327 s to compensate for the difference of the distance to the Sun (on 10 September 2017, the light was taking 327 more seconds to reach Mars than it took to reach the Earth). . . . .	134
5.27	Wavelet power spectrum (left panel) and time-averaged spectrum (right panel) of the observations of the X8.2 flare on 10 September 2017 in the Lyman- $\alpha$ channel of MAVEN/EUVM. In the left panel, three groups of periods are clearly visible around $\sim 15$ , $\sim 40$ s and $\sim 150$ s, all detected with a confidence above 95 % (and even above 99 % for the first two groups). The period at 150 s, however, is detected for a too short duration to be called an oscillation. . . . .	135

# List of Tables

1.1	Definition of the reference flare classes, based on the peak irradiance measured by GOES in the 1–8 Å passband. . . . .	16
2.1	Characteristics of the LYRA channels. Channel 2 was historically called "Herzberg channel" due to its relevance to the Herzberg continuum of molecular oxygen in the Earth's atmosphere. The purity is defined as the ratio of the flux in the nominal wavelength range ( <i>i.e.</i> the defined bandwidth) to the total output signal. Purities correspond to a solar-minimum-type spectrum. The thicknesses of the aluminum and zirconium filter layers are indicated in the second column, together with the Acton reference for the Lyman- $\alpha$ and Herzberg filters. . . . .	35
2.2	Main continua/lines contributing to the total signal in LYRA channels 1 and 2. The percentage contributions correspond to the time of the first light. . . . .	38
2.3	Summary of the main LYRA data products distributed to the scientific community. These products are processed after each data download ( <i>i.e.</i> every three to four hours). . . . .	41
2.4	Excess of spectral irradiance as observed by LYRA compared to TIMED/SEE and SORCE/SOLSTICE measurements. . . . .	50
2.5	Variation percentage in LYRA calibrated data induced by the use of an alternative reference spectrum (these values are for the nominal unit of LYRA). . . . .	57

4.1	Characteristics of the X9.3 Flare of 2017 September 6 Observed by LYRA and the Geostationary Operational Environmental Satellite (GOES) . . . . .	81
5.1	Periods associated to the fundamental mode of standing MHD waves. $L$ is the loop length, $C_{A0}$ and $C_{Ae}$ are the internal and external Alfvén speeds, $\rho_0$ and $\rho_e$ the internal and external plasma densities and $C_{S0}$ is the internal sound speed. . . . .	92
5.2	Periods detected in the flares of GOES class M5 and higher during Solar Cycle 24 observed by both PROBA2/LYRA in the zirconium channel and SDO/EVE/ESP-Q. Asterisks indicate that the flares occurred close to the limb ( <i>i.e.</i> at a longitude above $80^\circ$ east or west). . . . .	117
5.3	Line ratios and corresponding electron densities for the X4.9 flare on 25 February 2014. . . . .	125



# Preface

When I started this PhD, the main objective was to refine our understanding of solar flares - a vast topic with many unknowns - exploiting the data produced by a Belgian solar instrument, the LYRA radiometer onboard the PROBA2 microsatellite of the European Space Agency (ESA). The instrument was observing the Sun in four spectral bands in the ultraviolet/extreme ultraviolet with a high acquisition cadence, and was a promising tool for the analysis of flares.

We were planning to use the multi-wavelength observations of LYRA together with other instruments, to build a consistent picture of the flare evolution over the solar spectrum and to check its compatibility with the so-called "standard model" of flares.

We also wanted to exploit the high acquisition cadence of the instrument to shed a new light on the understanding of the short time-scale oscillations, called quasi-periodic pulsations (or QPPs), that are observed in the irradiance measurements, in particular during the impulsive phase of many flares. QPPs might indeed be related to some of the important questions about flares that remain unanswered and that compromise our ability to predict the properties of those events: Are MHD waves, and in particular Alfvén waves, always associated to the flaring process and could those waves play a role in the transport of energy from the reconnection site in the corona to the lower levels of the solar atmosphere? What triggers the reconnection process thought to be at the origin of the flare? Can it be caused by an external trigger, such as a nearby oscillating loop? Is it a steady process? For the time being, the origin of QPPs is still not well understood. But it is strongly believed that they are either caused by MHD waves or result from fluctuations of the particles acceleration that is a consequence of the magnetic reconnection process. In the first case, the QPPs would characterize the properties of MHD waves in flares. In the second case, the properties of QPPs would inform us on the conditions in which the reconnection occurs. In all cases, studies of QPPs promised to lead to new

advances in understanding the flaring process, and LYRA seemed to be an excellent tool for observing them.

In order to use the LYRA data properly, a lot of work was needed at the calibration level before it was possible to interpret the results. The PhD work therefore included a significant instrumental part.

Even if LYRA quickly proved to be a very good flare monitor with its two extreme ultraviolet (EUV) channels, only a few cases produced a signature in the two ultraviolet (UV) ones. The analysis of these few cases was complicated by instrumental problems, in particular by the strong contamination that progressively changed the spectral response of the instrument. In contrast, the fast acquisition cadence appeared to be a valuable asset for the detailed analysis of the flare temporal evolution in general, and of the QPPs in particular. Therefore, a big part of the observational and scientific work was devoted to this topic. The comparison of the temporal evolution of flares in multiple wavelengths was limited to the analysis of the only event that has produced (at the time of writing) a signature in all four channels of the instrument. This event proved to be crucial for improving our understanding of the flare emission processes at the UV wavelengths.

# Chapter 1

## Introduction

As introduced in the Preface, this thesis aims at contributing to the global understanding of solar flares. More specifically, it addresses the questions of how the flare emission is produced in various wavelength ranges and of what mechanism produces quasi-periodic pulsations (QPPs). This chapter recapitulates some general information about the Sun, the solar flares, and QPPs that is needed for the rest of the thesis. It also gives a brief introduction to measurements of the solar irradiance and to the LYRA radiometer, which is the main instrument used in this thesis.

### 1.1 The Sun: a Few Reminders...

Our star, the Sun, is a star of the Milky Way galaxy, situated at  $\simeq 26500$  light-years from its center, *i.e.* approximately midway of its radius. This is a common yellow dwarf belonging to the main sequence of the Hertzsprung-Russell diagram, with a blue-visible (B-V) index of 0.66, corresponding to a temperature of 5772 K (see Figure 1.1). The Sun is currently at the half of its life, which is estimated to 10 billion years (Foukal, 2004).

The Sun is mainly composed of hydrogen and helium (in mass proportions of respectively 78% and 20% at its surface level, see *e.g.* Clette, 2017), plus a number of heavier elements in much smaller proportions. However, those trace elements often play a key role in observations of the Sun, as we will see later.

The Sun is globally structured in several layers that require specific means of observations (Poedts, 2015). The 'interior' of the Sun is divided into the core,

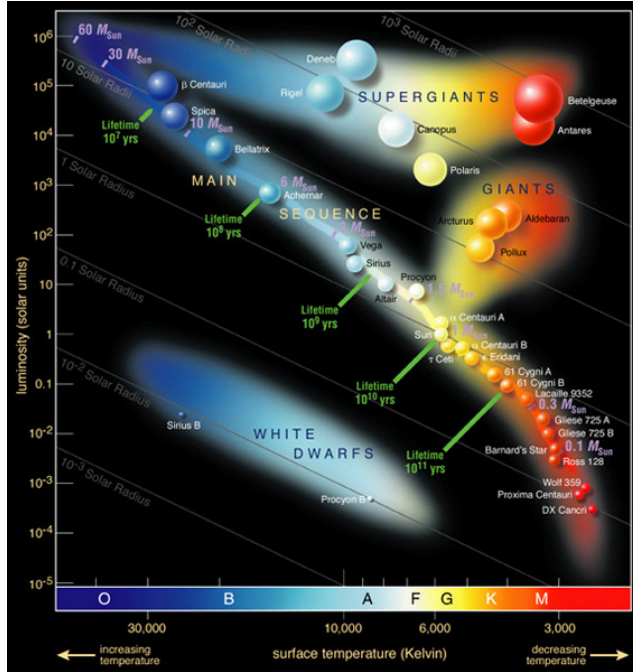


Figure 1.1: The Hertzsprung-Russell diagram (credit: ESO).

the radiative zone and the convection zone (see Figure 1.2). The core is the location where the fusion reactions that convert H into He take place. The temperature in the core reaches 15 million K. This is the origin of most of the energy radiated in the solar system. The radiative and convection zones differ by the way the energy produced in the core is transported through them. In the radiative zone, the very high density prevents most movements of the plasma and the energy propagates in a purely radiative way, while in the convection zone, the density has dropped sufficiently to allow convective movements of plasma to participate to the energy transport. The solar interior is optically thick to any wavelength. We have no direct visual means to investigate this part of the Sun, which is instead studied indirectly using helioseismology.

Above the convection zone, the 'atmosphere' of the Sun is comprised of the photosphere, the chromosphere and the corona, with the so-called 'transition region' constituting the interface between the latter two (Phillips et al., 2008). The three regions show drastic differences in terms of their temperature and density, as is illustrated in Figure 1.3.

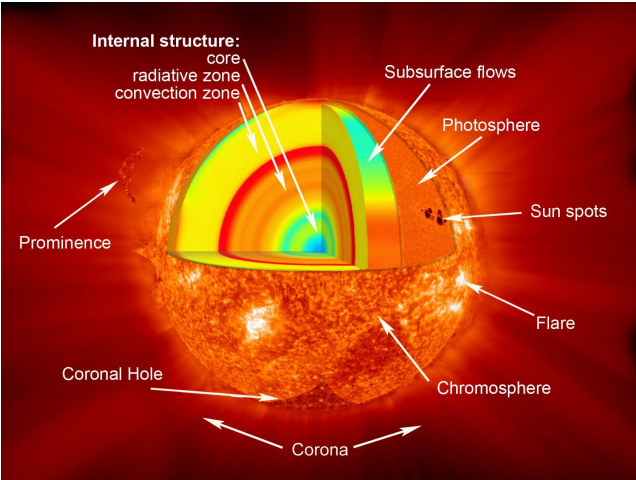


Figure 1.2: The various layers of the Sun (credit: NASA/Goddard).

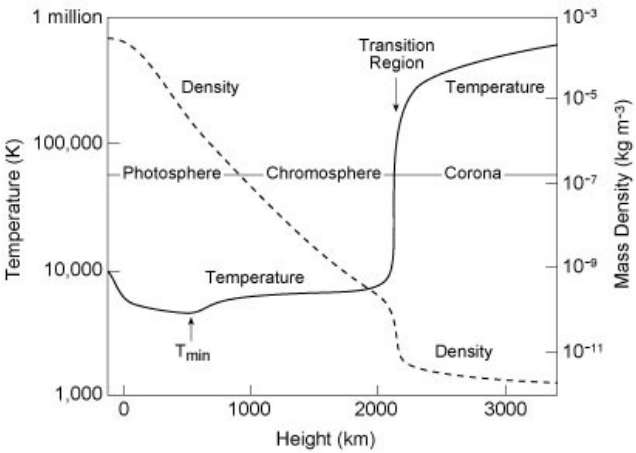


Figure 1.3: Structure of the temperature and density throughout the solar atmosphere (credit: E. Avrett, Smithsonian Astrophysical Observatory).

The photosphere, considered as the solar surface, is the place where the optical depth at  $5000 \text{ \AA}$   $\tau_{5000} = 2/3$ . Its temperature (around  $5772 \text{ K}$ ) is characterized by a negative gradient versus the altitude. Mainly observed in white light, its spectrum appears as a continuum dashed by absorption lines. In images, at large scales, it shows a uniform aspect, with faculae and occasional sunspots structuring it. But when looking at smaller scales, the homogeneous background is actually constituted of myriads of granules. This layer is also the only one for which we have been so far able to measure the magnetic field routinely (Phillips et al., 2008).

In the chromosphere, the temperature increases from its minimum around  $4000 \text{ K}$  up to  $20000 \text{ K}$  (Phillips et al., 2008). It shows another level of convection as super-granulation and various other structures, including prominences. The chromosphere can be imaged in various spectral lines and continua, also in the ultraviolet (UV) spectral range, the main one being the  $H\alpha$  line. The transition region between the chromosphere and the corona is the place of a dramatic increase of the temperature, which has been puzzling the solar scientists for more than half a century.

The upper part of the solar atmosphere, the corona, is where the signatures of the solar activity, such as flares, filament eruptions, coronal mass ejections (CMEs), EUV waves and dimmings, are the best seen (Golub and Pasachoff, 2009). It is usually imaged in the soft X-rays (SXR) and extreme ultraviolet (EUV).

In conclusion, the Sun is a very ordinary star. The main interest of studying it lies in its closeness to Earth (to which the mean distance is  $150$  million km), which makes it currently the only star allowing routine spatially resolved observations. As such, it constitutes the cornerstone on which we build our understanding of all the other stars.

## 1.2 Solar Radiation

As no instrument can currently be sent to the Sun to perform in-situ measurements of the photosphere and the chromosphere, most of the knowledge that we collected about our star was deduced from in-depth analysis of the light it emits. The global form of the solar spectrum, the position of the emission and absorption spectral lines, their width, intensity and Doppler shift inform us on the composition, density, temperature, pressure and flows that characterise the different zones of the Sun (Griem, 1997). The equation describing the emission and absorption by a volume of plasma is the radiative transfer equation (Golub

and Pasachoff, 2009):

$$\frac{dI_\nu}{ds} = -\alpha_\nu I_\nu + j_\nu, \quad (1.1)$$

where:

- $\nu$  is the frequency,
- $I_\nu$  is the specific intensity or spectral radiance,
- $j_\nu$  is the monochromatic emission coefficient,
- $\alpha_\nu$  is the absorption coefficient,
- $s$  is the distance travelled through the medium.

This equation can be re-written as

$$\frac{dI_\nu}{d\tau} = -I_\nu + S_\nu, \quad (1.2)$$

with:

- the source function  $S_\nu = \frac{j_\nu}{\alpha_\nu}$ ,
- the optical depth  $\tau_\nu(s) = \int_{s_0}^s \alpha_\nu(s') ds'$ , i.e.  $d\tau = \alpha_\nu ds$ . Its negative exponential function  $\exp(-\tau_\nu)$  describes the probability for an emitted photon to escape the atmospheric layer instead of being re-absorbed. We say that a medium is optically thick when  $\tau_\nu > 1$ . On the contrary, an optically thin (or transparent) medium is such that  $\tau_\nu < 1$ .

Solving Equation 1.2, after identification of  $S$  and  $\tau$ , helps interpreting the observations.

The Sun radiates in all wavelengths from  $\gamma$ -rays to radio. In the UV, visible (VIS) and infrared (IR) spectral ranges, which are emitted by the photosphere, the spectrum is close to that of a blackbody at the temperature of 5772 K, striped by absorption/emission lines and continua (see Figure 1.4, top panel). The source function is the Planck function  $B_\nu$  describing the blackbody emission (Phillips et al., 2008):

$$B_\nu(T) = \frac{2h\nu^3}{c^2} \frac{1}{\exp(\frac{h\nu}{kT}) - 1}, \quad (1.3)$$

where  $h$  is the Planck constant,  $c$  is the speed of light,  $\nu$  is the frequency,  $k$  is the Boltzmann constant, and  $T$  is the temperature.

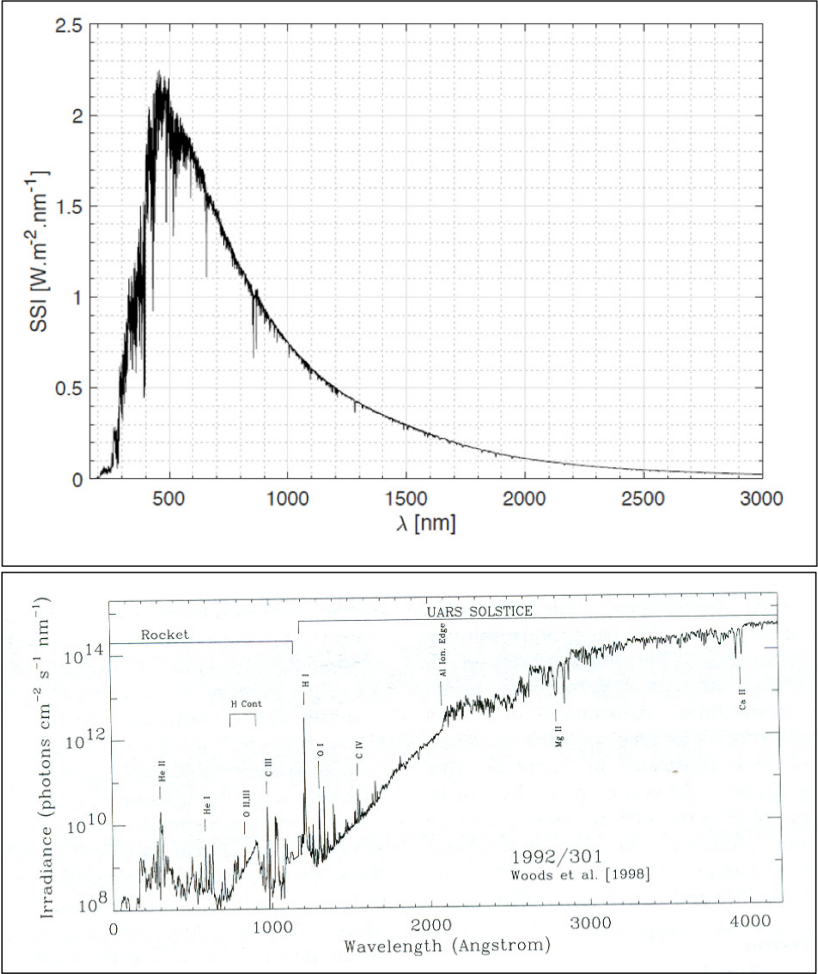


Figure 1.4: Top panel: The full reference solar spectrum based on ISS/SOLSPEC data. Credit: Meftah et al. (2018). Bottom panel: UARS observations of the wavelengths around 2000 Å, where the spectral lines change from absorption to emission. Credit: Woods et al. (1996)



The photospheric blackbody spectrum constitutes 99% of the total emission of the Sun. As the density in this layer of the solar atmosphere is high, collisions between particles are frequent. Furthermore, the emitted photons can easily be reabsorbed. These processes participate in establishing a balance between the thermal and average kinetic energy, resulting in local thermodynamic equilibrium (LTE) conditions where the emission only depends on the temperature and the density of the medium.

The comparatively low temperature of the photosphere allows a significant fraction of its atoms and ions to remain close to their fundamental levels, and the spectral lines corresponding to the transitions between low atomic levels can be observed. However, because of the negative temperature gradient characterizing the photosphere, those lines usually appear in absorption. Higher up in the chromosphere, where the temperature gradient has reverted, spectral lines are seen in emission (Foukal, 2004).

Indeed, the core of a spectral line of an element is emitted at a higher altitude than its wings (see Figure 1.5). This comes from the fact that a photon with the wavelength at the core of a spectral line has a higher probability to be re-absorbed than a photon of which the wavelength belongs to the line wings (i.e. the medium is optically thicker at the core of the line).

In the corona, where the density is much lower and the collisions are rare, the emission is no longer the one of a black-body. The medium is optically thin. The emission, which results from one of the following processes: de-excitation (bound-bound emission), recombination of ionized electrons with ions (free-bound emission), or bremsstrahlung (free-free emission), comes from the whole optical path. As the coronal temperature easily reaches the million degrees, the main elements are fully ionized, (although some remanent emission in spectral lines such as Lyman- $\alpha$  exist, primarily caused by resonance scattering of chromospheric Lyman- $\alpha$  from the residual neutral hydrogen in the corona, see *e.g.* Gabriel, 1971). The main elements to emit are the rarer ones that can undergo multiple ionizations, such as Fe, Si, S, or O, and each degree of ionization can only exist for a given range of temperatures (see Figure 1.6). For each temperature range, the number of allowed transitions is therefore limited, and the coronal spectrum could in principle be modelled by considering each of these transitions individually (Golub and Pasachoff, 2009):

$$I_{ji}(\nu) = \frac{1}{4\pi} \int_z \frac{hc}{\lambda_{ji}} A_{ji} \frac{N_j}{N_{ion}} \frac{N_{ion}}{N_{el}} \frac{N_{el}}{N_H} \frac{N_H}{N_e} N_e dz, \quad (1.4)$$

where:

- $I_{ji}(\nu)$  is the spectral radiance associated to the transition  $j \rightarrow i$ ,

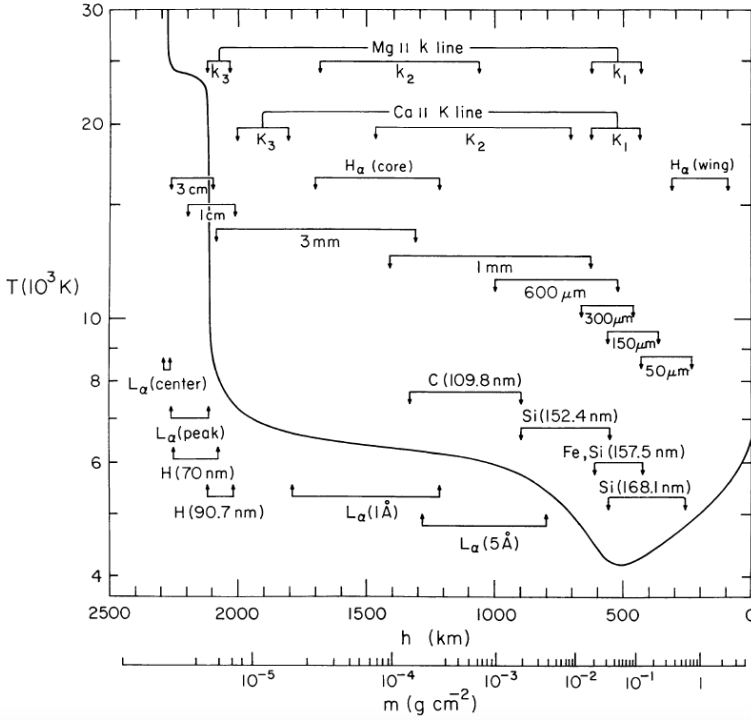


Figure 1.5: The quiet-Sun formation height for various spectral lines. The difference in the emission altitude corresponding to the core and the wings of a spectral line is well illustrated for the Lyman- $\alpha$  line. Credit: Vernazza et al. (1981).

- $z$  is the distance along the optical path,
- $\frac{hc}{\lambda_{ji}}$  is photon energy,
- $A_{ji}$  is Einstein spontaneous emission coefficient,
- $\frac{N_j}{N_{ion}}$  is the relative population of the excited level,
- $\frac{N_{ion}}{N_{el}}$  is the ionization fraction,
- $\frac{N_{el}}{N_H} = A_{el}$  is the relative abundance of the element to H,
- $N_e$  is the electron density,
- $\frac{N_H}{N_e}$  is approximately 0.8.

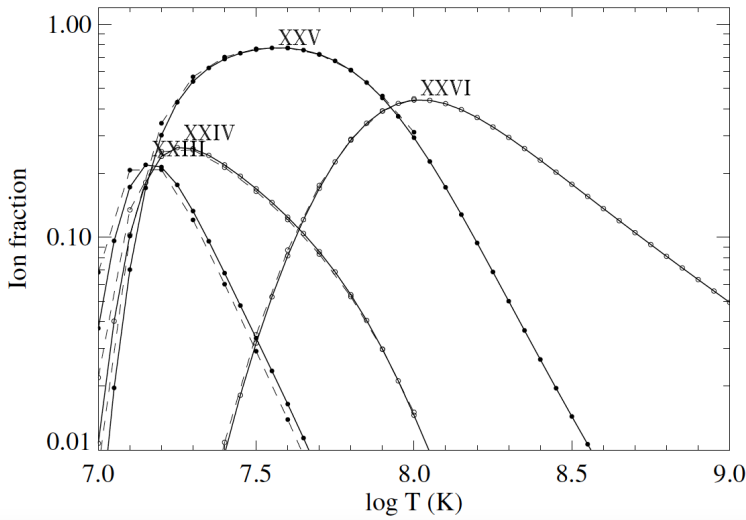


Figure 1.6: Ionization equilibria for Fe XXIV-XXVII as computed by Dere et al. (2009) (solid lines) in comparison with the previous work of Mazzotta et al. (1998) (dashed lines). Credit: Dere et al. (2009).

Practically however, such an approach remains an Herculean task, unless we rely on a few hypotheses:

- the corona is under ionization equilibrium, meaning that the number of ionizations is counterbalanced by the number of recombinations.
- the sum of collisional ionization plus auto-ionization is balanced by radiative and dielectronic recombinations. In other words, we can neglect the photo-ionization contribution as there is not enough photons with an energy high enough to cause the extra-ionization of elements that are often already multiply-ionized. On the contrary, because of the low density, the recombination is never triggered by a collision with a third particle (collisional recombination). It always induces the emission of a photon (radiative recombination). This results in relative abundancies of two levels of ionization for a given element that are essentially dependent on the temperature.
- the electrons in the excited levels are so easily ripped off that we can consider that each ion is in its ground state (two-level approximation).

- similarly, for the excitation processes, collisional excitation is balanced by radiative de-excitation. There is no radiative excitation or collisional de-excitation.

Under these hypotheses, the various ratios in Equation 1.2 simplify and can be estimated for each transition. It is common to regroup the physical parameters relative to the considered electronic transition between levels  $j$  and  $i$  in a *contribution function*  $G(T, N_e, A_{el})_{ji}$ , so that Equation 1.2 can be rewritten:

$$I_{ji}(\nu) = \frac{1}{4\pi} \int_z G(T, N_e, A_{el})_{ji} N_e^2 dz \quad (1.5)$$

$$= \frac{1}{4\pi} \int_T G(T, N_e, A_{el})_{ji} DEM(T) dT, \quad (1.6)$$

where:

- $G(T, N_e, A_{el})_{ji}$  is the contribution function,
- $DEM(T) = N_e^2 \frac{dz}{dT}$  is the so-called Differential Emission Measure Function.

The equation clearly highlights the dependance of the emission at a given wavelength on  $N_e^2$ .

To wrap-up, the contribution of different physical processes to each spectral range can be summarized as (Foukal, 2004):

- X-rays (wavelengths below 10 nm): emission line spectrum produced by highly ionized species,
- EUV (wavelengths between 10 and 120 nm): emission line spectrum produced by neutral and moderately ionized species, as well as a few recombination continua,
- UV (wavelengths between 120 nm and 400 nm): stronger recombination continua, emission and absorption line spectrum produced by the photosphere and chromosphere around the temperature minimum,
- Visible (wavelengths between 380 and 760 nm): H- bound-free continuum with absorption lines,
- IR (wavelengths between 760 nm and 1 mm): H- free-free continuum, mostly line-free, except for a few molecular bands,
- Radio (wavelengths above 1 mm): thermal and, increasingly, non-thermal emission continua.

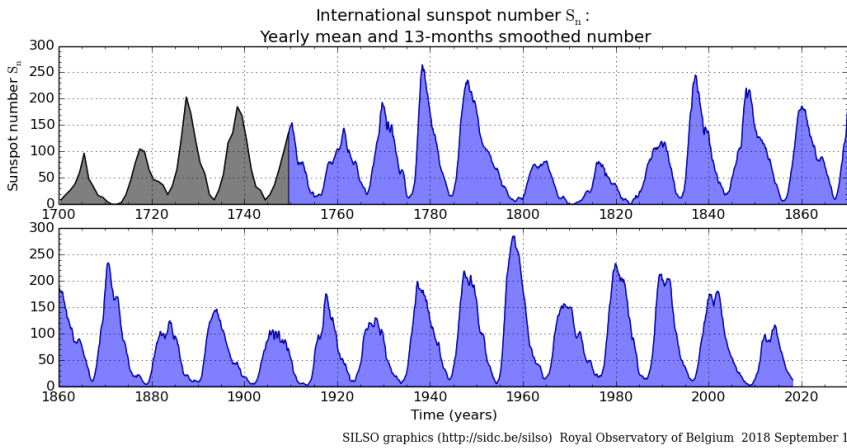


Figure 1.7: The sunspot number evolution since the beginning of the observations. The 11-year solar cycle is clearly visible. Credit: SILSO / Royal Observatory of Belgium

### 1.3 The Solar Activity Cycle

Most of the solar time series, such as the sunspot number or measurements of the solar irradiance (especially in the EUV or X-ray ranges), show a cyclic behaviour with the period of approximately 11 years, during which the Sun activity goes through phases of maximum and minimum (see Figure 1.7). Phases of maxima are characterized by an increase of the solar activity, of which the most spectacular manifestations are solar flares and coronal mass ejections (CMEs). During each cycle, the global solar magnetic field is progressively reconfigured, so that it has reverted at the end of the 11-years period.

This cycle is driven by the conjunction of two mechanisms (Paterno, 1998): the omega effect (see Figure 1.8, panels a to c) induced by the differential rotation, and the alpha effect (see Figure 1.8, panel d).

The differential rotation refers to the fact that the Sun does not rotate as a solid body. The rotation speed varies as a function of the radial distance from the Sun centre as well as a function of the latitude (the equator, at the surface level, rotates in 25 days, while 33 days are needed for the poles to complete their rotation). This differential rotation stretches the magnetic field lines in the Sun interior (the omega effect), progressively winding them, until they become unstable. At this point, a small instability can cause magnetic field lines to rise up and emerge above the solar surface, forming local magnetic

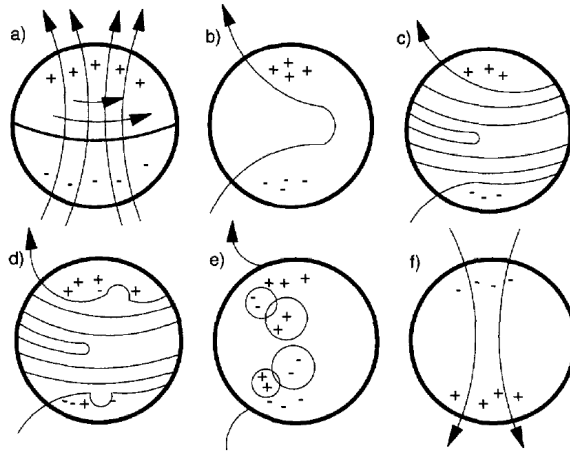


Figure 1.8: Evolution of the global internal magnetic field along the solar cycle. Panels a to c show the progressive winding of the internal field as it is stretched by the differential rotation of the Sun. Panel d shows the formation of a magnetic loop. Panel e shows the emergence of the magnetic loop above the photosphere. The positive and negative magnetic regions correspond to the footpoints of the emerged loop. Credit: Paterno (1998).

loops, often twisted under the Coriolis Force (the alpha effect). These magnetic structures, which can be more or less complex, evolve rapidly on a time scale of a few (tens of) days (see for example Babcock, 1961; Paterno, 1998, and Figure 1.8). Occasionally, two arms of such magnetic loops end up reconnecting, reconfiguring the local magnetic field and generating eruptions that can be characterized by flares, CMEs and/or acceleration of particles up to relativistic speeds.

## 1.4 A Manifestation of Solar Activity: Solar Flares

In this work, I will put a particular emphasis on flares, which could be described as a local transient increase of temperature and radiance over the whole solar spectrum from radio to gamma rays (Hudson, 2011).

Observationally, flares are usually first seen in the radio and HXR wavelengths (characterizing the non-thermal emission) where they show a very peaky profile. Chromospheric wavelengths (such as Lyman- $\alpha$  or H- $\alpha$ ) tend to track the

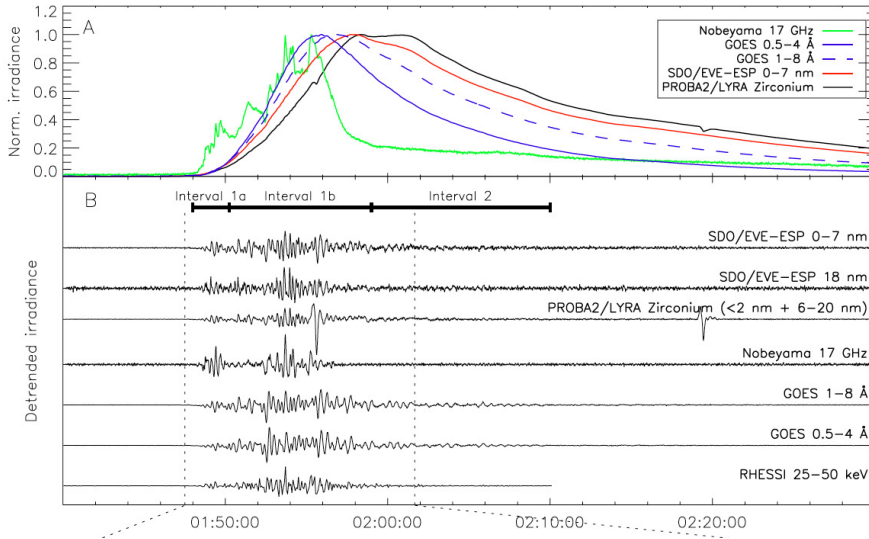


Figure 1.9: Observations of the X2.2 flare on 15 February 2011 in multiple bandpasses, in the radio (Nobeyama), SXR (GOES), and EUV (EVE and LYRA) ranges. The sequence in which the various wavelengths peak is clearly visible. Credit: Dolla et al. (2012).

non-thermal emission (Milligan and Chamberlin, 2016). Although the first observations of a flare was made in white light in 1859 by Carrington and by Hodgson (Carrington, 1859; Hodgson, 1859), white-light flares turn out to be quite rare and their location and emission mechanism are still debated (see e.g. Song et al., 2018). However, when observed, the white light emission is produced either simultaneously or soon after the non-thermal emission. Eventually, the flare becomes visible in the SXR and EUV wavelengths, starting with the ones that correspond to the hottest emission temperature. The profile of the flare in wavelengths associated to thermal emission is much smoother than in the non-thermal emission and it persists much longer, as is illustrated in Figure 1.9.

Detailed reviews of the observational characteristics of solar flares can be found in Fletcher et al. (2011) or Benz (2017).

Flares are usually categorized as a function of their peak irradiance in the 1–8 Å channel of the GOES satellite, which serves as the reference (see Table 1.4).

Conceptually, the flare mechanism is described by the CSHKP model (the so-called ‘standard model’, see Carmichael, 1964; Sturrock, 1968; Hirayama, 1974; Kopp and Pneuman, 1976; Svestka and Cliver, 1992, etc). Figure 1.10

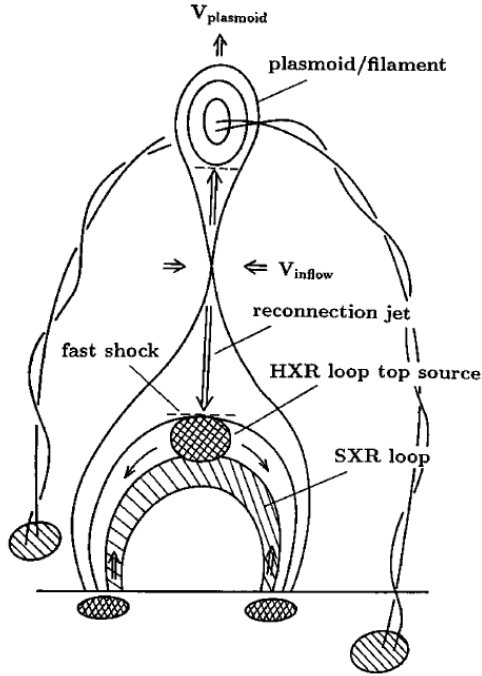


Figure 1.10: The standard model of a flare. Credit: Shibata et al. (1995).

Flare class	Peak irradiance ( $Wm^{-2}$ )
A	1.E-8 - 1.E-7
B	1.E-7 - 1.E-6
C	1.E-6 - 1.E-5
M	1.E-5 - 1.E-4
X	1.E-4 and above

Table 1.1: Definition of the reference flare classes, based on the peak irradiance measured by GOES in the 1–8 Å passband.



illustrates it in the context of a filament eruption. This situation, however, is not the only one for which the standard model is valid. Strictly speaking, this model applies to any two-ribbon eruptive flare.

The standard model scenario supposes that a significant amount of magnetic energy has been stored in corona prior to the flare, either by shearing and twisting existing magnetic loops, or by the emergence of new magnetic field. Sometimes, opposite magnetic field lines are compressed against each other, either over a point (we speak of an X-type neutral point), or over a longer segment (creating current sheets), steepening the magnetic field gradient and hence increasing the current density. Such configurations offer favourable conditions for magnetic reconnection to happen. Magnetic reconnection, although not being strictly speaking part of the standard model, is often considered as the first step of the flaring process. Magnetic reconnection accelerates coronal particles (mostly electrons) away from the reconnection site to non-thermal speeds. The particles accelerated downward propagate along the magnetic field lines almost collisionlessly, producing gyrosynchrotron emission in the radio range at first, then hard X-rays bremsstrahlung when the density increases (Aschwanden, 2005). Their journey ends in the much denser chromosphere, where they interact with the ambient plasma, heating it via Coulomb collisions to temperatures of millions degrees. Due to its higher temperature, the heated plasma fills up the newly reconnected loops and becomes visible in soft X-rays and in the longer wavelengths as the plasma cools down. This process is called the 'chromospheric evaporation'.

Shocks can also participate in the acceleration of particles and to the heating process (Aschwanden, 2005). Shocks have been found to happen in the flanks of the reconnection regions (Petschek mechanism), as well as at places where the accelerated electron beam hits the top of the reconnected loops (the termination shock – as illustrated in Figure 1.10).

The standard model provides an accurate phenomenological description of the flare. It explains most of the observations, in particular the flare emission increase in all wavelengths, and even the temporal sequence in which these wavelengths peak (see Figure 1.9 for an example). However, it leaves most of the details of the process not addressed and it has difficulties when trying to explain the quantitative aspects. One of the main pending questions is how the huge amount of energy released during flares is transported from the reconnection site in the corona to the chromosphere. Obviously, the beam of accelerated electrons could play this role, but it does not seem sufficient to explain the energy of  $10^{32}$  erg released during major flare events. Such energies would require emptying the portion of the corona above the active regions of its electrons. Not only is this rather unlikely, but also, as a reaction, we would expect a return current to replenish the corona. Such a return current was

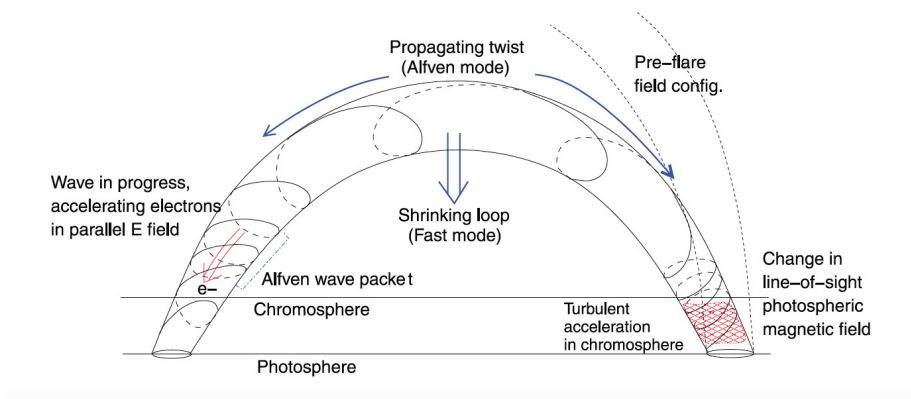


Figure 1.11: Transport of the energy from the reconnection site in the corona to the chromosphere by Alfvén waves. Credit: Fletcher and Hudson (2008).

never observed so far. Some authors therefore suggested that a part of the flare energy could rather be transported downward by Alfvén waves (see next Section), which would accelerate the chromospheric electrons in situ (Fletcher and Hudson, 2008, and Figure 1.11). The debate remains currently open. The detection of flare features that could be unambiguously related to Alfvén waves would be a strong argument in favor of this theory.

Another drawback of the model is that it does not address reconnection, which is thought to be the trigger mechanism at the origin of most flares and is likely to significantly impact the flare profile. Does reconnection happen in one shot? Is it a steady process? The two main models of reconnection, i.e. the Sweet-Parker model (Sweet, 1958) and the Petschek model (Petschek, 1964), see Figure 1.14 (left panel), respectively postulate a slow and a fast reconnection.

But the real situation is probably more complex. For example, numerical simulations (see Shibata and Takasao, 2016, and references therein) have shown that in current sheets with a Lundquist number  $S$  above  $\sim 10^4$ , magnetic islands tend to form as a result of a tearing instability (see Figure 1.14, right panel). Here,  $S = LC_A/\eta$ ,  $L$  is the length of the current sheet,  $C_A$  is the Alfvén speed and  $\eta$  is the magnetic diffusivity. These plasmoids can coalesce before being eventually ejected. Such a process results in non-continuous reconnection and could be at the origin of the Quasi-Periodic Pulsations (or QPPs) introduced in Section 1.5.

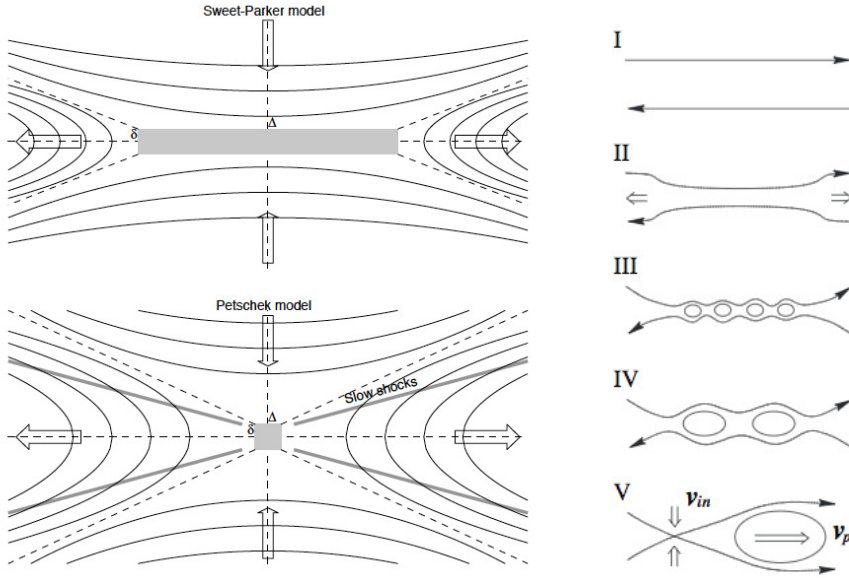


Figure 1.12: Various scenarii of reconnection. Top-left panel: the Sweet-Parker reconnection. Bottom-left panel: The Petschek reconnection. Both left panels are from (Aschwanden, 2005). Right panel: plasmoid-induced reconnection from (Shibata and Takasao, 2016)

## 1.5 Zooming on a Flare Curve: the Quasi-Periodic Pulsations (QPPs)

Quasi-periodic pulsation (QPP) is a generic term referring to an oscillatory pattern observed in integrated solar and stellar emission during flares. QPPs were initially observed in the hard X-rays (HXR) and radio wavelength ranges (see *e.g.* Parks and Winckler, 1969; Kane et al., 1983). In the past decade, a new generation of space instruments has allowed extending the observation of QPPs to other parts of the solar spectrum. In particular, the *Large Yield Radiometer* (LYRA – Hochedez et al., 2006; Dominique et al., 2013) onboard the *PROject for On-Board Autonomy 2* (PROBA2) and the *Extreme Ultraviolet Variability Experiment* (EVE – Woods et al., 2012) onboard the *Solar Dynamics Observatory* (SDO) detected QPPs in soft X-rays (SXR) and extreme ultraviolet (EUV) emission of the million-degree solar corona (*e.g.* Van Doorselaere et al., 2011; Dolla et al., 2012; Simões et al., 2015). The *Interface Region Imaging Spectrograph* (IRIS – De Pontieu et al., 2014) detected QPPs in the ultraviolet

emission of cooler layers of the solar atmosphere down to the chromosphere (*e.g.* Brosius and Daw, 2015; Brosius et al., 2016; Tian et al., 2016).

Figure 1.13 provides an example of QPPs taken from McLaughlin et al. (2018) for the X4.9 flare on 25 February 2014 in the HXR, radio, and EUV ranges.

Even though the QPP phenomenon has been known for decades, its origin remains highly debated and may depend on the considered range of periods and wavelengths. However, QPPs have also been reported during stellar flares (*e.g.* Mathioudakis et al., 2003, 2006; Mitra-Kraev et al., 2005), which probably points to a mechanism intrinsically correlated to the flare process itself.

Sub-second QPPs are often attributed to cyclic behaviors of self-organizing systems driven by wave–wave or wave–particle interactions (see for example reviews by Aschwanden, 1987; Zaitsev and Stepanov, 2008).

For QPPs with second-to-minute periods, two main mechanisms are usually considered (see Nakariakov and Melnikov, 2009; Van Doorselaere et al., 2016, for an update). The first mechanism is the fluctuating particle acceleration that could be caused, *e.g.* by an oscillatory magnetic reconnection (if reconnection is not a continuous process, but rather follows an energy load/unload sequence, the resulting acceleration of coronal electrons also proceeds at a fluctuating rate). The second mechanism is the perturbation of the flaring magnetic environment by magnetohydrodynamics (MHD) waves. Such waves could affect the newly reconnected post-flare magnetic loops along which the accelerated electron beam propagates, hence modulating the densities of the electron beam and/or heated chromospheric plasma.

Evidence of MHD waves in the corona are numerous (see *e.g.* Nakariakov and Verwichte, 2005). New models and simulations have also demonstrated that several mechanisms inherent to the magnetic reconnection and to the particles acceleration could produce QPPs (see *e.g.* Guidoni et al., 2016; Takasao and Shibata, 2016; McLaughlin et al., 2018, and references therein for a review). However, so far, observations have not been able to clearly distinguish between the two mechanisms.

QPPs associated to stellar flares show periodicities compatible with the ones found in solar flares, as well as longer ones (up to thousands of seconds), which could be explained by the relatively lower duration and amplitude of the solar events (see Van Doorselaere et al., 2016). Analyzing the periods (of several minutes or more) detected in the decaying phase of 11 stellar flares, Pugh et al. (2016) found no correlation with the star characteristics, such as its temperature, radius or rotation period.

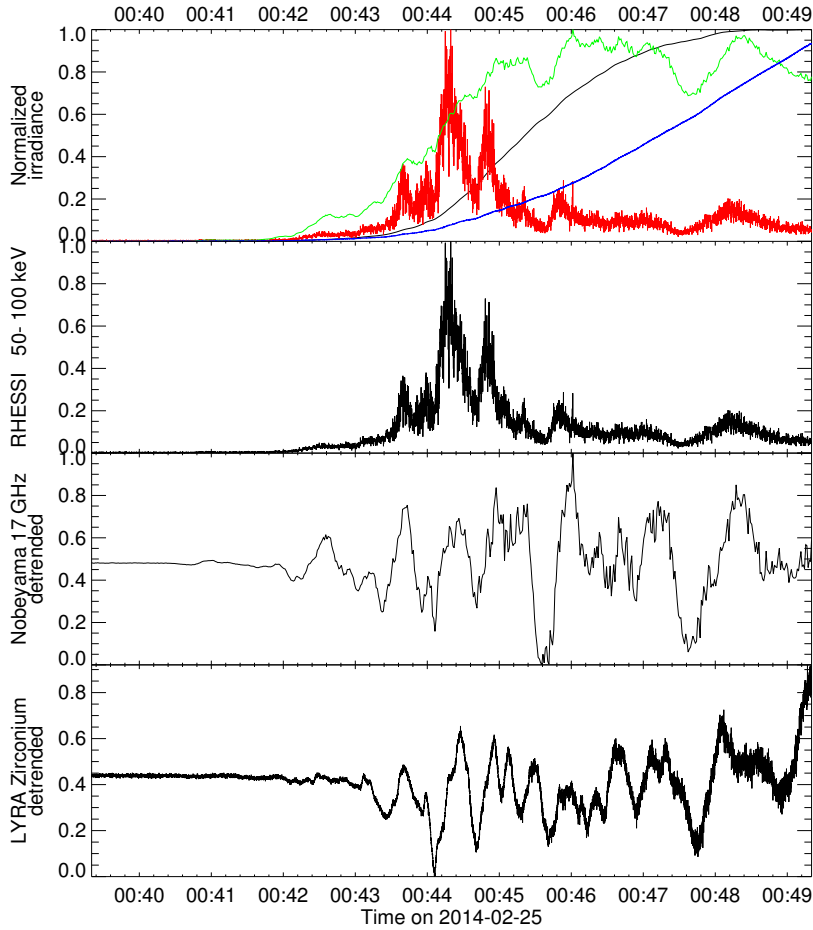


Figure 1.13: QPPs detected during the X4.9 flare of 25 February 2014. Top panel: the normalized irradiance from GOES 0.1–0.8 nm (black), LYRA 1–20 nm (blue), RHESSI 50–100 keV (red) and Nobeyama 17 GHz (green). Second, third and fourth panels: the same time series for respectively RHESSI, Nobeyama and LYRA, detrended with a 50 s window. The oscillating pattern was clearly visible in the HXR and radio time series, without the need to detrend the data. This is no longer the case when looking at SXR or EUV data, for which a detrending is required to highlight the oscillations. Credit: McLaughlin et al. (2018)

### 1.5.1 MHD Waves as a Source of QPPs

A possible source of QPPs in flares are magnetohydrodynamic (MHD) waves. Waves with a vast range of wavelengths and periods propagate in the solar atmosphere. Those with wavelengths and periods longer than respectively the ion gyroradius and the ion gyroperiod, can be adequately represented in the single-fluid MHD approximation, which provides a macroscopic description of the plasma behavior, without distinguishing between electrons and ions (Nakariakov and Verwichte, 2005; Goedbloed and Poedts, 2004). The ion gyroradius  $R_i$  and gyroperiod  $P_i$  can be expressed by:

$$R_i = v_{\perp,i} m_i / (ZeB), \quad (1.7)$$

$$P_i = 2\pi m_i / (ZeB), \quad (1.8)$$

where  $v_{\perp}$  is the component of the particle velocity that is perpendicular to the magnetic field  $B$ ,  $m$  is the particle mass,  $Z$  is the ion charge number ( $Z = 1$  for hydrogen), and  $e$  is the electron charge.

Typically, in coronal loops,  $B \sim 0.03$  T,  $R_e \sim 1$  mm,  $R_i \sim 4.9$  cm,  $P_e \sim 1.2 \cdot 10^{-9}$  s and  $P_i \sim 2.2 \cdot 10^{-6}$  s.

For non-relativistic speeds, the main equations constituting this framework are (Goedbloed and Poedts, 2004):

$$\frac{\partial \rho}{\partial t} + \nabla \cdot (\rho \mathbf{v}) = 0, \quad \text{Mass continuity equation} \quad (1.9)$$

$$\rho \left( \frac{\partial \mathbf{v}}{\partial t} + (\mathbf{v} \cdot \nabla) \mathbf{v} \right) + \nabla p - \rho \mathbf{g} - \mathbf{j} \times \mathbf{B} = 0, \quad \text{Momentum equation} \quad (1.10)$$

$$\frac{\partial p}{\partial t} + \mathbf{v} \cdot \nabla p + \gamma p \nabla \cdot \mathbf{v} = (\gamma - 1) \eta |\mathbf{j}|^2, \quad \text{Energy equation} \quad (1.11)$$

$$\frac{\partial \mathbf{B}}{\partial t} + \nabla \times \mathbf{E} = 0, \quad \text{Faraday equation} \quad (1.12)$$

$$\mathbf{j} = \frac{1}{\mu_0} \nabla \times \mathbf{B}, \quad \text{Ampère equation} \quad (1.13)$$

$$\mathbf{E} + \mathbf{v} \times \mathbf{B} = \eta \mathbf{j}, \quad \text{Ohm equation} \quad (1.14)$$

$$\nabla \cdot \mathbf{B} = 0, \quad (1.15)$$

where  $t$  is the time,  $\rho$  is the mass density,  $p$  is the plasma pressure,  $\mathbf{v}$  is the velocity field,  $\mathbf{B}$  is the magnetic field,  $\mathbf{E}$  is the electric field,  $\mathbf{j}$  is the current density,  $\mu_0$  is the vacuum permeability,  $\eta$  is the resistivity, and the adiabatic index  $\gamma$  is set to 5/3.

These equations can be linearized by considering small perturbations of the main quantities ( $p = p_0 + \tilde{p}$ ,  $\rho = \rho_0 + \tilde{\rho}$ ,  $\mathbf{v} = \mathbf{v}_0 + \tilde{\mathbf{v}}$  and  $\mathbf{B} = \mathbf{B}_0 + \tilde{\mathbf{B}}$ ) and coupled. Then, in a homogeneous medium in the static equilibrium, considering that these small perturbations can be expressed in terms of a superposition of plane waves, *e.g.*  $\tilde{\mathbf{v}}(\mathbf{r}, t) = \sum_{\mathbf{k}} \hat{\mathbf{v}}_{\mathbf{k}} e^{i(\mathbf{k} \cdot \mathbf{r} - \omega t)}$ , and choosing a reference frame in cartesian coordinates, in which the initial magnetic field  $\mathbf{B}_0 = (0, 0, B_0)$  is parallel to the Z axis yields the dispersion equation:

$$(\omega^2 - k_{\parallel}^2 \frac{B_0^2}{\rho_0}) \left[ \omega^4 - k^2 \left( \frac{B_0^2}{\rho_0} + \frac{\gamma p_0}{\rho_0} \right) \omega^2 + k_{\parallel}^2 k^2 \frac{B_0^2}{\rho_0} \frac{\gamma p_0}{\rho_0} \right] = 0, \quad (1.16)$$

where  $k_{\parallel}$  is the component of the wave vector that is parallel to  $B_0$ .

The dispersion equation allows three groups of solutions that each define a type of MHD waves (Goedbloed and Poedts, 2004):

- Alfvén waves, for which

$$\omega = \pm\omega_A = \pm k_{\parallel} \frac{B_0}{\sqrt{\rho_0}},$$

correspond to incompressible perturbations of the velocity  $\tilde{\mathbf{v}}$  perpendicular to the plane defined by  $\mathbf{k}$  and  $\mathbf{B}_0$ , which propagate along  $\mathbf{B}_0$ ,

- Fast magneto-acoustic waves, for which

$$\omega = \pm\omega_f = \pm k \sqrt{\frac{1}{2} \left( \frac{B_0^2}{\rho_0} + \frac{\gamma p_0}{\rho_0} \right) + \frac{1}{2} \sqrt{\left( \frac{B_0^2}{\rho_0} + \frac{\gamma p_0}{\rho_0} \right)^2 - 4(k_{\parallel}^2/k^2) \frac{B_0^2}{\rho_0} \frac{\gamma p_0}{\rho_0}}},$$

correspond to compressible perturbations of the velocity  $\tilde{\mathbf{v}}$  in the plane defined by  $\mathbf{k}$  and  $\mathbf{B}_0$ , propagating in all directions, but with a greater speed perpendicularly to  $\mathbf{B}_0$ ,

- Slow magneto-acoustic waves, for which

$$\omega = \pm\omega_s = \pm k \sqrt{\frac{1}{2} \left( \frac{B_0^2}{\rho_0} + \frac{\gamma p_0}{\rho_0} \right) - \frac{1}{2} \sqrt{\left( \frac{B_0^2}{\rho_0} + \frac{\gamma p_0}{\rho_0} \right)^2 - 4(k_{\parallel}^2/k^2) \frac{B_0^2}{\rho_0} \frac{\gamma p_0}{\rho_0}}},$$

correspond to compressible perturbations of the velocity  $\tilde{\mathbf{v}}$  into the plane defined by  $\mathbf{k}$  and  $\mathbf{B}_0$ , which propagate preferentially along  $\mathbf{B}_0$ .

The three types of MHD waves are characterized by  $\omega_s^2 \leq \omega_A^2 \leq \omega_f^2$  and  $\hat{\mathbf{v}}_s \perp \hat{\mathbf{v}}_A \perp \hat{\mathbf{v}}_f$ .

One can follow a similar approach for a cylinder filled by a homogeneous plasma and imbedded in another homogeneous plasma, at the interface of which the displacements as well as the total pressures equilibrate. Such a configuration resembles a coronal loop or a flux rope. If  $L$  is the length of the loop,  $C_{S0} = \sqrt{\frac{\gamma p_0}{\rho_0}}$  is the internal sound speed,  $C_{A0} = \frac{B_0}{\sqrt{\mu_0 \rho_0}}$  is the internal Alfvén speed, and  $C_{Ae} = \frac{B_e}{\sqrt{\mu_e \rho_e}}$  is the external Alfvén speed, then it results in four types of deformations called MHD modes (Nakariakov and Melnikov, 2009):

- longitudinal modes are compressions of the plasma density along  $\mathbf{B}_0$  with the fundamental period  $P_{long} = 2L/C_{T0}$ , where  $C_{T0} = \frac{C_{S0}C_{A0}}{\sqrt{C_{S0}^2 + C_{A0}^2}}$  is the internal tube speed,



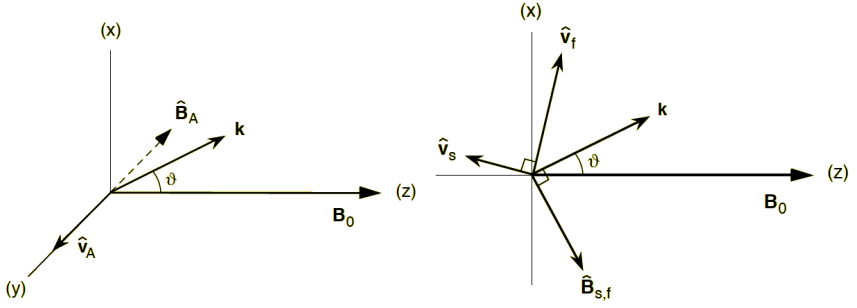


Figure 1.14: Velocity and magnetic field perturbations for Alfvén (left panel) and magneto-acoustic (right panel) waves, obtained from Equation 1.16. Credit: (Goedbloed and Poedts, 2004).

- sausage mode are compressive variations of the cylinder radius (Figure 1.15, Panel a) with the fundamental period  $P_{saus} = \frac{2L}{C_p}$ , where  $C_p$  is the phase speed of the sausage mode and  $C_{A0} < C_p < C_{Ae}$ ,
- kink modes are deformations of the cylinder axis (Figure 1.15, Panel b) with the fundamental period  $P_{kink} = \frac{2L}{C_k}$ , where  $C_k \simeq \sqrt{\left(\frac{2}{1+\rho_e/\rho_0}\right)} C_{A0}$ ,
- Torsional modes (Figure 1.15, Panel c) with the fundamental period  $P_{tors} = \frac{2L}{C_{A0}}$ .

It is important to distinguish between the speed at which the wave propagates and the type of deformation it induces. In the cylindrical approximation, Alfvén waves usually correspond to torsional deformations, while the longitudinal, kink and sausage modes can be either fast or slow. Under coronal conditions, the longitudinal modes are often associated to slow waves, while the kink and sausage modes usually correspond to fast waves. Note though that in realistic (complex) coronal conditions a strict separation of wave types may be very difficult, so the association of the wave speed and the type of deformation produced by the wave is not one-to-one.

MHD waves have been primarily studied for their potential implication in the coronal heating. Additionally, as the oscillations are dependent on the loop parameters, they provide a way to probe the magnetic loop characteristics, in particular its coronal magnetic field (coronal seismology). In this work, we will mainly consider MHD waves for their possible role in the production of QPPs (Nakariakov and Melnikov, 2009).

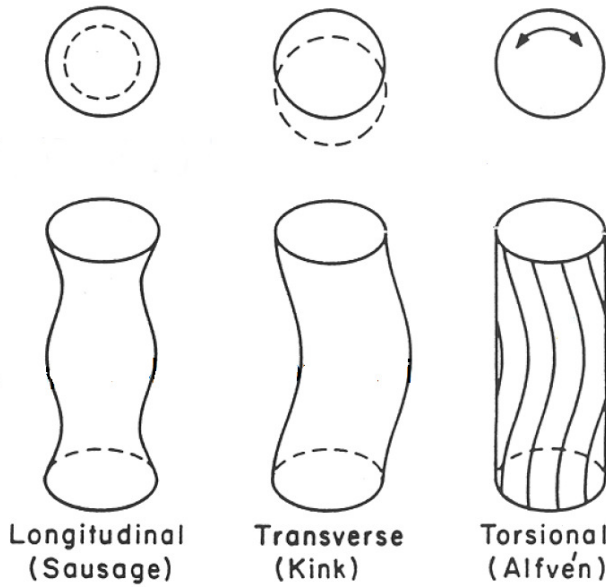


Figure 1.15: Illustration of different types of MHD oscillations in a plasma cylinder: sausage mode (Panel a), kink mode (Panel b), Torsional mode (Panel c). Credit: MPS

### 1.5.2 Fluctuating Particle Acceleration as a Source of QPPs

The other possible mechanism of QPPs is the acceleration of particles associated to the reconnection, if the reconnection does not proceed at a constant rate. Simulations showed that several processes could result in the particle acceleration being periodic (see McLaughlin et al., 2018, for a recent review).

For example, the reconnection could be repeatedly triggered by an external periodic driver, such as an oscillating neighbouring loop (Nakariakov et al., 2006). In some cases, even an aperiodic driver can result in a periodic modulation of the particle acceleration rate: a 2D X-type neutral point, if perturbed from its equilibrium position *e.g.* by a fast magnetoacoustic pulse (McLaughlin et al., 2009) or by the emergence of new magnetic flux (Murray et al., 2009), experiences "reconnection reversals", i.e. reconnections in which the directions of inflows and outflows are regularly inverted.

As we already mentioned in Section 1.4, the formation and coalescence of magnetic islands in a current sheet resulting from the tearing mode instability

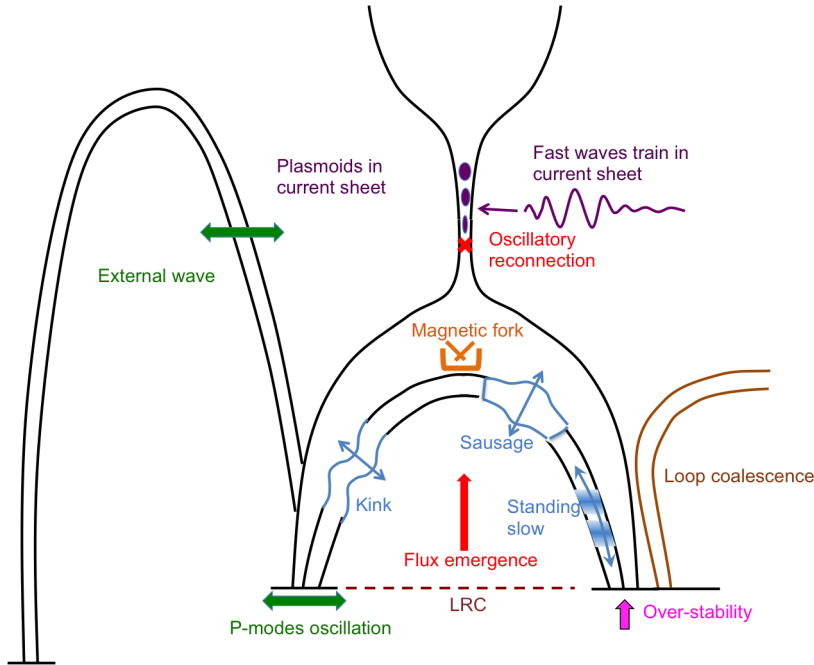


Figure 1.16: Illustration of possible mechanisms at the origin of QPPs.

also results in quasi-periodic variations in the particles acceleration rate (*e.g.* Bárta et al., 2011; Karlický et al., 2011).

Another possible source is the fluctuations of the termination shock structure resulting from interactions between the reconnection outflow, the top of the previously reconnected magnetic loops, and the back-flows in the "above-the-top-loop" region (Takasao and Shibata, 2016).

These are only a few examples among the possible mechanisms that could lead to a periodically fluctuating acceleration of non-thermal electrons. Figure 1.16 summarizes all the mechanisms that have been reported in the review by McLaughlin et al. (2018). In most cases, the oscillatory pattern is only dependent on the characteristics of the local plasma, not on the characteristics of the driver. McLaughlin et al. (2018) also speak of "self-oscillations". In some cases, however, it is the properties of the driver that prescribe the QPP period. This is for example the case if the reconnection is triggered periodically by the oscillation of a neighbouring loop (Nakariakov et al., 2006).

## 1.6 Observing the Solar Irradiance from Soft X-Rays to Ultraviolet

Solar flares are well seen in the time series of solar irradiance, *i.e.* the solar radiation integrated over the full solar disk (no spatial resolution). One can distinguish spectral and total solar irradiance, with the former depending on the spectral range and the latter being integrated over all the wavelengths.

The total solar irradiance (TSI) shows little variation over time. Its variations are of the order of 0.1%, so the total solar irradiance (TSI) is often referred to as the *solar constant*. However, the solar irradiance variability is more prominent in some parts of the solar spectrum (see e.g. Ermolli et al., 2013). In particular the extreme ultraviolet (EUV, 10–121 nm) and soft X-rays (SXR, 0.1–10 nm) ranges show fluctuations with the amplitude up to 100% and are therefore particularly well adapted to observing the manifestations of the solar activity (see Figure 1.17).

The visible (VIS, 380–760 nm) and infrared (IR, 760–1000000 nm) parts of the solar spectrum are the ranges in which the Sun emits the most of its energy and are therefore the main contributors to the terrestrial energy budget. The emission in the SXR to ultraviolet (UV, 100–400 nm) range is the driver of the ionisation processes that produce the Earth ionosphere. The solar UV emission, which can be further subdivided into the far ultraviolet (FUV, 122–200 nm), the mid-ultraviolet (MUV, 200–270 nm<sup>1</sup>) and the near-ultraviolet (NUV, 270–400 nm), also affects the temperature and the production of ozone in the stratosphere. It is these reasons that make the SXR to UV range an important target of observations and modelling (Ermolli et al., 2013).

However, the absorption by the Earth atmosphere results in a strong extinction of those wavelengths, which can only be measured by space-borne instruments. Routine measurements of the SXR to UV range only started after the beginning of the space era, around 1970, with the series of Orbiting Solar Observatory (OSO) satellites (see Figure 1.18 and Golub and Pasachoff, 2009). These measurements were at first sporadically distributed over the spectrum, but since the early 2000's, a full coverage of the EUV-SXR range has been reached by combining the various instruments in flight (see Figure 1.18). However, LYRA is currently the only operational radiometer to measure the FUV-MUV range. Maintaining a good coverage of the spectrum over a certain period is essential to build and test spectral solar irradiance (SSI) models (Schöll et al., 2016). It is worth to note that some of these instruments have a high spectral

---

<sup>1</sup>The official ISO definition places the transition between the MUV and NUV at 300 nm. However, in this thesis, we have adopted the convention used by the instrument IRIS, which considers wavelengths between 270 and 300 nm as being part of the NUV.

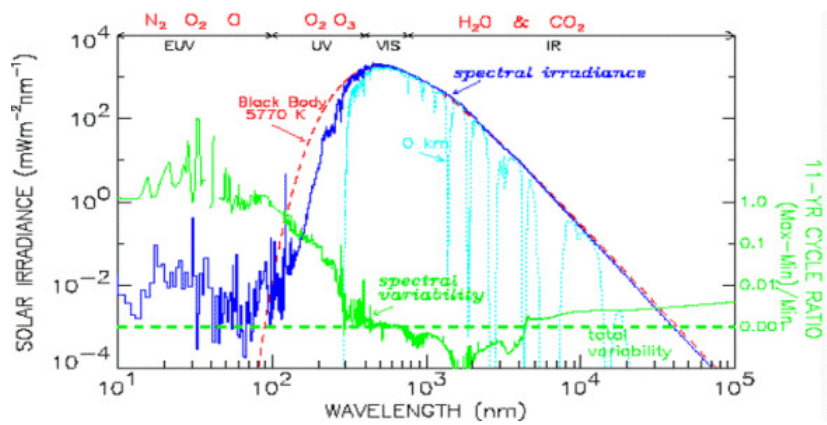


Figure 1.17: The average solar spectrum before (dark blue) and after (light blue) absorption by the Earth atmosphere. The variability of the solar spectrum over the solar cycle is shown with the green line. Credit: J. Lean, NRL

resolution, *e.g.* the *Solar Radiation and Climate Experiment/Solar Stellar Irradiance Comparison Experiment* (SORCE/SOLSTICE: Rottman et al., 1993; Woods et al., 1993) or the *Thermosphere Ionosphere Mesosphere Energetics and Dynamics/Solar EUV Experiment* (TIMED/SEE: Woodraska et al., 2004) with limited cadence of observations. Broadband instruments integrate over wide parts of the spectrum, but usually benefit from a higher sampling rate, *e.g.* the *Geostationary Operations Environmental Satellite/Extreme Ultraviolet Sensor* (GOES/EUVS) or the *Picard/Precision Monitor Sensor* (PREMOS: Schmutz et al., 2009).

LYRA is an SXR to MUV (soft X-ray to mid-ultraviolet) solar radiometer embarked on the European Space Agency *Project for On-Board Autonomy 2* (PROBA2) mission, which was launched on 2 November 2009.

It orbits the Earth in a Sun-synchronous orbit at an altitude of about 720 km and continuously faces the Sun. LYRA acquires solar-irradiance measurements in four broad spectral channels, from soft X-ray to UV, which have been chosen for their relevance to solar physics, space weather, and aeronomy.

The instrument has been designed to allow the detection of very small-amplitude flares that are thought to contribute to the coronal heating significantly, as well as the observation of the finest details in the temporal evolution of flares. It therefore provides time series of solar irradiance with a very high sampling cadence (up to 100 Hz – one of the highest cadences currently achieved in radiometers) and with a good signal-to-noise ratio (BenMoussa et al., 2009).

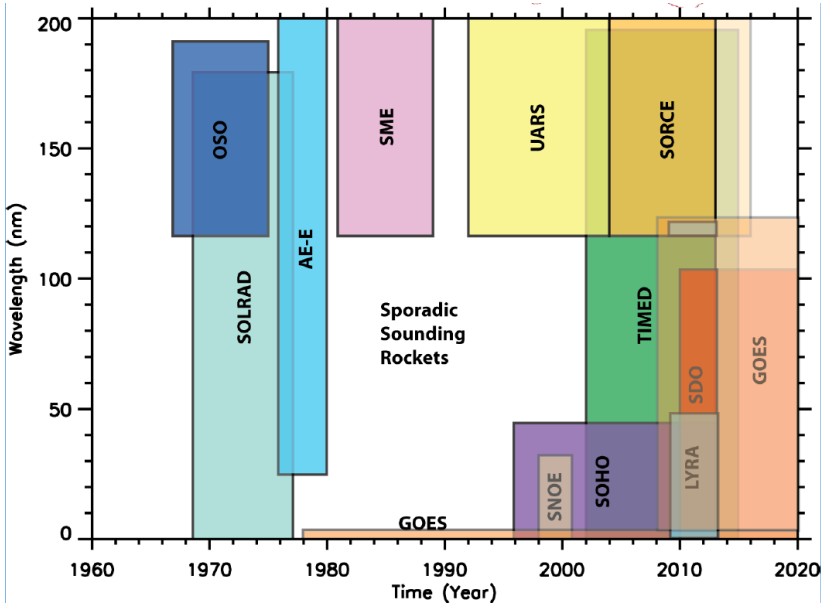


Figure 1.18: Overview of the main instruments measuring the EUV/SXR solar spectral irradiance. Note that LYRA observations continue up to now (2019). Credit: F.Eparvier, LASP

At the time of its conception, the instrument was also intended to measure the density distribution of the main constituents of the Earth atmosphere ( $O$ ,  $O_2$ ,  $N_2$ ) as well as of ozone, using the occultation technique (Dominique et al., 2009). This objective justified the presence of the two longer wavelength channels, in particular the "Herzberg channel" around  $2000 \text{ \AA}$ , which was named due to its relevance to the Herzberg continuum of the molecular oxygen in the Earth's atmosphere. However, shortly before the launch, the orbit of the spacecraft was modified, restraining the occultations to the winter period. The occultation analysis therefore became a secondary scientific objective of the instrument.

Last but not least, LYRA has a technological objective. It aims to test an innovative kind of wide band-gap diamond detectors. These detectors, which are radiation-hard and visible-blind, are particularly well adapted to observe the wavelengths targeted by LYRA.

The solar payload of the PROBA2 spacecraft, which besides LYRA also includes an EUV telescope called SWAP (Seaton et al., 2012; Halain et al., 2013), is operated by the Royal Observatory of Belgium. There, a team of operators continuously monitors the instruments' status, implements the lists of commands

to be transmitted to the spacecraft and processes the received data.

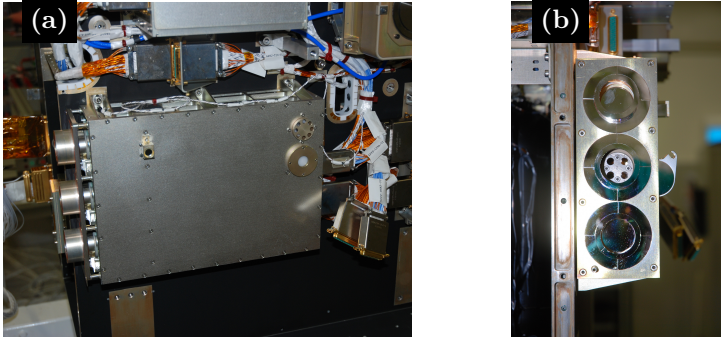


Figure 1.19: Panel (a): LYRA ( $315 \times 92.5 \times 222 \text{ mm}^3$ ) during its integration on PROBA2. Panel (b): the open cover of unit 2 reveals the four observation channels.

## 1.7 Objectives of this Thesis

The main objectives of this thesis are:

- calibration of the LYRA data and the analysis of the instrument performances over the lifetime of the instrument,
- analysis of flares based on LYRA observations taken in multiple bandpasses,
- investigation of the short-timescale phenomena detected during flares.

The calibration of the LYRA data is required before the data can be used for solar physics or aeronomy. The effects of temperature, degradation, the variation of the distance between the Sun and the spacecraft, etc., should be removed from the data. An estimate of the error budget resulting from the instrumental origin or induced by the calibration should be provided.

Flares emit the radiation in a very broad range of wavelengths, which correspond to very different temperatures and altitudes of emitting plasma. Observing a flare in various spectral ranges provides us with an important information on different emission mechanisms. We intend to use observations in multiple bandpasses to investigate these mechanisms and to check whether their observations agree

with the predictions of the "standard model" of flares. Considering the LYRA bandpasses, it is expected that the peak of the flare observed by the two EUV channels, which both correspond to thermal emission, is delayed with respect to peak observed in the longer-wavelength channels, which likely correspond to chromospheric emission and should therefore be co-temporal with non-thermal emission. However, since the bandpasses of LYRA cover broad ranges of the spectrum, it is first needed to identify the main emission mechanisms contributing to the two UV channels in order to confirm their chromospheric origin.

The investigation of short-timescale phenomena will be dedicated to the analysis of quasi-periodic pulsations. We intend to look for correlations of the detected periods with flare properties, with the goal to confirm or refute the wave origin of the pulsations. In particular, we will compare the observed periods to the local Alfvén speed, to the intensity of the flare and to its location on the solar disk.

The outline of the rest of the thesis is the following: Chapter 2 presents the LYRA instrument and the work that has been done to calibrate its measurements; Chapter 3 goes one step further into the instrumental aspects, detailing the degradation processes at work; Chapter 4 presents the multi-wavelength analysis of the strongest flare observed by LYRA, which was also the only flare that has been seen with its all four channels; Chapter 5 focusses on the QPP analysis; and finally Chapter 6 summarizes the main conclusions of this work.



## Chapter 2

# PROBA2/LYRA: Instrument Description

This chapter essentially reproduces the content of (Dominique et al., 2013). It describes in details the main instrument used in this thesis, *i.e.* the LYRA radiometer of which M. Dominique is the principal investigator (PI). This chapter presents the way the data are calibrated, the uncertainties affecting the data, and the various mechanisms that reduce the instrument performances. These aspects, in particular the calibration, are essential to interpret the measurements. Additionally, one of the main objectives of the mission was to test a new type of detector in space. M. Dominique coordinated the definition of the calibration procedure, made a decisive contribution to the correction of the degradation and the estimation of the errors affecting the instrument. She also implemented the routines to access and read the data, which are currently distributed to the user community through the Solar Software library.

### 2.1 Design of the Instrument

The LArge-Yield Radiometer (LYRA) is a radiometer integrating the full-Sun emission in four broad bandpasses in the SXR to MUV spectral range. LYRA is a shoe-box size instrument ( $315 \times 92.5 \times 222 \text{ mm}^3$ ) composed of three quasi-redundant units, each equipped with an individual cover and hosting four spectral channels (see Figure 1.19). A channel consists of a collimator, an optical filter, a detector, and two LEDs on the side. The LEDs are located

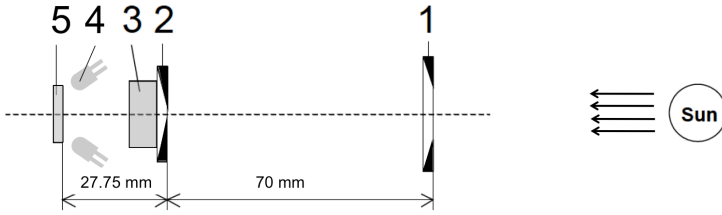


Figure 2.1: Schematic representation of one LYRA channel: 1 and 2 are respectively the view-limiting and precision apertures, together forming the collimator, 3 is the filter, 4 are the two LEDs at 375 and 470 nm located behind the filter, and 5 is the detector.

between the filter and the detector and emit at 375 and 470 nm (see Figure 2.1). They are used to estimate the impact of aging on the detectors.

The three units are essentially similar in terms of spectral coverage, but involve non-identical associations of filters and detectors (Table 2.1). The four bandpasses are indicated in the same table along with their purity (*i.e.* the ratio of the flux in the defined bandwidth to the total output signal). The bandpasses of all channels except the channel 1 on each unit were defined such that in quiet-Sun conditions, at least 95 % of the measured signal actually comes from the specified wavelength range. The bandpass of the channel 1 in each unit corresponds to the target wavelength range, as defined during the conception of the instrument. For historical reasons, contrarily to the other channels, its bandpass definition was not updated based the actual spectral response of the instrument. The purities were computed considering a quiet-Sun-type spectrum. They show that for channels 2 to 4, most of the detected signal comes from the defined bandpasses. Channel 1, however, is highly contaminated by out-of-band radiation.

In addition to wide-band-gap diamond detector prototypes, units 1 and 3 incorporate some classical silicon (Si) detectors that allow us to compare the two technologies. Diamond detectors are of two types: metal–semi-conductor–metal (MSM) photo-conductors and positive–intrinsic–negative (PIN) photodiodes (Figure 2.2), which are used for the Herzberg channels only (see Table 2.1). The characteristics of these detectors are detailed by (BenMoussa et al., 2004) and (BenMoussa et al., 2006). A few of these characteristics are recalled here, because they significantly affect LYRA data.

- An electrode is located on the surface of the MSM and PIN detector, which results in significant flat-field variations (see Figure 2.2).

Table 2.1: Characteristics of the LYRA channels. Channel 2 was historically called "Herzberg channel" due to its relevance to the Herzberg continuum of molecular oxygen in the Earth's atmosphere. The purity is defined as the ratio of the flux in the nominal wavelength range (*i.e.* the defined bandwidth) to the total output signal. Purities correspond to a solar-minimum-type spectrum. The thicknesses of the aluminum and zirconium filter layers are indicated in the second column, together with the Acton reference for the Lyman- $\alpha$  and Herzberg filters.

Channel	Filter label	Detector	Bandwidth	Purity
<i>Unit 1</i>				
1-1	Lyman- $\alpha$ [122XN]	MSM Diamond	120 – 123 nm	26 %
1-2	Herzberg [220B]	PIN Diamond	190 – 222 nm	95 %
1-3	Aluminum (158 nm)	MSM Diamond	0.1 – 5 nm + 17 – 80 nm	96.8 %
1-4	Zirconium (300 nm)	AXUV Si	0.1 – 2 nm + 6 – 20 nm	97 %
<i>Unit 2</i>				
2-1	Lyman- $\alpha$ [122XN]	MSM Diamond	120 – 123 nm	25.7 %
2-2	Herzberg [220B]	PIN Diamond	190 – 222 nm	95 %
2-3	Aluminum (158 nm)	MSM Diamond	0.1 – 5 nm + 17 – 80 nm	97.2 %
2-4	Zirconium (141 nm)	MSM Diamond	0.1 – 2 nm + 6 – 20 nm	92.2 %
<i>Unit 3</i>				
3-1	Lyman- $\alpha$ [122N+XN]	AXUV Si	120 – 123 nm	32.5 %
3-2	Herzberg [220B]	PIN Diamond	190 – 222 nm	95 %
3-3	Aluminum (158 nm)	AXUV Si	0.1 – 5 nm + 17 – 80 nm	96.6 %
3-4	Zirconium (300 nm)	AXUV Si	0.1 – 2 nm + 6 – 20 nm	95 %

- Trapping/detrapping of generated photoelectrons by defects (not bulk but surface defects) causes the signal of the MSM detectors to take quite a long time before stabilizing (see Figure 2.3).

Figure 2.4 illustrates the total responsivity of filter-detector combinations for all four channels of unit 1. These curves are the result of a radiometric model that uses pre-launch measurements of filter transmittance and detector responsivity as input.

Several spectral lines and continua contribute to the signal measured by each channel. The main contributions to channels 1 and 2 at the time of the first light are summarized in Figure 2.5 and in Table 2.1. Channels 3 and 4 cover very broad spectral ranges, and it is therefore impossible to provide the detailed list of all their contributors. In these panels, the solar spectrum has been divided into several spectral subsets, corresponding to the main continua plus the Lyman- $\alpha$  line. The contribution of each subset to the total signal measured by the channel has been overplotted to the solar spectrum. One can see that most of the signal in channel 1 comes from the Lyman- $\alpha$  line (considered here to cover the 1197–1235 Å range) and from the Si I, Al I, and Mg I continua that respectively cover the 1700–1950 Å, 1950–2077 Å, and 2077–2518 Å spectral

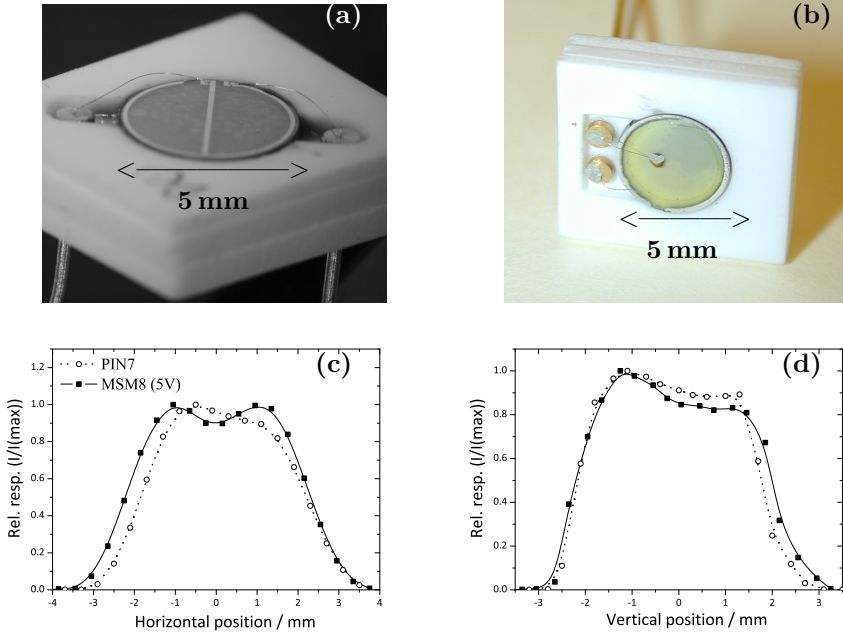


Figure 2.2: Two examples of diamond detectors: MSM (a) and PIN (b). In both cases, we note the position of an electrode (central bar for the MSM, off-center circle for the PIN). Those electrodes strongly affect the flat-field of the detectors, as shown in the plots of relative responsivity along two perpendicular directions in (c) and (d).

ranges. One can also note that these three continua are the main contributors to channel 2 and that their contribution is of similar importance in both channels. In theory, it is therefore possible to use the measurements by channel 2 to separate the Lyman- $\alpha$  contribution from the longer wavelengths.

Raw LYRA data, as transmitted by the spacecraft, are obtained from an onboard conversion of the photocurrents produced by the detectors into data numbers. Photocurrents are first converted to voltages in the 0–5 volts range by a resistor; their value is different for each channel. Voltages are then switched to frequencies by a voltage-to-frequency converter (VFC). The VFC are regularly connected to stable calibrated onboard voltage sources of 5 volts, 2.5 volts, and 0 volts. These measurements are interleaved in the telemetry, to be used as reference when the data are processed. At the end of the acquisition chain the number of pulses received during the integration period are counted. This

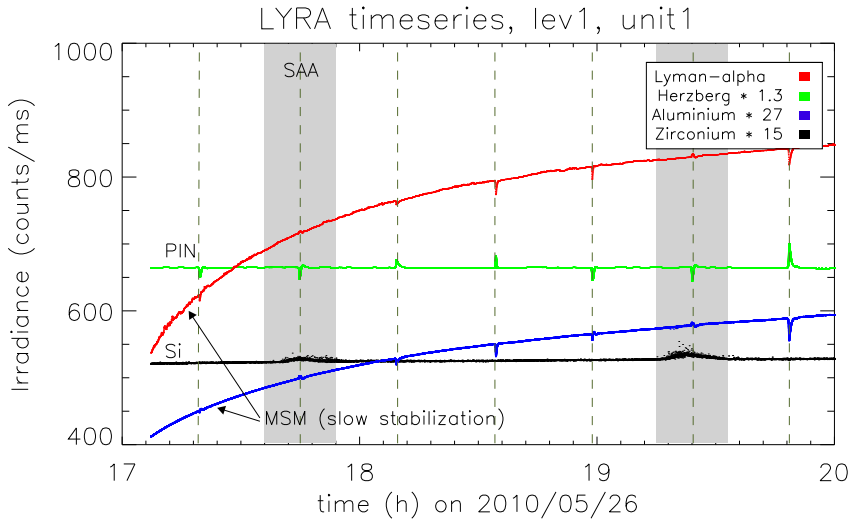


Figure 2.3: Slow stabilization of MSM detectors: the signal has not yet reached its stabilization level three hours after the detector was switched on. This figure also shows the perturbation in the Si-detector signal when the SAA is crossed. Compared to silicon, diamond technology has proven to be more resilient to the impact of high-energy protons (and their secondary electrons), which cause this noisy behavior. Gray bands indicate the South Atlantic Anomaly (SAA) and dashed vertical lines the wide-angle rotations of the spacecraft. Time series have been rescaled to fit the same range and appear in the same order as in the legend. Scaling coefficients are indicated in the legend.

number, which is expressed in counts, constitutes the LYRA data numbers that are downloaded as part of the telemetry.

## 2.2 LYRA Data Description

### 2.2.1 Data Products

LYRA produces time series of spectral irradiance in its four bandpasses in a quasi-uninterrupted way. Interruptions might happen during calibration campaigns (once every two weeks on average) or during the Winter occultation season, when the spacecraft transits the Earth shadow. Nevertheless, since PROBA2 is flying on a polar, dawn–dusk heliosynchronous orbit, these occultations are

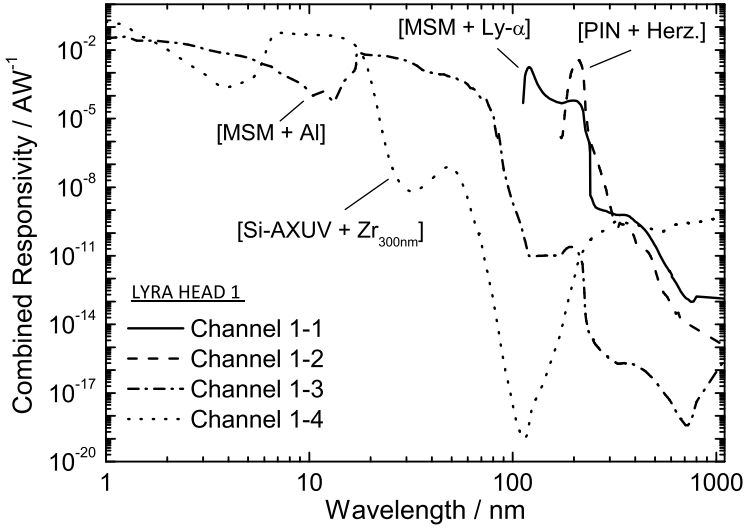


Figure 2.4: Simulated combined spectral (detector + filter) responsivities for LYRA unit 1 between 1 and 1000 nm, from (BenMoussa et al., 2009).

Table 2.2: Main continua/lines contributing to the total signal in LYRA channels 1 and 2. The percentage contributions correspond to the time of the first light.

Bandpass in Å	Main continuum / line	Seen in absorption or emission	Percentage contribution to channel 1 in %	Percentage contribution to channel 2 in %
below 912	H I	emission	-	-
912–1100	C I	emission	0.01	-
1100–1197	S I	emission	0.56	-
1197–1235	Lyman- $\alpha$	emission	27.26	-
1235–1527	Si I	emission	1.03	-
1527–1683	Si I	mixed	0.06	0.00
1683–1700	Fe I	absorption	8.00	1.46
1700–1950	Si I	absorption	14.02	17.19
1950–2077	Al I	absorption	48.45	78.32
2077–2518	Mg I	absorption	0.11	0.02
2518–3646	H I	absorption	0.11	0.00

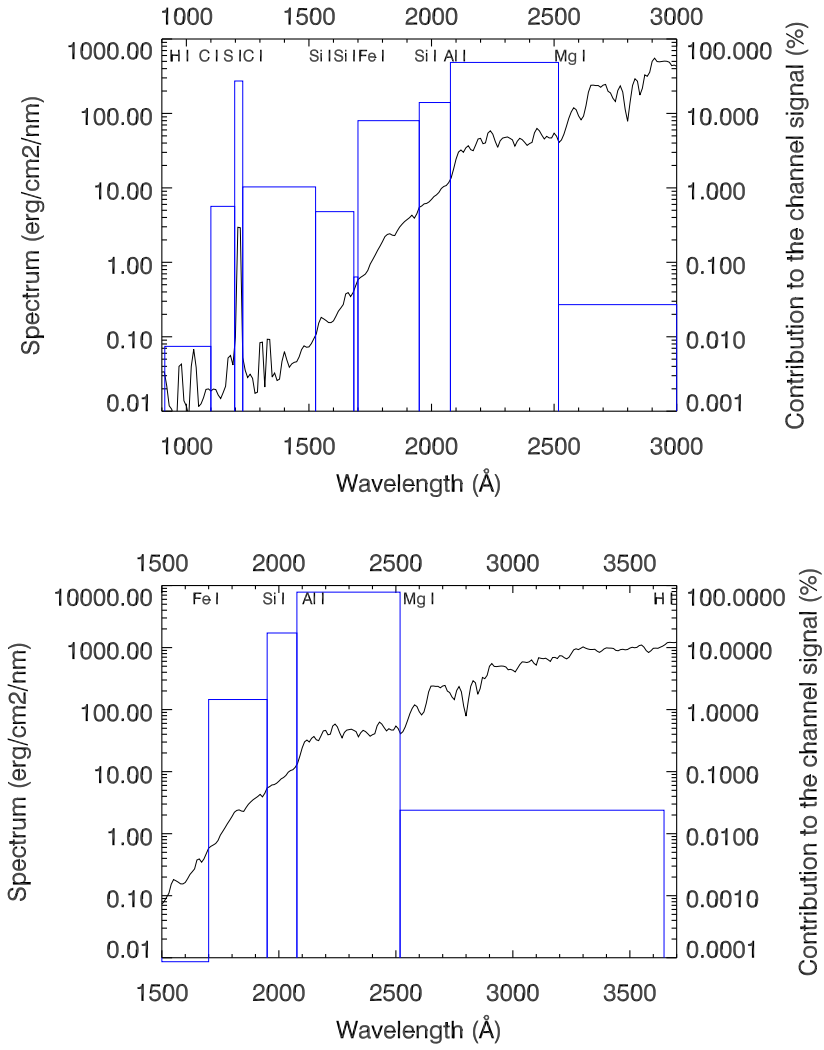


Figure 2.5: Percentage contribution of each continuum/line composing the bandpass of LYRA channels 1 (top panel) and 2 (bottom panel) to the total measured signal.

limited to a three-to-four months Winter period (depending on the channel) and last for a maximum of 25 minutes every orbit (one orbit is 100 minutes long).

As mentioned in Section 2.1, LYRA includes three units, which are similar from the spectral point of view. The four channels of a unit are operated in parallel, acquiring irradiance measurements at a nominal cadence of 20 Hertz, but could go up to 100 Hertz.

The strategy behind the redundancy is the following:

- The nominal unit (unit 2) is in permanent use, but therefore it is the most affected by degradation. In the Lyman- $\alpha$  and Herzberg channels of this unit (*i.e.* channels 1 and 2), the signal had dropped by about 99 % after the few first months of the mission. The degradation is so strong that the solar signal is now barely detectable in these two channels.
- Unit 3 is used in a campaign-driven way and keeps its cover closed the rest of the time to limit aging effects.
- Unit 1 is mostly unused. It acquires data for 40 minutes every three months on average and is therefore the most preserved. It is aimed to be a reference for estimating the degradation of units 2 and 3.

Data are usually available within four hours after their acquisition. Products with different levels of processing are distributed through the PROBA2 website (<http://proba2.oma.be>). They consist of uncalibrated and calibrated data, as well as various quicklook datasets (see Table 2.3).

Once downloaded, raw LYRA data in counts are converted back to counts  $\text{ms}^{-1}$ , dividing them by the integration time. They are distributed without further processing through the instrument website as **level-1/engineering data** in standard files – either from the nominal unit (`.std`) or from an additional back-up unit (`.bst`), which can be either unit 1 or unit 3. Information about the acquisition context (temperature, pointing, status of covers, status of LEDs, usage of a back-up unit, etc.) compose the ancillaries stored in the metadata (`.met`) file. Additional files gather the data acquired during calibration campaigns (dark currents, LED signals), or the rejected data (outliers, data acquired during transitions between acquisition modes).

**Level-2/calibrated data** are available through the same website. Currently, calibration includes subtraction of dark currents (which removes the temperature effects), compensation for degradation, rescaling to one astronomical unit, and conversion from counts  $\text{ms}^{-1}$  to irradiance units, but no correction for flat-field effects yet. Special features, such as imprints of wide-angle rotations of the



Table 2.3: Summary of the main LYRA data products distributed to the scientific community. These products are processed after each data download (*i.e.* every three to four hours).

Product	File extension on LYRA website	Format	Characteristics
Level 1 engineering data	*_lev1_std(bst).fits	FITS	unprocessed solar irradiance, in [counts ms <sup>-1</sup> ]
	*_lev1_cal(bca).fits	FITS	unprocessed calibration data, in [counts ms <sup>-1</sup> ]
	*_lev1_met.fits	FITS	ancillary data: temperature, pointing, etc.
	*_lev1_rej(bre).fits	FITS	rejected samples (outliers, etc.)
Level 2 basic science data	*_lev2_std.fits	FITS	calibrated solar irradiance, in [Wm <sup>-2</sup> ]
Level 3 averaged science data	*_lev3_std.fits	FITS	level 2 averaged over 1 min, in [Wm <sup>-2</sup> ]
Level 4 A quicklooks	*.png	image	daily plot of calibrated data for all LYRA channels
Level 4 B quicklooks	*.png	image	3-days GOES-like plot of calibrated data in aluminum and zirconium channels
Level 5 flare list	html	text file	List of flares with links to LYRA and GOES flux profiles
Level 6 density profiles	.txt	text file	Profiles of O+N <sub>2</sub> number density in the Earth atmosphere

spacecraft or perturbations due to the South Atlantic Anomaly (SAA), are also visible in the data. These features are described in detail in Section 2.2.3.

Basic IDL procedures to download and read the LYRA data, and to filter out the above-mentioned features are available through the Solar-Soft library ([sohowww.nascom.nasa.gov/solarsoft/](http://sohowww.nascom.nasa.gov/solarsoft/)) at the address [ssw/proba2/lyra/idl](http://ssw/proba2/lyra/idl).

## 2.2.2 Calibration of LYRA Data

### 2.3.2.1 Dark Current Subtraction

The dark current was measured as a function of temperature between  $-40^{\circ}\text{C}$  and  $+60^{\circ}\text{C}$  in the laboratory before the launch, but only in steps of  $10^{\circ}\text{C}$ . The relationship between temperature and dark current was generally linear below  $40^{\circ}\text{C}$  (*i.e.* over the estimated operational temperature range), which explains why no other tests with smaller steps were performed. Unfortunately, it turned out that the onboard temperature experienced in space was much hotter than expected – between  $+35^{\circ}\text{C}$  and  $+55^{\circ}\text{C}$  – in a range where the functional relation between temperature and dark current is nonlinear.

The actual relation had therefore to be tabulated in smaller steps, exploiting several calibration campaign observations with closed covers, and even some with open covers, when the solar component could be removed. The dark current ( $D$ ) was found to vary exponentially with the temperature ( $T$ ):

$$D(T) = a(t) + \exp(b(t)T + c(t)). \quad (2.1)$$

The  $a$ ,  $b$ , and  $c$  coefficients in Equation 2.1 slowly evolve with time, as the detectors are aging. Those coefficients have been estimated at several times of the mission based on dark-current measurements and are interpolated in-between. An example is illustrated in Figure 2.6 for channel 1 of unit 2. In the top panel, diamonds correspond to the measurements made before the launch. The small dots represent the measurements made in-flight, and the model described by Equation 2.1 is overplotted. Darker dots and lines correspond to the beginning of the mission, while grey dots and lines correspond to recent measurements and models. BenMoussa et al. (2015) studied the evolution of the dark current in the diamond detectors and found it to be of a smaller amplitude than the dark current in traditional silicon detectors.

It is usually expected that the dark current increases as the detector is aging, in particular as a result of the radiation produced by energetic particles. Tests made on detectors similar to those used in LYRA, during which the detectors were irradiated by protons, confirm this trend (BenMoussa, private communication). However, the MSM detectors embarked on LYRA behave differently. Their dark current has a tendency to decrease with time (see Figure 2.6). This behavior is still not fully understood. BenMoussa et al. (2015) suspect that it is due to an increase of the conductivity caused by the desorption of some surface contaminants.

The dark-current signal is subtracted from the measurements.

### 2.3.2.2 Correction for Degradation

From the very first hours after the covers were opened, LYRA suffered severe degradation, which seriously affected its longer-wavelength channels (Figure 2.7). As will be shown in Chapter 3, the most likely explanation for this degradation is UV-induced polymerization of outgassing molecules on the filter surface. This explanation is also consistent with the observed dependence of the drop of sensitivity in each unit to its exposition to solar flux. The resulting layer absorbs longer wavelengths more than shorter ones, which explains the different impact on different channels. In the Lyman- $\alpha$  and Herzberg channels of unit 2 (*i.e.* channels 1 and 2), the signal decreased by 70 % within the first month alone

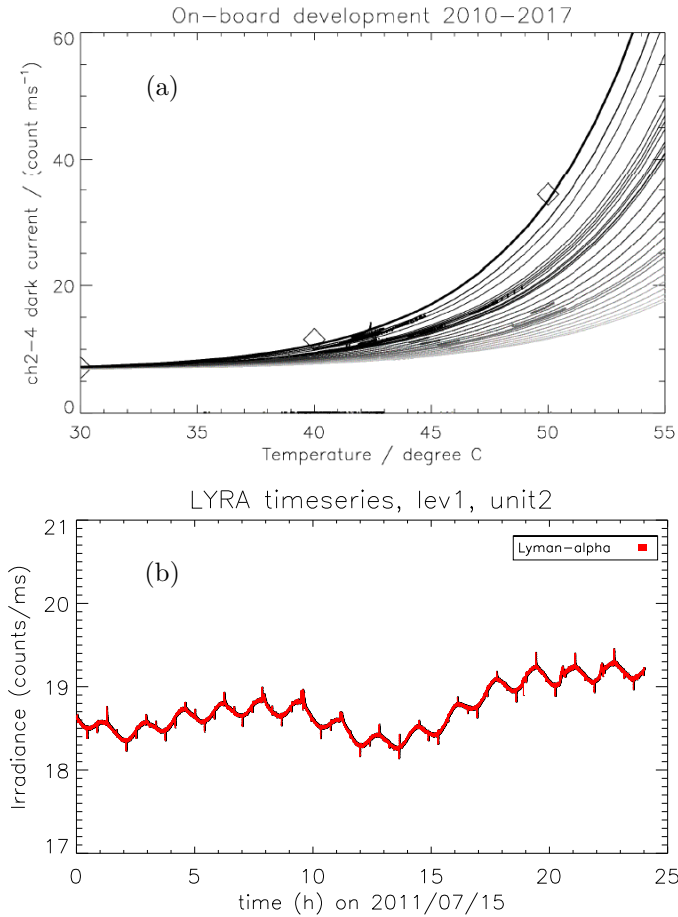


Figure 2.6: (a) Dark current in channel 1 of unit 2 *versus* temperature, as a function of time. Diamonds show pre-launch measurements and solid lines the dark current relation obtained after fitting the parameters  $a$ ,  $b$ , and  $c$  from Equation 2.1 for different times of the mission (dark/light lines respectively correspond to the beginning/end of the mission). (b) An example of quiet-day uncalibrated measurements by channel 1. The effect of orbital and daily temperature variations is clearly visible. After subtraction of dark current, the same time series turns into a flat line.

and a loss of 99 % was reached by mid-2012. Fortunately, preserved back-up units are available for observation campaigns. It was not possible in the long run to calibrate and compare LYRA with other instruments without first taking the degradation into account. This, in turn, meant that the degradation had to be separated from the solar variation.

To some extent, the degradation can be calculated by internal means. For the two shorter-wavelength channels (aluminum and zirconium, *i.e.* channels 3 and 4), this is done with the help of the spare unit 1, which so far was only used for very occasional campaigns. During the first six years of the mission, channel 4 of unit 1 showed no apparent sign of degradation and could be used as a reference for channels 3 and 4 of the other units after subtracting the variations induced by solar activity. The evolution of channels 3 and 4 is correlated.

Note that at the time of writing, *i.e.* after nine years of operation, even channel 4 of unit 1 starts to show a limited loss of signal caused by degradation. The last version of the degradation correction procedure therefore had to take it into account. It was estimated comparing two periods corresponding to the similar low levels of solar activity, one at the beginning of the mission and the other in the recent months. The loss of signal in channel 4 of unit 1 was estimated to  $\sim 25\%$  and linearly interpolated over the whole mission. The linear interpolation seems to be a reasonable choice as unit 1 is typically used in a very regular way (it is opened during one orbit every month).

Unfortunately, there is no such internal reference for the longer-wavelength channels (channels 1 and 2). Degradation was so rapid in those channels that even units 1 and 3 were affected. The solution we adopted is to conjecture that the quiet-Sun signal does not show any long-term trend. Any general deviation is considered to be an effect of degradation. The data analysis is somewhat biased in this approach, and can only focus on short-term variations of the solar irradiance.

The evolution of the LYRA signal, especially in channels 2-1 and 2-2, shows phases of different degradation velocity:

- The degradation trend in the first half year (day 1 – day 169 after first light) is fitted with a spline function through some manually selected data points. There is indeed no apparent mathematical function for the initial degradation; it seems to occur in various phases, and the physical processes behind it are not known well enough.
- The degradation trend after the first half year was initially fitted with a function of the type  $1/(a + bt)$ , where  $t$  is the time and  $a$  and  $b$  are fitting coefficients. This function represented the measurements reasonably well and was used during the first years of the mission. However, other

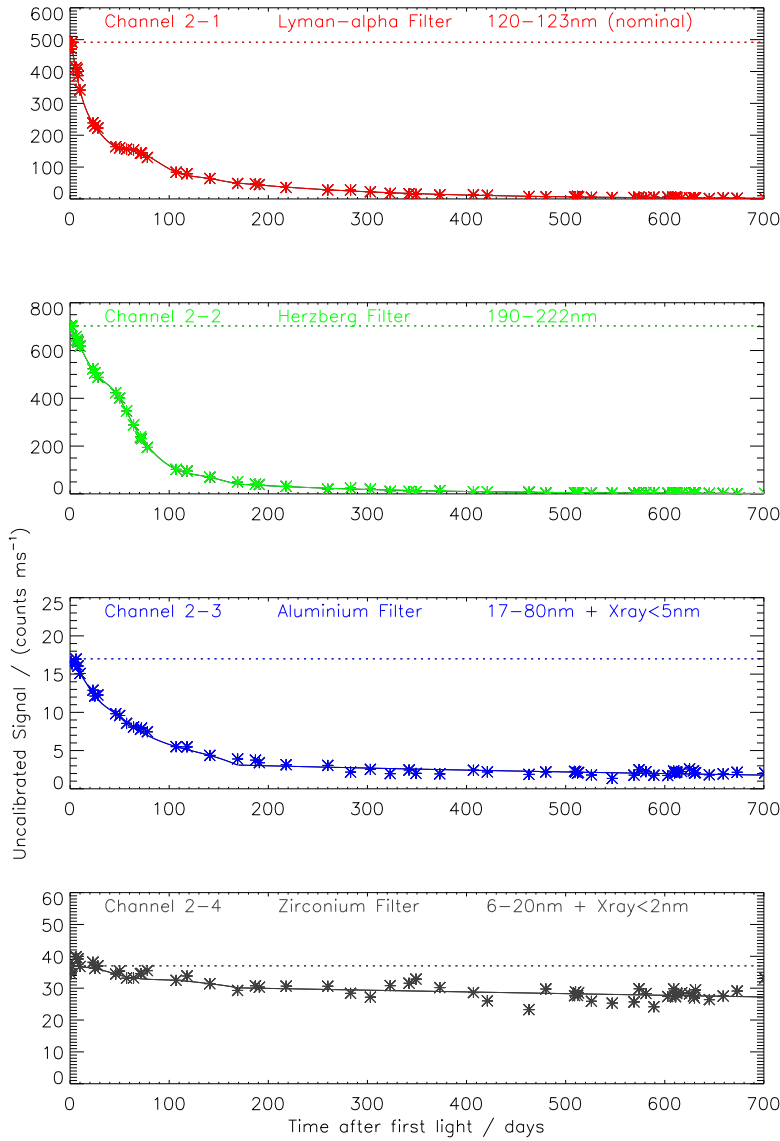


Figure 2.7: Loss of signal in the four channels of unit 2 from the beginning of the mission. The dark current is subtracted from the signal.

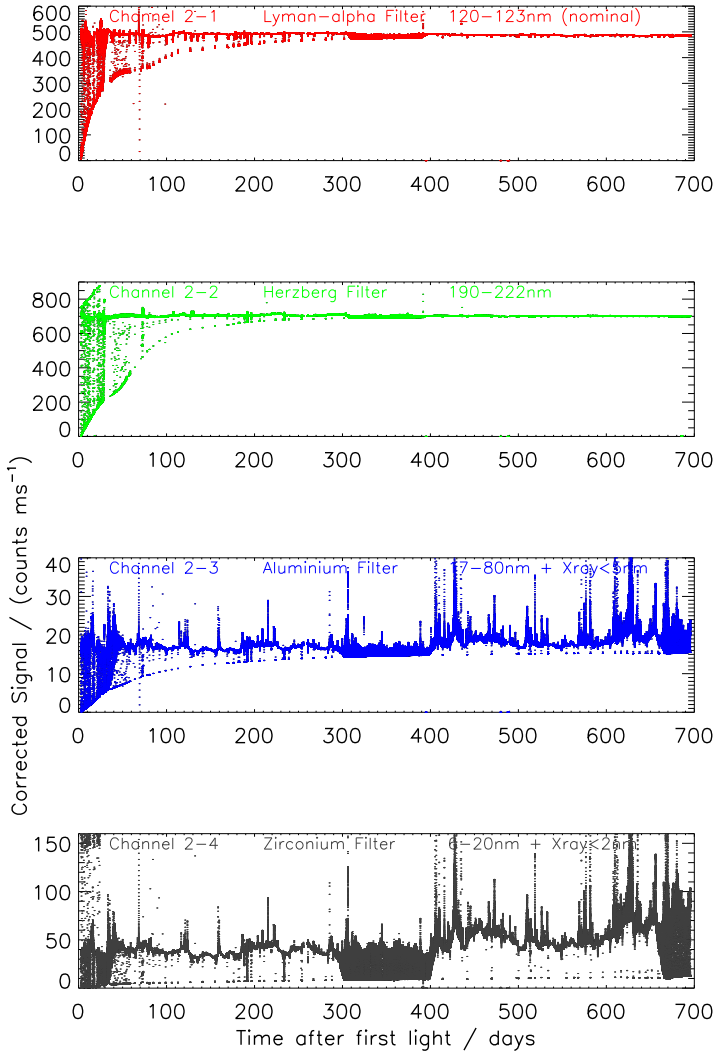


Figure 2.8: Unit 2 measurements from the beginning of the mission, after correcting for degradation (and subtracting dark current). During the season of occultations (days 0 to 40 and 300 to 400), the signal drops to the dark-current level during every orbit. As an unintended side effect of the additive correction for degradation, the level of the dark current – which is also the level reached during occultations – gives the impression of a progressive increase with time, while it is actually stable in general.

functions, negative exponentials in particular, were also tested. The results of the latter recently proved to be an even more reliable estimate for the future behavior. A function of the type  $\exp(a + bt)$  has been introduced in a recent update of the calibration software. Note that instead of fitting the degradation with the time, one could have used the received dose of radiation, of which any index representing the solar activity is a proxy. This option was not tested so far and is left for future work.

The loss caused by degradation was individually estimated with respect to the first light for each channel. The degradation was corrected for by adding the estimated loss to the measured signals. Correction by addition (as opposed to multiplication by a correction coefficient) has advantages, because degradation is a function of the wavelength and does not uniformly affect the broad LYRA channels across their whole spectral range. In particular, there is no apparent sensitivity loss in the X-ray range. Flares<sup>1</sup> of similar intensity in the GOES reference scale now peak at the same count rates in channels 3 and 4 as they did at the beginning of the mission. In the same time, the measurements of the EUV background in the same channels has significantly decreased. A multiplicative correction coefficient would artificially exaggerate the flares. On the contrary, correction by addition underestimated the EUV variability in the time series. Additionally, the occultation profiles become distorted since they no longer drop to zero. The latter effect is shown in Figure 2.8.

The effect of degradation on the spectral response of all channels is thoroughly discussed in Chapter 3.

### 2.3.2.3 Conversion into Physical Units

Photocurrents measured by LYRA detectors can be modeled by

$$i = i_s + i_d = \frac{A}{T} \int_t \int_\lambda E(\lambda, t) F(\lambda) D(\lambda) d\lambda dt + i_d, \quad (2.2)$$

where

- $i$  is the measured photocurrent, defined as the sum of the solar  $[i_s]$  and dark current  $[i_d]$  contributions,
- $\lambda$  is the wavelength,
- $t$  is the time and is integrated over an exposure,

---

<sup>1</sup>of which most of the signal measured by LYRA is believed to come from the SXR.

- $A$  is the aperture area, *i.e.* the exposed detector area,
- $T$  is the total exposure time (nominally 50 ms),
- $E(\lambda, t)$  is the solar spectral irradiance,
- $F(\lambda)$  is the filter transmittance,
- $D(\lambda)$  is the detector spectral responsivity,

and where the integral over  $\lambda$  is performed over the whole spectral range in which the instrument is sensitive (not restricted to the defined bandpass), which means that it also includes the out-of-band radiation. This out-of-band radiation constitutes a source of measurement error that may be important in channel 1 (see purities in Table 2.1).

Because LYRA channels cover broad spectral ranges, it is not possible to directly invert Equation (2.2) to retrieve the spectral irradiance  $E(\lambda, t)$  from the measured photocurrent  $i$ . For an absolute radiometric calibration, we compared data acquired at any time  $t$  to a pre-degradation reference LYRA measurement (the first-light on 6 January 2010), for which this conversion into irradiance units is known. This comparison was performed after correcting for the degradation, as detailed in Section 2.2.2. It assumes that the relationship between LYRA count rate and irradiance in physical units is linear,

$$E_{\text{cal}} = \frac{i_{\text{uncal}} - i_{\text{d}} + \text{corr}}{i_{\text{uncal}}^{\text{FL}} - i_{\text{d}}^{\text{FL}}} E_{\text{cal}}^{\text{FL}}, \quad (2.3)$$

where

- $E_{\text{cal}}$  and  $E_{\text{cal}}^{\text{FL}}$  [ $\text{W m}^{-2}$ ] are the irradiance measurements by one LYRA channel at any time  $t$  and at the time of the first-light,
- $i_{\text{uncal}}$  and  $i_{\text{uncal}}^{\text{FL}}$  [A] are the photocurrents measured at any time  $t$  and at the time of the first light,
- $i_{\text{d}}$  and  $i_{\text{d}}^{\text{FL}}$  [A] are the dark-current photocurrents at any time  $t$  and at the time of the first light,
- $\text{corr}$  is the corrective term for degradation.

LYRA measurements at the reference time can be converted into irradiance units by comparing them to spectrally resolved measurements provided by other instruments at the same time. We used a concatenation of spectra measured



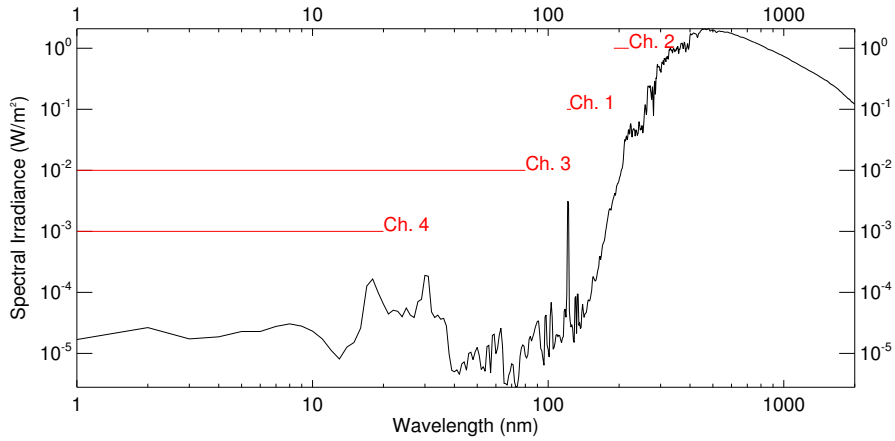


Figure 2.9: Reference solar spectrum reconstructed from TIMED/SEE and SORCE/SOLSTICE level-3 data on 6 January 2010, used as a reference to infer LYRA radiometric calibration. Wavelength coverage of different LYRA channels is marked with red lines.

by TIMED/SEE from 0.5 nm to 115.5 nm and SORCE/SOLSTICE from 116.5 nm to 2412.3 nm (see Figure 2.9).

This spectrum was inserted into Equation (2.2) to produce an estimate of the expected LYRA photocurrent. The difference of the estimated photocurrent to the measured one was converted into an excess/default of spectral irradiance with respect to the one observed by SEE and SOLSTICE (integrated over the LYRA spectral range).

In other words, we calculated the LYRA first-light spectral irradiance in a given channel using

$$E_{\text{cal}}^{\text{FL}} = \frac{i_{\text{uncal}}^{\text{FL}} - i_{\text{d}}^{\text{FL}}}{\frac{A}{T} \int_t \int_{\text{sol.spec.}} E_{\text{S}}(\lambda, t) F(\lambda) D(\lambda) d\lambda dt} \int_{\text{bandpass}} E_{\text{S}}(\lambda) d\lambda, \quad (2.4)$$

where  $E_{\text{S}}$  is the solar spectral irradiance (full spectral resolution) from SEE-SOLSTICE on 6 January 2010.

In Equation (2.4), the integrals over  $\lambda$  cover either the whole solar spectrum (denominator) or the official spectral range of a channel (numerator) only, because the latter estimates what would have been measured by a perfect instrument.

Table 2.4: Excess of spectral irradiance as observed by LYRA compared to TIMED/SEE and SORCE/SOLSTICE measurements.

Lyman- $\alpha$	Herzberg	Aluminum	Zirconium
?	+18.0 %	+13.3 %	+9.2 %

An additional complication was that the excess values computed for channel 1 in the three units differed significantly (unit 1: +81.3%, unit 2: +91.2%, unit 3: +3.3%). Moreover, it was difficult to compare units 1 and 2 (MSM diamond detectors) to unit 3 (Si detector), because the diamond detectors response has an additional secondary peak around 200 nm, while the silicon detector collects 70 % of its non-nominal input between 200 and 1100 nm, with a peak between 900 and 1000 nm. Therefore, it is hard to make a statement such as "LYRA observes  $x$  % more irradiance as compared to SORCE/SOLSTICE" – which explains the question mark in Table 2.4. For channel 1, we considered that the reference value was the spectrum measured by TIMED/SEE and SORCE/SOLSTICE integrated over the channel bandpass (*i.e.* we assumed the excess value to be 0%).

The other channels showed more consistency, so we used the average value over the three units (see Table 2.4).

Combining Equations (2.3) and (2.4), and taking into account that the solar irradiance might be considered as constant over sub-second periods, we obtain

$$E_{\text{cal}} = \frac{i_{\text{uncal}} - i_{\text{d}} + \text{corr}}{A \int_{\text{sol.spec.}} E_{\text{S}}(\lambda) F(\lambda) D(\lambda) d\lambda} \int_{\text{bandpass}} E_{\text{S}}(\lambda) d\lambda. \quad (2.5)$$

### 2.2.3 Non-Solar Features in the LYRA Data

Undesired features, such as imprints of wide-angle rotations of the spacecraft or perturbations due to the SAA, are present in LYRA data and must not be interpreted as solar signal variation. This section provides a list of those features, of which most (*i.e.* the wide-angle rotations, the occultations, and the South-Atlantic Anomaly) can be filtered out of the data by the *remove\_events* routine available in the Solar-Soft library.

### 2.3.3.1 Flat-Field Effects

As described in Section 2.2.2, the calibration process does not correct the data for variations associated with pointing fluctuations. An analysis of the PROBA2 attitude over several orbits reveals that pointing is stable up to 90 arcseconds. Spacecraft jitter introduces fluctuations in the LYRA signal of less than 1 %.

Nevertheless, it often happens that PROBA2 is off-pointed in the framework of calibration or scientific campaigns, introducing signal fluctuations whose amplitude depends on the new pointing (see Figure 2.10).

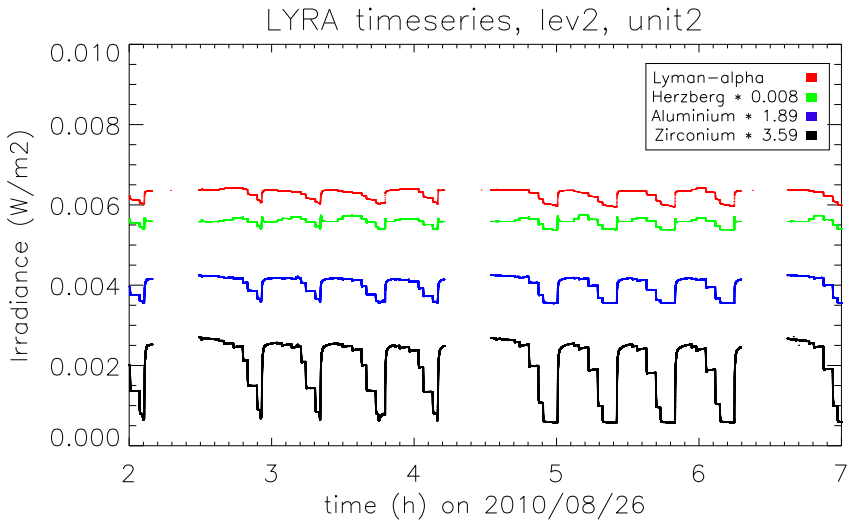


Figure 2.10: Flat-field campaign of 26 August 2010: the spacecraft is off-pointed from  $0^\circ$  to  $3^\circ$  in steps of  $0.5^\circ$  in the S, E, N, W, SE, NE, NW, and SW directions. Results are plotted for unit 2 channels. Time series have been rescaled to fit the same range and appear in the same order as in the legend. Scaling coefficients are indicated in the legend.

### 2.3.3.2 Wide-Angle Rotations of the Spacecraft

Four times per orbit, the spacecraft rotates  $90^\circ$  around the axis pointing toward the Sun to avoid the Earth shadowing its star trackers. Because of the inhomogeneous flat field of the diamond detectors, these rotations are clearly visible in the time series (see Figures 2.11 to 2.12). Unfortunately, the pointing parameters are acquired at a limited cadence, not fast enough to deduce the

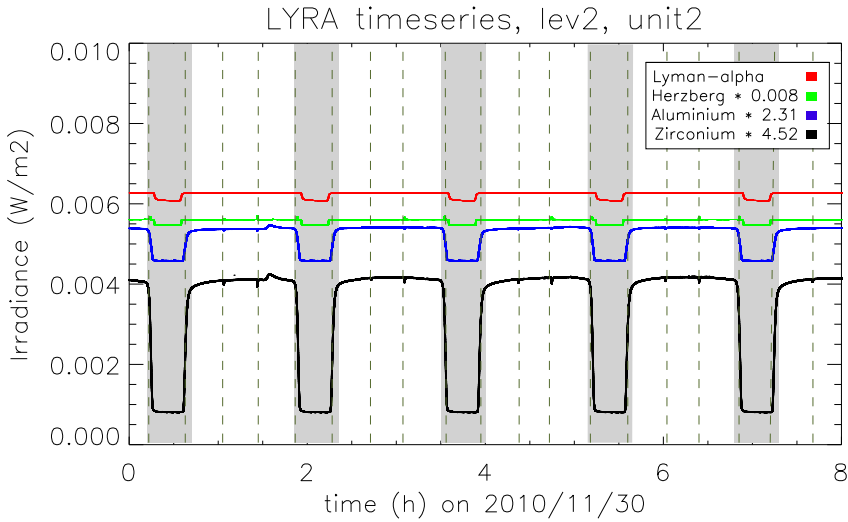


Figure 2.11: Drop of signal when the spacecraft transits the Earth shadow (highlighted with gray). Vertical dashed lines indicate the wide-angle rotations of the spacecraft. Time series have been rescaled to fit the same range and appear in the same order as in the legend. Scaling coefficients are indicated in the legend.

spacecraft movement during these maneuvers with sufficient accuracy to allow for any correction. Wide-angle rotations are systematic and therefore should not be confused with natural solar variability.

### 2.3.3.3 Occultations

From November to February (approximately), the orbit of PROBA2 crosses the Earth shadow. This produces a progressive attenuation of the solar signal when LYRA is observing the Sun through deeper layers of the Earth's atmosphere and finally produces total extinction, see Figure 2.11. These features are easily identifiable by an observer because of their regularity.

### 2.3.3.4 Slow Stabilization of MSM Detectors

MSM detectors need time to stabilize when they are exposed to light (see Figure 2.3). This phenomenon is likely due to the existence of surface defects

that trap the photoelectrons and prevent them from being collected at the electrodes. Similarly, when the covers are closed, the trapped photoelectrons are slowly released and the MSM detector signal does not immediately drop to zero. Trapped electrons may even take several hours to leak out.

### 2.3.3.5 South Atlantic Anomaly Perturbations

When transiting the SAA, secondary electrons generated by high-energy protons hit the detectors and make the LYRA signal more noisy. This effect mostly affects Si detectors, independently of the spectral range, while MSM and PIN detectors – which are radiationhard – usually do not show significant perturbations (the effect of the SAA on the LYRA measurements is visible in Figure 2.3). It is worth mentioning here that four channels of LYRA are amplified tenfold onboard to amend for their otherwise low signal: all three Lyman- $\alpha$  channels and the zirconium channel of unit 2. In these channels, the SAA perturbations appear magnified.

### 2.3.3.6 Auroral Perturbations

Auroral zones usually do not have any impact on the LYRA signal, with one noticeable exception: the perturbations (see Figure 2.12) appear in geomagnetic-storm conditions (the probability to observe those perturbations correlates well with the Kp index). These perturbations have been attributed to ultra-relativistic electrons that reach the spacecraft altitude when the geomagnetic field is perturbed (see Katsiyannis et al., 2018).

## 2.2.4 Radiometric Accuracy

From Equation (2.5), the maximal uncertainty on the calibrated LYRA data is described by

$$\frac{\Delta E_{\text{cal}}}{E_{\text{cal}}} = \frac{\Delta i}{i} + \frac{\Delta \left( \int_{\lambda} E d\lambda \right)}{\left( \int_{\lambda} E d\lambda \right)} + \frac{\Delta A}{A} + \frac{\Delta \left( \int_{\lambda} E F D d\lambda \right)}{\left( \int_{\lambda} E F D d\lambda \right)}, \quad (2.6)$$

where  $i = i_{\text{uncal}} + i_{\text{d}} + \text{corr}$ . We discuss the terms of this equation individually.

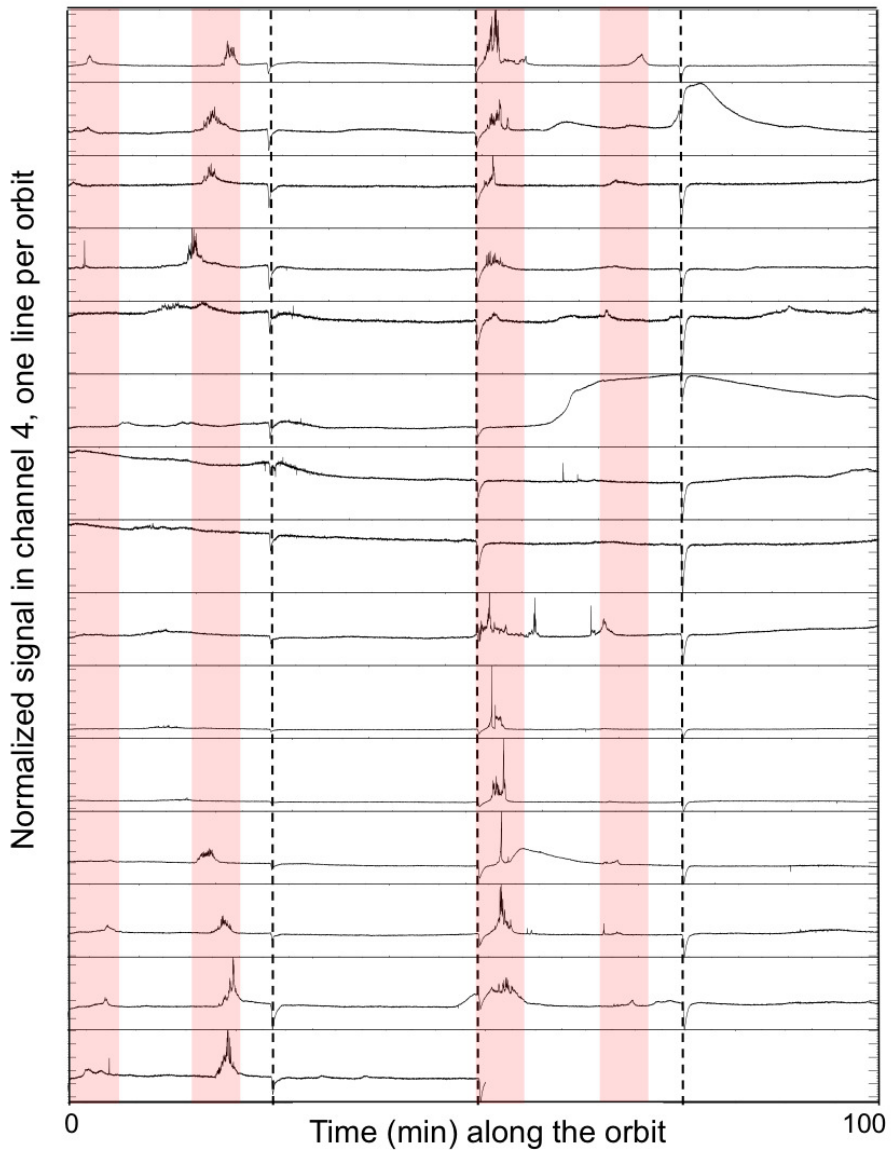


Figure 2.12: Perturbations that appear when the auroral zone is crossed during or after a geomagnetic storm. Each horizontal line corresponds to one orbit. Four zones of perturbations are identified for each orbit (highlighted with red). They occur systematically in the same range of latitudes (north and south auroral ovals are each crossed twice during an orbit). Dashed vertical lines indicate the wide-angle rotations of the spacecraft.

### 2.3.4.1 Error on the Measured Currents

The first term of Equation (2.6) takes into account the measurement error on the solar signal and on the dark current, as well as the error estimate introduced by the corrective term. Both solar signal and dark current depend on

- a quantization error,
- the stability of three onboard reference voltages (0 V, 2.5 V and 5 V), which are used to convert data expressed in data numbers into voltages. This conversion implies a polynomial fit (second order) of the three reference voltages, which also introduces its own error,
- the uncertainty on the internal resistor, used to convert the voltages into currents,
- the uncertainty on the integration time, which is related to the quartz stability.

BenMoussa et al. (2009) estimated the relative uncertainty associated with these four parameters for each LYRA channel, and obtained an associated error of 0.03 % at maximum.

Additionally,  $i_{\text{uncal}}$  is also affected by the pointing stability (jitter). For Sun-centered acquisitions, the jitter combined with flat-field non-homogeneities results in an uncertainty  $\leq 1\%$  in all channels.

Furthermore,  $i_{\text{uncal}}$  can be split into its in-band and out-of-band components. The latter are considered part of the measurement error and are on the same order as the complement to the purity in Table 2.1. This is one of the main sources of uncertainty because it is on the order of 5 % of  $i_{\text{uncal}}$  in most channels and even of 75 % in channel 1.

Last but not least, the error associated to the corrective term is hard to estimate. This term is based on the assumption that channel 4 of unit 1, which is used as a reference, degrades linearly and that the solar emission over the bandpasses of channels 1 and 2 do not show any long-term trend. Therefore, one might consider that the error introduced by the corrective term for channels 3 and 4 is lower than the actual degradation of channel 4 of unit 1 (*i.e.* a few per cent of the corrective term<sup>2</sup>), and that it is of the order of the solar variability over the solar cycle for channels 1 and 2. The Lyman- $\alpha$  line shows variations that can reach up to 100 % during very active period, but which are closer to 75 %

---

<sup>2</sup>At the time of writing the corrective term has reached 15%.

on average (Kretzschmar et al., 2018). The variability around 200 nm is of the order of 5 %.

In conclusion, the uncertainty on the measured current is mostly caused by the correction for degradation and by the out-of-band radiation. For channels 1 and 2, the importance of the corrective term for the degradation increases over time. However, the error that it induces on the calibrated measurements, which was estimated using a priori knowledge of the solar variability in this channel, remains approximately constant. This is not the case for the error induced by the out-of-band contribution, as the spectral response of the instrument might change as a result of the degradation. This aspect is analyzed in Chapter 3. For channels 3 and 4, the error associated to both effects is likely to increase over time. At the time of the first light, we consider an overall uncertainty on the measured current of about 150 % in channel 1, of 11 % in channel 2 and of 6 % in the other channels.

#### **2.3.4.2 Error on the Spectrum**

The second term in Equation (2.6) depends on the accuracy of the SORCE/SOLSTICE and TIMED/SEE measurements that have been used to produce the reference spectrum needed to convert the LYRA data numbers into irradiance units. The accuracy on those two spectra are on the order of 5 % and 10–20 % respectively. The first value applies to channels 1 and 2, while the second value is used for channels 3 and 4.

#### **2.3.4.3 Error on the Aperture Area**

The aperture area was measured at the Swiss Federal Office of Metrology and Accreditation (METAS) with an uncertainty of 0.07 % (see BenMoussa et al., 2009).

#### **2.3.4.4 Error on the Simulated Current**

Combining the uncertainty on the filter and detector characterization, which is provided in (BenMoussa et al., 2009), with that of the solar spectrum yields an estimated error of 15–20 % in all channels.



Table 2.5: Variation percentage in LYRA calibrated data induced by the use of an alternative reference spectrum (these values are for the nominal unit of LYRA).

Spectrum	Lyman- $\alpha$	Herzberg	Aluminum	Zirconium
NRLSSI	-17.5 %	-0.4 %	-7.8 %	+0.6 %
SATIRE	+19.1 %	-3.5 %	0 %	0 %
SRPM	+2.3 %	-4.2 %	0 %	0 %
EVE	-	-	+3.7 %	+24.1 %

### 2.3.4.5 Summary of the radiometric accuracy

We consider the uncertainty on LYRA calibrated data at the beginning of the mission to be about 35–45 % for all channels except for channel 1, where it is about 175 %.

In an attempt to validate these uncertainties, we used alternative spectra in Equation (2.5) and saw how the LYRA data were affected. Unfortunately, for the considered date (6 January 2010) and spectral ranges, we are not aware of any other measured spectra than the TIMED/SEE and SORCE/SOLSTICE ones. Even empirical models such as NRLSSI (Lean et al., 2005) and SATIRE (Krivova et al., 2009) are not provided for periods after 2006 and 2007, respectively. We therefore tried to find a date with a similar solar-activity context as during LYRA first-light, for which these models produced spectra. We chose 10 November 2005. We also tested the SRPM model (Fontenla et al., 2009), which applies for very quiet-Sun conditions. Additionally, to also cover the shortest wavelength ranges in LYRA, we picked a date after 6 January 2010 when SDO/EVE was in use and repeated the exercise. The selected day is 16 June 2010. The obtained spectra are plotted in Figure 2.13.

The variations induced by changing the reference spectrum in the LYRA calibration are summarized in Table 2.5 and are all within the sum of the errors related to spectrum and simulated current.

## 2.3 Conclusion

At the time of writing, the LYRA radiometer has produced high-cadence time series of solar irradiance in the SXR–EUV–MUV range for nine years. The instrument performances have been analyzed and an error budget has been

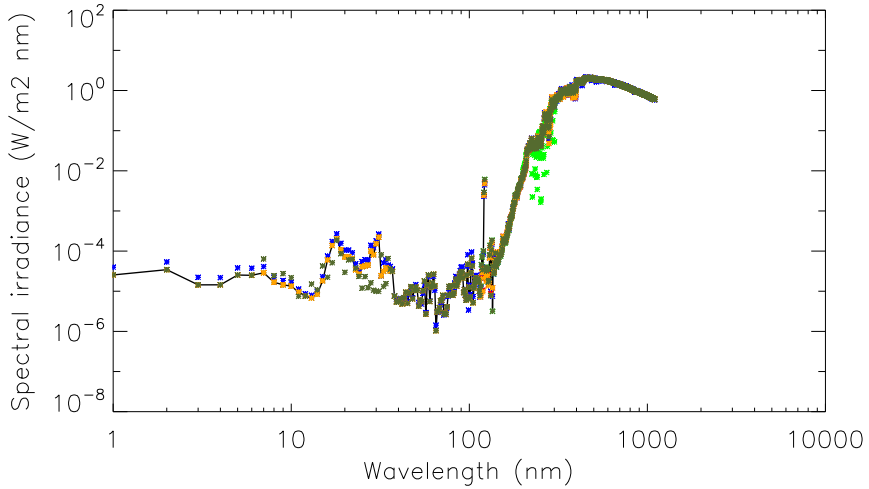


Figure 2.13: Alternative spectra used to calibrate LYRA data. The full black line represents the TIMED/SEE-SORCE/SOLSTICE reference spectrum. Alternative spectra that were tested are overplotted and correspond to NRLSSI (blue), SRPM (green), SATIRE (orange), and EVE (olive).

established. The data calibration includes subtraction of the dark current, rescaling to 1 AU, correction of the degradation and conversion of the received data numbers into physical irradiance units. The degradation experienced by the instrument is severe and is currently corrected by adding an offset to the measured values. Fortunately, the instrument benefits from a triple redundancy, so that units with a limited degradation are available for occasional observation campaigns. The degradation does not seem to originate from the pioneering diamond detectors of LYRA, as the evolution of their dark current is limited over the mission, and even slower than for classical silicon detectors. The diamond detectors are therefore good candidates to be used for future missions dedicated to solar observations in the SXR – MUV spectral range. However, two of the detector properties should be improved: their flat-field should be more uniform and they should stabilize faster.

## Chapter 3

# Analysis of the Spectral Degradation of LYRA

As mentioned in Section 2.2.2, the two main sources of error in the calibrated LYRA data (especially in the data acquired with channel 1) are the out-of-band contributions and the degradation. Additionally, these sources of error are likely to become more important as the instrument ages, which might affect its spectral response. It is important to understand the degradation processes as they might change the range of temperatures to which LYRA is sensitive and impact its detection capabilities.

The correction of the degradation that is currently applied in the data calibration is additive: the estimated loss of signal caused by degradation is added to the measurements. This prevents from artificially increasing the intensity of flares, which was found to remain unchanged over time. However, an additive correction might be a poor representation of the actual degradation mechanism. In this chapter, we investigate the degradation process in more detail and propose a model that may better reflect the reality. This work was not published so far.

### 3.1 Identification of the Source of Degradation

Several physical mechanisms can be at the origin of the degradation that affects space instruments (see *e.g.* BenMoussa et al., 2013, for a review), and most of the optical components can be affected. A few examples are polymerization of contaminants on optical surfaces, radiation-induced decrease of the quantum

efficiency of the detectors, "burn-in" of the most exposed parts of the detectors, decrease of mirror reflectivity under UV exposure, etc.

LYRA regularly performs in-flight calibration campaigns during which it closes its covers and acquires sequences of dark-current and LED measurements. Since the calibration LEDs are located between the filters and the detectors (see Figure 2.1), they allow separating the evolution of the detector performance from that of the rest of the optical channel. The inspection of the LED signal over the first few months of the instrument life time revealed almost no evolution, while at the same time, the drop of signal in the nominal unit was dramatic. Also, the evolution of the dark current with time, which is an indicator of detector aging caused, among others, by the impact of energetic particles, appeared very limited (it was hardly detectable over the first months of the mission).

This evidence indicates a degradation mechanism that has its origin at the filters. Moreover, since the loss of signal was found to differ strongly from one channel to the other, the degradation is clearly spectrally dependant. One mechanism that frequently affects space-borne instruments is linked to a layer of contaminant that is deposited and polymerized on optical surfaces. In most cases, the contaminants are hydrocarbons coming from the fuel and spacecraft outgassing. Therefore, when no information on the nature of contamination is available, it is often attributed to carbon (see *e.g.* BenMoussa et al., 2013; Wieman et al., 2014; Schäfer et al., 2017, etc). However, when checking the list of materials that have been used to build LYRA, we also discovered the presence of RTV, a silicon-rubber that is known to produce absorption in the EUV. Silicon was therefore considered as a candidate contaminant as well.

## 3.2 Model of Contamination

Equation 2.2 can be easily modified to include the absorption by a layer of contaminant:

$$i = i_s + i_d = \frac{A}{T} \int_t \int_\lambda E(\lambda, t) F(\lambda) \exp \left( - \sum_i \sigma_i(\lambda) L_i \right) D(\lambda) d\lambda dt + i_d, \quad (3.1)$$

where

- $\sigma_i$  is the absorption cross-section of the contaminant  $i$ ,
- $L_i$  is the thickness of the contaminant  $i$ .

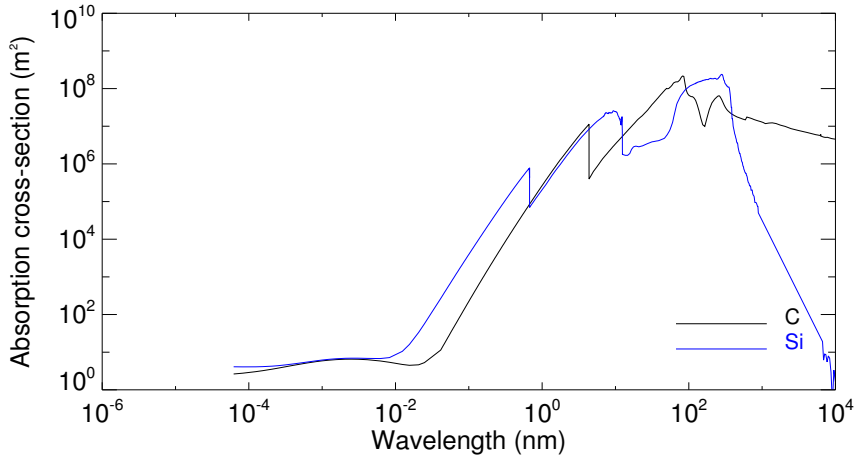


Figure 3.1: Spectral dependency of the absorption cross-section of the carbon (black line) and silicon (blue line). The data were obtained from the Centre for X-Ray Optics (<https://www.cxro.lbl.gov/>).

The absorption cross-section varies as a function of the wavelength in a way that is specific to each contaminant, see Figure 3.1. Therefore, comparing the signal attenuation in the four LYRA channels provides a diagnostic tool to determine which contaminants are contributing to the degradation.

Based on the hypothesis that the thickness of a contaminant layer that is deposited on one LYRA unit does not vary from channel to channel and using Equation 3.1, we can fit the thicknesses of carbon and silicon layers that best match the degradation measurements in the four channels at any time  $t$ .

For example, after 200 days of operation, the four channels of the nominal unit had respectively lost 91%, 95%, 79%, and 16% of their sensitivity. This would correspond to 5.764 nm of silicon + 143.4 nm of carbon. The resulting transmission is illustrated on Figure 3.2. In this plot, the soft X-ray spectral range has been presented separately from the channels 3 and 4 (while actually being a part of their bandpasses) because this part of the spectrum is suspected to show little degradation. This is deduced from the consistency of the flare amplitude (most of the flare irradiance comes from the short wavelengths) independently from the level of degradation.

Repeating this exercise for any time  $t$ , we determine the evolution of the contaminant layer thicknesses over the mission, as illustrated for unit 2 in

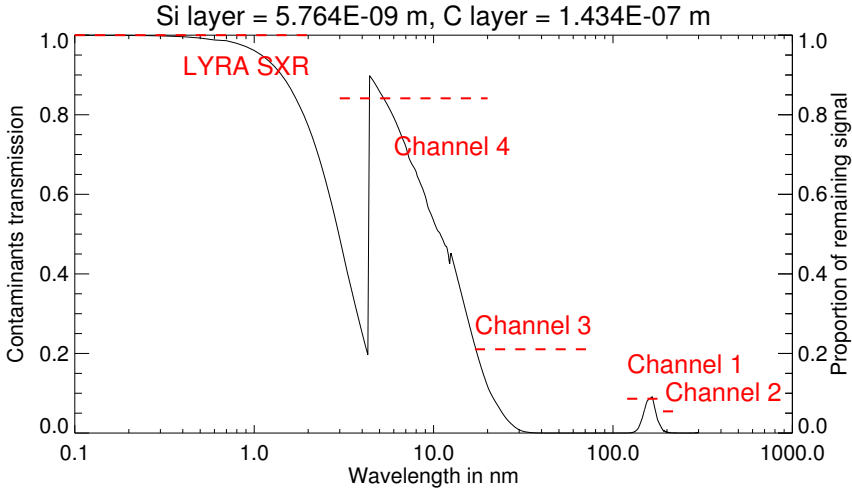


Figure 3.2: Normalized spectral transmission of 5.764 nm of silicon + 143.4 nm of carbon (solid line) and comparison with the proportion of remaining signal in each channel of LYRA after 200 days of mission as compared to the first light (red dashed lines). The proportion of remaining signal in the SXR spectral range has been represented separately from channels 3 and 4 (while being actually part of their bandpasses) as this part of the spectrum is believed to be little affected by degradation.

Figure 3.3. Except for a few dates for which the routine seemed to experience difficulties to disentangle between the two species (blue points), the fitting process converges to a contamination that is fully attributed to the carbon (no silicon at all) and that mostly took place during the first six months of the mission.

There is a reasonable agreement between the observed degradation (represented by the horizontal bars in red) and the modelled extinction by contaminants (the black line) in Figure 3.2. However, it is not fully convincing: the extinction obtained from the fitting procedure seems too strong in channels 1, 2, and 4, while it is not sufficient to explain the loss of signal in channel 3. We suspect that the degradation process affecting channel 3 differs from that affecting the other channels. It should be noted however that to be fully comparable to the measurements, the extinction curve should be multiplied by the solar spectrum and the spectral response of the instrument, integrated over the bandpass of each channel and compared to first light. This exercise has been done in Figure 3.6, which therefore constitutes a better way to validate the quality of the fit.

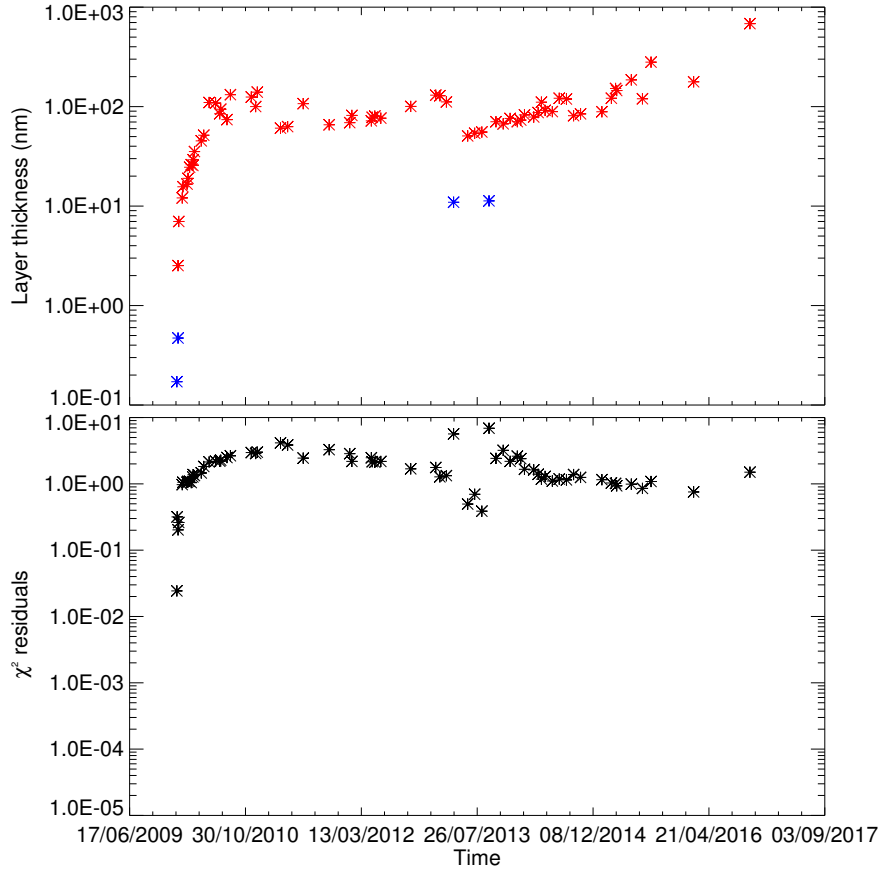


Figure 3.3: Top panel: evolution over time of the thickness of the silicon (blue symbols) and carbon (red symbols) layers obtained by fitting the model of degradation to the loss of signal observed in the four channels of the unit 2 of LYRA. Bottom panel:  $\chi^2$  residuals of the fitting procedure.

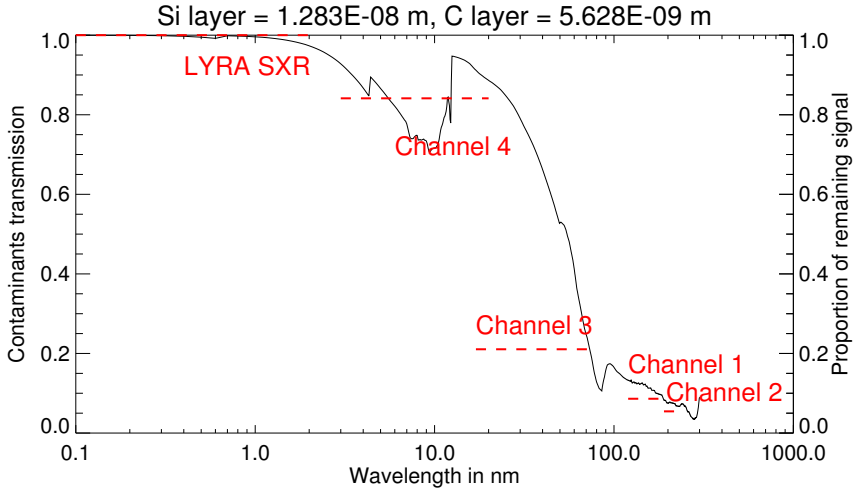


Figure 3.4: Spectral transmission of 13.82 nm of silicon + 5.63 nm of carbon (solid line) and comparison with the proportion of remaining signal in each channel of LYRA after 200 days of mission as compared to the first light (red dashed lines). The proportion of the remaining signal in the SXR spectral range has been represented separately from channels 3 and 4 (while being actually part of their bandpasses) as this part of the spectrum is believed to be little affected by degradation.

Interestingly, this channel includes a metallic aluminum filter. A similar difference between aluminum and non-metallic filters has been observed on SDO/EVE (Jones et al., 2013; BenMoussa et al., 2013), and was attributed to the development of a UV-enhanced oxide layer. Laboratory measurements have shown that under UV exposure, oxide termination layers (that would have normally remained stable) tend to over-develop (Boller et al., 1983).

We therefore repeated the same exercise excluding the channel 3 from the fitting process. For 200th day of operation, it resulted in a mixed silicon-carbon contamination, with a predominance of silicon (13.82 nm of silicon *vs* 5.63 nm of carbon), which seems in a better agreement with the observations for that specific day (see Figure 3.4). This conclusion seems to be valid over the whole mission: the result of the fitting procedure points to a contamination that would be dominated by the silicon, with the carbon playing a role only during the few first months following the launch and possibly in the later phase of the mission (see Figure 3.5).

Such a behavior is unlikely, though, as in this case, it would be difficult to explain



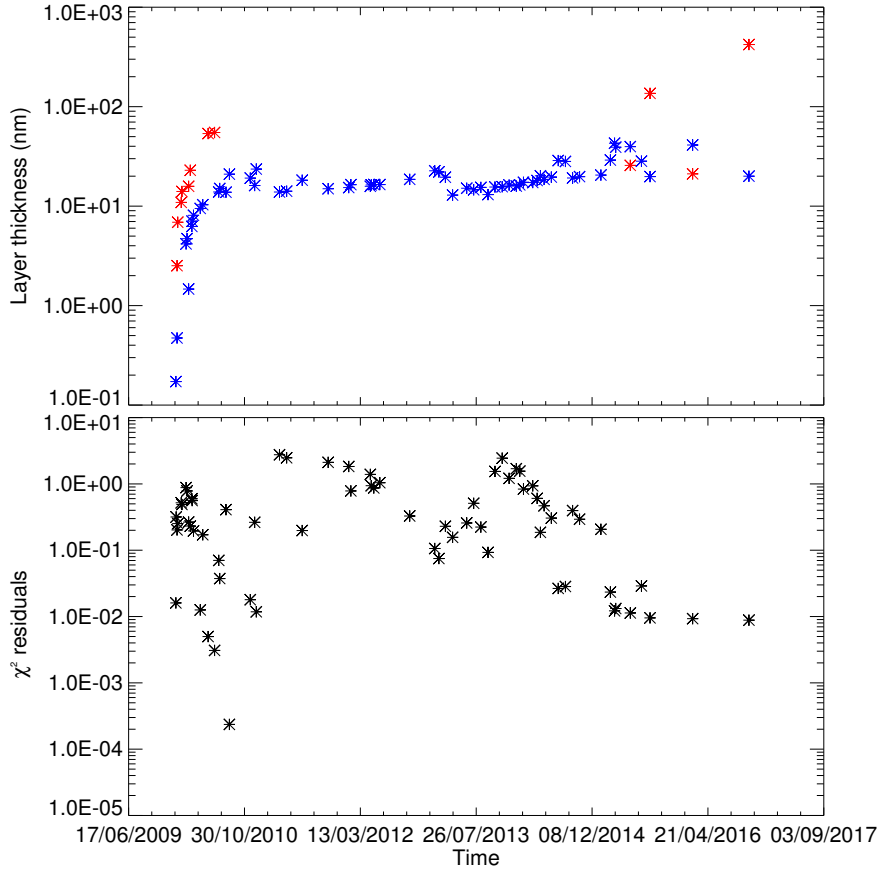


Figure 3.5: Top panel: evolution over time of the thickness of the silicon (blue symbols) and carbon (red symbols) layers obtained by fitting the model of degradation to the loss of signal observed in channels 1, 2, and 4 of the unit 2 of LYRA (*i.e.* excluding the measurements of channel 3 from the fitting procedure). Bottom panel:  $\chi^2$  residuals of the fitting procedure.

a reduction of the carbon layer over time. We rather believe that the absorption cross-sections  $\sigma_i$  (see Equation 3.1) of the two contaminants are too similar and that the fitting procedure does not manage to distinguish them properly. We therefore believe that the carbon-dominated contamination fitted on the four channels is the preferred model. We intend to continue this investigation in the future. In particular, we intend to check the effect of an oxide layer on the aluminum filter (channel 3) and determine if such an oxidation process would also be affecting the other metallic filter (the zirconium filter used in channel 4).

Figure 3.6 compares the evolution over time of the measured loss of sensitivity in the four channels of unit 2 to the one modelled using a carbon-based contamination (*i.e.* using the contaminant layer thicknesses shown in Figure 3.3). The degradation of the channel 3 is poorly represented by the model (which could be expected if it is affected by another source of degradation as explained above), the results are quite convincing for the other channels.

The same analysis has been performed on units 1 and 3. For unit 3, the contamination is dominated by carbon, consistent with what was observed in unit 2 (see Figure 3.7). For unit 1, the contamination is found to alternate between the carbon (mainly at the beginning of the mission) and the silicon. Again, such a behaviour is unlikely. Considering the carbon as the only contaminant, the degradation curve shown in Figure 3.8 is obtained.

### 3.3 Effect of the Contamination on the Spectral Response of the Instrument

The broad spectral ranges of LYRA correspond to similarly broad ranges of plasma temperature, which determine what solar structures are visible in each channel. Since the degradation affects the spectral composition of LYRA channels, it also changes their temperature sensitivity, and solar features that were observable at the beginning of the mission might no longer be visible once the degradation reaches a certain level. It is therefore important to track the aging effects not only in the integrated signal, but also over the spectral range.

The most striking example is the Lyman- $\alpha$  channel, which is actually a blend of the Lyman- $\alpha$  line and of emission at wavelengths longer than 200 nm, as described in Section 2.1. At the beginning of the mission, LYRA observed several flares in this channel (see Kretzschmar et al., 2013). However, no flare signature was detected in this channel after March 2010 by the nominal unit, even during the strongest flares of the solar cycle. Unit 3, which was used more rarely, continued producing flare signatures until 2012. After that no flares

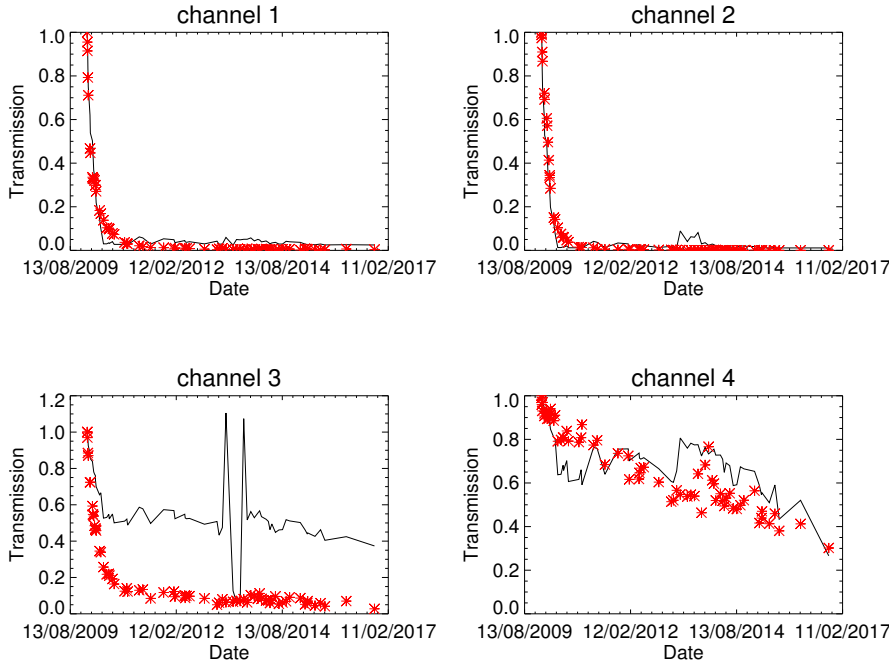


Figure 3.6: Measured (red stars) and modelled (black lines) evolution of the transmission of the four channels of unit 2. The modelled curve is based on a contamination that is dominated by carbon (see Figure 3.3).

were observed by unit 3, although the Lyman- $\alpha$  channel in this unit had only lost 40% of its initial signal as of early 2018. It seems that the lost signal was mostly coming from around the Lyman- $\alpha$  line, drastically changing the purity of the channel. This can be demonstrated using LYRA measurements made during occultations of the Sun by the Earth.

### 3.3.1 Using Occultation Data to Determine the Evolution of the Spectral Response.

During an occultation, the orbit of the spacecraft crosses the Earth shadow. The instruments then experience eclipse conditions during which they cannot see the Sun anymore. Just before disappearing behind the disk of the Earth and just after reappearing on the other side, the instruments observe the Sun

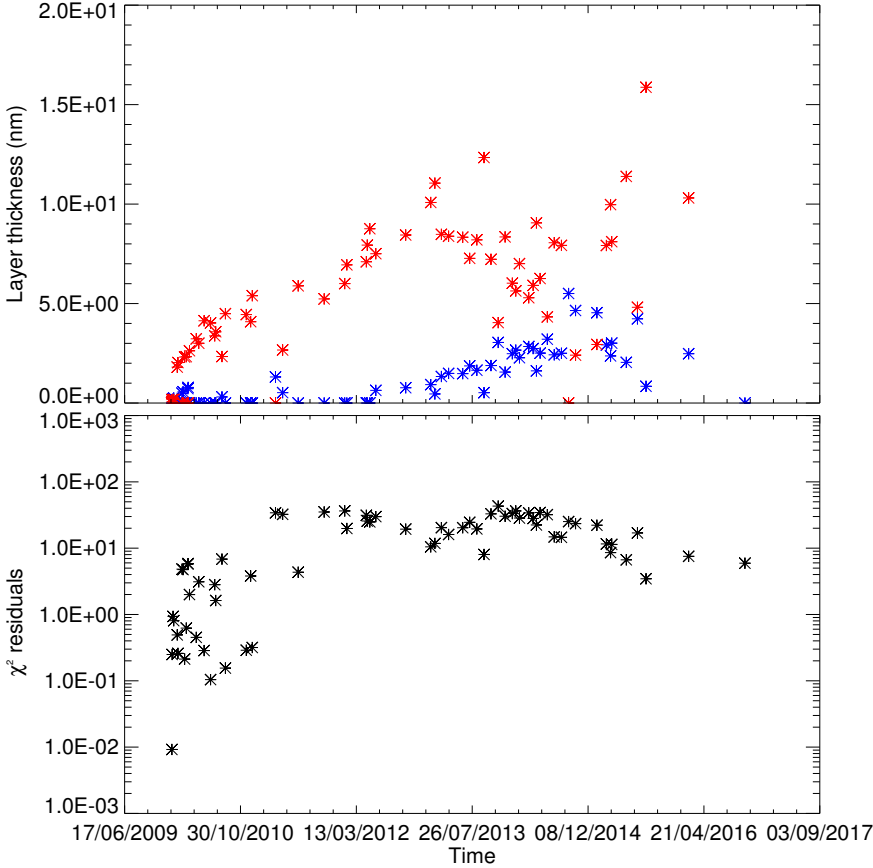


Figure 3.7: Top panel: evolution over time of the thickness of the silicon (blue symbols) and carbon (red symbols) layers obtained by fitting the model of degradation to the loss of signals observed in the four channels of the unit 3 of LYRA. Bottom panel:  $\chi^2$  residuals of the fitting procedure.

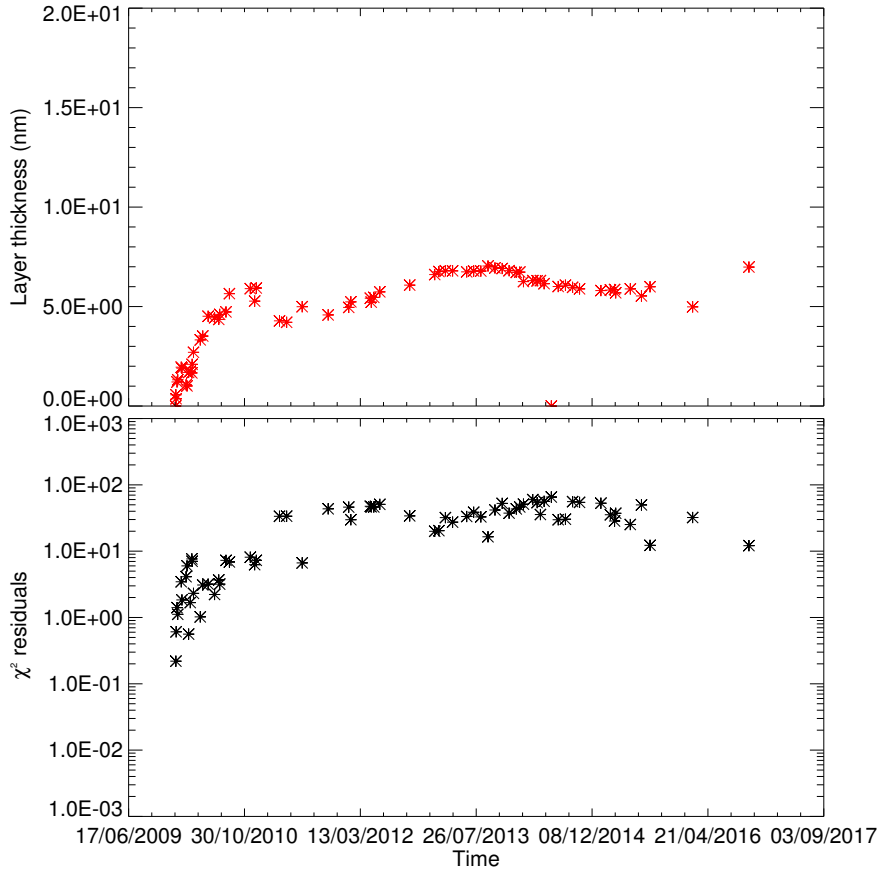


Figure 3.8: Top panel: evolution over time of the thickness of the carbon layer obtained by fitting the pure-carbon model of degradation to the loss of signal observed in the four channels of the unit 1 of LYRA. Bottom panel:  $\chi^2$  residuals of the fitting procedure.

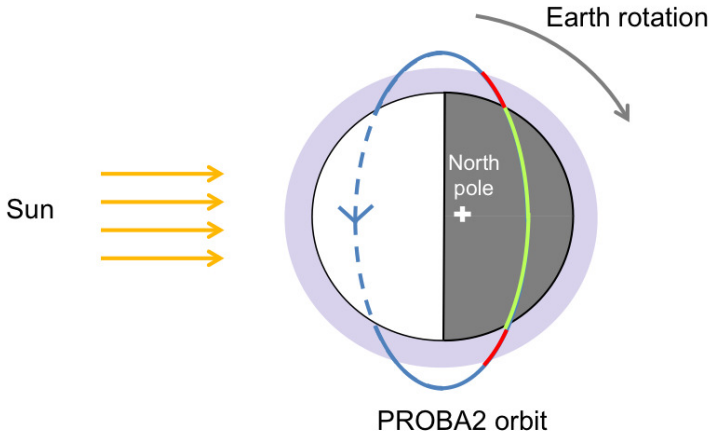


Figure 3.9: Illustration of an occultation. The part of the orbit in green corresponds to the one during which the spacecraft is in the Earth shadow, while the parts in red are the ones during which the satellite observes the Sun through the Earth atmosphere, *i.e.* the occultation.

through the Earth's atmosphere (see Figure 3.9). Since some of the atmospheric constituents absorb the wavelengths to which LYRA is sensitive, they produce in each channel an extinction profile, which is a function of the lowest altitude crossed by the optical path (the so-called tangential altitude, where most of the absorption happens) and which depends on the atmospheric composition. These measurements offer us a unique opportunity to test our model of contamination.

PROBA2 rarely experiences such occultation as its orbit was chosen to maximize visibility of the Sun. However, they still happen during the winter season. Observing the yearly evolution of the extinction profile of a channel highlights the changes in its spectral response. Alternatively, such measurements can be used to determine the number density profiles of some atmospheric constituents and their evolution (see Dominique et al., 2009; Thiemann et al., 2017), but this goes beyond the scope of this thesis.

The top panel of Figure 3.10 illustrates how the extinction profile of the Lyman- $\alpha$  channel of unit 3 evolved from year to year. The measured extinction shows a two-step drop, the one at higher altitudes corresponding to the absorption of the wavelengths around the Lyman- $\alpha$  line, while the one at lower altitudes corresponds to the absorption of wavelengths longer than 135 nm. As anticipated from the pre-launch measurements of the channel purity, at the beginning of the mission, the relative importance of the first and second drops as compared

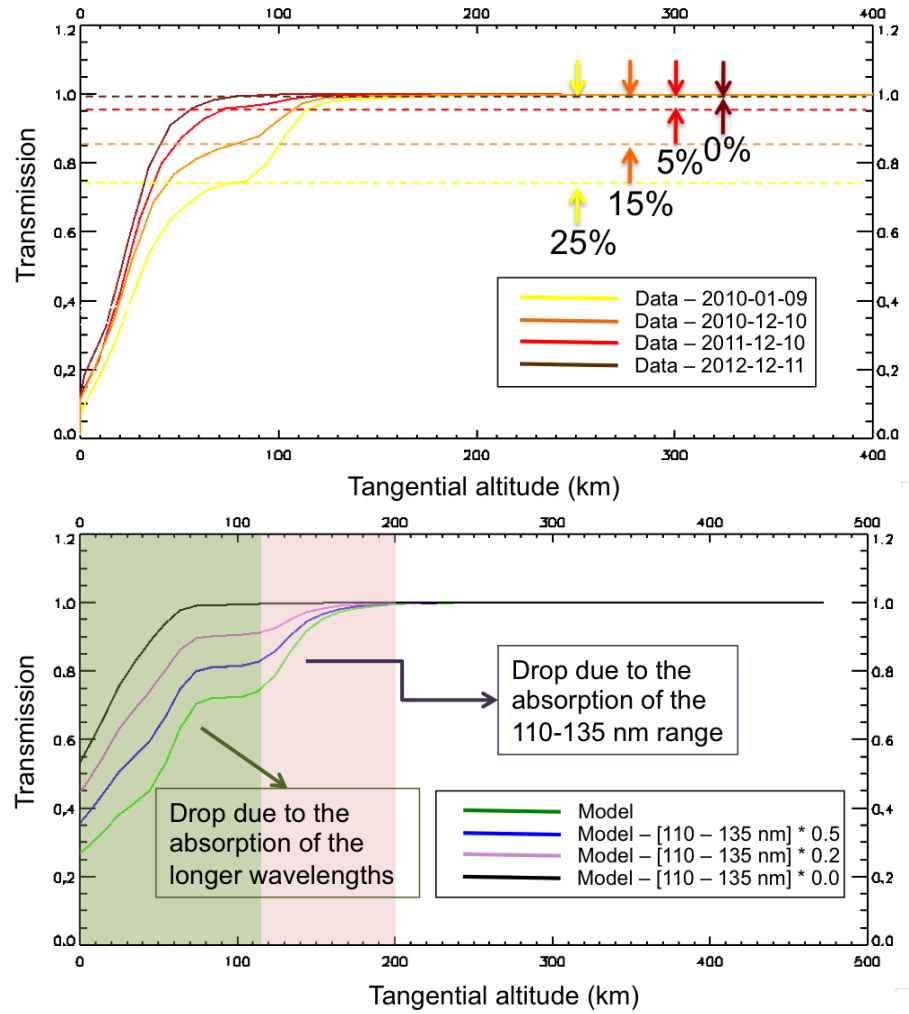


Figure 3.10: Measured (top panel) and modeled (bottom panel) occultation profile of the channel 1 of unit 3. The measured extinction shows a two-step drop, the one at the highest altitudes corresponding to the absorption of the wavelengths around the Lyman- $\alpha$  line, while the one at lower altitude corresponding to the absorption of wavelengths longer than 135 nm. The relative importance of each drops clearly evolves with time, which can be reproduced in the bottom panel by reducing the purity of the instrument.

to the total extinction are 25% and 75% respectively. However, these ratios evolve with time, and after 2012, the first drop completely vanishes.

The extinction of the solar emission by the Earth's atmosphere at a given wavelength  $\lambda$  can be modelled based on the well-known Beer-Lambert (or Bouguer) law

$$E(\lambda, dS) = E_0(\lambda, dS) \exp(-\tau(\lambda, dS)), \quad (3.2)$$

where  $E_0(\lambda, dS)$  is the spectral irradiance at the top of the Earth's atmosphere emitted by a unit surface of the Sun  $dS$  at the wavelength  $\lambda$ ,  $E(\lambda, dS)$  is the solar spectral irradiance after absorption by the atmosphere, and the optical thickness  $\tau(\lambda, dS)$  is defined by

$$\tau(\lambda, dS) = \int_0^L \sum_{i=0}^N n_i(z(s)) \sigma_i(\lambda) ds, \quad (3.3)$$

where:

- $N$  is the number of atmospheric constituents showing a significant absorption over the channel bandpass. In this case, only  $O_2$  and  $O_3$  are considered;
- the integration is performed over the optical path  $s$  (with  $L$ , the distance between the Sun and the satellite, measured along this path);
- $n_i(z(s))$  is the density of the atmospheric constituent  $i$  at the altitude  $z(s)$ ;
- $\sigma_i(\lambda)$  is the absorption cross-section of constituent  $i$  at the wavelength  $\lambda$ .

Note that in equation 3.3, only absorption takes part in the extinction process. The contribution of molecular scattering was considered negligible in the spectral range of channel 1.

Equation 3.2, once integrated over the whole solar disk (here considered to emit uniformly), can be used to model the extinction profile observed by LYRA. However, since the Sun has a significant angular extension (as seen from the PROBA2 orbit, the solar diameter crosses 25 km of the Earth's atmosphere along the tangential height), it results in a non-negligible error. Instead of considering the solar surface as a whole, it is best to divide it in several horizontal slices and to treat them separately. In our case, we considered slices of which the apparent size is 1 km high along the tangential height (*i.e.*  $\sim 25$  slices).



This results in the green curve in the bottom panel of Figure 3.10. The blue, purple and black curves were obtained by modifying the spectral response of the instrument, so that its purity is artificially reduced to 50%, 20% and 0% of its initial value, respectively. This reproduces quite well the observations, at least qualitatively. It therefore seems that a loss of purity could indeed explain the evolution of the channel extinction curve.

### 3.3.2 Spectral Degradation

The changes induced by the degradation in the spectral response of the instrument can be modelled at any time of the mission using the thickness of the layers of contaminant determined in Section 3.2. For example, Figure 3.11 represents the evolution of the spectral response of each channel of unit 2 over the mission. It was obtained by multiplying the spectral response of each channel by  $\exp(-\sigma_C L_C - \sigma_{Si} L_{Si})$  for six periods of the mission.

We note that, as the degradation progresses, the Lyman- $\alpha$  line is more and more rejected from the spectral response of channel 1, of which the peak responsivity moves to  $\simeq 150$  nm. This behaviour is consistent with observations made in occultation and could explain why no flare was observed by the nominal unit in channel 1 after February 2010. Also, the EUV part of channels 3 and 4 is more and more attenuated, so that these channels progressively turn into pure SXR channels. That could explain why, despite the degradation, the amplitude of flares (which mostly emit in the SXR) remains unchanged. However, this also opens perspectives for future improvements of the routine correction of degradation. As long as the EUV part of the spectrum slightly contributes to the signal measured by channel 3, it can be estimated from a comparison with the measurements by channel 4. Such a correction was already suggested by Kretzschmar et al. (2012) and should be tested in the future.

## 3.4 Conclusion

In this chapter we investigated the degradation process affecting the instrument in details. The main contribution seems to be caused by the deposit of contaminants on the front filter. Comparing the loss of signal in the four channels of each unit allowed us to determine the main contaminants, their evolution over the mission and their impact on the spectral response of the instrument. In the case of LYRA, most of the contamination seems to be due to carbon, and silicon seems to play a smaller role. Also, we cannot rule out that an additional aging process affects the channels 3 of the three units. Comparing

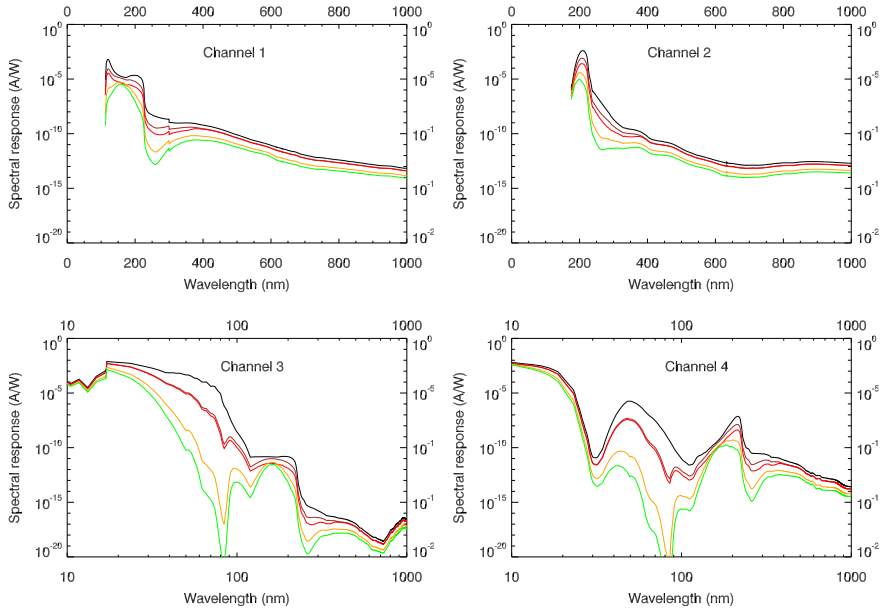


Figure 3.11: Evolution of the spectral response of each channel of the unit 2. The different colours represent different times of the mission: Black: 6 January 2010 (first-light acquisition, no degradation), brown: 24 March 2010, red: 15 May 2013, orange: 15 May 2014, green: 25 February 2015

the situation on LYRA to that on SDO/EVE, this other aging process could be due to the development of an extra layer of oxide on the aluminum filters.

Our results once more highlight the importance of a strong cleanliness policy when building space instruments, especially when those are devoted to the observation of the UV spectral range. The possibility of an oxide layer must be investigated further, as it might condition the choice of filters in future missions.

The contamination tends to modify the spectral response of the instrument. In particular, channel 1 becomes less and less sensitive to the wavelengths neighbouring the Lyman- $\alpha$  line, and sees its peak wavelength progressively shifting to 150 nm. As a consequence, this channel loses its ability to detect solar flares. Also, channels 3 and 4 progressively turn into pure SXR channels, which has an impact on their long-term variability. However, gaining information on how the degradation affects the spectral response of the instrument also opens new perspectives for updating the degradation correction in the data

calibration. This allows us to continue using LYRA, in particular for flare observations.



## Chapter 4

# Multi-Wavelength Analysis of the Strongest Solar Flare of Solar Cycle 24

This chapter provides an analysis of the only flare event that was observed by the four channels of LYRA. Except for Section 4.5, it is reproduced from Dominique et al. (2018b). M. Dominique implemented a model of flare emission in the Balmer continuum of the hydrogen and compared its predictions with the observations by the channel 2 of LYRA.

### 4.1 Introduction

Solar flares and associated coronal mass ejections are among the most powerful energy release events in the solar system. Surprisingly little is known about the distribution of the flare energy over the full solar spectrum (Veselovsky and Koutchmy, 2006). Routine measurements of the X-ray and extreme-ultraviolet (EUV) emissions probe only a small part of the total energy radiated during a flare (*e.g.* Emslie et al., 2012). Most of the flare radiation is emitted at longer wavelengths, but observations in this spectral range covering spectral lines and broadband continua are rare (Kretzschmar, 2011; Kleint et al., 2016). The parts of the solar spectrum between 1000 and 3000 Å, *i.e.* far-ultraviolet (FUV), mid-ultraviolet (MUV), and near-ultraviolet (NUV), probably provide an important but still poorly known contribution to the total energy emitted

during flares (*e.g.* Woods et al., 2006; Milligan et al., 2014). The flare emission at these wavelengths also has a strong influence on the terrestrial atmosphere (Simon, 1978).

Solar spectra at the FUV to NUV wavelengths have been measured by rocket-borne and space-borne experiments (Durand et al., 1949; Bonnet and Blamont, 1968; Curdt et al., 2001; Woods et al., 2012; Meftah et al., 2018). Semi-empirical quiet-Sun models have been developed (Vernazza et al., 1981; Fontenla et al., 1993). As described, for example, by Gingerich et al. (1971) and Phillips et al. (2008), below 1527 Å the quiet-Sun spectrum consists of emission continua and emission lines (the strongest line being the H I Ly- $\alpha$  line at 1216 Å) and is mostly produced by the chromosphere. Above  $\sim 1800$  Å the spectrum consists of a number of continua blanketed by numerous absorption lines (Labs and Neckel, 1972), mostly produced by the upper photosphere. The spectrum between 1527 Å and  $\sim 1800$  Å is an absorption continuum with mostly emission lines, and is produced around the temperature minimum.

The FUV to NUV spectra taken during flares are quite rare (Cook and Brueckner, 1979; Lemaire et al., 1984; Doyle and Cook, 1992; Brekke et al., 1996). Woods et al. (2006) have observed FUV irradiance spectra for four of the largest flares of solar cycle 23; however, with the exception of the Mg IIk line, the flare signature above 1900 Å was too low to be detected. Heinzel and Kleint (2014) presented the first Interface Region Imaging Spectrometer (IRIS; De Pontieu et al., 2014) measurements of the Balmer continuum during flares in the NUV channel around 2826 Å. Other, quite rare flare detections in the Balmer continuum were made close to the Balmer recombination edge at 3646 Å by ground-based instruments (*e.g.* Hiei, 1982; Neidig, 1983; Kotrč et al., 2016). The contributions of the spectral line emission and continua into the total flare radiation may vary strongly, with either line or continuum emission being dominant depending on time and location (Kleint et al., 2017). The hydrogen Balmer continuum is produced by the recombination of free electrons generated during strong flare heating in the chromosphere (Avrett et al., 1986). The flare emission in the recombination continua is expected to be almost synchronous with the non-thermal hard X-rays bremsstrahlung emission produced by the beam of accelerated electrons (see *e.g.* Heinzel and Kleint, 2014).

## 4.2 Data description

LYRA takes high-cadence (nominally 20 Hz) spatially integrated solar irradiance measurements in its four wide spectral channels (that are recalled in the first two columns of Table 4.1), two of which are in the FUV and MUV. Channel

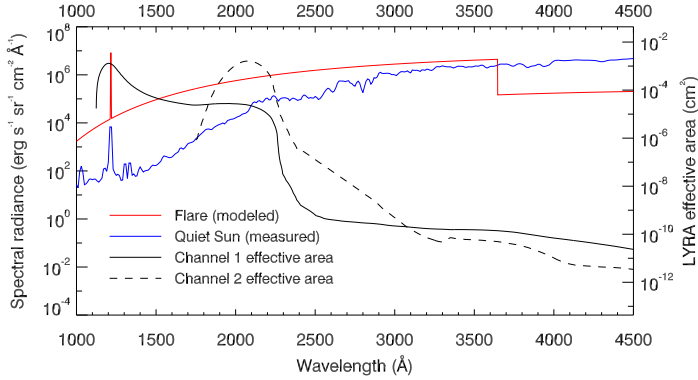


Figure 4.1: Solar radiance corresponding to typical quiet-Sun conditions and the increase (without the quiet-Sun background) of radiance produced by the flare. The spectrum  $I_\lambda$  (red line) of the flare of 2017 September 6 has been calculated following the procedure described in Section 4.4. The jump observed at 3646 Å is caused by the transition from the Balmer to the Paschen continua. The quiet-Sun spectrum (blue line) obtained by concatenating the measurements by SDO/EVE, SORCE/SOLSTICE and TIMED/SEE on 2010 January 7, is shown for comparison. The effective areas of the LYRA channels 1 (solid line) and 2 (dashed line) of the spare unit used during the flare campaign are overplotted in black.

1 (also called the Ly- $\alpha$  channel) takes observations around the Ly- $\alpha$  line and nearby continua. Channel 2 observes between 1900 and 2220 Å.

LYRA was calibrated before the launch at the PTB/BESSY II synchrotron (Dominique et al., 2013). The pre-launch effective area for channels 1 and 2, which is derived from the spectral response illustrated in Figure 2.4, is shown in Figure 4.1. Note that, as already mentioned in Section 2.1, channel 2 has a high spectral purity; *i.e.*, almost 100% of the measured signal effectively comes from the 1900 to 2220 Å wavelength range. However, this is not the case for channel 1, for which only 25% of the measured irradiance comes from the spectral range around Ly- $\alpha$ , while 75% originates from a plateau in the channel responsivity around 2000 Å. The latter interval overlaps the spectral range of channel 2, which can be used to disentangle the emission measured in the two channels. The last two channels observe the soft X-rays/EUV range and cover the 1–800 and 1–200 Å intervals, respectively.

We also use the data from the 1 to 8 Å channel of GOES-15 (acquired at a cadence of 2 s), as well as the Solar Dynamics Observatory/Helioseismic and Magnetic Imager (SDO/HMI) continuum images (Schou et al., 2012) to

determine the surface of the flaring region.



Table 4.1: Characteristics of the X9.3 Flare of 2017 September 6 Observed by LYRA and the Geostationary Operational Environmental Satellite (GOES)

Channel	Bandpass, Å	Pre-flare irradiance, $\text{erg s}^{-1} \text{cm}^{-2}$	Peak irradiance (11:58 UT), $\text{erg s}^{-1} \text{cm}^{-2}$	Flare increase, $\text{erg s}^{-1} \text{cm}^{-2}$	Flare increase, %
channel 1 (Lyman- $\alpha$ )	1200 – 1230*	6.85	6.92	0.07	0.97
channel 2 (Herzberg)	1900 – 2220*	690.1	692.6	2.5	0.35
channel 3 (Aluminum)	1 – 800	4.2	30.0	25.8	614
channel 4 (Zirconium)	1 – 200	1.45	25.5	24.05	1658
Lyman- $\alpha$ residual	1200–1550	-	-	0.05	-
GOES	1 – 8	0.007	1.35	1.34	19185

**Notes:** The Ly- $\alpha$  residual  $E'_1$  is obtained from the channel 1 irradiance  $E_1$  after subtraction of the contribution of the hydrogen Balmer continuum derived from channel 2 irradiance  $E_2$  (see Section 4.4).  $E'_1$  is dominated by the emission in a few strong lines, mostly the Ly- $\alpha$  and the C lines in the 1200–1550 Å range.

\* The bandpass provided here is as listed in (Dominique et al., 2013). See Figure 4.1 for the detailed spectral transmissions of LYRA channels 1 and 2 that are of importance for this work.

### 4.3 Observations

After several months of relative quiet, a sudden increase of solar activity was observed starting on 2017 September 4, when the NOAA AR 12673 started to grow quickly. This region produced multiple strong flares (27 M-class flares and 4 X-class flares) before disappearing behind the west solar limb on September 10. Among them were the two strongest flares observed so far during the solar cycle 24: the X9.3 flare on September 6 and the limb X8.2 flare on September 10.

At the time of these events, LYRA was performing a special flare observation campaign, involving one of its spare units (*i.e.*, its calibration unit, or unit 1). As this unit was only sporadically opened over the mission, it is relatively well preserved from the ageing process that otherwise affects the instrument (see Chapters 2 and 3), so it delivered clear observations of the X9.3 flare in all channels. Although about 35% and 20% of the sensitivity has been lost since the launch in channels 1 and 2, respectively, the degradation, which is thought to be caused by the deposit of a  $\sim 10$  nm thick layer of carbon on the entrance filter (see Figure 3.8), did not modify the spectral characteristics of the instrument (see Section 4.5).

The LYRA data set for the X9.3 flare is rather unique. The SXR/EUV channels of LYRA (channels 3 and 4) are specifically used for monitoring solar flares and have captured hundreds of them, but flare observations are relatively rare in channel 1 (Kretzschmar et al., 2013). The X9.3 flare was the first flare detected in channel 2 of LYRA.

The X8.2 flare, despite being the second strongest flare of the solar cycle, did not produce any signature in LYRA channels 1 and 2. This may be due to the fact that at least one of the footpoints of this flare was located behind the solar limb, hiding the source of the chromospheric emission (see also Chamberlin et al., 2018). Channels 3 and 4, which are the only channels of LYRA measuring coronal emissions, provided clear observations of the flare.

The increase of irradiance produced by the X9.3 flare observed by LYRA<sup>1</sup> and by GOES (in the 1–8 Å passband) is listed in Table 4.1 and shown in Figure 4.2. The estimated residual Ly- $\alpha$  irradiances listed in Table 4.1 were extracted from LYRA channel 1 following the procedure described in Section 4.4. In Figure 4.2, the pre-flare irradiance has been subtracted from each timeseries.

---

<sup>1</sup>The data in the LYRA channel 3 look very similar to the data taken in channel 4, and are not shown in Figure 4.2.

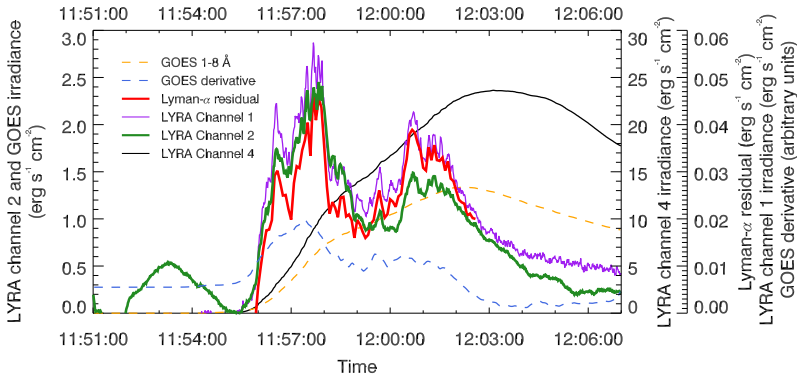


Figure 4.2: Solar irradiance during the X9.3 flare of 2017 September 6 (with the pre-flare irradiance subtracted), observed by GOES (orange line) and LYRA channels 1, 2, and 4 (respectively the purple, green, and black lines for  $E_1$ ,  $E_2$ , and  $E_4$ ), as well as the Ly- $\alpha$  residual irradiance  $E'_1$  (red line) extracted from  $E_1$ . The LYRA data were rebinned to the cadence of 1 s. The time derivative of GOES 1–8 Å data is also shown (blue line) as a proxy of the non-thermal flare emission. Different scales were used for the various time series for the sake of clarity.

Unfortunately, no hard X-ray measurements are available for this flare<sup>2</sup>. Therefore, we plotted in Figure 4.2 the derivative of the GOES data, which constitutes a good proxy for the flare non-thermal emission (Neupert, 1968). One immediately sees from Figure 4.2 that the emission in channels 1 and 2 looks different from the one in GOES and LYRA channel 4: it is highly modulated and peaks around 5 minutes earlier. It is similar to the derivative of the GOES 1–8 Å curve. It confirms the non-thermal temporal behavior of emission observed in LYRA channels 1 and 2.

## 4.4 Spectral Modeling

To assess what causes the flare emission in the channel 2 of LYRA, we need to model the flare spectrum around 2000 Å. Emission in the hydrogen free-bound and free-free continua, in the  $H^-$  continuum, as well as in spectral lines, has been considered in the literature (Damé and Cram, 1983; Damé and Vial, 1985; Avrett et al., 1986; Neidig et al., 1993; Kerr and Fletcher, 2014; Heinzel et al.,

<sup>2</sup>Most of the operational instruments were not observing the active region that produced the flare.

2017). For strong flares in the wavelength range of interest, the emission in the free-bound continuum is expected to be by far the strongest (Avrett et al., 1986; Neidig et al., 1993).

We therefore adopt the hypothesis that the increase of the irradiance in channel 2 during the flare is primarily due to enhancement of the free-bound continuum of Hydrogen. To calculate the Balmer continuum, we assume that the emission is produced by an optically thin chromospheric slab of plasma with the electron density  $n_e$  that is enhanced due to increased ionization during the flare. This model was tested *e.g.*, by Neidig et al. (1993), and for Paschen continuum by Kerr and Fletcher (2014) and recently by Heinzel et al. (2017). Dominant contribution of the Balmer continuum in MUV and NUV was also predicted by Avrett et al. (1986). The input parameters for a simple slab model are the electron temperature  $T$ , the electron density  $n_e$ , and the thickness of the emitting layer  $L$ . The emissivity in the hydrogen recombination continua takes the form (Hubeny and Mihalas, 2015):

$$\eta_\nu^i = n_e^2 F_i(\nu, T), \quad (4.1)$$

where  $i=2$  or  $3$  for Balmer or Paschen continuum, *i.e.* for the wavelengths below or above  $3646\text{\AA}$ , respectively, and  $\nu$  is the frequency of the continuum radiation. The function  $F_i$  is expressed as

$$F_i(\nu, T) = 1.166 \times 10^{14} g(i, \nu) T^{-3/2} B_\nu(T) \times \\ \exp(h\nu_i/kT)(1 - \exp(-h\nu/kT))/(i\nu)^3, \quad (4.2)$$

where  $\nu_i$  is the continuum-head frequency,  $g(i, \nu)$  the Gaunt factor,  $B_\nu(T)$  the Planck function, and  $h$  and  $k$  are the Planck and Boltzmann constants, respectively (Hubeny and Mihalas, 2015). For an optically thin case, this emissivity is multiplied by  $L$  to get the continuum radiance  $I_\nu$  (*i.e.* the specific intensity). Here we assumed an equality between proton and electron densities which is a good approximation in a flaring chromosphere. Furthermore, for the sake of simplicity we took  $g(i, \nu)=1$ , which is accurate enough for the considered continua. Here the continuum radiance  $I_\nu$  has units  $\text{erg s}^{-1} \text{cm}^{-2} \text{sr}^{-1} \text{Hz}^{-1}$ , which we convert to  $I_\lambda$  in  $\text{erg s}^{-1} \text{cm}^{-2} \text{sr}^{-1} \text{\AA}^{-1}$  by multiplying  $I_\nu$  with the factor  $3 \times 10^{18}/\lambda^2$ , where  $\lambda$  is the continuum wavelength in  $\text{\AA}$ .

Following Kerr and Fletcher (2014), we assumed a typical flare slab temperature of 10000 K. Then, we adjusted the emission measure  $n_e^2 L$  so that the resulting spectral radiance, once converted into irradiance, multiplied by the instrumental

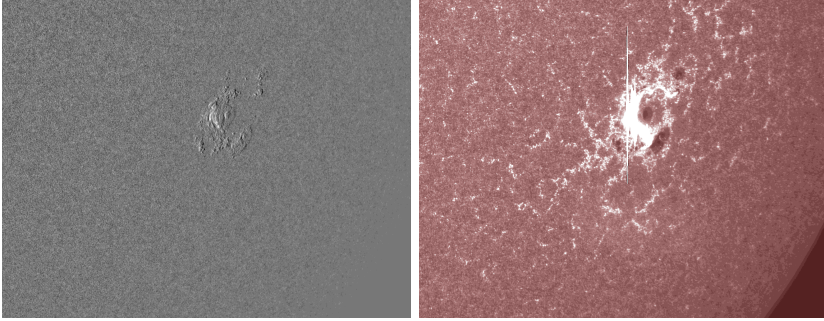


Figure 4.3: Left panel: difference between the SDO/HMI continuum images taken on 6 September 2017 at 11:59 and 11:50 UT. Right panel: SDO/AIA 1700 Å image (Lemen et al., 2012) at 11:59 UT.

response of the channel 2 of LYRA (see dashed line in Figure 4.1) and integrated over its bandpass, provides a result consistent with the channel 2 measurements at any time  $t$ :

$$E_2(t) = C_2 \int_{\lambda} A \frac{I_{\lambda}(t)}{d^2} S_2(\lambda) \lambda d\lambda, \quad (4.3)$$

where  $E_2$  is the irradiance measured by the channel 2 of LYRA,  $d$  is the Sun–Earth distance,  $C_2$  is the calibration coefficient of the channel 2, and  $S_2$  is the effective area of channel 2.  $A$  is the emitting area estimated using the method by Mravcová and Švanda (2017) to be  $240 \text{ Mm}^2$  at 11:58 UT (the peak time in LYRA channel 2) based on the SDO/HMI observations of the flare in the wing of the Fe I 6173 Å line (M. Švanda 2018, private communication- see Figure 4.3, left panel). Strictly speaking, this corresponds to the area of the emitting surface in the photosphere. However, as the emission in the Balmer continuum originates from the flare ribbons, we expect its area to be similar. The ribbon structure is particularly well visible in the right panel of Figure 4.3, which corresponds to region of the temperature minimum.

The value of the emission measure  $n_e^2 L$  producing a spectrum that matches the observations of channel 2 was found to be of  $9.1 \times 10^{34} \text{ cm}^{-5}$  at the time of the peak of the flare. Heinzl et al. (2017) derived the slab thickness around 200 km for a limb flare detected by SDO/HMI. Considering this value as a representative value for the Balmer-continuum formation region, this results in electron densities of the order of  $6.7 \times 10^{13} \text{ cm}^{-3}$ , consistent with the values found by Neidig et al. (1993) and Kerr and Fletcher (2014). Under these conditions, we can use the formulas from Heinzl and Shibata (2018) to estimate the optical thickness at 2000 Å. To do this, we have considered that the density in flaring

chromosphere is much higher compared to quiet chromosphere, so that the population of the hydrogen atoms in the level corresponding to the Balmer transition (level 2) is not far from local thermodynamic equilibrium. P. Heinzel (private communication) did this exercise and estimated the optical thickness at 2000 Å to be around 0.015, which confirms the hypothesis of an optically thin slab.

The obtained spectral radiance increase produced by the flare (without the quiet-Sun background) is shown with the red line in Figure 4.1. A composite mean quiet-Sun background spectrum is also shown as the blue line for comparison. This spectrum was obtained by merging the full-Sun integrated data sets taken on 2010 January 7 by three spectrometers: Thermosphere, Ionosphere, Mesosphere, Energetics and Dynamics/Solar EUV Experiment (TIMED/SEE; Woodraska et al., 2004) from 1000 to 1300 Å, Solar Radiation & Climate Experiment/Solar Stellar Irradiance Comparison Experiment (SORCE/SOLSTICE; Rottman et al., 1993) from 1300 to 3100 Å, and SORCE/Spectral Irradiance Monitor (SIM; Harder et al., 2005) from 3100 to 4000 Å, and converting it into spectral radiance per unit of emitting surface assuming the uniform emission of the quiet-Sun disk.

As was mentioned in Section 4.2, only 35% of the irradiance measured by the channel 1 of LYRA at low solar activity comes from the spectral range around Ly- $\alpha$ , while 65% originates from a plateau in the channel responsivity around 2000 Å. Once the Balmer continuum spectrum has been calculated based on the measurements of channel 2, its contribution can be subtracted from the channel 1 measurements:

$$E'_1(t) = E_1(t) - C_1 \int_{\lambda} A \frac{I_{\lambda}(t)}{d^2} S_1(\lambda) \lambda d\lambda. \quad (4.4)$$

The remaining emission that we call here "Lyman- $\alpha$  residual" consists mostly of the hydrogen Ly- $\alpha$  emission and a few strong lines, the most prominent of them being the Si III line at 1206 Å, the C II line at 1335 Å, the Si IV doublet around 1400 Å, the Si II line at 1533 Å, and the C IV doublet at 1548 Å (Avrett et al., 1986; Simões et al., 2018). According to Table 4.1, the Ly- $\alpha$  residual contributes around 70% to the total flare emission measured in channel 1 of LYRA.

If the entirety of the remaining signal were attributed to the emission in the Ly- $\alpha$  line, here modeled by a Gaussian centered at 1216 Å with a 1 Å FWHM (although the line, far from being Gaussian, has extended wings), then the line would be around 500 times more intense than the Balmer continuum, as shown by the peak on the red curve in Figure 4.1. It is important to note, however,

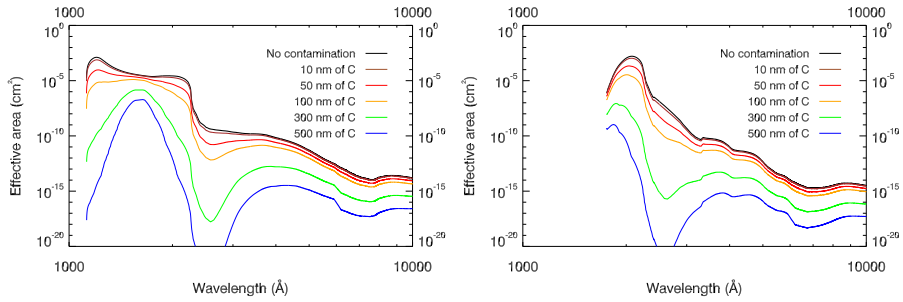


Figure 4.4: Effect of the absorption by a layer of carbon on the spectral sensitivity of LYRA channels 1 (left panel) and 2 (right panel). The colours black, brown, red, yellow, green, and blue correspond to thicknesses of C of 0 nm (no contamination), 10 nm, 50 nm, 100 nm, 300 nm, and 500 nm respectively. Note the units of the X-axis in Å.

that even if the Ly- $\alpha$  line were responsible for most of the remaining signal, the contribution of other neighboring lines should not be excluded. In comparison to the line contributions, the emission in the continua around Ly- $\alpha$  is expected to be small.

## 4.5 Impact of Degradation

We mentioned it in the previous chapters: since its launch, LYRA has experienced a strong degradation. It comes from the absorption of incident light by a layer of contaminant (10 nm of carbon, in the case of unit 1) that gets deposited on the front filter due to the non-ideal cleanliness of the PROBA2 environment. The applied correction for degradation is made by adding an offset to the measured value to compensate for the loss of signal. This additive correction does not account for the fact that the carbon absorption is not uniform over the passband (see Figure 3.1), and that such a contaminant layer might therefore change the spectral response of the instrument.

In the case of the reported observations, the least degraded unit has been used. But even in this unit, at the moment of the campaign, about 35% of the signal had been lost since the launch for channel 1, while channel 2 had experienced a 20% drop. To correctly interpret the observations, it was necessary to check that no severe modification of the spectral sensitivity of the channels had occurred.

To do this, we calculated how the spectral absorption by the carbon layer affects the measured irradiance  $E''$  for various thicknesses of the contaminant:

$$E''(t) = C \int_{\lambda} A \frac{I_{\lambda}(t)}{d^2} S(\lambda) \exp(-\sigma(\lambda)l) \lambda d\lambda, \quad (4.5)$$

where  $\sigma$  is the absorption cross-section of carbon and  $l$  is the thickness of the contaminant layer.

Figure 4.4 shows the resulting spectral sensitivities for channels 1 (left panel) and 2 (right panel) for the carbon layer thicknesses of 10 nm, 50 nm, 100 nm, 300 nm, and 500 nm. Integrating over the wavelength of each of these curves multiplied by the solar spectrum and comparing the result to the non-degraded value provides an estimation of the signal drop. The impact on the spectral response by thick layers of carbon is clearly visible in the Figure 4.4. However, for a 10 nm-thick layer of carbon (corresponding to the brown curves in the Figure), we can confirm that there is no significant modification of the spectral properties of the passband of the two channels.

## 4.6 Summary and Discussion

The X9.3 flare on 2017 September 6 was observed by PROBA2/LYRA in its four channels. This was the first LYRA observation of a solar flare in the MUV wavelengths around 2000 Å. We demonstrated that the emission detected at these wavelengths by LYRA is consistent with the hydrogen Balmer continuum emission produced by an optically thin chromospheric slab heated up to 10,000 K. The densities around  $6.7 \times 10^{13} \text{ cm}^{-3}$  required for the slab thickness of around 200 km are consistent with previous works (Neidig et al., 1993; Kerr and Fletcher, 2014; Heinzel et al., 2017). Simultaneous observations in channels 1 and 2 of LYRA allow the separation of the line emissions (primarily from the hydrogen Ly- $\alpha$  line at 1216 Å) from the Balmer continuum emission generated at longer wavelengths. Our calculations shed light on the contributions of different emission processes in solar flares.

Recently, the Balmer continuum emission from an X1 flare was observed by IRIS around 2826 Å, as reported by Heinzel and Kleint (2014). Our radiance at the flare peak computed at 2000 Å is  $5.7 \times 10^5 \text{ erg s}^{-1} \text{ sr}^{-1} \text{ cm}^{-2} \text{ Å}^{-1}$ . Converting this to IRIS NUV we get  $2.3 \times 10^6 \text{ erg s}^{-1} \text{ sr}^{-1} \text{ cm}^{-2} \text{ Å}^{-1}$ , which is about eight times more as compared to the value given by Heinzel and Kleint (2014) for a weaker X1 flare. The results for the two flares are consistent with each other. We can also convert our radiance to wavelength 6173 Å used by



SDO/HMI (*i.e.*, dominated by Paschen continuum), getting the value  $2.6 \times 10^5 \text{ erg s}^{-1} \text{ sr}^{-1} \text{ cm}^{-2} \text{ \AA}^{-1}$ . This latter value can be compared with visible-continuum flare detections, but one has to keep in mind that our value of the radiance is the mean value averaged over the flare area. Also a comparison with HMI enhancement may be problematic because during strong flares the HMI "continuum" signal seems to be strongly contaminated by the flare emission in the Fe I line (Švanda et al., 2018).

The contribution of other continua around 2000 Å (which are usually produced by the quiet photosphere, see Bonnet and Blamont, 1968) is probably small (Avrett et al., 1986). Our value of the peak radiance at 2000 Å is consistent with models of Avrett et al. (1986) and lies somewhere between the radiance produced by their F2 and F3 models. This may contribute to a better understanding of the physics of white-light flares, although we are detecting enhancements in MUV, not in the white (visible) light. However, the conversion to Paschen-continuum enhancement is a signature of the white-light flare.

Reports of flares in Ly- $\alpha$  in the literature (*e.g.*, Lemaire et al., 1984; Rubio da Costa et al., 2009; Kretzschmar et al., 2013; Milligan et al., 2017) are relatively rare and often debated. A recent paper by Milligan and Chamberlin (2016) questioned the origin of the Ly- $\alpha$  flare emission reported by broadband instruments (in particular SDO/Extreme Ultraviolet Variability Experiment, Woods et al., 2012, and LYRA), as these detections displayed a thermal-like temporal profile and peaked much later than the non-thermal emission, contrarily to the spectroscopic observation by Lemaire et al. (1984). They suggested that these observations might rather correspond to out-of-band emission. LYRA produced very few observations of flares in its Ly- $\alpha$  channel (channel 1; see Kretzschmar et al., 2013) due to its fast degradation (BenMoussa et al., 2013). The previous few LYRA observations were all acquired with its nominal or the main backup unit, and some showed a thermal behavior similar to that described by Milligan and Chamberlin (2016). The X9.3 flare on 2017 September 6 is the first flare observed by channel 1 of the calibration unit, which was better preserved from degradation.

The temporal correlation of the flare emission measured by LYRA channels 1 and 2 with the GOES derivative confirms that the emission in those channels comes from regions of non-thermal behavior. The Ly- $\alpha$  residual irradiance clearly follows a non-thermal profile (see Figure 4.2). It is therefore likely that the anomalous behavior (reported by Milligan and Chamberlin, 2016) of the previous detections by SDO/EVE and in channel 1 of the other two units of LYRA is of instrumental origin (in the case of LYRA, it is probably due to the fast degradation of the nominal unit and the broad spectral range of the main backup unit).

A limitation of the presented observations is that LYRA integrates the solar flux over the full solar disk and over wavelengths. This does not allow for a clear separation of different continua and spectral lines in the wavelength range of interest (1150–2500 Å). Spatially and spectrally resolved observations of flares over a wide wavelength range (including visible light) are necessary to constrain the physics of the broadband emission in flares (Veselovsky and Koutchmy, 2009).

## Chapter 5

# Quasi-Periodic Pulsations in Solar Flares

This chapter, dedicated to Quasi-Periodic Pulsations in solar flares, covers the work by M. Dominique that has been only partly published. Sections 5.2 to 5.4 and a big part of Section 5.7 are extracted from Dominique et al. (2018a), but Sections 5.5 and 5.6 cover the work that was not published so far.

As described in Section 1.5, QPPs are expected to be intimately related to the flaring process. They might provide indications on how the magnetic reconnection occurs. They might also provide the evidence of the presence of MHD waves during flares. Using the LYRA data, we tried to answer the following questions: Are QPPs regularly observed in solar flares? What are their characteristic periods? Do these periods correlate with those produced by waves propagating at the Alfvén speed? What is the mechanism at the origin of the QPPs and where are they produced?

### 5.1 Introduction

As was mentioned in Section 1.5, Quasi-Periodic Pulsations (QPPs) refer to nearly-periodic oscillations that are often observed in irradiance time series during solar and stellar flares. Two families of mechanisms are usually invoked to explain QPPs: MHD waves and quasi-periodic particle acceleration.

Both mechanisms can explain that QPPs affect various parts of the solar

Table 5.1: Periods associated to the fundamental mode of standing MHD waves.  $L$  is the loop length,  $C_{A0}$  and  $C_{Ae}$  are the internal and external Alfvén speeds,  $\rho_0$  and  $\rho_e$  the internal and external plasma densities and  $C_{S0}$  is the internal sound speed.

	Longitudinal	Kink	Sausage	Torsional
<b>Period</b>	$2L/C_T$	$2L/C_k$	$2L/C_p$	$2L/C_{A0}$
<b>with</b>	$C_T = \frac{C_{S0}C_{A0}}{\sqrt{C_{S0}^2 + C_{A0}^2}} \quad C_k \simeq \sqrt{\frac{2}{1+\rho_e/\rho_0}}C_{A0} \quad C_{A0} < C_p < C_{Ae}$			

spectrum. In both cases, one can also expect that the QPPs observed in various wavelengths behave similarly, but with slight time offsets between each other. These offsets should be compatible with the electron precipitation processes in the various layers of the solar atmosphere, as should be evidenced in comparison of different non-thermal wavelengths. Namely, QPPs observed in the wavelengths corresponding to faster electrons should be slightly ahead of the ones corresponding to slower electrons. The time offsets should also be compatible with heating/cooling processes observed in thermal wavelengths. The QPPs observed in wavelengths corresponding to hotter plasma should be ahead to of those observed in cooler plasma. Such offsets have been reported by Dolla et al. (2012) during the X2.2 flare of 15 February 2011. Some observational signatures might point more directly to a specific mechanism.

Examples of observational signatures of QPPs that can be investigated are as follows (see Nakariakov and Melnikov, 2009; McLaughlin et al., 2018, for reviews).

- **The period.**

The period might be specific to the trigger mechanism or reflect the eigenfrequencies of the loop system.

In case of MHD waves, the period of the QPPs is expected to be determined by the characteristics of the plasma (for example its mass density or pressure) and of the wave guiding structure (*i.e.* the loop main dimensions and magnetic field). The periods also depend on the type of the MHD wave that is involved in the process. The periods expected when QPPs are triggered by the fundamental mode of a standing MHD wave are summarized in Table 5.1. If the standing wave affects the loop system connecting the flaring site to the photosphere, the period will reflect the characteristics of the flaring environment. But the leaky part of an MHD

wave could also periodically trigger the reconnection in a nearby loop system, in which case the observed period would be unrelated to the flaring environment itself and would rather reflect the characteristics of the oscillating loop.

The oscillatory reconnection produced by the relaxation of an X-type neutral point after the perturbation by a fast magnetoacoustic wave produces QPPs with periods of the order of  $2 \ln S$ , where  $S = LC_{A0}/\eta$  is the Lundquist number and  $\eta$  is the magnetic diffusivity (McLaughlin et al., 2009).

Thermal over-stability, *i.e.* the competition of plasma heating with radiative and conductive losses can also lead to the spontaneous appearance of QPPs with periods that mainly depend on the length of the loop and the temperature.

In presence of the tearing mode instability in a current sheet, the alternance between Petschek and Sweet-Parker reconnection regimes results in bursts in the particle acceleration with a period  $P_R \propto n_0^{-1} T_0^2 B_0^{-1}$ , where  $n_0$ ,  $T_0$  and  $B_0$  are the plasma density, the temperature and the magnetic field outside the current sheet.

The magnetic tuning fork, a phenomenon that results from the periodic evolution of the shock created when the supersonic outflow produced by the reconnection piles up on the top of the reconnected loops and flows back, results in QPPs with periods  $P \propto w/v_{bf}$  where  $w$  is the size of the above-the-loop-top region and where the backflow speed  $v_{bf}$  is of the order of the Alfvén speed.

- **The period drift**

Because of their dispersive nature (*i.e.* the fact that their phase and group speed depend on the frequencies and wave numbers), impulsively created fast magnetoacoustic modes develop into quasi-periodic wave trains when guided along plasma structures such as loop, filament or even current sheets. Simulations using sausage modes have highlighted a spectral evolution of the "tadpole" type, with a progressive increase of the oscillation amplitude and a decrease of the period.

Since the period of standing MHD waves is proportional to the length of the loop, the period of QPPs produced by such waves is expected to increase with time, as the reconnection point moves upward.

- **The damping**

The oscillatory reconnection produces exponentially-decaying pulsations. QPPs produced by thermal over-stability can be damped, decayless or even increasing.

Depending on the mechanism that generates the oscillations, the analysis of QPPs might either reveal fundamental characteristics of the reconnection process or provide a way to probe the environment in which the reconnection occurs using coronal seismology.

In all cases, one needs confidence in the methods used to detect periodicities from time series. Although techniques such as Fourier and wavelet analysis are well mastered, obtaining lists of periodicities that are significant and are not artifacts of the detection method remains challenging. Applying these techniques blindly may lead to detection of false periodicities. Inglis et al. (2015) and Inglis et al. (2016) highlighted the need to account properly for the type of noise affecting the dataset to avoid overestimating the confidence level of some peaks detected in Fourier and wavelet spectra. Vaughan (2005) and Pugh et al. (2017) proposed refined methods to compute the significance of a peak in a periodogram in presence of the red noise (where the term "red noise" is to be understood in its extended meaning, referring to a spectrum with higher power at longer periods). Auchère et al. (2016) demonstrated the pitfalls of detrending the data before applying the wavelet transform, *i.e.* of removing the global trend of the time series in order to leave only short timescales variations, and recommended avoiding the detrending. Unfortunately, if the detection of QPPs is rather trivial in undetrended observations of the non-thermal emission (*e.g.* hard X-rays or radio), where the amplitude of QPPs is on the order of the global variations, this is not the case for thermal emission such as SXR or EUV, where QPPs consist of small variations (about a few percents) of the overall flaring curve. This often impairs the detection of QPPs from undetrended data as the corresponding peak in Fourier or wavelet spectra is not significant enough.

These limitations constitute an intrinsic difficulty in the analysis of QPPs, as HXR and radio instruments currently in use are subject to duty cycles and to limited fields of view, and therefore miss many events. In contrast, the last generation of EUV/SXR instruments such as LYRA and EVE benefits from quasi-continuous observations at high temporal resolution, which opens up the field to statistical surveys.

In this chapter, we examine the effect of detrending on wavelet spectra of solar flares and propose criteria for identifying the false positives caused by data processing. We then apply these criteria to the datasets provided by PROBA2/LYRA and SDO/EVE, to detect QPPs with periods between 1 and 100 s in flares stronger than M5.0 that occurred during Solar Cycle 24 (as of 31 December 2018). The periods found are searched for correlations with the main characteristics of the flare and magnetic environment. Finally, we compare the two strongest flares of Solar Cycle 24, which showed big differences in terms of QPPs despite being produced by the same active region.

## 5.2 Wavelet Detection: the Wavelet Transform - Ideal Case Studies

Before starting a statistical analysis of EUV datasets, it is important to recall some of the limitations of the wavelet transform. To illustrate them, we applied the wavelet detection to synthetic sinusoidal signals trying to mimic the characteristics of the time series to be used in our analysis. We started with a synthetic signal  $S_1$  consisting of a sum of two sinusoids (with periods  $p_1$  and  $p'_1$ ) sampled at a cadence  $\Delta t = 0.05$  s and with a difference in phase of  $\phi_1$  and ratio in amplitude of  $A_1$  between the two components. First, we tried to detect the periods directly in the wavelet power spectrum of the signal. Then, we used a cross-correlation with another synthetic sinusoidal signal  $S_2$  with a single component with the period  $p_2 = p_1$ . Series  $S_1$  and  $S_2$  are noiseless, and we introduce series  $S_3$  and  $S_4$  that are affected by red noise  $N$ :

$$S_1[i] = A_1 \sin(2\pi i \Delta t / p_1) + \sin(2\pi i \Delta t / p'_1 + \phi_1), \quad (5.1)$$

$$S_2[i] = A_2 \sin(2\pi i \Delta t / p_2 + \phi_2), \quad (5.2)$$

$$S_3[i] = S_1[i] + N_3[i], \quad (5.3)$$

$$S_4[i] = S_2[i] + N_4[i]. \quad (5.4)$$

The noise was modeled by a lag-1 auto-regressive process, following Gilman et al. (1963) and the implementation in the Torrence and Compo library<sup>1</sup> (Torrence and Compo, 1998) that was used for this analysis:

$$N_j[i] = \alpha N_j[i - 1] + A_N Z_j[i], \quad (5.5)$$

where

- $N_j[0] = 0$ ,
- $\alpha$  is the lag-1 autocorrelation. In the simulations, it was set to 0.995, which is close to the values usually observed in LYRA and ESP time series,

---

<sup>1</sup><http://paos.colorado.edu/research/wavelets>

- $Z_j[i]$  is a random variable following a normal distribution with the mean 0 and the standard deviation 1. Multiplied by  $A_N$ , it represents the white noise with a tuneable amplitude.

We only used the Morlet wavelet; its profile shows similarities both to the sinusoids used for the analysis of synthetic cases and to the QPPs in real signals.

### 5.2.1 Period Detection by Wavelet Transform

In the absence of noise, the wavelet analysis succeeds in identifying the periods in the signal, as illustrated in Figure 5.1 for the series  $S_1$  with  $p_1 = 5$  s and  $p'_1 = 50$  s. We note that the absolute amplitude of the peak corresponding to the shorter period (5 s) is an order of magnitude lower than that of the longer period (50 s), in contrast to the amplitudes of the two sinusoids, which are equal ( $A_1 = 1$ ). This is a well-known side effect of the wavelet method that uses different width of wavelet filters to analyze different scales. To avoid this visual bias, when dealing with real observations in Section 5.3, we display the wavelet power spectrum divided by the significance, which takes this effect into account.

Furthermore, the peaks in the power spectra are affected by a significant uncertainty (they have a significant width) that depends on the considered period. This uncertainty may affect the detection of multiple periodicities situated too closely to each other. This is illustrated in Figure 5.2, where periods of  $p_1 = 15$  s and  $p'_1 = 20$  s in  $S_1$  are resolved in the averaged power spectrum, but not periods of 16 and 20 s. We empirically determined that the peaks corresponding to two periods differing by less than 25% of the longer of them would not be resolved. The value of 25% may be specific to the length of the time series that we analyzed and should be reassessed when investigating time series of different lengths or damped datasets. Note that these examples were provided for  $\phi_1 = 0$  and  $A_1 = 1$ . Modifying the relative importance of the sinusoid amplitudes complicates the detection of the two distinct peaks even further. On the other hand, changing the respective phases did not seem to affect the detection. Therefore, this 25% resolution holds when the Morlet wavelet is used to analyze a signal composed of (at least) two periodic components of similar amplitudes that can be considered as undamped over the size of the mother wavelet. We repeated this analysis for other pairs of periods (1 s and 1.33 s, 75 s and 100 s, 100 s and 133 s), and it confirmed the 25% resolution.

Finally, several peaks corresponding to periods above 50 s are detected in the averaged spectra of Figures 5.1 and 5.2. These peaks are many orders of



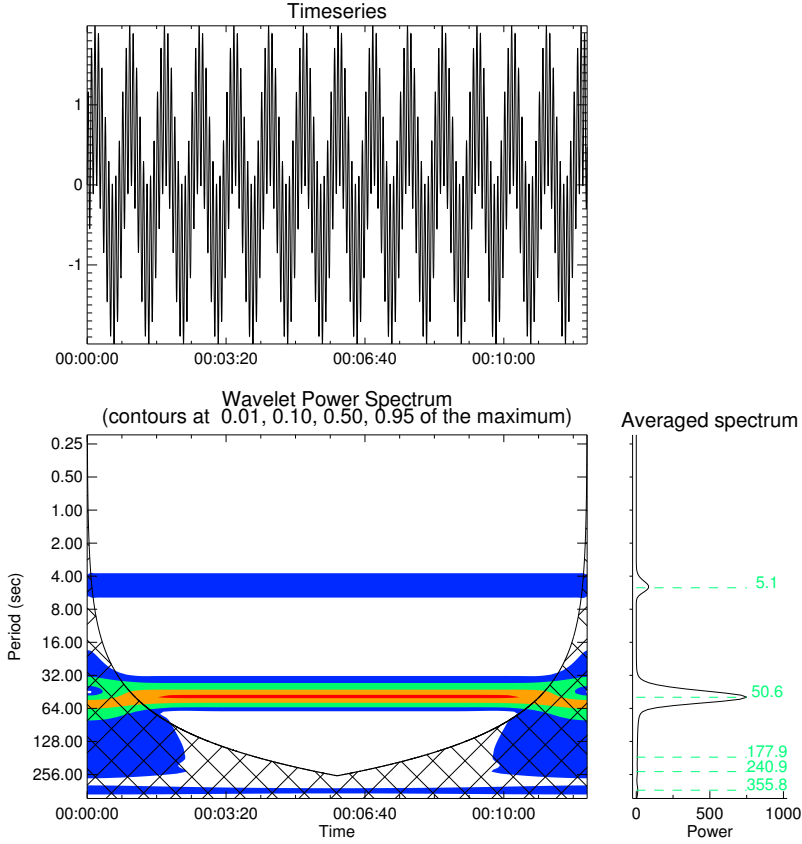


Figure 5.1: Time series  $S_1$  (*top panel*), its wavelet power spectrum (*bottom left panel*), and the power spectrum averaged over time (*bottom right panel*) for the case with  $p_1 = 5$  s,  $p'_1 = 50$  s,  $\phi_1 = 0$ ,  $A_1 = 1$ . The *hashed area* in the bottom left plot represents the cone of influence, where the border effects affect the detected periodicities, which are therefore not reliable. *Green lines* in the bottom right panel mark the local peaks in the average wavelet power spectra, and the *green numbers* show corresponding periods in seconds.

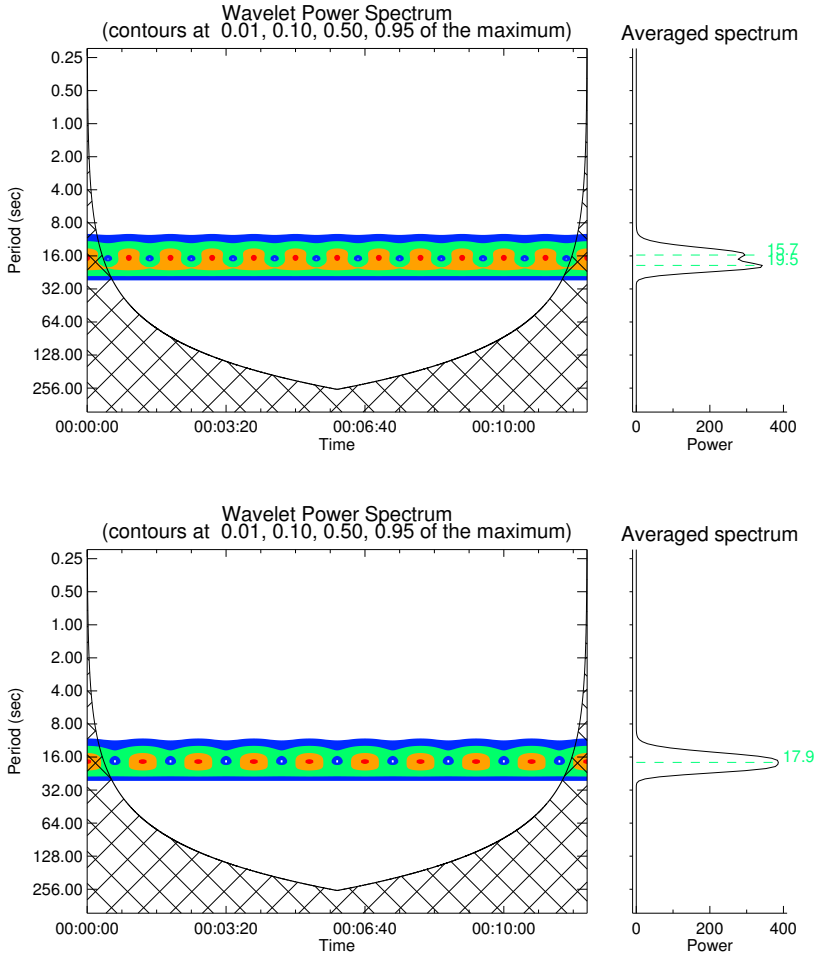


Figure 5.2: Periods detected in series  $S_1$  for  $p_1 = 15$  s and  $p'_1 = 20$  s (*top panel*) and for  $p_1 = 16$  s and  $p'_1 = 20$  s (*bottom panel*). The other parameters are  $\phi_1 = 0$ ,  $A_1 = 1$ . Because of the intrinsic uncertainty that affects the detection of periods, the wavelets fail to separate periods that are too closely to each other.

magnitude below the two main peaks. They are clearly not significant and are most likely caused by the discretization process.

We now examine how the noise affects the detection of periods. Figures 5.3 and 5.4 illustrate the results of detection of periodicities for series  $S_3$  with two

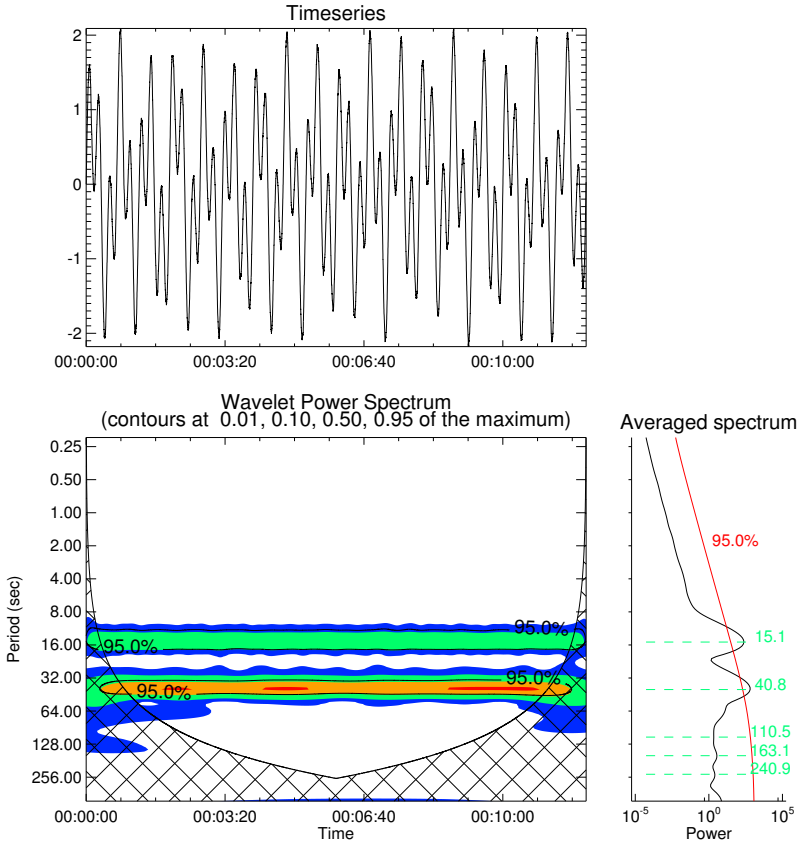


Figure 5.3: Time-series  $S_3$  (top panel), its wavelet power spectrum (bottom left panel), and the power spectrum averaged over time (bottom right panel) for the case with  $p_1 = 15$  s,  $p'_1 = 40$  s,  $\phi_1 = 0$ ,  $A_1 = 1$ ,  $\alpha = 0.995$ , and  $A_N = 0.01$ . The 95% confidence level is shown in the two bottom panels.

different amplitudes of  $A_N$ . The difference of the amplitudes of two peaks in the power spectrum that was already noticed in Figure 5.1 is enhanced as it cumulates with the effect of the red noise, which is also of higher level for longer periods.

Figures 5.3 and 5.4 also illustrate how strongly the presence of red noise complicates the detection. When the red noise level increases, the amplitude of the two peaks corresponding to the true periods in the signal becomes relatively

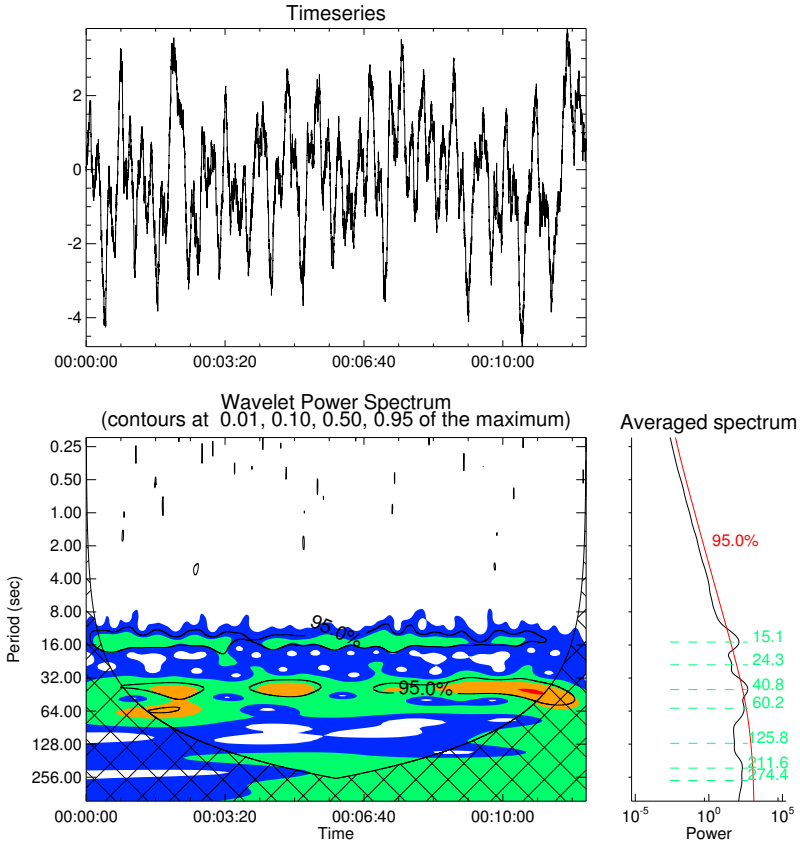


Figure 5.4: Same as Figure 5.3, but with  $A_N = 0.1$ .

less important when compared to the overall noise level, which makes the peak detection less clear. Furthermore, secondary artificial peaks appear in addition to the two true peaks, especially in the longer-period range, where the artificial peaks approach the 95% confidence level (see Figure 5.4).

Next, we investigate what happens when the data are detrended, *i.e.* when we subtract a boxcar average of the signal when varying the width of the boxcar  $l$  (*i.e.* the width of the detrending window) by steps of 5 s. As illustrated by Auchère et al. (2016), this operation is likely to create spurious detections of periods of the order of  $l$ . This is confirmed in Figure 5.5, where the left panels illustrate the periods detected in  $S_2$ , with varying width of the detrending window. The plots were obtained for  $p_2 = 15$  s without the addition of red noise (top) and for  $p_2 = 80$  s with the addition of red noise (bottom). Note that the periods represented in the left panels of Figure 5.5 correspond to all the maxima of the averaged power spectrum, not only to those reaching the 95% level of confidence. This illustrates the importance of adequately choosing the level of confidence when analyzing real cases. The middle and right panels correspond to the wavelet power spectrum and the averaged spectrum for a specific width of detrending window (305 s). The peaks detected in the average spectra therefore correspond to the horizontal red lines in the left panels for the considered width of the detrending window. Spurious detections of periods appear not only around the boxcar width, *i.e.* the size of the detrending window (represented by the black lines in the left panels), but also at several of its harmonics (blue lines). However, in the noiseless series, those spurious detections correspond to peaks of a smaller amplitude.

The bottom-left panel of Figure 5.5 shows several spurious detections of periods higher than  $l$  (to the left to the black line). Sometimes, these artificial periods are also detected below but close to  $l$ . In these ranges, most of the detections fluctuate highly, independently of whether they correspond to real periods of the signal or to artifacts. Therefore, a detrending window of width  $l$  should not be used to detect periods greater than  $l$ . In the range below  $l$ , we considered as valid any period that remained more or less constant independently of the width of the detrending window.

The bottom panels of Figure 5.5 also reveal an artificial period around 25 s that almost reaches the 95% confidence level. This detected period was found to fluctuate when the sampling rate or the size of the dataset were changed.

It is important to note that the detrending process affects the overall shape of the averaged power spectrum, which no longer follows a red noise profile. To compute the 95% confidence level, we produced 20 synthetic red noise series by randomly changing the white noise in Equation 5.5 and computed their wavelet power spectrum. Then, we averaged all the obtained power spectra and used

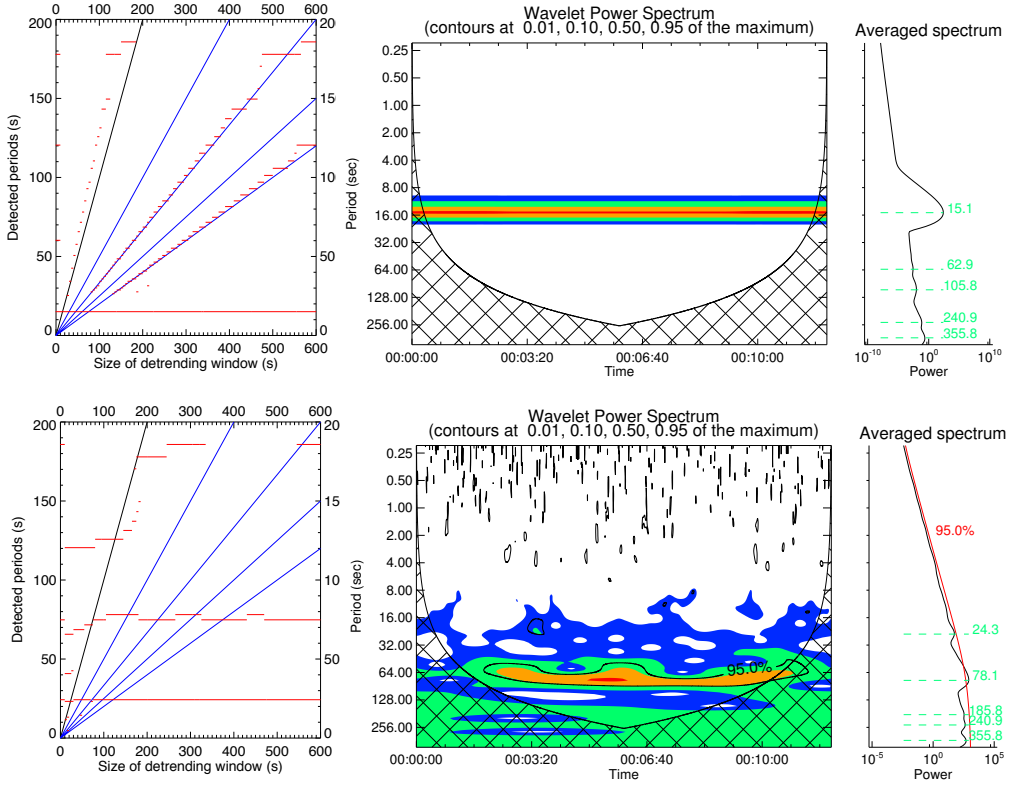


Figure 5.5: *Left panels:* Periods corresponding to peaks in wavelet power spectrum of a synthetic sinusoidal signal depending on the size of the detrending window (all peaks are shown here, not only the ones reaching the 95% level of confidence). The signal is noiseless (*top panels*, corresponding to  $S_2$  with  $p_2 = 15$  s) or affected by a red noise with a 10% standard deviation (*bottom panels*, corresponding to  $S_4$  with  $p_2 = 80$  s). The parameters of the series are  $\alpha = 0.995$ , and  $A_N = 0.1$ . The *black line* represents the periods corresponding to the size of the detrending window  $l$ , while its successive harmonics  $l/2$ ,  $l/4$ ,  $l/8$ , and  $l/16$  are represented by the *blue lines*. *Middle panels:* Examples of wavelet power spectra for the noiseless series  $S_2$  and noisy series  $S_4$  respectively, obtained for the detrending window of 305 s. *Right panels:* the averaged spectra.

the result as the expected background in the routine of Torrence and Compo (1998).

### 5.2.2 Wavelet Coherence

To highlight the periods of QPPs without relying on detrending, one could also opt for a wavelet coherence analysis of two different time series. This method is described in (Torrence and Webster, 1999) and basically consists of identifying the period ranges that show a high normalized covariance between the wavelet power spectra of two time series  $S_3$  and  $S_4$ . This method has been successfully used with EUV or SXR time series without any preliminary detrending by Dolla et al. (2012) in their analysis of the X2.2 flare that occurred on 15 February 2011. To illustrate the concept, we apply it to the two sinusoidal time series used in Section 5.2.1.

Figures 5.6 and 5.7 show that the common period of 15 s is well detected when the noise is limited. However, the value of the detected period is affected by a significant uncertainty. Although the amplitude of the detected peaks becomes slightly less prominent when the level of noise increases, the detected period itself becomes better constrained.

However, one can note the multiple peaks in the cross-coherence map. Such peaks would easily mask a real periodicity in a non-ideal or more noisy time series. This illustrates the greatest problem with this method well: as the wavelet coherence represents the normalized covariance of the two time series, it provides good results when comparing datasets that show very different spectral characteristics except for one (or several) common periodicities. However, when it is applied to datasets that are too similar, the method tends to highlight too many periods. Datasets such as the LYRA Zirconium channel and the EVE ESP Q channel correspond to the emission generated at similar plasma temperatures and therefore show too much similarity to give valuable results when the wavelet coherence method is used. Other channels of ESP that correspond to different emission temperatures, as was done by Dolla et al. (2012), would give better results. However, since these channels are affected by much stronger noise, only strong flares can be analyzed in this way. We therefore decided not to use the wavelet coherence method in this study.

### 5.2.3 Detection Criteria

The analysis of ideal cases described in Sections 5.2.1 and 5.2.2 led us to choose a set of criteria that we used in this study to determine whether a detection is real or an artifact of the detrending process or of the noise. We note that these are not sufficient but necessary conditions. Some of the detected periods might still not be real, as was illustrated in Figure 5.5. However, we believe that these criteria are sufficient to eliminate most of the false detections. At

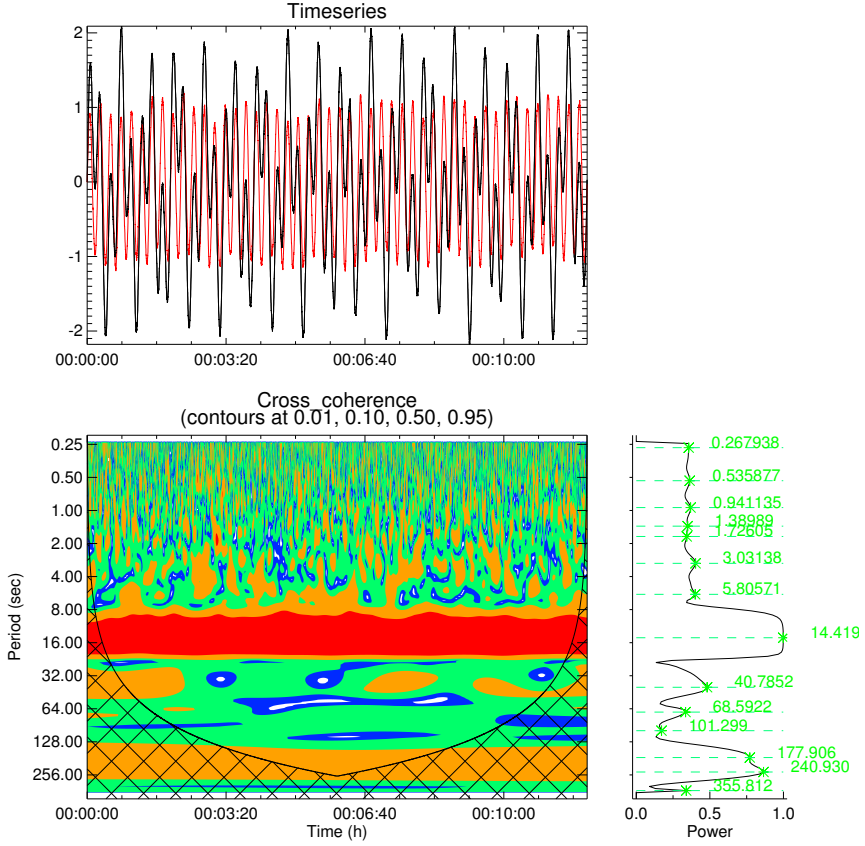


Figure 5.6: Periods detected by cross-coherence between series  $S_3$  and  $S_4$ , where  $p_1 = 15$  s,  $p'_1 = 40$  s,  $p_2 = 15$  s,  $\phi_1 = \phi_2 = 0$ ,  $A_1 = A_2 = 1$ ,  $\alpha = 0.995$ , and  $A_{noise} = 0.01$ .



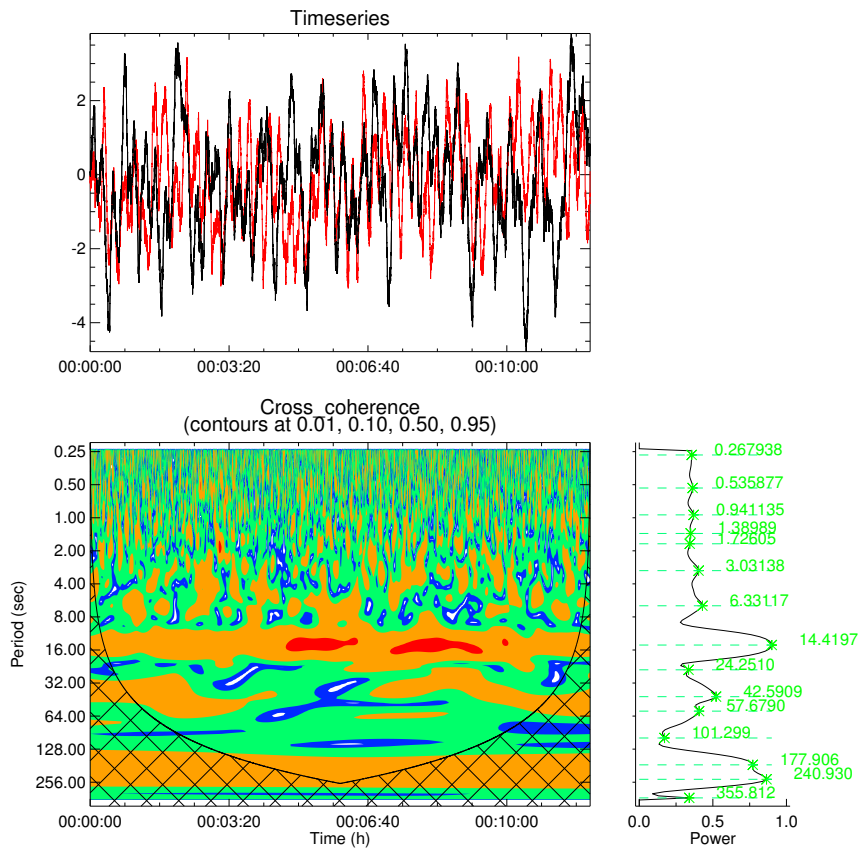


Figure 5.7: Same as in Figure 5.6, but for  $A_{noise} = 0.1$ .

the same time, our criteria are probably too restrictive and therefore some real periods may be missed.

- (1) A detection corresponds to a maximum in the wavelet power spectrum.
- (2) Periods inside the cone of influence are excluded.
- (3) Only periods below  $l$  are considered, where  $l$  is the width of the detrending window. In this range, we selected only the periods that did not change much with the varying  $l$ . This allows to filter out the artificial period at the size of the detrending window reported by Auchère et al. (2016)
- (4) We have limited our analysis to samples of the same duration (12 minutes), acquired during the impulsive phase of the flare (whenever possible covering the period in which the derivative of the GOES time series is the highest), when there was no maneuver of the PROBA2 spacecraft. This condition must be kept in mind when investigating flares with long impulsive phases, as only a small part of the impulsive phase is then analyzed.
- (5) Owing to the limitation on the flare duration (see (4)) and the fact that we detect periods that are stable over a wide range of  $l$  (see (3)), we set the upper limit on the detected periods to 100 s. We did not consider periods below 1 s either to comply with the Shannon theorem (ESP and LYRA sampling rates are 0.25 s and 0.05 s, respectively)
- (6) The significant periods reach the 95% level of confidence in the wavelet power spectrum (not in the time-averaged power spectrum) for a duration at least twice as long as the value of the period, considering that the data are affected by red noise.
- (7) Only periods appearing in the data taken by both LYRA and ESP and being significant (see (6) and (2)) in at least one of the data sets were kept in the analysis. Periods differing by less than 25% in the two time series were assumed to be common to both datasets. The use of two datasets also reduces the influence of the noise, which should be different in the two instruments.

We would like to emphasize here the importance of properly estimating the 95% confidence level. In the synthetic cases, the data were affected by red noise, as described by Equation 5.5. However, the noise affecting real observations might differ slightly from pure red noise. This is even more the case when the data are detrended. To produce the confidence levels for the analysis of real cases, we still relied on Equation 5.5 as in Section 5.2.1. The red noise parameter  $\alpha$  was estimated from the actual observations as in (Torrence and Compo, 1998)

by  $(\alpha_1 + \sqrt{\alpha_2})/2$ , where  $\alpha_1$  and  $\alpha_2$  are the lag-1 and lag-2 autocorrelations of the dataset (before any detrending). This method was tested on several synthetic time series, with either one or two sinusoidal components (Equations 5.3 and 5.4) when varying the periods of the sinusoids and the level of noise. The method was found to retrieve  $\alpha$  correctly, with an error below 0.5 %. The value of  $\alpha$  was also tested on all the PROBA2/LYRA and SDO/EVE/ESP time series corresponding to flares of class M5 and above (in GOES scale) that have been observed by both instruments during Solar Cycle 24. In all cases, it was found to be very close to 1 (more precisely, it belongs to the range 0.9922 to 0.9998 for ESP and to the range 0.9834 to 0.9999 for LYRA). The white noise standard deviation  $A_N$  was chosen in such a way that the resulting red noise fits the time-averaged wavelet power spectrum of the observations.

For each analyzed case, we produced 20 such red noise time series<sup>2</sup> by varying the white noise (*i.e.* by changing  $Z_j$  in Equation 5.5). These 20 time series were detrended and their averaged wavelet power spectra were computed. The mean of the resulting spectra provided the expected noise background to be used as a basis for determining the confidence level.

### 5.3 Examples of Real Case Studies: Solar Flares

We now illustrate the application of the criteria listed in Section 5.2.3 to two real events: the X2.2 flare of 15 February, 2011 (SOL20110215) and the X1.1 flare of 6 July 2012 (SOL20120706). The detections of periods are relatively easy for the first flare, and the situation is more complex for the second flare.

The QPPs of the first flare have been analyzed frequently in the literature. Dolla et al. (2012) reported QPPs with periods in the range 8–32 s in HXR, SXR/EUV and radio data sets, and analyzed the phase difference between pulsations in these energy ranges. Tan and Tan (2012) observed QPPs in the microwave range and reported superfine structures corresponding to millisecond bursts beside the main  $\sim 20$  s period. Simões et al. (2015) confirmed the presence of QPPs with periods of 13–30 s in their statistical study. Inglis et al. (2015) revisited this flare, as well as three other flares, applying Fourier transform to *Fermi/Gamma-ray Burst Monitor* and LYRA data. Inglis et al. (2016) extended this analysis to 261 flares that were observed by *FERMI/Gamma-ray Burst Monitor* or GOES. Inglis et al. (2015, 2016) both compared the relevance of different models to explain the Fourier power spectrum of the analyzed flares. The models that

---

<sup>2</sup>The limitation to 20 spectra was dictated by the computational load. However, for a few cases including the two illustrated in Sections 5.3.1 and 5.3.2, we tested whether using more spectra (*e.g.* 1000) affected the confidence level. The effect was found to be negligible.

were tested were a power law representing pure red noise, a broken power law, and a power law with a peak corresponding to a quasi-periodic source added. They checked whether the likelihood for the model with QPPs to explain the observed power spectrum is higher than that for the other models (as well as whether it is a suitable model at all), in which case one may conclude that the flare exhibits QPPs. The conclusion of Inglis et al. (2015) regarding the SOL20110215 event was that, taking into account the red noise that affects the data, no peak in the spectrum was unequivocally associated with the QPPs, and that pure red noise would be more likely. In contrast, when using the GOES data, Inglis et al. (2016) confirmed the presence of 20.8 s period for this flare.

The second flare (6 July 2012) is chosen as a typical case for which the method followed by Inglis et al. (2016) shows its limitations, as we discuss in Section 5.3.2. For this flare, Inglis et al. (2016) reported 14.2 s period from the GOES data, but considered that the likelihood for the model with QPPs was not significantly higher than that for the pure red noise model. This flare was also listed by Simões et al. (2015) as exhibiting periods in the 10–30 s range.

### 5.3.1 X2.2 Flare SOL20110215

For this flare, an example of period detection in the LYRA Zr data is shown in Figure 5.8. The periods detected in the LYRA Zr and EVE ESP Q channel data with different widths of the detrending window are displayed in Figure 5.9.

The periods found in the LYRA data and those found in the ESP data generally match exceedingly well. We also see that the periods reaching the 95% confidence level that are found with both instruments are relatively stable independently of the width of the detrending window. Neglecting all periods above 100 s and those that differ by more than 25% between LYRA and ESP, we conclude that periods of  $\sim 16$  s,  $\sim 27$  s, and  $\sim 60$  s are significant. The first two periods match the detections previously reported in the literature. A period of  $\sim 100$  s was also detected above the 95% level of confidence in part of the wavelet spectrum, but only for sizes of the detrending window below 100 s. Although this period is very stable, we therefore did not retain it. We note also that periods of 16 s, 27 s, and 60 s are close to multiples of each other, which may mean that some of these periods are harmonically related to each other.

### 5.3.2 X1.1 Flare SOL20120706

For the second flare, the detected periods are shown in Figures 5.10 and 5.11. The periods below 100 s found in the ESP and LYRA time series are similar,

but they do not match as well as in the flare on 15 February 2011. Differences on the order of a few seconds can be found, as illustrated in Figure 5.11. These differences are below the 25% uncertainty mentioned in Section 5.2.3, criterion (7), however, so the detections are considered as corresponding to the same period. Two of the detected periods satisfy our full set of criteria listed in Section 5.2.3: around 15 s and around 20 s.

Another peculiarity of this flare is that these two periods do not appear exactly in the same time interval. The  $\sim 15$  s period is prominent from 23:05 UT to 23:08 UT, while the  $\sim 20$  s period appears only before 23:06:30, see Figure 5.10, middle and bottom panels. The two periods therefore coexist during at least 1.5 minutes. However, Inglis et al. (2016) only reported the 14 s period in their analysis. This seems to be a limitation of the models they considered: their QPP model only accounts for a single (although broad) peak in the wavelet power spectrum corresponding to a single distinct period. If more than one distinct period is present, their model will likely be a poor representation of the observations. Therefore, although the cases detected by Inglis et al. (2016) are strong, their study probably underestimates the number of QPP periods present in flares.

## 5.4 Statistical Survey

The set of criteria described in Section 5.2.3 was applied to all flares of class M5 and above that were detected by both LYRA and ESP during Solar Cycle 24. This analysis covers 90 flares that occurred between the beginning of the cycle and 31 December 2018. The detected periods as well as the flare characteristics are summarized in Table 5.2.

Most of the flares exhibit one or several periodicities between 1 and 100 s during the impulsive phase, with a clear predominance of periods below 30 s. The distribution of the detected periods is shown in Figure 5.12, right panel. We also checked the correlation between the periods determined from the LYRA and the ESP datasets. The left panel of Figure 5.12 shows that the correlation is good, with no clear bias in one of the two instruments for short periods. For periods of the order of 60 s or more, LYRA tends to detect longer periods than ESP.

Only 9 of the 90 analyzed flares did not show any periodicity that satisfied our set of criteria. It is worth noting that two of these flares originated from the limb region (longitude above  $80^\circ$ ). In our experience, limb flares are usually more difficult to analyze: they frequently appear noisier, which could mask the presence of QPPs. Still, QPPs were observed during flares occurring at all

longitudes, with no apparent effect of the longitude on the detected periods (see Figure 5.13). This strengthens the idea that QPPs are intrinsically related to the flaring process, as was already suspected from previous surveys (Kupriyanova et al., 2010; Simões et al., 2015; Inglis et al., 2016).

We also failed to find a correlation between the detected periods and the strength of the flare (see Figure 5.14), which confirms the result of Inglis et al. (2016).

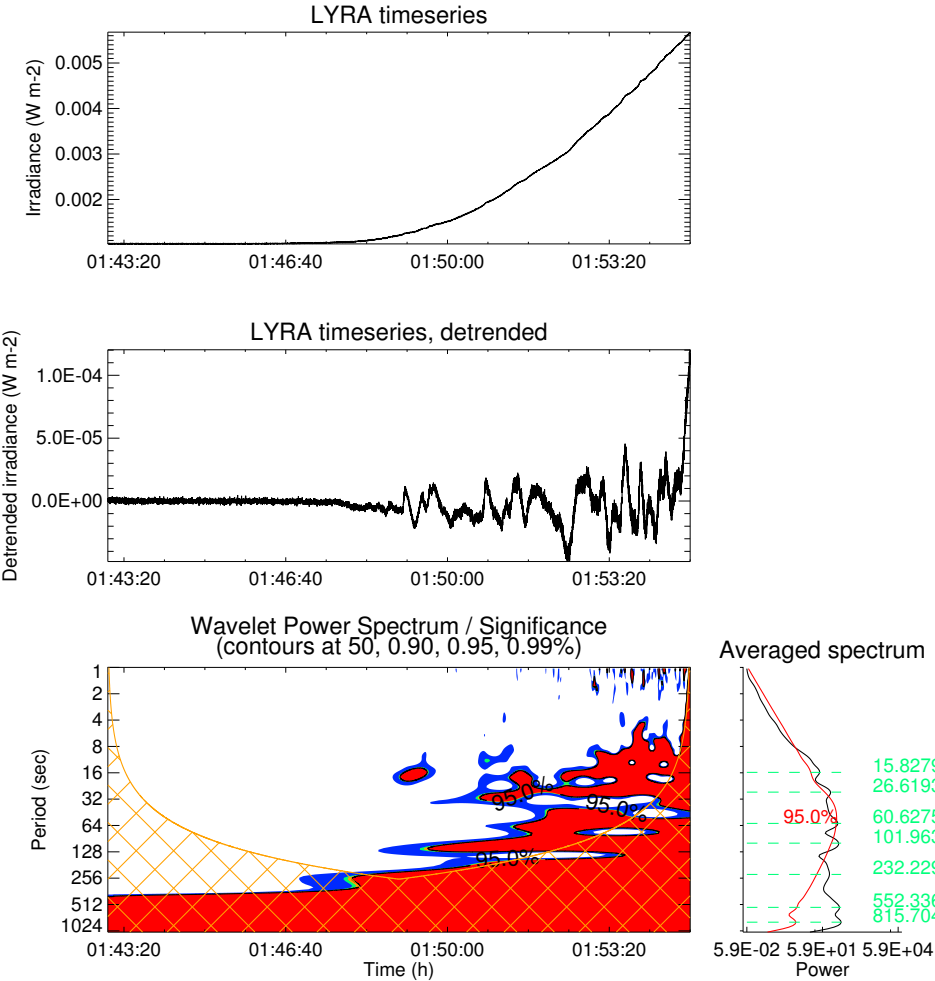


Figure 5.8: Solar flux measured in the zirconium channel of LYRA (*top panel*), detrended flux (*middle panel*) and wavelet power spectrum of the detrended flux (*bottom panel*) during the rising phase of the X2.2 flare on 15 February 2011, for the width of the detrending window of 50 s.

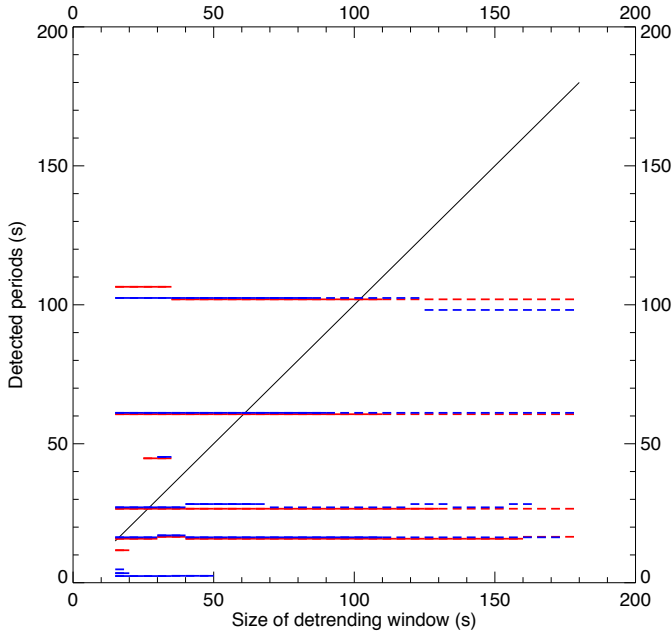


Figure 5.9: Effect of the detrending window size  $l$  on the periods detected for the X2.2 flare on 15 February 2011. The periods shown with *red lines* correspond to the periods found in the LYRA Zr data that reach (*solid lines*) and do not reach (*dashed lines*) the 95% level of confidence in the power spectrum during a time interval that is at least twice longer than the period. Similarly, the periods shown with *blue lines* were found in the ESP-Q data. Only the periods to the *right of the black diagonal line* (corresponding to the detected period equal to  $l$ ) are reliably detected. The periods found in ESP-Q have been shifted up by 0.5 s for clarity.



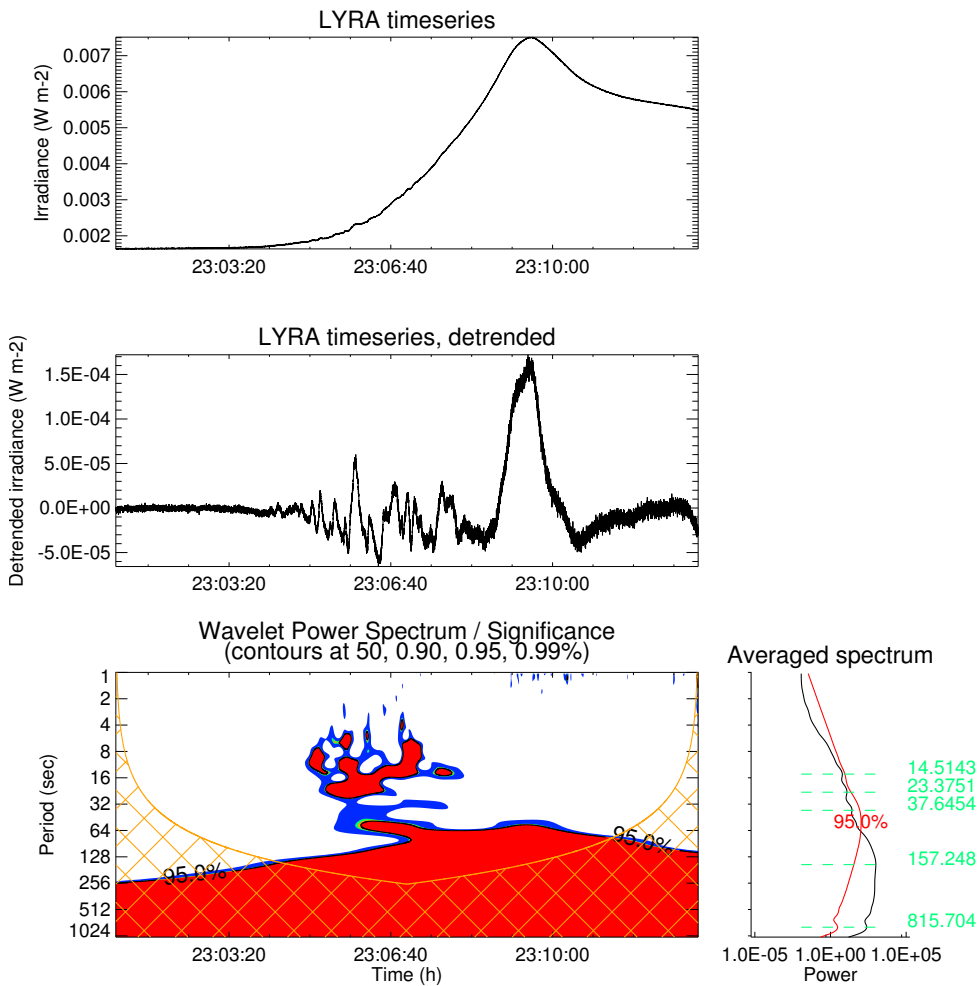


Figure 5.10: Solar flux measured in the zirconium channel of LYRA (*top panel*), detrended flux (*middle panel*) and wavelet power spectrum of the detrended flux (*bottom panel*) during the rising phase of the X1.1 flare on 06 July 2012, for the width of the detrending window of 50 s

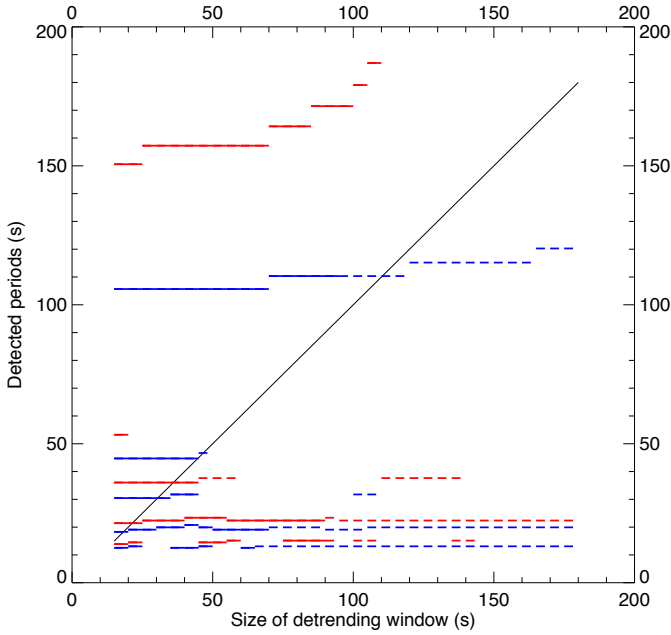


Figure 5.11: Effect of the detrending window on the periods detected for the X1.1 flare on 6 July 2012. The periods shown with *red lines* correspond to the periods found in the LYRA Zr data that reach (*solid lines*) and do not reach (*dashed lines*) the 95% level of confidence in the power spectrum during a time interval at least twice longer than the period. Similarly, the periods shown with *blue lines* were found in the ESP-Q data. Only the periods to the *right of the black diagonal line* (corresponding to the detected period equal to  $l$ ) are considered reliably detected. The periods found in ESP-Q have been shifted up by 0.5 s for clarity.

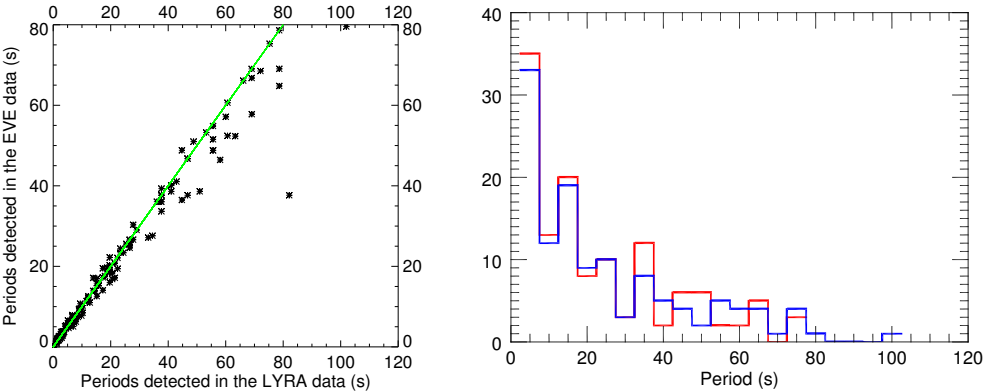


Figure 5.12: *Left panel:* Correlation of the periods detected in the ESP-Q and LYRA Zr data for all flares of Solar Cycle 24 with the GOES class above M5. *Right panel:* Histogram of all periods detected in these flares that were observed by LYRA (*blue*) and ESP-Q (*red*).

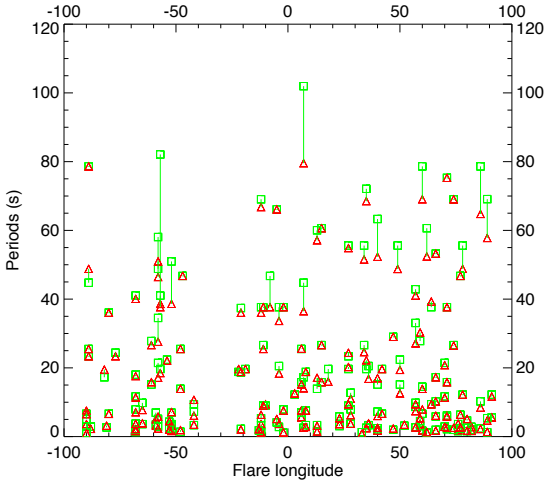


Figure 5.13: Periods detected in the ESP-Q (*blue*) and LYRA Zr (*green*) data for all flares of Cycle 24 with the GOES class above M5 as a function of the flare longitude. *Green vertical bars* connect periods in the LYRA and ESP-Q data that differ by less than 25%. According to the criterion (7), these bars are considered to represent the probable interval of the true period(s) in the flare data.

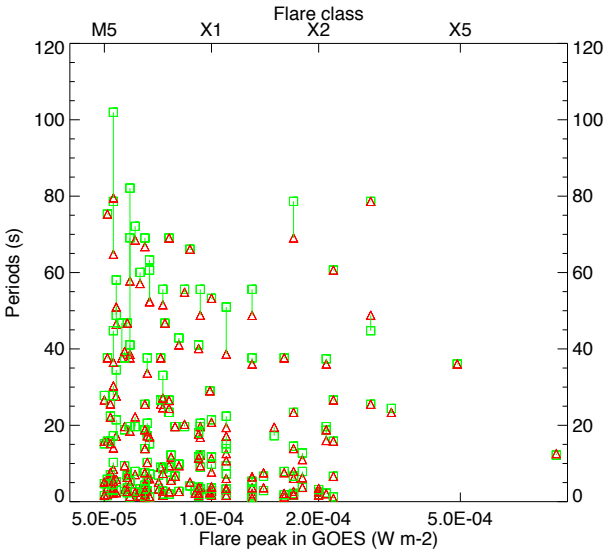


Figure 5.14: Periods detected in the ESP-Q (*blue*) and LYRA Zr (*green*) data as a function of the flare peak irradiance detected by GOES in the 1–8 Å channel. *Green vertical bars* connect periods in the LYRA and ESP-Q data that differ by less than 25%. According to the criterion (7), these bars are considered to represent the probable interval of the true period(s) in the flare data.

Table 5.2: Periods detected in the flares of GOES class M5 and higher during Solar Cycle 24 observed by both PROBA2/LYRA in the zirconium channel and SDO/EVE/ESP-Q. Asterisks indicate that the flares occurred close to the limb (*i.e.* at a longitude above 80° east or west).

Peak time of the flare (yyyy-mm-dd UT)	Flare class	Analyzed Start time	Analyzed End time	LYRA periods, s				ESP periods, s			
2010-11-06 15:36:00	M5.4	15:24:00	15:36:00	21.4	34.5	58.0		17.1	27.6	46.4	
2011-02-13 17:38:00	M6.6	17:28:00	17:40:00	2.8	20.5	37.7		3.7	18.4	33.7	
2011-02-15 01:56:00	X2.2	01:43:00	01:55:00	15.8	26.6	60.6		15.8	26.6	60.6	
2011-02-18 10:11:00	M6.6	10:10:30	10:22:30	5.8	10.3	17.3		6.1	10.3	17.3	
2011-03-08 10:44:00*	M5.3	10:37:00	10:49:00	2.4	10.3	78.6		2.2	8.5	64.8	
2011-03-09 23:23:00	X1.5	23:11:00	23:23:00								
2011-07-30 02:09:00	M9.3	01:59:00	02:11:00	19.7				19.7			
2011-08-04 03:57:00	M9.3	03:54:00	04:06:00	3.3	20.5			3.9	16.9		
2011-08-09 08:05:00	X6.9	07:55:00	08:07:00								
2011-09-06 01:50:00	M5.3	01:40:00	01:57:00	2.6	17.3	44.8	102.0	2.6	14.1	36.5	79.6
2011-09-06 22:20:00	X2.1	22:17:00	22:29:00	19.7				16.0			
2011-09-07 22:38:00	X1.8	22:24:30	22:36:30	3.8	7.9	12.8		6.3	11.0		
2011-09-08 15:46:00	M6.7	15:37:00	15:49:00	7.3	15.2	63.3		6.0	17.0	52.3	
2011-09-22 11:01:00*	X1.4	10:48:00	11:00:00	2.9	6.7			3.7	7.6		
2011-09-24 09:40:00	X1.9	09:33:00	09:45:00	5.8	13.9	31.7		5.8	13.7	31.2	
2011-09-24 13:20:00	M7.1	12:49:00	13:01:00	3.5	7.0			3.3	5.0		
2011-09-24 20:36:00	M5.8	20:22:30	20:34:30	3.7	7.0			3.6	7.2		
2011-09-25 04:50:00	M7.4	04:38:00	04:50:00	46.8				46.8			
2012-01-27 18:37:00	X1.7	18:15:00	18:27:00	2.2	6.1			2.7	6.1		
2012-03-05 04:09:00	X1.1	03:43:00	04:55:00	1.7	3.2	51.0		1.6	3.1	38.6	
2012-03-07 00:24:00	X5.4	00:05:00	00:17:00								
2012-03-07 01:14:00	X1.3	00:58:00	01:10:00	1.5	3.3	5.4	37.7	2.1	3.6	6.4	36.1
2012-03-09 03:53:00	M6.3	03:37:00	03:49:00	1.5	3.3	60.0		1.5	3.1	57.1	
2012-03-10 17:44:00	M8.4	17:19:00	17:31:00	19.7	55.6			20.3	54.9		
2012-05-10 04:18:00	M5.7	04:08:00	04:20:00	18.8				19.7			
2012-05-17 01:47:00	M5.1	01:26:00	01:38:00	1.6	3.6			1.9	3.8		
2012-07-02 10:52:00	M5.6	10:43:00	10:55:00	46.8				37.7			
2012-07-05 11:44:00	M6.1	11:37:00	11:49:00	7.9				7.1			
2012-07-06 23:08:00	X1.1	23:01:00	23:13:00	15.2	22.4			12.6	19.4		
2012-07-08 16:32:00	M6.9	16:24:00	16:36:00								
2012-07-19 05:58:00*	M7.7	05:23:00	05:35:00	5.6	12.2			5.6	11.7		
2012-10-20 18:14:00*	M9.0	18:08:00	18:20:00	2.9				2.3			
2012-10-22 18:51:00	M5.0	18:40:00	18:52:00	15.2	27.8			15.8	26.6		
2013-04-11 07:16:00	M6.5	07:06:00	07:18:00	1.1	69.1			1.2	66.8		

Table 5.2 – *Continued*

Peak time	Class	Start time	End time	LYRA periods (s)						ESP periods (s)					
2013-05-03 17:32:00*	M5.7	17:24:00	17:36:00	2.7						3.2					
2013-05-13 02:17:00*	X1.7	01:59:00	02:11:00	23.4						23.4					
2013-05-13 16:05:00*	X2.8	15:52:00	16:04:00	25.5	44.8	78.6				25.5	48.8	78.6			
2013-05-14 01:11:00	X3.2	01:00:00	01:12:00	24.4						23.4					
2013-05-15 01:48:00	X1.2	01:31:00	01:43:00												
2013-06-07 22:49:00*	M5.9	22:29:00	22:41:00	1.3	5.4	69.1				1.4	4.7	57.8			
2013-10-24 00:30:00	M9.3	00:20:00	00:32:00	9.0						9.4					
2013-10-25 08:01:00	X1.7	07:50:00	08:02:00	1.7	6.7	14.5	78.6			1.8	7.9	13.9	69.1		
2013-10-28 02:03:00	X1.0	01:50:00	02:02:00	2.0	53.2					1.7	53.2				
2013-10-28 04:41:00	M5.1	04:28:00	04:40:00	5.8	15.8	37.7	75.3			5.8	15.8	37.7	75.3		
2013-11-10 05:14:00	X1.1	05:12:00	05:17:00	13.9						17.1					
2013-11-19 10:26:00	X1.0	10:17:00	10:29:00	2.9	11.7	21.4				2.8	11.3	20.8			
2014-01-01 18:52:00	M9.9	18:40:00	18:52:00	2.0	29.0					2.4	29.0				
2014-01-07 10:13:00	M7.2	10:10:00	10:22:00	9.0	26.6	37.7				9.0	25.5	37.7			
2014-01-07 18:32:00	X1.2	18:11:00	18:23:00												
2014-02-04 04:00:00	M5.2	03:58:00	04:10:00	5.6	7.0	15.8	25.5			5.6	7.6	15.2	25.6		
2014-02-25 00:49:00*	X4.9	00:38:00	00:50:00	36.1						36.1					
2014-03-12 22:34:00	M9.3	22:24:00	22:36:00	12.2	55.6					12.2	48.8				
2014-04-02 14:05:00	M6.5	13:31:00	13:43:00	2.4	4.3					2.0	4.5				
2014-04-18 13:03:00	M7.3	12:40:00	13:52:00	26.6	55.6					24.6	51.5				
2014-04-25 00:27:00*	X1.3	00:14:30	00:26:30	1.1	5.1					1.0	6.5				
2014-05-08 10:07:00	M5.2	10:03:00	10:15:00	22.4						22.1					
2014-06-10 11:42:00*	X2.2	11:38:30	11:50:30	6.7						6.6					
2014-06-10 12:52:00*	X1.5	12:36:00	12:48:00	17.3						19.5					
2014-06-11 09:06:00	X1.0	08:53:00	09:05:00	3.6	9.8					3.9	7.7				
2014-07-08 16:20:00	M6.5	15:59:30	16:11:30	1.4	13.9	25.5				1.9	13.9	25.5			
2014-08-24 12:17:00	M5.9	12:05:00	12:17:00	19.7	41.1	82.1				18.5	38.6	37.7			
2014-09-10 17:45:00	X1.6	17:22:00	17:34:00	1.1	7.9	37.7				1.2	7.6	37.7			
2014-09-28 02:58:00	M5.1	02:45:00	02:57:00	3.1	5.8					3.6	5.3				
2014-10-02 19:01:00*	M7.3	18:49:00	19:01:00	2.0	2.8					1.7	2.8				
2014-10-19 05:03:00	X1.1	04:36:00	04:48:00	3.3	7.3	9.4				3.5	6.1	10.7			
2014-10-22 01:59:00	M8.7	01:36:00	01:48:00	4.1	66.1					5.1	66.1				
2014-10-22 14:28:00	X1.6	14:02:00	14:14:00	1.8						2.2					
2014-10-24 21:41:00	X3.1	21:07:00	21:19:00												
2014-10-26 10:56:00	X2.0	10:40:00	10:52:00	1.8	2.4					1.7	2.6				
2014-10-27 14:47:00	X2.0	14:17:00	14:29:00	3.1						3.5					
2014-11-06 03:46:00	M5.4	03:36:00	03:48:00	2.9	5.1	48.8				2.4	5.8	51.0			
2014-12-04 18:25:00	M6.1	18:05:00	18:17:00	2.6	19.7	72.1				2.4	22.2	68.5			
2015-03-03 01:35:00*	M8.2	01:27:00	01:39:00												
2015-03-07 22:22:00	M9.2	21:43:00	21:55:00	1.3	2.0	3.8	11.7	18.0	41.1	1.6	2.2	3.7	11.4	17.6	40.1

Table 5.2 – *Continued*

Peak time	Class	Start time	End time	LYRA periods (s)			ESP periods (s)		
2015-03-11 16:22:00	X2.1	16:11:00	16:23:00	2.2	18.7	37.4	2.1	18.8	36.1
2015-06-22 18:23:00	M6.5	17:47:00	17:59:00	3.3	7.6	18.8	2.8	7.6	18.8
2015-06-25 08:16:00	M7.9	08:11:00	08:23:00	6.7	19.7		6.7	19.7	
2015-09-28 14:58:00	M7.6	14:47:00	14:59:00	9.0	23.4		9.4	24.4	
2016-04-18 00:29:00	M6.7	00:14:00	00:26:00	1.2	60.6		1.3	52.4	
2016-07-23 02:11:00*	M5.0	02:01:00	02:13:00	1.6	4.7		1.7	5.1	
2016-07-23 05:16:00	M7.6	05:11:00	05:23:00	2.0	26.6	69.0	2.6	26.5	69.0
2017-04-02 08:02:00	M5.3	07:52:00	08:04:00	3.1	4.5	27.8	3.6	5.4	30.3
2017-04-02 20:33:00	M5.7	20:29:00	20:41:00	9.4	37.7		9.4	39.3	
2017-04-03 14:29:00	M5.8	14:19:00	14:31:00	2.4	6.4	46.8	2.7	6.4	46.8
2017-09-06 09:10:00	X2.2	08:58:00	09:10:00	1.3			0.9		
2017-09-06 12:02:00	X9.3	11:53:00	12:05:00	12.1	18.8		12.6	22.1	
2017-09-07 10:15:00	M7.3	10:10:00	10:22:00	8.6	33.1		7.4	27.1	
2017-09-07 14:36:00	X1.3	14:28:00	14:40:00	55.6			48.8		
2017-09-08 07:49:00	M8.1	07:40:00	07:52:00	2.7	9.8	42.9	2.7	9.4	41.1
2017-09-10 16:06:00*	X8.2	15:55:00	16:07:00						

The results presented in Table 5.2 only partly match those of (Inglis et al., 2016), even when only one significant period was found in our analysis. Of the 40 flares for which Inglis et al. (2016) found a period in the GOES data and for which we also detected QPPs with one or more periods, one of our periods matches theirs with 25% margin in 24 cases. For the *Fermi* data, this ratio is 10 flares out of 16. This represents a match in  $\sim 60\%$  of the cases for both datasets (see Figure 5.15). This is an encouraging result when we consider that the methods and instruments used to determine the QPP periods are very different, and taking into account that we limited our investigation to periods below 100 s and to 12 minute intervals during the impulsive phase. Additionally, since GOES acquires at the 2 s cadence, Inglis et al. (2016) did not look for any period below 5 s.

The percentage of flares investigated by Simões et al. (2015) for which the retrieved interval of periods contains at least one detection from our study is on the order of  $\sim 66\%$  (see Figure 5.16).

Finally, some of the flares presented in Table 5.2 have occasionally been studied in the literature. Chowdhury et al. (2015) reported periods of 53 s and 72 s in the X3.2 flare on 14 May 2013, which could be harmonically linked to the  $\sim 25$  s found by Dennis et al. (2017) at the end of the impulsive phase and in our analysis. During the impulsive phase of the X1.0 flare on 28 October 2013, Hayes et al. (2016) found a period of  $\sim 20$  s in both thermal and non-thermal emission, which is not confirmed by our analysis. On the other hand, they reported a period of  $\sim 55$  s in the non-thermal emission, for which they found no counterpart in the thermal emission, while we detect it in LYRA and ESP. A period of  $\sim 35$  s has been detected in the X4.9 flare on 25 February 2014, by McLaughlin et al. (2018), which is confirmed by our analysis, in contrast to the  $\sim 60$  s period reported by Cho et al. (2016). The 30–120 s interval reported by Ning (2017) for the X1.6 flare on 10 September 2014, is consistent with the period of  $\sim 40$  s from our analysis. Pugh et al. (2017) found no significant period in the M8.7 flare on 22 October 2014. Although a peak is visible in their periodogram around 3.5 s (close to the period of 4.1 s found in the LYRA data), it is not significant in their analysis. The periods of 54 s and 20.5 s found by Cho et al. (2016) in the X1.2 flare on 7 January 2014, and in the X1.1 flare on 11 June 2014, respectively, do not correspond to any of our detections. The lack of correspondence between our detections and some of the detections reported in the literature can be explained by different data sets, different detection methods, and different criteria used to establish the reliability of detection. However, our observations generally match reasonably well the ones from other studies. This strengthens our confidence that our detections are real.



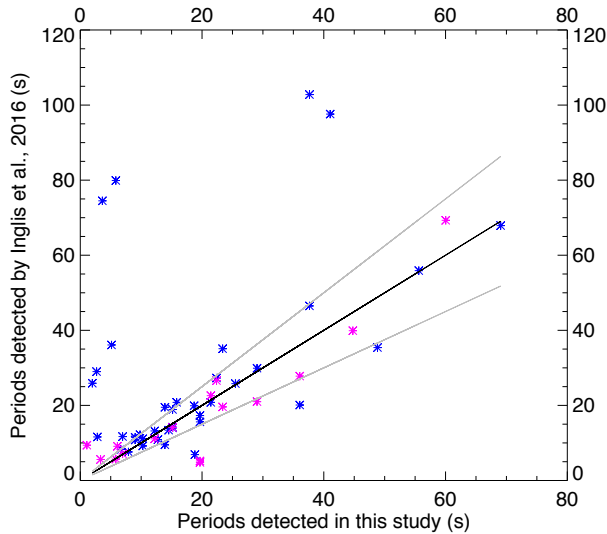


Figure 5.15: Correlation between the periods detected in the GOES (*blue*) and Fermi (*magenta*) data by Inglis et al. (2016) on the one hand, and those found in our study of the LYRA Zr data on the other hand, for flares of Solar Cycle 24 with GOES class M5 or higher. When more than one period was detected in the LYRA data, the plotted period is the one closest to the period detected in the GOES or *Fermi* data. The *grey lines* represent the  $\pm 25\%$  uncertainty on the period detection.

## 5.5 Correlation with the Alfvén Speed

Several mechanisms that may potentially be at the origin of QPPs are expected to produce periods inversely proportional to the Alfvén speed, see Section 5.1. This is in particular the case for QPPs produced by Alfvén and fast kink modes, for which we have:

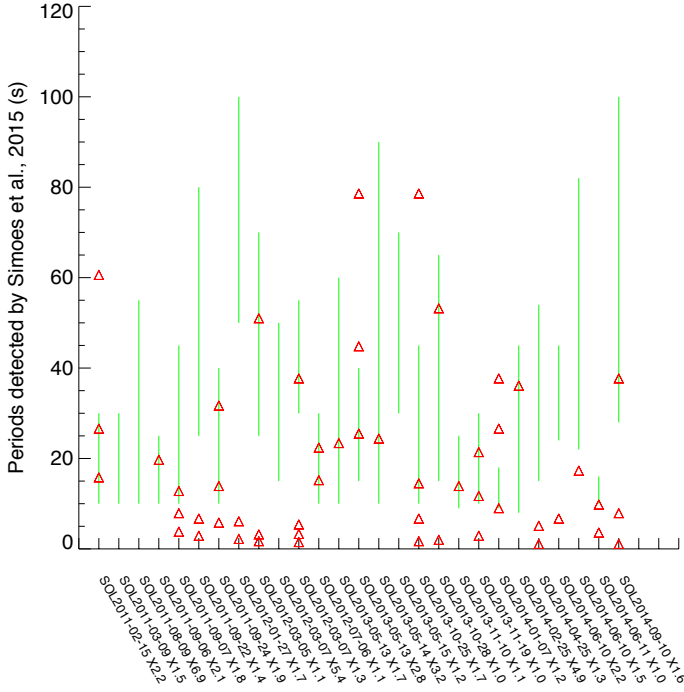


Figure 5.16: Comparison between the periods detected in the GOES data (*green intervals*) by Simões et al. (2015) and those found in the LYRA data for the same flares (*red triangles*). In 66% of the cases, one of the periods detected in our study is within the interval detected by Simões et al. (2015) in the GOES data.

$$P_a = \frac{2L}{C_{A0}}, \quad \text{for Alfvén waves} \quad (5.6)$$

$$P_k = \frac{2L}{C_{A0}} \sqrt{\frac{1 + \rho_e/\rho_0}{2}}, \quad \text{for fast kink waves} \quad (5.7)$$

where  $P_a$  and  $P_k$  are the periods triggered by the fundamental modes of a standing Alfvén and a fast kink wave respectively,  $L$  is the length of the loop,

$C_{A0}$  is the Alfvén speed inside the loop, and  $\rho_0$  and  $\rho_e$  are the mass densities inside and outside the loop respectively.

We therefore checked whether a correlation exists between the periods obtained for a subset of the flares analyzed in Section 5.4 with  $2L/C_{A0}$ , *i.e.* with  $2L\sqrt{\mu_0\rho_0}/B_0$ , where  $B_0$  is the magnetic field inside the loop.

However, the parameters of the plasma inside the loop are hard to estimate and may vary. This is particularly true for the magnetic field, which can only be measured in the photosphere and must be extrapolated to higher altitudes. We therefore needed to rely on a few assumptions. We assumed that the temperature was above 10 MK, which might be valid in flaring conditions, so that we use the density-sensitive intensity ratio of coronal lines forming at high temperatures. We also considered that the magnetic field, taken to be its mean value along the loop, is potential, *i.e.*  $\nabla \times \mathbf{B} = 0$  in the MHD equations (see Section 1.5.1), and can be obtained by running a Potential Field Source Surface (PFSS) extrapolation.

### 5.5.1 Estimation of the Magnetic Field and of the Length of the Loop

For this analysis, we used the Potential Field Source Surface model (PFSS – Altschuler and Newkirk, 1969; Schatten et al., 1969; Hoeksema, 1984; Wang and Sheeley, 1992) package of the Solar Software library (<https://www.lmsal.com/~derosa/pfsspack/>), which uses SDO/HMI magnetograms as boundary condition. The PFSS model calculates the magnetic field between the photosphere and the source surface in the corona, using its measured value at the photospheric level as lower boundary condition and assuming it to be radial at the source surface level. The PFSS model relies on the hypothesis that there is no electric current between the photosphere and the source surface ( $\nabla \times \mathbf{B} = 0$  in Equation 1.13). The PFSS assumption may seem irrelevant at first sight, since the magnetic field in an active region is known to be far from potential. And indeed, when comparing the obtained field line structures to the morphology of hot flaring loops as observed in AIA 211 Å (corresponding to an emission temperature of 2 MK) or 193 Å (corresponding to a mix of emission temperatures of 1.5 and 20 MK)<sup>3</sup>, we observed that the PFSS model was failing to capture the twisted loop configurations. Nevertheless, the uncertainty on

---

<sup>3</sup>AIA provides an even hotter passband at 94 Å, which is most sensitive the plasma with temperature around 6.3 MK. Nevertheless, the loop structures in this channel were similar to the ones seen in the other passbands. We therefore did not use it. In a few occasions, when the AIA 193 Å and AIA 211 Å images saturated, we used AIA 171 Å images instead. This channel is most sensitive to the plasma with temperature around 0.6 MK.

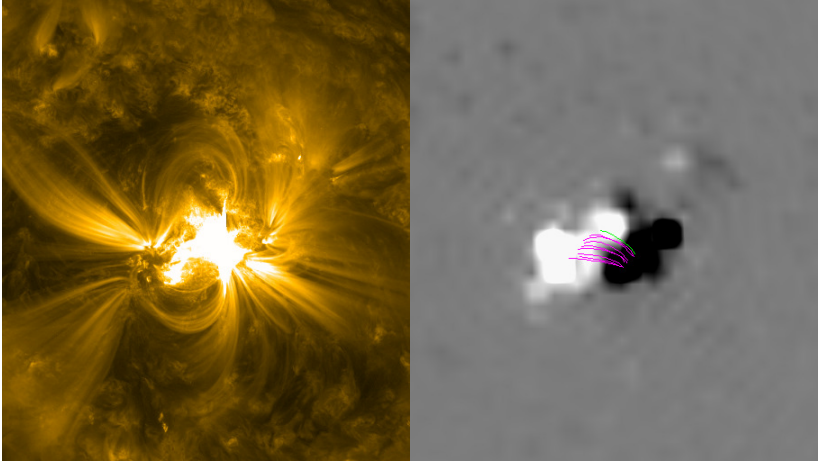


Figure 5.17: Comparison between the observed loop structures (left panel: an image taken by SDO/AIA in the 171 Å passband) and the ones provided by the PFSS model (right panel: the background image taken by SDO/HMI) for the X1.5 flare on 9 March 2011.

the various parameters needed to compute the Alfvén speed was such that we considered the PFSS sufficient to get a rough estimate of the magnetic field. Additionally, we are only interested in the amplitude of the magnetic field, not its orientation. We therefore favored the PFSS extrapolation as compared to more accurate extrapolation schemes such as the Non-Linear Force-Free Field (NLFFF) to reduce the computational load. In this, we followed other studies, such as (Verwichte et al., 2013). However, we limited our analysis to the events in which the resulting field lines were similar to the structures observed with SDO/AIA. We also discarded the flares that were taking place at longitudes above  $60^\circ$  from the solar central meridian, to avoid complications associated with projection effects, as well as the flares for which LYRA data were missing or too scarce. All in all, it resulted in a set of 18 flares, of M5 class or higher in the GOES scale, observed between 26 March 2010 and 27 May 2014 (dates for which we have EVE data, which are used to estimate the electron density, see Section 5.5.2), for which one or several field lines produced by the PFSS extrapolation were matching the observed flaring loops well enough. Those lines were selected by a visual inspection. Finally, we averaged the value of the magnetic field and the loop length over the set of selected lines.

Table 5.3: Line ratios and corresponding electron densities for the X4.9 flare on 25 February 2014.

Lines involved (in nm)	Line ratio	Density (in $\text{cm}^{-3}$ )
12.121/12.875	0.086	$7.5 \times 10^{11}$
(14.214 + 14.228)/12.875	0.121	$5.4 \times 10^{11}$
14.573/12.875	0.057	$2.1 \times 10^{11}$

### 5.5.2 Estimation of the Coronal Mass Density

As a first approximation, considering only hydrogen and helium ions, the mass density can be considered proportional to the electron density:  $\rho = 1.12 \times n_e m_p$ , with  $n_e$  the electron density and  $m_p$  the mass of the proton.

The coronal electron density in flares was obtained following the method proposed by Milligan et al. (2012). This method uses density-sensitive spectral line ratios measured by the EVE/MEGS-A spectrometer onboard SDO in the 6.5 to 37 nm range. The authors suggest three ratios, all involving Fe XXI lines, with the formation temperature above 10 MK that are not blended with the emission of other atomic transitions and are detected in most flares. These ratios are (wavelengths in nm) 12.121/12.875, (14.214 + 14.228)/12.875 (this ratio involves two neighbouring lines that are not resolved in EVE), and 14.573/12.875.

For each flare, we selected the MEGS-A spectrum that was the closest to the flare peak time, from which we subtracted a pre-flare spectrum. By doing so, we removed any influence of some cooler lines that could be blended with the flare lines involved in the ratios. In practice, this operation mostly had an impact on the 14.573/12.875 ratio. We then fitted the resulting spectrum with a constant background to which we added 17 gaussian-shaped spectral lines. Here, following Milligan et al. (2012), we considered that the background could be assumed constant over the whole spectral band. The fitting parameters for the gaussian profiles were the center wavelength, the peak amplitude and the width. An example of a fitted spectrum for the X4.9 flare on 25 February 2014 is shown in Figure 5.18.

Finally, we compared the ratios of the fitted amplitudes of the gaussian lines to the theoretical line ratio function obtained from the CHIANTI atomic database (Dere et al., 1997; Landi et al., 2012) and shown in Figure 5.19. For the X4.9 flare on 25 February 2014, the obtained line ratios and densities are summarized in Table 5.3.

As noted by Milligan et al. (2012), the 12.121 nm line is not always resolved

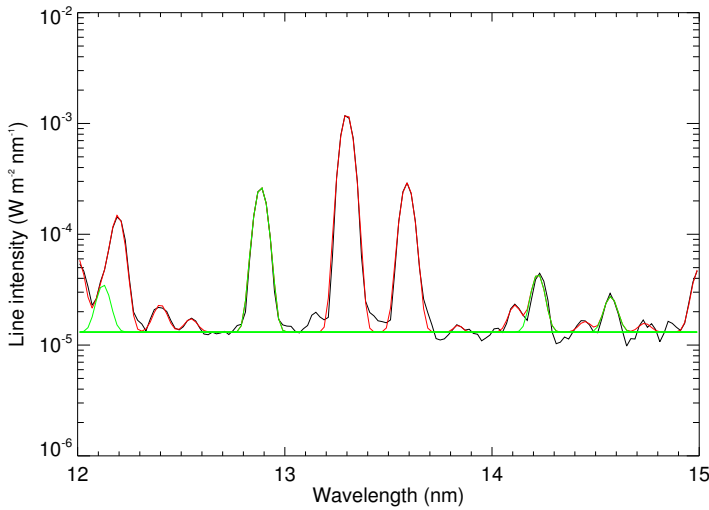


Figure 5.18: The flare spectrum (*i.e.* after subtraction of the pre-flare spectrum) measured by SDO/EVE/MEGS-A during the X4.9 flare on 25 February 2014 (black line), with the fitted spectrum overplotted (red line). The fitted background and the lines involved in the density-sensitive ratios are shown in green.

from the Fe XX line at 12.184 nm (except for the strongest flares). This was indeed the case for most of the flares that we analyzed, so we decided to discard the corresponding ratio. The lines involved in the 14.573/12.875 ratio were badly fitted on several occasions and strongly depends on the pre-flare spectrum selected. Therefore, for this analysis, we primarily considered the ratio  $(14.214 + 14.228/12.875)$ , which leads to the density of  $5.4 \times 10^{11} \text{ cm}^{-3}$  for the flare illustrated in Figure 5.18. Note, however, that the chosen ratio is of a lower accuracy when dealing with densities below  $5 \times 10^{11} \text{ cm}^{-3}$ , as is illustrated in Figure 5.19. For a few flares with lower densities, this ratio provided unrealistic values. In those cases, the 14.573/12.875 ratio was used instead.

### 5.5.3 Comparison Between the Observed and Predicted Periods

The comparison between the periods of observed QPPs and the ones predicted considering the fundamental mode of a standing Alfvén wave is shown in Figure 5.20. When several periods have been detected for a flare, we considered the

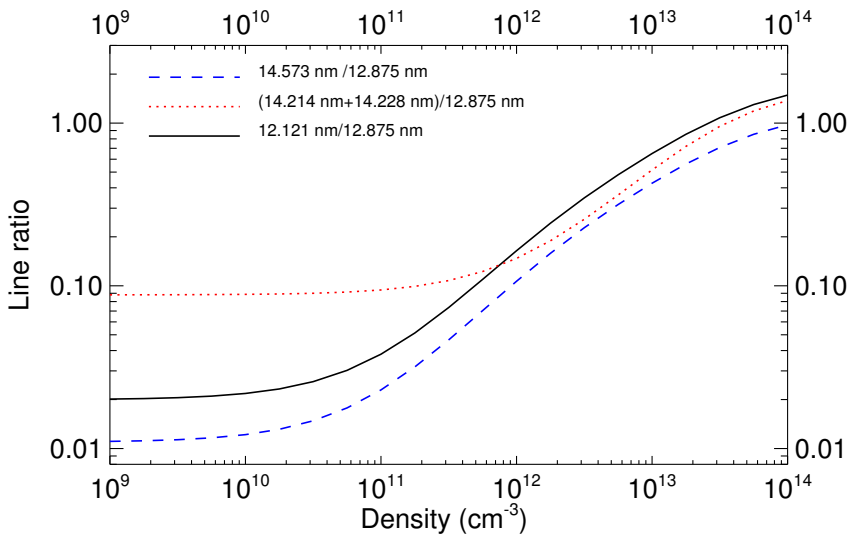


Figure 5.19: Theoretical relationships between the selected line ratios and density from CHIANTI. The lines involved in the ratios are expressed in nm.

period closest to the predicted value. However, no obvious correlation can be found. This does not fully discard the MHD wave origin of QPPs, though, as significant uncertainties affect the estimation of the parameters used to compute the Alfvén speed, in particular the magnetic field. We estimated, for each of the flares, the value of the magnetic field that would give rise to the main measured QPP period assuming that it corresponds to the fundamental mode of the standing Alfvén wave (Figure 5.21). These values can be compared to the magnetic field values calculated using the PFSS model (Figure 5.22). In some cases, significant differences can be seen. More realistic extrapolation schemes, such as the Non-Linear Force-Free Field (NLFFF), should probably be tested. Also, the correlation with the Alfvén speed is only strictly expected for Alfvén and fast kink modes and might be less appropriate to describe sausage modes. However, it is striking to see that despite the wide variety of active regions considered, with very different sizes and magnetic fields, most of the flares show QPPs with periods of the order of 5-20 s (see Figure 5.12). This may be an indication that at least those periods are from the other origin than an MHD wave.

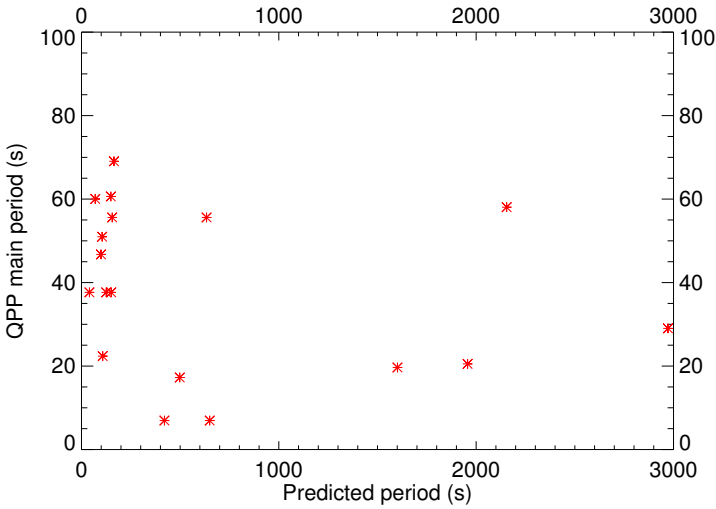


Figure 5.20: Comparison between the periods of observed QPPs and the ones predicted considering the fundamental mode of a standing Alfvén wave.

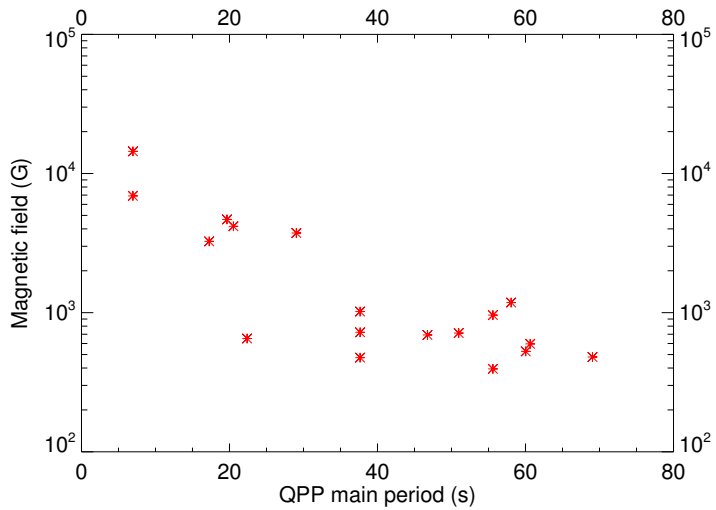


Figure 5.21: Value of the magnetic field that corresponds to the main observed QPP period, considering the fundamental mode of a standing Alfvén wave.



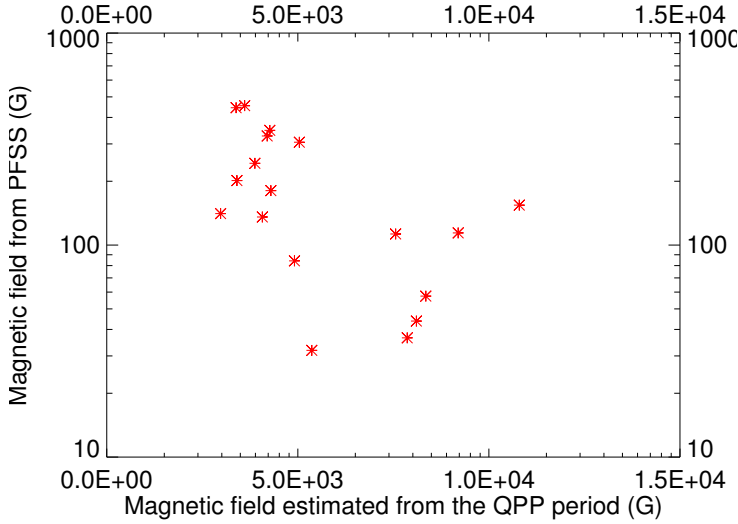


Figure 5.22: Comparison between the magnetic field deduced from the observed QPP periods considering the fundamental mode of a standing Alfvén wave and the magnetic field calculated using the PFSS extrapolation.

## 5.6 Quasi-Periodic Pulsations in the Two Strongest Flares of Solar Cycle 24

The X9.3 flare on 6 September 2017 presented in Chapter 4 was also investigated to look for the presence of QPPs. Channels 3 and 4 were analyzed after detrending, following the method and the set of criteria described in Section 5.2.3. They showed QPPs with the periods  $\sim 12$  s and  $\sim 19$  s.

We also checked whether QPPs were present in channels 1 and 2. For those channels, no detrending was needed, given the high amplitude of the oscillations. Comparing the periods found in those channels with those from channels 3 and 4 therefore provides a way to validate our set of detection criteria in detrended time series.

To identify the main periodicities in channels 1 and 2 we have performed a direct wavelet detection, which showed in both data sets the periodicities of  $\sim 12$  s,  $\sim 17$  s,  $\sim 90$  s, and  $\sim 300$  s, as illustrated in the two upper rows of Figure 5.23. For this figure, the data have been smoothed to the cadence of 0.5 s. An additional  $\sim 40$  s periodicity was detected in channel 1. The periods around  $\sim 12$  s and  $\sim 17$  s are consistent with the peaks found in the detrended data set of channel

4, using the method described in Section 5.2.3, as illustrated in the bottom row of Figure 5.23 for the size of the detrending window of 60 s. In this figure, the detection around 55 s in channel 4 is likely a spurious detection caused by the detrending process. The periods longer than 100 s are also dubious as they are well above the size of the detrending window (see Section 5.2). Kolotkov et al. (2018) also reported the  $\sim 12$  s period for this flare.

This is to our knowledge the first detection of QPPs in the 1900–2220 Å range, and only the second report of QPPs in Lyman- $\alpha$  (120- and 300-second oscillations have been previously reported in SOL2011-02-15T01:56 by Milligan et al. (2017)). This provides further evidence that, whatever the mechanism producing the QPPs is, it also affects the chromospheric emission, which is primarily caused by hydrogen recombination (see Chapter 4).

The same analysis was performed for the X8.2 flare on 10 September 2017. This event was the second strongest flare of Solar Cycle 24. It was produced by the same active region as the X9.3 flare, in a similar magnetic environment. One could therefore expect it to produce QPPs with periodicities in the same range as the X9.3 flare. However, the two flares differ in one important aspect: the X9.3 flare was located at the longitude of  $\sim 33^\circ$ W from the solar central meridian, while at the time of the X8.2 flare, most of the active region had disappeared behind the west solar limb, so that at least one of the footpoints of the post-flare arcade was situated on the far side of the Sun.

In LYRA observations, the two flares also differ significantly. Despite the high amplitude of the X8.2 flare, we could not detect it in LYRA channels 1 and 2. This can hardly be explained by an enhanced degradation, as the two flares occurred only a few days apart. As mentioned in Chapter 4, we attributed the absence of flare signal in channels 1 and 2 to the fact that the source of the chromospheric emission was hidden behind the limb.

However, the flare was clearly seen in channels 3 and 4, which measure coronal emissions. We therefore applied our detection method to the channel 4 of unit 1. No period was found to satisfy our set of detection criteria. Looking closer, periods of  $\sim 20$  s and  $\sim 50$  s seemed to be present in both LYRA channel 4 and EVE/ESP data but they do not reach the 95% level of confidence, see Figure 5.24.

This flare was also observed by the EUV-Monitor (EUVM) onboard the Mars Atmosphere and Volatile Evolution (MAVEN) mission (Eparvier et al., 2015). MAVEN is a satellite orbiting Mars that was at that moment situated  $155^\circ$  westward of the Earth in the heliographic longitude (Figure 5.25). From the MAVEN vantage point the flaring active region was situated on the front side of the disk. The EUVM instrument has three channels nicely complementing

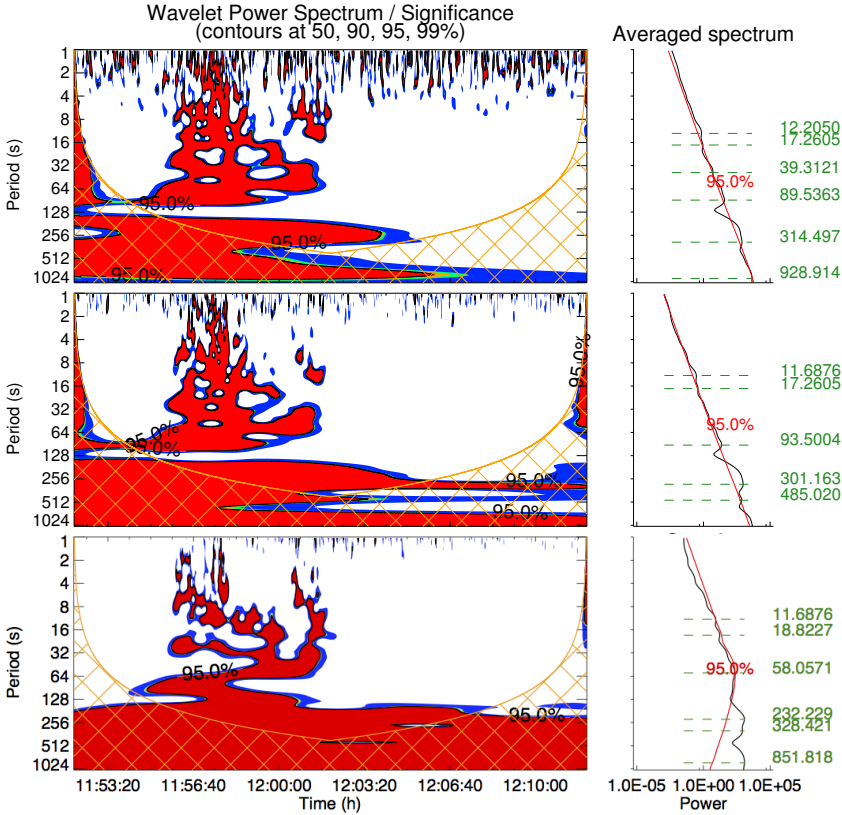


Figure 5.23: Wavelet power spectra (left panels) and time-averaged spectra (right panels) of the 6 September 2017 flare measured by LYRA in channel 1 (top), channel 2 (middle), and channel 4 (bottom). The power spectra were normalized to the 95% significance. The channel 4 observations were detrended using the size of the detrending window of 60 s prior to applying the wavelet transform. The observations in channels 1 and 2 were not detrended. The red curve in the right panels corresponds to the 95% confidence level. It takes into account that the data are detrended when applicable, see Section 5.2. The peaks (in seconds) reaching the 95% confidence level are marked in green in the right panels.

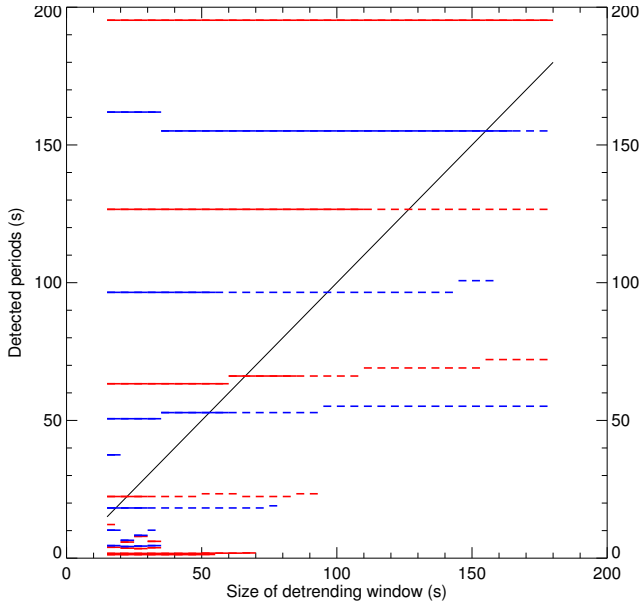


Figure 5.24: Effect of the detrending window on the periods detected in the LYRA data for the X8.2 flare on 10 September 2017. The periods shown with *red lines* correspond to the periods found in the LYRA unit 1 Zr data that reach (*solid lines*) and do not reach (*dashed lines*) the 95% level of confidence in the power spectrum during a time interval at least twice longer than the period. Similarly, the periods shown with *blue lines* were found in the ESP-Q data. Only the periods to the *right of the black diagonal line* (corresponding to the detected period equal to the size of the detrending window) are considered to be reliably detected. The periods found in ESP-Q have been shifted up by 0.5 s for clarity.

the ones of LYRA and its observations should be similar to those obtained from LYRA. Those channels are the SXR channel (0.1–7 nm), the EUV channel (0.1–3 + 17–22 nm), and the Lyman- $\alpha$  channel (121–122 nm). Interestingly, this instrument clearly detected the flare in all its channels, including the Lyman- $\alpha$  one (see Figure 5.26). Applying a direct wavelet detection to this data set showed the presence of QPPs with the periods of  $\sim 15$  s,  $\sim 40$  s and  $\sim 150$  s. The first two oscillations reached the 95 % confidence level during more than two periods (see Figure 5.27, left panel). These periods also appear in the averaged spectrum (Figure 5.27, right panel), although not reaching the 95% confidence level.

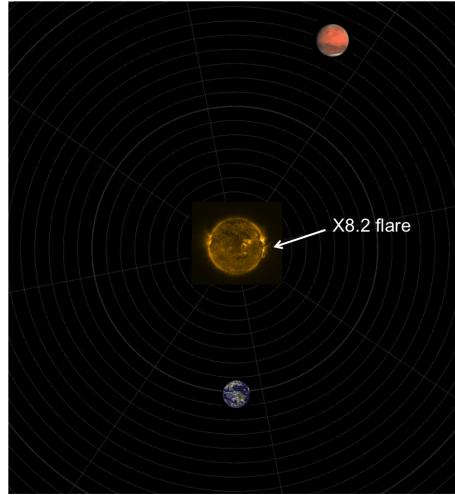


Figure 5.25: Respective positions of the Sun, Earth and Mars at the time of the X8.2 flare on 10 September 2017. From the perspective of the Earth, and therefore from PROBA2, the flare marked with the arrow was visible at the west limb, while from the perspective of Mars and from MAVEN, it was located on the disk in the eastern hemisphere of the Sun. The sizes of the Sun, Earth, and Mars are shown not to scale.

These observations argue in favor of the QPPs being mainly produced at the footpoints of the loop. Even when detected in coronal wavelengths, the oscillations do not seem to originate from the whole body of the loop, but rather be limited to the lower layers of the solar atmosphere. However, further investigation would be needed to confirm this hypothesis.

## 5.7 Conclusions

New space instruments such as PROBA2/LYRA and SDO/EVE/ESP make it possible to conduct statistical studies of QPPs as these instruments observe the full Sun in a quasi-uninterrupted way. The observations are made in the EUV and SXR wavelengths, in which the relative amplitude of QPPs is much smaller than that usually observed in HXR or radio wavelengths. The ESP and LYRA data must therefore be first detrended in order to allow the detection of QPPs using wavelet power spectra, which may result in producing artificial periods. These periods vary with the width of the detrending window, which makes them

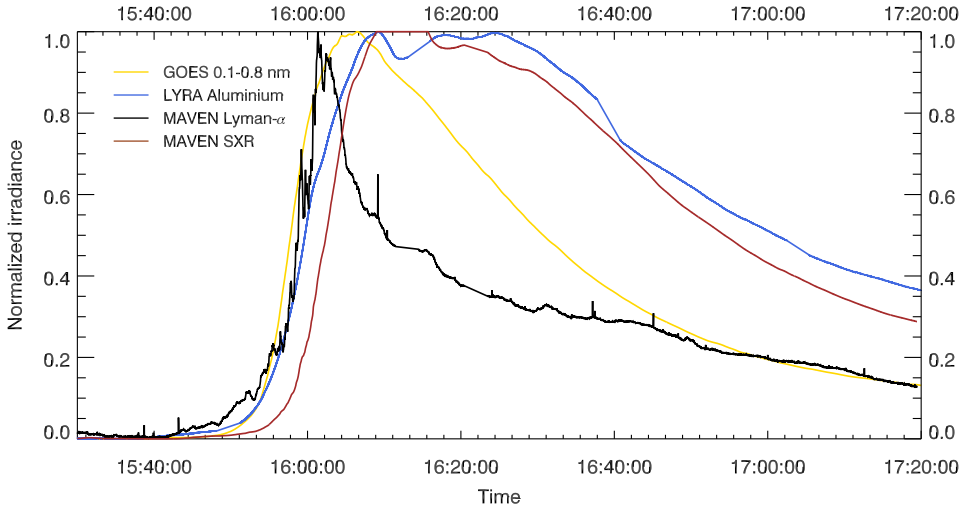


Figure 5.26: The X8.2 flare on 10 September 2017, as observed by MAVEN Lyman- $\alpha$  (*black line*), MAVEN SXR (*brown line*), GOES 0.1–0.8 nm (*gold line*) and LYRA channel 3 (*blue line*). Note that the MAVEN time series have been shifted by 327 s to compensate for the difference of the distance to the Sun (on 10 September 2017, the light was taking 327 more seconds to reach Mars than it took to reach the Earth).

identifiable. We proposed a set of criteria to be used to distinguish real periods from artifacts appearing due to detrending or to the noise (see Section 5.2.3).

We applied these criteria to all flares stronger than M5 in the GOES scale that occurred during Solar Cycle 24 (until 31 December 2018) that were observed by both LYRA and EVE/ESP. Only 9 of 90 flares did not exhibit any period satisfying our criteria. All the other flares showed QPP periods between 1 and 100 s that could be reliably identified using our set of criteria. No dependence on the flare longitude or the flare class was found. The correspondence of detected periods to those identified in the similar investigations made earlier is reasonably good, even if the detection methods differ completely. This consolidates the validity of our detection criteria and also confirms that QPPs are inherent to the physics of the flaring process.

We then tried to correlate the QPP period detected in a subset of these events with the period of the fundamental mode of a standing Alfvén wave, but could not find any correlation. Even if the lack of correlation is not sufficient to

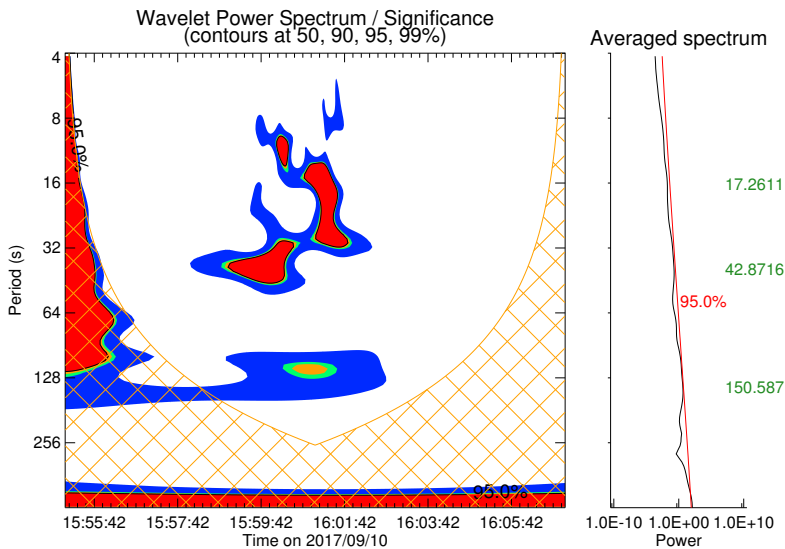


Figure 5.27: Wavelet power spectrum (left panel) and time-averaged spectrum (right panel) of the observations of the X8.2 flare on 10 September 2017 in the Lyman- $\alpha$  channel of MAVEN/EUVM. In the left panel, three groups of periods are clearly visible around  $\sim 15$ ,  $\sim 40$  s and  $\sim 150$  s, all detected with a confidence above 95 % (and even above 99 % for the first two groups). The period at 150 s, however, is detected for a too short duration to be called an oscillation.

discard the MHD wave origin, the fact that very different active regions all tend to produce QPPs with periods of the order of 5-20 s independently of their size, density or magnetic field may be an indication that at least these periods are from the origin other than an MHD wave.

Finally, we compared the two strongest flares of Solar Cycle 24, *i.e.* the X9.3 and the X8.2 flares on 6 and 10 September 2017 respectively. LYRA and EVE data sets indicated the presence of QPPs only in the first of these flares. However, the second flare did produce QPPs as well, as was demonstrated by the analysis of the data taken by the third instrument: the EUV Monitor onboard MAVEN that is orbiting Mars. The main difference between LYRA and EVE on the one hand and EUVM on the other hand is that at least one footpoint of the flaring arcade was hidden from LYRA and EVE by the limb and MAVEN observed both footpoints. This is a strong indication that QPPs are mainly produced in the lower layers of the Sun atmosphere.





# Chapter 6

## Conclusions

### 6.1 Summary

Solar flares are impressive phenomena, releasing huge amounts of energy during the restructuring of the local magnetic configuration. Together with the coronal mass ejections, to which they are often associated, flares constitute a major external source of perturbation of the Earth environment, the so-called "space weather", and can significantly affect the human activities, so as to be now considered by several countries as a potential threat to human technology.

However, while solar flares are known since late 19th century and regularly monitored since decades, many details of the underlying physical mechanisms remain elusive. The general scenario of a coronal magnetic reconnection that accelerates electrons, which in turn heat the chromospheric plasma by Coulomb collisions, hence producing an increase of radiation all over the solar spectrum is widely accepted. However, the quantitative aspects are not so clear. Can this scenario explain the amount of energy dissipated in flares? How is this energy stored in the corona before the reconnection starts? And what triggers the reconnection? There are so many important questions that remain without a clear answer. But our understanding of the process progresses step by step, with every new study and every new set of observations adding its own building block to our knowledge.

In this context, with its four channels chosen for their relevance to solar physics, space weather, and aeronomy, its high sampling rate (nominally 20 Hz) and its three redundant units, the LYRA radiometer onboard the ESA micro-satellite PROBA2, has an important role to play. The instrument was launched in late

2009 and observes the SXR–MUV spectral range in four broadband channels, covering the emissions by the chromosphere and the low corona. The description of the instrument is detailed in chapter 2.

The main purpose of this PhD was to increase our knowledge about solar flares, by exploiting the multispectral and high-cadence observations delivered by the LYRA radiometer. To do so, the instrument first had to be calibrated. Therefore, this PhD work is divided into two main parts: the first one corresponds to chapters 2 and 3 and is dedicated to instrumental aspects, while the second part, including chapters 4 and 5, addresses two aspects of solar flares for which the LYRA data were an asset, *i.e.* the comparison of a flare evolution in multiple bandpasses and quasi-periodic pulsations.

More specifically, after some general reminders about the Sun that constitute Chapter 1, Chapter 2 briefly reviewed the design of the instrument, gave an overview of the data products distributed on the instrument website, and described how the data are calibrated. The main calibration steps consist in removing the dark current (*i.e.* the thermal signal of the instrument), rescaling the data to the constant distance of 1 A.U., correcting the degradation, and converting the measured photocurrents into irradiance units.

Among those steps, the later two proved to be tricky, as LYRA observes in very broadband channels (several tens of nm wide), which cover a few portions of the spectrum over which the solar emission may not evolve in the same manner. Having no way to estimate how the solar emission is distributed over each channel's passband, the daily calibration assumes that its distribution remains constant over time. This is however a very strong assumption, which we know to break in some cases. In particular during flares, the irradiance is strongly biased toward the SXRs.

Additionally, the instrument is affected by a strong degradation, which evolved so rapidly in the nominal unit (which is used permanently) that channels 1 and 2 died within a few months of activity. Some degradation processes can modify the spectral response of the instrument.

Therefore, to understand the implications of this strong assumption, in Chapter 3, we went deeper into the analysis of the degradation. We used calibration dark current and LED measurements performed in-flight to attribute the origin of the degradation to the polymerization of a layer of contaminant on the front filters. By comparing the loss of signal in the four channels of each LYRA unit, we were able to identify the contaminants at play and to estimate the evolution of the thickness of the contaminant layer over the mission. The degradation was found to be caused predominantly by carbon, with possibly some contribution of silicon. Such a contamination explains the observed attenuation of signal

in three of the four channels of each unit. But channel 3 sometimes seems to behave differently. A similar situation was observed by the EVE instrument on board SDO, for which some channels, all using metallic filters, were aging differently than the other ones. Both for EVE and LYRA, this behavior is attributed to the presence of an oxide layer on top of the metallic filters.

Having identified the main source of degradation in LYRA, we could build a radiometric model of the instrument that accounts for the contamination. We used it to monitor the evolution of the spectral response of each channel. It was found that Channel 1 in particular experiences significant changes in its bandpass, with its peak transmission shifting from 121.6 nm to  $\sim 150$  nm. This possibly explains why this channel was not able to detect any flare after the first few months of operation.

The work on degradation will be continued in the future. During the last few years, the developers of EUV space instruments realized the importance of degradation, and in particular of contamination, for their targeted spectral range. Most of the instruments currently in orbit are affected. There seems to be a real wish to join the force to understand in depth the processes at stake to avoid repeating some mistakes with the next generation of instruments. Some materials, although labelled "space qualified" are not suitable when observing the EUV. The importance of a strong cleanliness programme has been demonstrated.

In Chapter 2, we also estimated the error affecting the raw and calibrated LYRA data. The error calculation (30–40% for channels 2 to 4, and 120 % for channel 1) takes into account that the channel is sensitive to wavelengths outside its nominal bandpass. This is the reason why it is so important for channel 1, for which the purity is only on the order of 25%.

The second part of this PhD starts with Chapter 4, with a multi-channel analysis of the strongest flare of Solar Cycle 24. This event provided the first detection of the solar flare emission at middle-ultraviolet wavelengths around 2000 Å by the channel 2 of LYRA, which allowed a thorough analysis of the mechanism of the flare chromospheric emission. The flare (SOL20170906) was also observed in channel 1 of LYRA centered at the H I Lyman- $\alpha$  line at 1216 Å, showing a clear non-thermal temporal profile in both channels. The flare radiation in channel 2 is consistent with the hydrogen Balmer continuum emission produced by an optically thin chromospheric slab heated up to 10000 K. Simultaneous observations in channels 1 and 2 allowed the separation of the line emission (primarily from the Lyman- $\alpha$  line) from the Balmer continuum emission. Together with the recent detection of the Balmer continuum emission in the near-ultraviolet by IRIS, the LYRA observations strengthen the interpretation of broadband flare emission as the hydrogen recombination continua originating in the chromosphere.

The last part of this PhD work was dedicated to quasi-periodic pulsations (QPPs). These oscillations are regularly observed in the impulsive phase of flares since the 1970s and sometimes persist in the decaying phase. In the range of periods from 1 to 100 s that was studied in this work, their origin is usually attributed to two main physical processes: the modulation of the electron beam and of the newly reconnected loop by an MHD wave, or a fluctuating particle acceleration that could be caused *e.g.* by an oscillatory magnetic reconnection. Simulations have shown that both mechanisms are able to produce periods in this range. Another approach to determine the QPPs origin is observational: in the frame of broad surveys, we can try to identify trends or correlations with the characteristics of the magnetic environment that would point to a particular mechanism.

This is probably why, in the past years, the studies of QPPs regained interest with the advent of a new generation of soft X-ray/extreme ultraviolet radiometers, among which LYRA, that pave the way for statistical surveys. Since the amplitude of QPPs in these wavelengths is rather small, detecting them implies that the overall trend of the time series needs to be removed before applying any Fourier or wavelet transform. This detrending process is known to produce artificial detection of periods that must then be distinguished from real ones.

Therefore, our first step was to estimate the performances of the wavelet transform for the type of events that we were interested in. We proposed a set of criteria to help identify real periods and discard artifacts. We then applied these criteria to the data taken by EVE/ESP and LYRA to search for QPPs in flares stronger than M5.0 that occurred during Solar Cycle 24. Most of the flares exhibited QPPs with periods between 1 and 100 s.

We compared our detections to those of other surveys and found good agreements, even when the detection method was fundamentally different. No dependence on the flare longitude or the flare class was found.

For a subset of the flares analyzed in this survey, we also searched for a correlation with the period of the fundamental mode of a standing Alfvén wave  $2L/C_{A0}$ , which would be a strong indication of an MHD-related origin. We performed PFSS extrapolations to estimate the magnetic field and the length of the loops. Electron densities were obtained by using density-sensitive spectral line ratios measured by the EVE/MEGS-A. This analysis highlighted the absence of correlation between the measured period and  $2L/C_{A0}$ .

Finally, we provided an in-depth analysis of the two strongest flares of Solar cycle 24, *i.e.* the X9.3 flare on 6 September 2017 located at a latitude of  $33^\circ\text{W}$  and the X8.2 flare on 8 September 2017 for which at least one of the footpoints was occulted by the solar limb. The two flares showed significant differences in

LYRA observations despite being produced by the same active region and being of similar amplitudes. While the X9.3 flare was observed by the four channels of LYRA, no signature could be found in the channels 1 and 2 for the X8.2 flare. Similarly, during the impulsive phase of the X9.3 flare, quasi-periodic pulsations of the flare emission with periods around 12 and 17 s were clearly detected in all four channels of LYRA, including channels 3 and 4, which are sensitive to the EUV and X-ray radiation. In contrast, no QPP could be confirmed in those channels during the X8.2 flare. We then compared the observations by LYRA to those by MAVEN/EUVM, an instrument orbiting Mars that had a full visibility of the X8.2 flare. Not only did the event produce a detectable signature in Lyman- $\alpha$ , but also QPPs with periods of  $\sim 15$ ,  $\sim 40$  s and possibly  $\sim 150$  s were observed. This may suggest that QPPs are produced close to the footpoints of the reconnecting loops. However, more work will be needed to confirm this hypothesis.

## 6.2 Lessons Learned

The initial goal of this PhD was two-fold. On the instrumental side, it aimed at calibrating the LYRA data and at analyzing the potential of its prototype wide band-gap detectors. On the scientific side, it aimed at shedding new light on the mechanism of solar flares, mainly by collecting high-cadence information about its radiation in several passbands.

Regarding the instrumental aspects, the wide-bandgap detectors proved to be well adapted to use in space conditions. LYRA experienced a strong degradation, but it was not originating from the detectors, which on the contrary proved to be very stable. The limited evolution of the detectors' dark current over the mission was easily correctable and they proved to be far less affected by radiation (*e.g.* caused by the particles in the South Atlantic Anomaly) than the traditional silicon detectors. The main drawback of these detectors are their inhomogeneous flat-field and their slow stabilization. These aspects have been significantly improved in the new generations that have been produced for the missions following PROBA2, in particular for the EUI instrument that will fly onboard Solar Orbiter. We certainly recommend their use in future missions dedicated to observations of the Sun in the SXR-UV range.

The contamination appears to be particularly critical when observing in the UV range. This amply justifies the need for a strict cleanliness programme during the instrument development and a careful selection of the materials used to build it. The degradation of the instrument sensitivity due to contamination requires regular calibration of the instrument once in-flight, which implies the

presence of covers to detect any evolution of the dark current, simultaneity with other missions with an overlapping bandpass for cross-calibration, addition of internal reference light sources, etc. Whenever possible, including some redundancy provides a big advantage. Without its three redundant units, the LYRA observations would have been limited to flare monitoring after a few months of operations.

Another lesson learned from the LYRA instrument is that too broad bandpasses should be avoided whenever possible, as they dramatically complicate both the calibration of the data and the interpretation of the results. This is particularly true when observing in the spectral range around the hydrogen Lyman- $\alpha$  line, which contains several neighbouring spectral lines and continua produced at very different temperatures by different parts of the solar atmosphere.

Regarding the solar physics aspects, a correlation of the detected periods of quasi-periodic pulsations (QPPs) with the Alfvén speed would have demonstrated that Alfvén waves are massively present during flares and can participate in the energy transfer from the reconnection site in the corona to the chromosphere where the plasma is heated. No such correlation was found. However, this does not allow us to conclude that Alfvén waves do not take part in the process. Firstly, if QPPs are produced by more than one mechanism, such a correlation would only apply to a subset of flares. Secondly, the reported analysis highlights how difficult it is to determine with certainty the period of QPPs present in the noisy data.

This work allowed to show that QPPs with periods between 1 and 100 s are systematically present in solar flares, so any realistic flare model should aim at explaining them. It also seems that these QPPs are mainly produced in the low layers of the solar atmosphere, even when they are detected in coronal wavelengths, which is an important new finding.

## 6.3 Future Prospects

To confirm the hypothesis of QPPs being produced in the lower layers of the solar atmosphere, it would be interesting to search for other flares observed by LYRA, EVE and MAVEN which are partially occulted from one of the vantage points. Once such flares are observed, the analysis that we performed for the X8.2 flare on 10 September 2017 should be repeated. The last generation of GOES spacecraft includes the Lyman- $\alpha$  channel that seems to be more sensitive and to have a better spectral purity than the Lyman- $\alpha$  channel on LYRA. As the analysis of QPPs in this channel does not require detrending the data, it

would be an interesting dataset to investigate. However, at the time of writing, the Lyman- $\alpha$  data from GOES were not yet publicly released.

We would also like to estimate the Lyman- $\alpha$  emission coming from the loops of the X8.2 flare using a 2D non-LTE radiative transfer model to confirm that this emission is indeed too faint to be detected by LYRA. A comparison with the Lyman- $\alpha$  channel of GOES would, once again, bring valuable information.

More generally, we would like to go further with the analysis of the QPP properties, aiming at the identification of their physical mechanism. The lack of correlation with the Alfvén speed did not allow us to reach any conclusion in this respect. This analysis could be refined *e.g.* by using a more adapted model of extrapolation of the magnetic field. However, the uncertainty on the value of the QPP period is such that finding such a correlation would probably be difficult. Perhaps we could extract more valuable information from the analysis of the temporal evolution of the QPPs. For example, looking at the bottom panel of Figure 5.23, it seems that the three main QPP periods increase during the flare. In the MHD hypothesis, such a behavior could be explained by an increase of the length of reconnecting loops as the flare proceeds and the reconnection point reaches higher altitudes. Also, even if QPPs are widely present in solar flares, their origin mechanism might differ from one case to the other. An analysis of the temporal evolution of the periods might help disentangling various kinds of QPPs.

From the instrumental point of view, we intend to go further with the analysis of the degradation. Mainly, we would like to test if the presence of an extra oxide layer could explain the puzzling behavior of channel 3. If it does, then we should investigate if such a layer is present on the filter of channel 4 as well, as this channel also uses a metal filter. We could also use the occultation profiles to confirm our contamination model.

Finally, we intend to update the correction of the degradation of channel 3 in the calibration procedure, based on the comparison between the measurements made by channels 3 and 4, as suggested by Kretzschmar et al. (2012).





# Beknopte Samenvatting

Zonnevlammen zijn ongetwijfeld bij de meest indrukwekkende fenomenen in het zonnestelsel. Deze gebeurtenissen, waarbij het magnetveld zich lokaal herstructureert, produceren buitengewone hoeveelheden energie. Samen met de coronale massa-uitstoten, met dewelke ze dikwijls geassocieerd worden, vormen zonnevlammen een belangrijke bron van verstoringen voor de aardse omgeving. Deze verstoringen, ook "ruimteweer" genoemd, kunnen menselijke activiteiten significant beïnvloeden, zodat ze door verschillende landen nu gezien worden als een potentiële bedreiging voor menselijke technologie.

Alhoewel zonnevlammen al gekend zijn sinds de late 19de eeuw en sinds tientallen jaren routinematig opgevolgd worden, zijn de details van het fysisch mechanisme dat aan de basis ligt nog onbekend. Het algemeen scenario van een coronale magnetische reconnectie waarbij elektronen versneld worden, en op hun beurt het chromosferisch plasma opwarmen door Coulombbotsingen, is algemeen aanvaard. Desalniettemin zijn de kwantitatieve aspecten verre van duidelijk. Kan dit scenario de grote hoeveelheid energie verklaren die vrijkomt bij zonnevlammen? Hoe wordt de energie opgeslagen in de corona voordat de reconnectie van start gaat? En wat zet de reconnectie in gang? Er zijn zoveel belangrijke vragen die onbeantwoord blijven. Maar ons begrip van het proces verbetert stap voor stap, waarbij elke nieuwe studie en elke nieuwe waarnemingsronde zijn steentje bijdraagt aan de opbouw van onze kennis.

LYRA, aan boord van de ESA-microsatelliet PROBA2, heeft een belangrijke rol te spelen in deze context. De vier kanalen van LYRA werden gekozen voor hun relevantie voor zonnephysica, ruimteweer en aëronomie, en kunnen met een hoge frequentie uitgelezen worden (nominaal 20 Hz). Het instrument werd gelanceerd eind 2009 en neemt in zijn vier breedbandkanalen, het SXR-MUV deel van het spectrum waar dat emissies van de chromosfeer en de corona omvat. Het instrument wordt beschreven in hoofdstuk 2.

Het hoofddoel van dit werk was het ten volle benutten van LYRA-gegevens om

ons begrip van zonnevlammen te verfijnen. Om dit te verwezenlijken, moest het instrument eerst geijkt worden. Daarom is deze thesis opgedeeld in twee delen. Het eerste deel bestaat uit hoofdstuk 2 en 3 en behandelt instrumentele aspecten, terwijl het tweede deel (hoofdstuk 4 en 5) twee aspecten van zonnevlammen aankaart waarvoor LYRA-gegevens een troef zijn, namelijk de studie van de evolutie van een zonnevlam in verschillende golflengten, en quasi-periodieke pulsaties.

Hoofdstuk 1 presenteert een algemene beschrijving van de zon. In hoofdstuk 2 wordt het ontwerp van het instrument kort belicht, samen met een overzicht van de dataproducten die beschikbaar zijn op de instrumentwebsite, en van de methode om de gegevens te ijken. De belangrijkste stappen in het ijkproces zijn het verwijderen van de dark current (het thermisch signaal van het instrument), het herschalen van de gegevens naar een constante afstand van 1 AE, het corrigeren van de degradatie en het omzetten van de gemeten elektrische stroom in irradiantie-eenheden. De laatste twee van deze stappen bleken de meest uitdagende, omdat LYRA waarnemingen maakt in zeer brede golflengtebanden (verscheidene tientallen nm breed), die verschillende delen van het zonnespectrum bestrijken waarin het spectrum zich niet op dezelfde manier gedraagt.

Bij gebrek aan een manier om te schatten hoe de zonne-emissie verdeeld is over elke golflengteband, neemt de dagelijkse ijking aan dat deze verdeling constant blijft over de tijd. Dit is echter een gedurfde aanname, waarvan we weten dat ze niet altijd klopt. In het bijzonder wordt het SXR-gedeelte van de irradiantie sterk overgerepresenteerd gedurende zonnevlammen.

Verder is het instrument onderworpen aan een sterke degradatie, die zo snel evolueerde in de nominale unit (die permanent gebruikt wordt) dat kanalen 1 en 2 al hun signaal verloren gedurende de eerste waarnemingsmaanden. Sommige degradatieprocessen kunnen de spectrale respons van het instrument wijzigen.

Om de implicaties van deze sterke aanname beter te begrijpen, gingen we in hoofdstuk 3 dieper in op de analyse van de degradatie. We gebruikten in-flight dark current en LED-metingen om te modelleren hoe de degradatie zijn oorsprong vindt in de polymerisatie van een laag van contaminanten op de front filters. Door het vergelijken van het signaalverlies in de vier kanalen van elke LYRA-unit slaagden we erin om de contaminanten te identificeren en om de evolutie van de dikte van de contaminatielaag te schatten over de hele missie. We concludeerden dat de degradatie vooral te wijten is aan koolstof, met mogelijk een bijdrage van silicium. Zulke contaminatie verklaart de waargenomen verzwakking van het signaal in drie van de vier kanalen van elke unit. Kanaal 3 lijkt zich echter soms anders te gedragen. Een gelijkaardige situatie werd opgetekend bij het EVE-instrument aan boord van SDO, waarvoor sommige kanalen (allemaal metaalfilters) op een andere manier verouderden dan

andere kanalen. Zowel voor EVE als voor LYRA wordt dit gedrag toegeschreven aan de aanwezigheid van een oxidelaag bovenop de metaalfilters.

Nadat we de hoofdbron van de LYRA-degradatie geïdentificeerd hadden, hebben we een radiometrisch model van het instrument opgesteld dat de contaminatie in rekening brengt. Dit model werd dan gebruikt om de evolutie van de spectrale gevoeligheid van elke kanaal op te volgen. Het bleek dat Kanaal 1, in het bijzonder, significante veranderingen in zijn spectrale gevoeligheid vertoonde, met een piektransmissie die verschoof van 121.6 nm naar  $\sim 150$  nm. Dit verklaart mogelijk waarom dit kanaal geen zonnevlammen meer heeft kunnen waarnemen na de eerste maanden sinds de lancering.

Het werk over degradatie zal doorgezet worden in de toekomst. De laatste jaren hebben de ontwikkelaars van EUV ruimte-instrumenten het belang ingezien van degradatie, en in het bijzonder van contaminatie, van het spectraal bereik waarnaar ze streven. De meeste instrumenten die zich momenteel in de ruimte bevinden, ondervinden degradatie. Het lijkt dat de wil er is om samen te werken en een diepgaande kennis te ontwikkelen van de onderliggende processen om zo te voorkomen dat we sommige van dezelfde fouten maken met de volgende generatie instrumenten. Sommige materialen zijn ondanks hun etiket 'space qualified' niet geschikt voor observaties in EUV. Het belang van een sterk properheidsprogramma is hiermee aangetoond.

In hoofdstuk 2 hebben we een schatting gemaakt van de onzekerheid op de ruwe en geijkte LYRA data. De berekening van de onzekerheid (30–40% voor kanaal 2 tot 4, en 120 % voor kanaal 1) houdt rekening met de gevoeligheid van de kanalen voor golflengten buiten hun nominale golflengteband. Om deze reden is dit zo belangrijk voor kanaal 1, waarvoor de zuiverheid enkel van de orde van 25% is.

Het tweede deel van dit doctoraat start in hoofdstuk 4 met een meerbandenanalyse van de sterkste zonnevlam van zonnecyclus 24. Deze gebeurtenis heeft geleid tot de eerste waarneming van zonnevlammenstraling in midden-ultraviolette golflengtes rond 2000 Å in kanaal 2 van LYRA. De zonnevlam (SOL20170906) werd ook waargenomen in kanaal 1 van LYRA, centraal rond de H I Lyman- $\alpha$  lijn met een golflengte van 1216 Å, met een duidelijke niet-thermische tijdsevolutie in de twee kanalen. De straling van de zonnevlam in kanaal 2 is in overeenstemming met de waterstof Balmer continuüm-emissie die geproduceerd wordt door een optisch dunne chromosferische laag die tot 10000 K opgewarmd wordt. De LYRA-waarnemingen, samen met de meest recente waarneming van de Balmer continuüm-emissie in het nabije-ultraviolet door IRIS, versterken de interpretatie van breedband zonnevlam-emissie door de voortdurende recombinitie van waterstof in de chromosfeer.

Het laatste stuk van dit doctoraal onderzoek stond in het teken van quasi-periodieke pulsaties (QPPs). Deze trillingen worden sinds de jaren 1970 regelmatig waargenomen in de impulsieve fase van zonnevlammen. Soms blijven ze aanhouden tot in de uitstervende fase. De oorsprong van de perioden tussen 1 en 100 s, die in dit werk bestudeerd werden, wordt meestal toegeschreven aan hoofdzakelijk twee fysische processen: de verandering van de elektronenstroom en van de lus die nog maar pas gereconnecteerd werd door een MHD-golf, of een veranderende versnelling van de deeltjes die bijvoorbeeld veroorzaakt kan worden door een oscillerende magnetische reconnectie. Simulaties hebben aangetoond dat beide mechanismen in staat zijn om perioden te veroorzaken in dit interval. Een andere aanpak om de oorsprong van QPPs te achterhalen is observationeel: in het kader van grote studies kunnen we proberen om tendensen of correlaties met de kenmerken van de magnetische omgeving te identificeren, die in de richting van een specifiek mechanisme kunnen wijzen.

Dat is waarschijnlijk de reden waarom de studies van QPPs in de laatste jaren terug aan belang gewonnen hebben met de komst van een nieuwe generatie van radiometers in zachte röntgenstralen/extreem ultraviolet, waaronder LYRA, die de weg openen naar statistische studies. Aangezien de amplitudes van de QPPs in deze golflengten eerder klein zijn, is het noodzakelijk dat de algemene tendens in de tijdslijnen eerst verwijderd wordt voordat er een Fourier- of wavelet-transformatie toegepast wordt. Dit proces voor het verwijderen van tendensen is ervoor gekend dat het kunstmatige perioden introduceert die onderscheiden moeten worden van de echte perioden.

Daarom hebben we eerst geschat hoe doeltreffend wavelet-transformaties zijn voor het type van gebeurtenissen waarin we geïnteresseerd zijn. We hebben een lijst van voorwaarden opgesteld die kunnen helpen om de echte perioden te identificeren en de valse te kunnen verwijderen. Daarna hebben we deze criteria toegepast op de data die door EVE/ESP en LYRA bekomen werden om te zoeken naar QPPs in zonnevlammen die zich hebben voorgedaan in zonnecyclus 24 en helderder dan M5.0 waren. Het merendeel van de zonnevlammen vertonen QPPs met perioden tussen 1 en 100 s.

We hebben onze resultaten vergeleken met die van andere studies. Ze komen goed met elkaar overeen, ook al was de ontdekkingsmethode fundamenteel verschillend. Er werd geen verband met de lengtegraad van de zonnevlammen of met de klasse van zonnevlammen gevonden.

Voor een deel van de zonnevlammen geanalyseerd in deze studie, hebben we gezocht naar een correlatie met de inverse van de Alfvén-snelheid  $1/C_{A0}$ , wat een sterke indicatie zou zijn van een MHD-gerelateerde oorsprong. We hebben een PFSS-extrapolatie uitgevoerd om een schatting te maken van het magnetisch veld en de lengte van de lussen. Elektronendichtheden werden berekend door het

gebruik van dichtheid-gevoelige spectrale lijnratio's gemeten door EVE/MEGS-A. Deze analyse toonde duidelijk aan dat er geen correlatie is tussen de gemeten periode en  $1/C_{A0}$ .

Tenslotte voerden we een grondige analyse uit van de twee helderste zonnevlammen van zonnecyclus 24, d.w.z. de X9.3-zonnevlam van 6 september 2017, die plaatsvond op een breedte van  $33^\circ\text{W}$ , en de X8.2-zonnevlam van 8 september 2017, waarvan op zijn minst één voetpunt verduisterd werd door de rand van de zon. De twee zonnevlammen hadden aanzienlijke verschillen in de LYRA-waarnemingen ondanks het feit dat ze allebei voortkomen uit hetzelfde actieve gebied en een gelijkaardige amplitude hebben. Terwijl de X9.3-zonnevlam waargenomen is in de vier LYRA-kanalen, kon geen signaal gevonden worden in kanaal 1 en 2 van de X8.2-zonnevlam. Op een gelijkaardige manier, tijdens de impulsieve fase van de X9.3-zonnevlam, werden quasi-periodische pulsaties van de zonnevlamstraling met perioden rond de 10 en 17 seconden duidelijk gedetecteerd in alle vier de kanalen van LYRA, inclusief kanaal 3 en 4, die gevoelig zijn voor EUV- en röntgenstraling. Daarentegen konden tijdens de X8.2-zonnevlam geen QPPs bevestigd worden in deze kanalen. We hebben dan de waarnemingen door LYRA vergeleken met de waarnemingen van MAVEN/EUVM, een instrument in een baan rond Mars dat totale zichtbaarheid had van de X8.2-zonnevlam. Het evenement heeft niet enkel een detecteerbaar signaal geproduceerd in Lyman- $\alpha$ , maar ook QPPs met perioden van  $\sim 15$ ,  $\sim 40$  s en  $\sim 150$  s werden waargenomen. Dit kan een indicatie zijn dat QPPs aangemaakt worden dicht bij de voetpunten van de reconnecterende lussen. Toch is er meer werk nodig om deze hypothese te bevestigen.



# Bibliography

- Altschuler, M. D. and Newkirk, G. (1969). Magnetic Fields and the Structure of the Solar Corona. I: Methods of Calculating Coronal Fields. *Solar Phys.*, 9:131–149.
- Aschwanden, M. J. (1987). Theory of radio pulsations in coronal loops. *Solar Phys.*, 111:113–136.
- Aschwanden, M. J. (2005). *Physics of the Solar Corona. An Introduction with Problems and Solutions (2nd edition)*.
- Auchère, F., Froment, C., Bocchialini, K., Buchlin, E., and Solomon, J. (2016). On the Fourier and Wavelet Analysis of Coronal Time Series. *Astrophys. J.*, 825:110.
- Avrett, E. H., Machado, M. E., and Kurucz, R. L. (1986). Chromospheric flare models. In Neidig, D. F. and Machado, M. E., editors, *The lower atmosphere of solar flares*, p. 216 - 281, pages 216–281.
- Babcock, H. W. (1961). The Topology of the Sun’s Magnetic Field and the 22-YEAR Cycle. *Astrophys. J.*, 133:572.
- Banerjee, D. (2013). Phenomenological description of the solar interior and the photosphere. KU Leuven, Numerical Plasma Astrophysics - GOA06a.
- Bárta, M., Büchner, J., Karlický, M., and Skála, J. (2011). Spontaneous Current-layer Fragmentation and Cascading Reconnection in Solar Flares. I. Model and Analysis. *Astrophys. J.*, 737:24.
- BenMoussa, A., Dammasch, I. E., Hochedez, J.-F., Schühle, U., Koller, S., Stockman, Y., Scholze, F., Richter, M., Kroth, U., Laubis, C., Dominique, M., Kretzschmar, M., Mekaoui, S., Gissot, S., Theissen, A., Giordanengo, B., Bolsee, D., Hermans, C., Gillotay, D., Defise, J.-M., and Schmutz, W. (2009). Pre-flight calibration of LYRA, the solar VUV radiometer on board PROBA2. *Astron. Astrophys.*, 508:1085–1094.

- BenMoussa, A., Giordanengo, B., Gissot, S., Dammasch, I. E., Dominique, M., Hochedez, J. F., Soltani, A., Bourzgui, N., Saito, T., Schühle, U., Gottwald, A., Kroth, U., and Jones, A. R. (2015). Degradation assessment of LYRA after 5 years on orbit - Technology Demonstration -. *Experimental Astronomy*, 39:29–43.
- BenMoussa, A., Gissot, S., Schühle, U., Del Zanna, G., Auchère, F., Mekaoui, S., Jones, A. R., Walton, D., Eyles, C. J., Thuillier, G., Seaton, D., Dammasch, I. E., Cessateur, G., Meftah, M., Andretta, V., Berghmans, D., Bewsher, D., Bolsée, D., Bradley, L., Brown, D. S., Chamberlin, P. C., Dewitte, S., Didkovsky, L. V., Dominique, M., Eparvier, F. G., Foujols, T., Gillotay, D., Giordanengo, B., Halain, J. P., Hock, R. A., Irbah, A., Jeppesen, C., Judge, D. L., Kretzschmar, M., McMullin, D. R., Nicula, B., Schmutz, W., Ucker, G., Wieman, S., Woodraska, D., and Woods, T. N. (2013). On-Orbit Degradation of Solar Instruments. *Solar Phys.*, 288:389–434.
- BenMoussa, A., Schühle, U., Haenen, K., Nesládek, M., Koizumi, S., and Hochedez, J.-F. (2004). PIN diamond detector development for LYRA, the solar VUV radiometer on board PROBA II. *Physica Status Solidi Applied Research*, 201:2536–2541.
- BenMoussa, A., Theissen, A., Scholze, F., Hochedez, J. F., Schühle, U., Schmutz, W., Haenen, K., Stockman, Y., Soltani, A., McMullin, D., Vest, R. E., Kroth, U., Laubis, C., Richter, M., Mortet, V., Gissot, S., Delouille, V., Dominique, M., Koller, S., Halain, J. P., Remes, Z., Petersen, R., D’Olieslaeger, M., and Defise, J.-M. (2006). Performance of diamond detectors for VUV applications. *Nuclear Instruments and Methods in Physics Research A*, 568:398–405.
- Benz, A. O. (2017). Flare Observations. *Living Reviews in Solar Physics*, 14:2.
- Boller, K., Haelrich, R.-P., Hogrefe, H., Jark, W., and Kunz, C. (1983). Investigation of carbon contamination of mirror surfaces exposed to synchrotron radiation. *Nuclear Instruments and Methods in Physics Research*, 208:273–279.
- Bonnet, R. M. and Blamont, J. E. (1968). Limb-Darkening Observations between 1800 and 2900 Å. *Solar Phys.*, 3:64–81.
- Brekke, P., Rottman, G. J., Fontenla, J., and Judge, P. G. (1996). The Ultraviolet Spectrum of a 3B Class Flare Observed with SOLSTICE. *Astrophys. J.*, 468:418.
- Brosius, J. W. and Daw, A. N. (2015). Quasi-periodic Fluctuations and Chromospheric Evaporation in a Solar Flare Ribbon Observed by IRIS. *Astrophys. J.*, 810:45.



- Brosius, J. W., Daw, A. N., and Inglis, A. R. (2016). Quasi-periodic Fluctuations and Chromospheric Evaporation in a Solar Flare Ribbon Observed by Hinode/EIS, IRIS, and RHESSI. *Astrophys. J.*, 830:101.
- Carmichael, H. (1964). A Process for Flares. *NASA Special Publication*, 50:451.
- Carrington, R. C. (1859). Description of a Singular Appearance seen in the Sun on September 1, 1859. *Mon. Not. Roy. Astron. Soc.*, 20:13–15.
- Chamberlin, P. C., Woods, T. N., Didkovsky, L., Eparvier, F. G., Jones, A. R., Machol, J. L., Mason, J. P., Snow, M., Thiemann, E. M. B., Viereck, R. A., and Woodraska, D. L. (2018). Solar Ultraviolet Irradiance Observations of the Solar Flares During the Intense September 2017 Storm Period. *Space Weather*, 16:1470–1487.
- Cho, I.-H., Cho, K.-S., Nakariakov, V. M., Kim, S., and Kumar, P. (2016). Comparison of Damped Oscillations in Solar and Stellar X-Ray flares. *Astrophys. J.*, 830:110.
- Chowdhury, P., Srivastava, A. K., Dwivedi, B. N., Sych, R., and Moon, Y.-J. (2015). Study of multi-periodic coronal pulsations during an X-class solar flare. *Advances in Space Research*, 56:2769–2778.
- Clette, F. (2017). Phenomenological description of the solar interior and the photosphere. Royal Observatory of Belgium, Basic Solar Physics Seminars (1/13). <https://events.oma.be/indico/event/34/>.
- Cook, J. W. and Brueckner, G. E. (1979). EUV continua of solar flares 1420 - 1960 Å. *Astrophys. J.*, 227:645–647.
- Curdt, W., Brekke, P., Feldman, U., Wilhelm, K., Dwivedi, B. N., Schühle, U., and Lemaire, P. (2001). The SUMER spectral atlas of solar-disk features. *Astron. Astrophys.*, 375:591–613.
- Damé, L. and Cram, L. (1983). White-light radiation from semi-empirical flare models. *Solar Phys.*, 87:329–335.
- Damé, L. and Vial, J. C. (1985). On the origin of the blue continuum of white-light flares. *Astrophys. J.*, 299:L103–L106.
- De Pontieu, B., Title, A. M., Lemen, J. R., Kushner, G. D., Akin, D. J., Allard, B., Berger, T., Boerner, P., Cheung, M., Chou, C., Drake, J. F., Duncan, D. W., Freeland, S., Heyman, G. F., Hoffman, C., Hurlburt, N. E., Lindgren, R. W., Mathur, D., Rehse, R., Sabolish, D., Seguin, R., Schrijver, C. J., Tarbell, T. D., Wülser, J.-P., Wolfson, C. J., Yanari, C., Mudge, J., Nguyen-Phuc, N., Timmons, R., van Bezooijen, R., Weingrod, I., Brookner,

- R., Butcher, G., Dougherty, B., Eder, J., Knagenhjelm, V., Larsen, S., Mansir, D., Phan, L., Boyle, P., Cheimets, P. N., DeLuca, E. E., Golub, L., Gates, R., Hertz, E., McKillop, S., Park, S., Perry, T., Podgorski, W. A., Reeves, K., Saar, S., Testa, P., Tian, H., Weber, M., Dunn, C., Eccles, S., Jaeggli, S. A., Kankelborg, C. C., Mashburn, K., Pust, N., Springer, L., Carvalho, R., Kleint, L., Marmie, J., Mazmanian, E., Pereira, T. M. D., Sawyer, S., Strong, J., Worden, S. P., Carlsson, M., Hansteen, V. H., Leenaarts, J., Wiesmann, M., Aloise, J., Chu, K.-C., Bush, R. I., Scherrer, P. H., Brekke, P., Martinez-Sykora, J., Lites, B. W., McIntosh, S. W., Uitenbroek, H., Okamoto, T. J., Gummin, M. A., Auken, G., Jerram, P., Pool, P., and Waltham, N. (2014). The Interface Region Imaging Spectrograph (IRIS). *Solar Phys.*, 289:2733–2779.
- Dennis, B. R., Tolbert, A. K., Inglis, A., Ireland, J., Wang, T., Holman, G. D., Hayes, L. A., and Gallagher, P. T. (2017). Detection and Interpretation of Long-lived X-Ray Quasi-periodic Pulsations in the X-class Solar Flare on 2013 May 14. *Astrophys. J.*, 836:84.
- Dere, K. P., Landi, E., Mason, H. E., Monsignori Fossi, B. C., and Young, P. R. (1997). CHIANTI - an atomic database for emission lines. *Astronomy and Astrophysics Supplement Series*, 125:149–173.
- Dere, K. P., Landi, E., Young, P. R., Del Zanna, G., Landini, M., and Mason, H. E. (2009). CHIANTI - an atomic database for emission lines. IX. Ionization rates, recombination rates, ionization equilibria for the elements hydrogen through zinc and updated atomic data. *Astron. Astrophys.*, 498:915–929.
- Dolla, L., Marqué, C., Seaton, D. B., Van Doorselaere, T., Dominique, M., Berghmans, D., Cabanas, C., De Groof, A., Schmutz, W., Verdini, A., West, M. J., Zender, J., and Zhukov, A. N. (2012). Time Delays in Quasi-periodic Pulsations Observed during the X2.2 Solar Flare on 2011 February 15. *Astrophys. J. Lett.*, 749:L16.
- Dominique, M., Gillotay, D., Cessateur, G., Cabanas, C., Dammasch, I., De Groof, A., Kretzschmar, M., Nicula, B., Tetard, C., Vanhellefont, F., and Zender, J. (2009). The contribution of PROBA2-LYRA occultations to Earth atmosphere composition analysis. pages 285–295.
- Dominique, M., Hochedez, J.-F., Schmutz, W., Dammasch, I. E., Shapiro, A. I., Kretzschmar, M., Zhukov, A. N., Gillotay, D., Stockman, Y., and BenMoussa, A. (2013). The LYRA Instrument Onboard PROBA2: Description and In-Flight Performance. *Solar Phys.*, 286:21–42.
- Dominique, M., Zhukov, A. N., Dolla, L., Inglis, A., and Lapenta, G. (2018a). Detection of Quasi-Periodic Pulsations in Solar EUV Time Series. *Solar Phys.*, 293:61.

- Dominique, M., Zhukov, A. N., Heinzel, P., Dammasch, I. E., Wauters, L., Dolla, L., Shestov, S., Kretzschmar, M., Machol, J., Lapenta, G., and Schmutz, W. (2018b). First Detection of Solar Flare Emission in Mid-ultraviolet Balmer Continuum. *Astrophys. J.*, 867:L24.
- Doyle, J. G. and Cook, J. W. (1992). The Sun as a Star: High Spectral Resolution Solar Data Degraded to Low- Dispersion IUE Resolution. *Astrophys. J.*, 391:393.
- Durand, E., Oberly, J. J., and Tousey, R. (1949). Analysis of the First Rocket Ultraviolet Solar Spectra. *Astrophys. J.*, 109:1.
- Emslie, A. G., Dennis, B. R., Shih, A. Y., Chamberlin, P. C., Mewaldt, R. A., Moore, C. S., Share, G. H., Vourlidas, A., and Welsch, B. T. (2012). Global Energetics of Thirty-eight Large Solar Eruptive Events. *Astrophys. J.*, 759:71.
- Eparvier, F. G., Chamberlin, P. C., Woods, T. N., and Thiemann, E. M. B. (2015). The Solar Extreme Ultraviolet Monitor for MAVEN. *Space Sci. Rev.*, 195:293–301.
- Ermolli, I., Matthes, K., Dudok de Wit, T., Krivova, N. A., Tourpali, K., Weber, M., Unruh, Y. C., Gray, L., Langematz, U., Pilewskie, P., Rozanov, E., Schmutz, W., Shapiro, A., Solanki, S. K., and Woods, T. N. (2013). Recent variability of the solar spectral irradiance and its impact on climate modelling. *Atmospheric Chemistry & Physics*, 13:3945–3977.
- Fletcher, L., Dennis, B. R., Hudson, H. S., Krucker, S., Phillips, K., Veronig, A., Battaglia, M., Bone, L., Caspi, A., Chen, Q., Gallagher, P., Grigis, P. T., Ji, H., Liu, W., Milligan, R. O., and Temmer, M. (2011). An Observational Overview of Solar Flares. *Space Sci. Rev.*, 159:19–106.
- Fletcher, L. and Hudson, H. S. (2008). Impulsive Phase Flare Energy Transport by Large-Scale Alfvén Waves and the Electron Acceleration Problem. *Astrophys. J.*, 675:1645–1655.
- Fontenla, J. M., Avrett, E. H., and Loeser, R. (1993). Energy Balance in the Solar Transition Region. III. Helium Emission in Hydrostatic, Constant-Abundance Models with Diffusion. *Astrophys. J.*, 406:319.
- Fontenla, J. M., Curdt, W., Haberreiter, M., Harder, J., and Tian, H. (2009). Semiempirical Models of the Solar Atmosphere. III. Set of Non-LTE Models for Far-Ultraviolet/Extreme-Ultraviolet Irradiance Computation. *Astrophys. J.*, 707:482–502.
- Foukal, P. V. (2004). *Solar Astrophysics, 2nd, Revised Edition*.

- Gabriel, A. H. (1971). Measurements on the Lyman Alpha Corona (Papers presented at the Proceedings of the International Symposium on the 1970 Solar Eclipse, held in Seattle, U. S. A. , 18-21 June, 1971.). *Solar Phys.*, 21:392–400.
- Gilman, D. L., Fuglister, F. J., and Mitchell, Jr., J. M. (1963). On the Power Spectrum of ‘Red Noise’. *Journal of Atmospheric Sciences*, 20:182–184.
- Gingerich, O., Noyes, R. W., Kalkofen, W., and Cuny, Y. (1971). The Harvard-Smithsonian reference atmosphere. *Solar Phys.*, 18:347–365.
- Goedbloed, J. P. H. and Poedts, S. (2004). *Principles of Magnetohydrodynamics*.
- Golub, L. and Pasachoff, J. M. (2009). *The Solar Corona*.
- Griem, H. R. (1997). Principles of plasma spectroscopy. *Proceedings of the Physical Society*.
- Guidoni, S. E., DeVore, C. R., Karpen, J. T., and Lynch, B. J. (2016). Magnetic-island Contraction and Particle Acceleration in Simulated Eruptive Solar Flares. *Astrophys. J.*, 820:60.
- Halain, J.-P., Berghmans, D., Seaton, D. B., Nicula, B., De Groof, A., Mierla, M., Mazzoli, A., Defise, J.-M., and Rochus, P. (2013). The SWAP EUV Imaging Telescope. Part II: In-flight Performance and Calibration. *Solar Phys.*, 286:67–91.
- Harder, J., Lawrence, G., Fontenla, J., Rottman, G., and Woods, T. (2005). The Spectral Irradiance Monitor: Scientific Requirements, Instrument Design, and Operation Modes. *Solar Phys.*, 230:141–167.
- Hayes, L. A., Gallagher, P. T., Dennis, B. R., Ireland, J., Inglis, A. R., and Ryan, D. F. (2016). Quasi-periodic Pulsations during the Impulsive and Decay phases of an X-class Flare. *Astrophys. J. Lett.*, 827:L30.
- Heinzel, P. and Kleint, L. (2014). Hydrogen Balmer Continuum in Solar Flares Detected by the Interface Region Imaging Spectrograph (IRIS). *Astrophys. J.*, 794:L23.
- Heinzel, P., Kleint, L., Kašparová, J., and Krucker, S. (2017). On the Nature of Off-limb Flare Continuum Sources Detected by SDO/HMI. *Astrophys. J.*, 847:48.
- Heinzel, P. and Shibata, K. (2018). Can Flare Loops Contribute to the White-light Emission of Stellar Superflares? *Astrophys. J.*, 859:143.
- Hiei, E. (1982). A Continuous Spectrum of a White-Light Flare. *Solar Phys.*, 80:113–127.

- Hirayama, T. (1974). Theoretical Model of Flares and Prominences. I: Evaporating Flare Model. *Solar Phys.*, 34:323–338.
- Hochedez, J.-F., Schmutz, W., Stockman, Y., Schühle, U., Benmoussa, A., Koller, S., Haenen, K., Berghmans, D., Defise, J.-M., Halain, J.-P., Theissen, A., Delouille, V., Slemzin, V., Gillotay, D., Fussen, D., Dominique, M., Vanhellemont, F., McMullin, D., Kretzschmar, M., Mitrofanov, A., Nicula, B., Wauters, L., Roth, H., Rozanov, E., Rüedi, I., Wehrli, C., Soltani, A., Amano, H., van der Linden, R., Zhukov, A., Clette, F., Koizumi, S., Mortet, V., Remes, Z., Petersen, R., Nesládek, M., D’Olieslaeger, M., Roggen, J., and Rochus, P. (2006). LYRA, a solar UV radiometer on Proba2. *Adv. Space Res.*, 37:303–312.
- Hodgson, R. (1859). On a curious Appearance seen in the Sun. *Mon. Not. Roy. Astron. Soc.*, 20:15–16.
- Hoeksema, J. T. (1984). *Structure and evolution of the large scale solar and heliospheric magnetic fields*. PhD thesis, Stanford Univ., CA.
- Hubeny, I. and Mihalas, D. (2015). *Theory of Stellar Atmospheres*.
- Hudson, H. S. (2011). Global Properties of Solar Flares. *Space Sci. Rev.*, 158:5–41.
- Inglis, A. R., Ireland, J., Dennis, B. R., Hayes, L., and Gallagher, P. (2016). A Large-scale Search for Evidence of Quasi-periodic Pulsations in Solar Flares. *Astrophys. J.*, 833:284.
- Inglis, A. R., Ireland, J., and Dominique, M. (2015). Quasi-periodic Pulsations in Solar and Stellar Flares: Re-evaluating their Nature in the Context of Power-law Flare Fourier Spectra. *Astrophys. J.*, 798:108.
- Jones, A. R., McMullin, D. R., Dominique, M., and Dammasch, I. (2013). Progress Towards Understanding the Degradation and Performance Characteristics of the PROBA2-LYRA Instrument. *AGU Fall Meeting Abstracts*, pages GC51C–0988.
- Kane, S. R., Kai, K., Kosugi, T., Enome, S., Landecker, P. B., and McKenzie, D. L. (1983). Acceleration and confinement of energetic particles in the 1980 June 7 solar flare. *Astrophys. J.*, 271:376–387.
- Karlický, M., Jelínek, P., and Mészárosóvá, H. (2011). Magnetoacoustic waves in the narrowband dm-spikes sources. *Astron. Astrophys.*, 529:A96.
- Katsiyannis, A. C., Dominique, M., Pierrard, V., Rosson, G. L., Keyser, J. D., Berghmans, D., Kruglanski, M., Dammasch, I. E., and Donder, E. D. (2018).

- The detection of ultra-relativistic electrons in low Earth orbit. *Journal of Space Weather and Space Climate*, 8(27):A01.
- Kerr, G. S. and Fletcher, L. (2014). Physical Properties of White-light Sources in the 2011 February 15 Solar Flare. *Astrophys. J.*, 783:98.
- Kleint, L., Heinzel, P., Judge, P., and Krucker, S. (2016). Continuum Enhancements in the Ultraviolet, the Visible and the Infrared during the X1 Flare on 2014 March 29. *Astrophys. J.*, 816:88.
- Kleint, L., Heinzel, P., and Krucker, S. (2017). On the Origin of the Flare Emission in IRIS’ SJI 2832 Filter: Balmer Continuum or Spectral Lines? *Astrophys. J.*, 837:160.
- Kolotkov, D. Y., Pugh, C. E., Broomhall, A.-M., and Nakariakov, V. M. (2018). Quasi-periodic Pulsations in the Most Powerful Solar Flare of Cycle 24. *Astrophys. J.*, 858:L3.
- Kopp, R. A. and Pneuman, G. W. (1976). Magnetic reconnection in the corona and the loop prominence phenomenon. *Solar Phys.*, 50:85–98.
- Kotrč, P., Procházka, O., and Heinzel, P. (2016). New Observations of Balmer Continuum Flux in Solar Flares. Instrument Description and First Results. *Solar Phys.*, 291:779–789.
- Kretzschmar, M. (2011). The Sun as a star: observations of white-light flares. *Astron. Astrophys.*, 530:A84.
- Kretzschmar, M., Dammasch, I. E., Dominique, M., Zender, J., Cessateur, G., and D’Huys, E. (2012). Extreme ultraviolet solar irradiance during the rising phase of solar cycle 24 observed by PROBA2/LYRA. *Journal of Space Weather and Space Climate*, 2(27):A14.
- Kretzschmar, M., Dominique, M., and Dammasch, I. E. (2013). Sun-as-a-Star Observation of Flares in Lyman  $\alpha$  by the PROBA2/LYRA Radiometer. *Solar Phys.*, 286:221–239.
- Kretzschmar, M., Snow, M., and Curdt, W. (2018). An Empirical Model of the Variation of the Solar Lyman- $\alpha$  Spectral Irradiance. *Geophys. Res. Lett.*, 45:2138–2144.
- Krivova, N. A., Solanki, S. K., Wenzler, T., and Podlipnik, B. (2009). Reconstruction of solar UV irradiance since 1974. *Journal of Geophysical Research (Atmospheres)*, 114:0.
- Kupriyanova, E. G., Melnikov, V. F., Nakariakov, V. M., and Shibasaki, K. (2010). Types of Microwave Quasi-Periodic Pulsations in Single Flaring Loops. *Solar Phys.*, 267:329–342.

- Labs, D. and Neckel, H. (1972). Remarks on the Convergency of Photospheric Model Conceptions and the Solar Quasi Continuum. *Solar Phys.*, 22:64–69.
- Landi, E., Del Zanna, G., Young, P. R., Dere, K. P., and Mason, H. E. (2012). CHIANTI—An Atomic Database for Emission Lines. XII. Version 7 of the Database. *Astrophys. J.*, 744:99.
- Lean, J., Rottman, G., Harder, J., and Kopp, G. (2005). SORCE Contributions to New Understanding of Global Change and Solar Variability. *Solar Phys.*, 230:27–53.
- Lemaire, P., Choucq-Bruston, M., and Vial, J. C. (1984). Simultaneous H and K Ca ii, h and k Mg ii,  $L\alpha$  and  $L\beta$  H i profiles of the April 15, 1978 solar flare observed with the OSO-8/L.P.S.P. experiment. *Solar Phys.*, 90:63–82.
- Lemen, J. R., Title, A. M., Akin, D. J., Boerner, P. F., Chou, C., Drake, J. F., Duncan, D. W., Edwards, C. G., Friedlaender, F. M., Heyman, G. F., Hurlburt, N. E., Katz, N. L., Kushner, G. D., Levay, M., Lindgren, R. W., Mathur, D. P., McFeaters, E. L., Mitchell, S., Rehse, R. A., Schrijver, C. J., Springer, L. A., Stern, R. A., Tarbell, T. D., Wuelser, J.-P., Wolfson, C. J., Yanari, C., Bookbinder, J. A., Cheimets, P. N., Caldwell, D., Deluca, E. E., Gates, R., Golub, L., Park, S., Podgorski, W. A., Bush, R. I., Scherrer, P. H., Gummin, M. A., Smith, P., Auker, G., Jerram, P., Pool, P., Soufi, R., Windt, D. L., Beardsley, S., Clapp, M., Lang, J., and Waltham, N. (2012). The Atmospheric Imaging Assembly (AIA) on the Solar Dynamics Observatory (SDO). *Solar Phys.*, 275:17–40.
- Mathioudakis, M., Bloomfield, D. S., Jess, D. B., Dhillon, V. S., and Marsh, T. R. (2006). The periodic variations of a white-light flare observed with ULTRACAM. *Astron. Astrophys.*, 456:323–327.
- Mathioudakis, M., Seiradakis, J. H., Williams, D. R., Avgoloupis, S., Bloomfield, D. S., and McAteer, R. T. J. (2003). White-light oscillations during a flare on II Peg. *Astron. Astrophys.*, 403:1101–1104.
- Mazzotta, P., Mazzitelli, G., Colafrancesco, S., and Vittorio, N. (1998). Ionization balance for optically thin plasmas: Rate coefficients for all atoms and ions of the elements H to NI. *Astron. Astrophys. Suppl.*, 133:403–409.
- McLaughlin, J. A., De Moortel, I., Hood, A. W., and Brady, C. S. (2009). Nonlinear fast magnetoacoustic wave propagation in the neighbourhood of a 2D magnetic X-point: oscillatory reconnection. *Astron. Astrophys.*, 493:227–240.
- McLaughlin, J. A., Nakariakov, V. M., Dominique, M., Jelínek, P., and Takasao, S. (2018). Modelling Quasi-Periodic Pulsations in Solar and Stellar Flares. *Space Sci. Rev.*, 214:45.

- Meftah, M., Damé, L., Bolsée, D., Hauchecorne, A., Pereira, N., Sluse, D., Cessateur, G., Irbah, A., Bureau, J., Weber, M., Bramstedt, K., Hilbig, T., Thiéblemont, R., Marchand, M., Lefèvre, F., Sarkissian, A., and Bekki, S. (2018). SOLAR-ISS: A new reference spectrum based on SOLAR/SOLSPEC observations. *Astron. Astrophys.*, 611:A1.
- Milligan, R. O. and Chamberlin, P. C. (2016). Anomalous temporal behaviour of broadband Ly $\alpha$  observations during solar flares from SDO/EVE. *Astron. Astrophys.*, 587:A123.
- Milligan, R. O., Fleck, B., Ireland, J., Fletcher, L., and Dennis, B. R. (2017). Detection of Three-minute Oscillations in Full-disk Ly $\alpha$  Emission during a Solar Flare. *Astrophys. J.*, 848:L8.
- Milligan, R. O., Kennedy, M. B., Mathioudakis, M., and Keenan, F. P. (2012). Time-dependent Density Diagnostics of Solar Flare Plasmas Using SDO/EVE. *Astrophys. J. Lett.*, 755:L16.
- Milligan, R. O., Kerr, G. S., Dennis, B. R., Hudson, H. S., Fletcher, L., Allred, J. C., Chamberlin, P. C., Ireland, J., Mathioudakis, M., and Keenan, F. P. (2014). The Radiated Energy Budget of Chromospheric Plasma in a Major Solar Flare Deduced from Multi-wavelength Observations. *Astrophys. J.*, 793:70.
- Mitra-Kraev, U., Harra, L. K., Williams, D. R., and Kraev, E. (2005). The first observed stellar X-ray flare oscillation: Constraints on the flare loop length and the magnetic field. *Astron. Astrophys.*, 436:1041–1047.
- Mravcová, L. and Švanda, M. (2017). Automatic detection of white-light flare kernels in SDO/HMI intensitygrams. *NA*, 57:14–21.
- Murray, M. J., van Driel-Gesztelyi, L., and Baker, D. (2009). Simulations of emerging flux in a coronal hole: oscillatory reconnection. *Astron. Astrophys.*, 494:329–337.
- Nakariakov, V. M., Foullon, C., Verwichte, E., and Young, N. P. (2006). Quasi-periodic modulation of solar and stellar flaring emission by magnetohydrodynamic oscillations in a nearby loop. *Astron. Astrophys.*, 452:343–346.
- Nakariakov, V. M. and Melnikov, V. F. (2009). Quasi-Periodic Pulsations in Solar Flares. *Space Sci. Rev.*, 149:119–151.
- Nakariakov, V. M. and Verwichte, E. (2005). Coronal Waves and Oscillations. *Living Reviews in Solar Physics*, 2:3.



- Neidig, D. F. (1983). Spectral analysis of the optical continuum in the 24 April 1981 flare. *Solar Phys.*, 85:285–302.
- Neidig, D. F., Kiplinger, A. L., Cohl, H. S., and Wiborg, P. H. (1993). The Solar White-Light Flare of 1989 March 7: Simultaneous Multiwavelength Observations at High Time Resolution. *Astrophys. J.*, 406:306.
- Neupert, W. M. (1968). Comparison of Solar X-Ray Line Emission with Microwave Emission during Flares. *Astrophys. J.*, 153:L59.
- Ning, Z. (2017). One-Minute Quasi-Periodic Pulsations Seen in a Solar Flare. *Solar Phys.*, 292:11.
- Parks, G. K. and Winckler, J. R. (1969). Sixteen-Second Periodic Pulsations Observed in the Correlated Microwave and Energetic X-Ray Emission from a Solar Flare. *Astrophys. J. Lett.*, 155:L117.
- Paterno, L. (1998). Do we understand the 22-year solar activity cycle? *Academie des Sciences Paris Comptes Rendus Serie B Sciences Physiques*, 326:393–405.
- Petschek, H. E. (1964). Magnetic Field Annihilation. *NASA Special Publication*, 50:425.
- Phillips, K. J. H., Feldman, U., and Landi, E. (2008). *Ultraviolet and X-ray Spectroscopy of the Solar Atmosphere*.
- Poedts, S. (2015). Plasma physics of the sun. KU Leuven, Numerical Plasma Astrophysics - GOB28A.
- Pugh, C. E., Armstrong, D. J., Nakariakov, V. M., and Broomhall, A.-M. (2016). Statistical properties of quasi-periodic pulsations in white-light flares observed with Kepler. *Mon. Not. Roy. Astron. Soc.*, 459:3659–3676.
- Pugh, C. E., Broomhall, A.-M., and Nakariakov, V. M. (2017). Significance testing for quasi-periodic pulsations in solar and stellar flares. *Astron. Astrophys.*, 602:A47.
- Rottman, G. J., Woods, T. N., and Sparn, T. P. (1993). Solar-Stellar Irradiance Comparison Experiment 1. I - Instrument design and operation. *J. Geophys. Res.*, 981:10667–+.
- Rubio da Costa, F., Fletcher, L., Labrosse, N., and Zuccarello, F. (2009). Observations of a solar flare and filament eruption in Lyman  $\alpha$  and X-rays. *Astron. Astrophys.*, 507:1005–1014.

- Schäfer, R., Schmidtke, G., Strahl, T., Pfeifer, M., and Brunner, R. (2017). EUV data processing methods of the Solar Auto-Calibrating EUV Spectrometers (SolACES) aboard the International Space Station. *Advances in Space Research*, 59:2207–2228.
- Schatten, K. H., Wilcox, J. M., and Ness, N. F. (1969). A model of interplanetary and coronal magnetic fields. *Solar Phys.*, 6:442–455.
- Schmutz, W., Fehlmann, A., Hülsen, G., Meindl, P., Winkler, R., Thuillier, G., Blattner, P., Buisson, F., Egorova, T., Finsterle, W., Fox, N., Gröbner, J., Hochedez, J.-F., Koller, S., Meftah, M., Meissonnier, M., Nyeki, S., Pfiffner, D., Roth, H., Rozanov, E., Spescha, M., Wehrli, C., Werner, L., and Wyss, J. U. (2009). The PREMOS/PICARD instrument calibration. *Metrologia*, 46:202–+.
- Schöll, M., Dudok de Wit, T., Kretzschmar, M., and Haberreiter, M. (2016). Making of a solar spectral irradiance dataset I: observations, uncertainties, and methods. *Journal of Space Weather and Space Climate*, 6(27):A14.
- Schou, J., Scherrer, P. H., Bush, R. I., Wachter, R., Couvidat, S., Rabello-Soares, M. C., Bogart, R. S., Hoeksema, J. T., Liu, Y., Duvall, T. L., Akin, D. J., Allard, B. A., Miles, J. W., Rairden, R., Shine, R. A., Tarbell, T. D., Title, A. M., Wolfson, C. J., Elmore, D. F., Norton, A. A., and Tomczyk, S. (2012). Design and Ground Calibration of the Helioseismic and Magnetic Imager (HMI) Instrument on the Solar Dynamics Observatory (SDO). *Solar Phys.*, 275:229–259.
- Seaton, D. B., Berghmans, D., Nicula, B., Halain, J.-P., De Groof, A., Thibert, T., Bloomfield, D. S., Raftery, C. L., Gallagher, P. T., Auchère, F., Defise, J.-M., D’Huys, E., Lecat, J.-H., Mazy, E., Rochus, P., Rossi, L., Schühle, U., Slemzin, V., Yalim, M. S., and Zender, J. (2012). The SWAP EUV Imaging Telescope Part I: Instrument Overview and Pre-Flight Testing. *Solar Phys.*, This issue.:217.
- Shibata, K., Masuda, S., Shimojo, M., Hara, H., Yokoyama, T., Tsuneta, S., Kosugi, T., and Ogawara, Y. (1995). Hot-Plasma Ejections Associated with Compact-Loop Solar Flares. *Astrophys. J. Lett.*, 451:L83.
- Shibata, K. and Takasao, S. (2016). Fractal Reconnection in Solar and Stellar Environments. In Gonzalez, W. and Parker, E., editors, *Magnetic Reconnection: Concepts and Applications*, volume 427 of *Astrophysics and Space Science Library*, page 373.
- Simões, P. J. A., Hudson, H. S., and Fletcher, L. (2015). Soft X-Ray Pulsations in Solar Flares. *Solar Phys.*, 290:3625–3639.

- Simões, P. J. A., Reid, H. A. S., Milligan, R. O., and Fletcher, L. (2018). The spectral content of SDO/AIA 1600 and 1700 Å filters from flare and plage observations. *arXiv e-prints*, page arXiv:1808.01488.
- Simon, P. (1978). Activité solaire : Indices et catalogues. *L'Astronomie*, 92:61.
- Song, Y. L., Guo, Y., Tian, H., Zhu, X. S., Zhang, M., and Zhu, Y. J. (2018). Observations of a White-light Flare Associated with a Filament Eruption. *Astrophys. J.*, 854:64.
- Sturrock, P. A. (1968). A Model of Solar Flares. In Kiepenheuer, K. O., editor, *Structure and Development of Solar Active Regions*, volume 35 of *IAU Symposium*, page 471.
- Svestka, Z. and Cliver, E. W. (1992). History and Basic Characteristics of Eruptive Flares. In Svestka, Z., Jackson, B. V., and Machado, M. E., editors, *IAU Colloq. 133: Eruptive Solar Flares*, volume 399 of *Lecture Notes in Physics*, Berlin Springer Verlag, page 1.
- Sweet, P. A. (1958). The Neutral Point Theory of Solar Flares. In Lehnert, B., editor, *Electromagnetic Phenomena in Cosmical Physics*, volume 6 of *IAU Symposium*, page 123.
- Takasao, S. and Shibata, K. (2016). Above-the-loop-top Oscillation and Quasi-periodic Coronal Wave Generation in Solar Flares. *Astrophys. J.*, 823:150.
- Tan, B. and Tan, C. (2012). Microwave Quasi-periodic Pulsation with Millisecond Bursts in a Solar Flare on 2011 August 9. *Astrophys. J.*, 749:28.
- Thiemann, E. M. B., Dominique, M., Pilinski, M. D., and Eparvier, F. G. (2017). Vertical Thermospheric Density Profiles From EUV Solar Occultations Made by PROBA2 LYRA for Solar Cycle 24. *Space Weather*, 15:1649–1660.
- Tian, H., Young, P. R., Reeves, K. K., Wang, T., Antolin, P., Chen, B., and He, J. (2016). Global Sausage Oscillation of Solar Flare Loops Detected by the Interface Region Imaging Spectrograph. *Astrophys. J. Lett.*, 823:L16.
- Torrence, C. and Compo, G. P. (1998). A Practical Guide to Wavelet Analysis. *Bulletin of the American Meteorological Society*, 79:61–78.
- Torrence, C. and Webster, P. J. (1999). Interdecadal Changes in the ENSO-Monsoon System. *Journal of Climate*, 12:2679–2690.
- Van Doorselaere, T., De Groof, A., Zender, J., Berghmans, D., and Goossens, M. (2011). LYRA Observations of Two Oscillation Modes in a Single Flare. *Astrophys. J.*, 740:90.

- Van Doorselaere, T., Kupriyanova, E. G., and Yuan, D. (2016). Quasi-periodic Pulsations in Solar and Stellar Flares: An Overview of Recent Results (Invited Review). *Solar Phys.*, 291:3143–3164.
- Vaughan, S. (2005). A simple test for periodic signals in red noise. *Astron. Astrophys.*, 431:391–403.
- Vernazza, J. E., Avrett, E. H., and Loeser, R. (1981). Structure of the solar chromosphere. III - Models of the EUV brightness components of the quiet-sun. *Astrophys. J. Suppl. Series*, 45:635–725.
- Verwichte, E., Van Doorselaere, T., Foullon, C., and White, R. S. (2013). Coronal Alfvén Speed Determination: Consistency between Seismology Using AIA/SDO Transverse Loop Oscillations and Magnetic Extrapolation. *Astrophys. J.*, 767:16.
- Veselovsky, I. S. and Koutchmy, S. (2006). On the solar white-light high resolution observations from space. *Advances in Space Research*, 37:1576–1582.
- Veselovsky, I. S. and Koutchmy, S. (2009). Scientific requirements for future spatially resolved white-light and broad-band high-cadence observations of the Sun. *Advances in Space Research*, 43:995–1000.
- Švanda, M., Jurčák, J., Kašparová, J., and Kleint, L. (2018). Understanding the HMI Pseudocontinuum in White-light Solar Flares. *Astrophys. J.*, 860:144.
- Wang, Y.-M. and Sheeley, Jr., N. R. (1992). On potential field models of the solar corona. *Astrophys. J.*, 392:310–319.
- Wieman, S. R., Didkovsky, L. V., and Judge, D. L. (2014). Resolving Differences in Absolute Irradiance Measurements Between the SOHO/CELIAS/SEM and the SDO/EVE. *Solar Phys.*, 289:2907–2925.
- Woodraska, D. L., Woods, T. N., and Eparvier, F. G. (2004). In-flight calibration and performance of the Solar Extreme ultraviolet Experiment (SEE) aboard the TIMED Satellite. In C. A. Nardell, P. G. Lucey, J.-H. Yee, & J. B. Garvin, editor, *Society of Photo-Optical Instrumentation Engineers (SPIE) Conference Series*, volume 5660 of *Society of Photo-Optical Instrumentation Engineers (SPIE) Conference Series*, pages 36–47.
- Woods, T. N., Eparvier, F. G., Hock, R., Jones, A. R., Woodraska, D., Judge, D., Didkovsky, L., Lean, J., Mariska, J., Warren, H., McMullin, D., Chamberlin, P., Berthiaume, G., Bailey, S., Fuller-Rowell, T., Sojka, J., Tobiska, W. K., and Viereck, R. (2012). Extreme Ultraviolet Variability Experiment (EVE) on the Solar Dynamics Observatory (SDO): Overview of Science Objectives,

- Instrument Design, Data Products, and Model Developments. *Solar Phys.*, 275:115–143.
- Woods, T. N., Kopp, G., and Chamberlin, P. C. (2006). Contributions of the solar ultraviolet irradiance to the total solar irradiance during large flares. *Journal of Geophysical Research (Space Physics)*, 111:A10S14.
- Woods, T. N., Prinz, D. K., Rottman, G. J., London, J., Crane, P. C., Cebula, R. P., Hilsenrath, E., Brueckner, G. E., Andrews, M. D., White, O. R., VanHoosier, M. E., Floyd, L. E., Herring, L. C., Knapp, B. G., Pankratz, C. K., and Reiser, P. A. (1996). Validation of the UARS solar ultraviolet irradiances: Comparison with the ATLAS 1 and 2 measurements. *J. Geophys. Res.*, 101:9541–9570.
- Woods, T. N., Rottman, G. J., and Ucker, G. J. (1993). Solar-Stellar Irradiance Comparison Experiment 1. II - Instrument calibrations. *J. Geophys. Res.*, 981:10679–+.
- Zaitsev, V. V. and Stepanov, A. V. (2008). Coronal magnetic loops. *Physics Uspekhi*, 51:1123–1160.



# Short Curriculum Vitae

**Marie DOMINIQUE**

## **Education**

- Post-master degree in physics, 2003, University of Liège (Belgium)
- Master degree of physics engineering, 2001, University of Liège (Belgium)

## **Professional experience**

- Since 2009: researcher at the Royal Observatory of Belgium
- 2004-2009: researcher position shared between the Royal Observatory of Belgium and the Belgian Institute for Space Aeronomy
- 2001-2003: research engineer at the University of Liège (in the laboratory of optics HOLOLAB).

## **Profile**

Marie Dominique is a researcher in solar physics at the Royal Observatory of Belgium. She joined the Observatory in 2004 to work as an instrument scientist. Her main contribution was to the PROBA2/LYRA instrument, a UV-EUV radiometer, of which she became the PI in mid-2010. In parallel, she joined the SIDC group, which is devoted to the analysis of solar activity, to work on solar flares. She is among others involved in the multi-spectral analysis of quasi-periodic pulsations. Her other fields of interest include the analysis of the evolution of space instrument performances and the remote sensing analysis of the Earth's atmosphere composition via the occultation technique.





# Peer-Reviewed Publications

The list provided here corresponds to the publications to which M. Dominique collaborated in the frame of her PhD. The complete list of her publications can be found on NASA ADS.

## First author publications:

1. *First Detection of Solar Flare Emission in Middle-Ultraviolet Balmer Continuum*; Dominique, M.; Zhukov, A. N.; Heinzel, P.; Dammasch, I. E.; et al.; The Astrophysical Journal Letters, Volume 867, Issue 2, article id. L24, 5 pp. (2018)
2. *Detection of Quasi-Periodic Pulsations in Solar EUV Timeseries*; Dominique, M.; Zhukov, A.; Dolla, L.; Inglis, A.; Lapenta, G.; Solar Physics, Volume 293, Issue 4 (2018)
3. *The LYRA instrument onboard PROBA2: description and in-flight performance*; Dominique, M.; Hochedez, J.-F.; Schmutz, W.; Dammasch, I.E.; et al.; Solar Physics, 286, pp. 21-42 (2013)

## Co-author publications:

1. *Mars Thermospheric Variability Revealed by MAVEN EUVM Solar Occultations: Structure at Aphelion and Perihelion, and Response to EUV Forcing*; Thiemann, E. M. B.; Eparvier, F. G.; Bougher, S. W.; Dominique, M.; et al.; Journal of Geophysical Research: Planets, Volume 123, Issue 9, pp. 2248-2269 (2018)
2. *Modelling Quasi-Periodic Pulsations in Solar and Stellar Flares*; McLaughlin, J. A.; Nakariakov, V. M.; Dominique, M.; Jelínek, P.; Takasao, S.; Space Science Reviews, Volume 214, Issue 1 (2018)

3. *The detection of ultra-relativistic electrons in low Earth orbit*; Katsiyannis, T.; Dominique, M.; Pierrard, V.; Lopez Rosson, G.; et al.; Journal of Space Weather and Space Climate, Volume 8, id.A01 (2018)
4. *Vertical Thermospheric Density Profiles from EUV Solar Occultations made by PROBA2 LYRA for Solar Cycle 24*; Thiemann, E. M. B.; Dominique, M.; Pilinski, M. D.; Eparvier, F. G.; Space Weather, Volume 15, Issue 12, pp. 1649-1660 (2017)
5. *On-orbit degradation of recent space-based solar instruments and understanding of the degradation processes*; Meftah, M.; Dominique, M.; BenMoussa, A.; Dammasch, I. E. et al.; Proceedings of the SPIE, 10196 (2017)
6. *Multi-instrument observations of the solar eclipse on 20 March 2015 and its effects on the ionosphere over Belgium and Europe*; Stankov, S.; Bergeot, N. ; Berghmans, D. ; Bolsée, D.; et al.; Journal of Space Weather and Space Climate (2017)
7. *LYRA Mid-Term Periodicities*; Wauters, L.; Dominique, M.; Dammasch, I. E.; Solar Physics, 291, pp. 2135-2144 (2016)
8. *Effects of flare definitions on the statistics of derived flare distributions*; Ryan, D.; Dominique, M.; Seaton, D.; Stegen, K.; White, A.; Astronomy & Astrophysics, 592 issue A133 (2016)
9. *Validation of the Earth atmosphere models using the solar EUV solar occultation data from the CORONAS and PROBA 2 instruments*; Slemzin, V.A.; Ulyanov, A.; Gaikovich, K.; Kuzin, S.V.; et al.; Journal of Space Weather and Space Climate, Volume 6, id.A7, 6 issue 27 (2016)
10. *Degradation assessment of LYRA after 5 years on orbit - Technology Demonstration*; BenMoussa, A.; Giordanengo, B.; Gissot, S.; Dammasch, I.E.; et al; Experimental Astronomy, 39, pp. 29-43 (2015)
11. *Quasi-periodic pulsations in solar and stellar flares: re-evaluating their nature in the context of power-law flare Fourier spectra*; Inglis, A.; Ireland, J.; Dominique, M.; Astrophysical Journal, 798 (2015)
12. *Sun-as-a-Star Observation of Flares in Lyman- $\alpha$  by the PROBA2/LYRA Radiometer*; Kretschmar, M.; Dominique, M.; Dammasch, I.E.; Solar Physics, 286, pp. 221-239 (2013)
13. *On-Orbit Degradation of Solar Instruments*; BenMoussa, A.; Gissot, S.; Schühle, U.; Del Zanna, G.; et al; Solar Physics, 288, pp. 389-434 (2013)

14. *The Projects for Onboard Autonomy (PROBA2) Science Centre: Sun Watcher Using APS Detectors and Image Processing (SWAP) and Large-Yield Radiometer (LYRA) Science Operations and Data Products*; Zender, J.; Berghmans, D.; Bloomfield, D.S.; Cabanas Parada, C.; et al. ; Solar Physics, 286, pp. 93-110 (2013)
15. *Eclipses Observed by Large Yield RAdiometer (LYRA) - A Sensitive Tool to Test Models for the Solar Irradiance*; Shapiro, A. I.; Schmutz, W.; Dominique, M.; Shapiro, A.V.; Solar Physics, 286, pp. 271-287 (2013)
16. *Detection of Solar Rotational Variability in the Large Yield RAdiometer (LYRA) 190 - 222 nm Spectral Band*; Shapiro, A.V.; Shapiro, A. I.; Dominique, M.; Dammasch, I.E.; et al.; Solar Physics, 286, pp. 289-301 (2013)
17. *Extreme Ultraviolet Solar Irradiance during the Rising Phase of Solar Cycle 24 Observed by PROBA2/LYRA*; Kretzschmar, M.; Dammasch, I.E.; Dominique, M.; Zender, J.; et al.; Journal of Space Weather and Space Climate, 2, pp. A14 (2012)
18. *Time delays in quasi-periodic pulsations observed during the X2.2 solar flare on 2011 February 15*; Dolla, L.; Marqué, C.; Seaton, D.B.; Van Doorsseleare, T.; et al.; Astrophysical Journal, 749, pp. L16 (2012)
19. *Preliminary Results on Irradiance Measurements from Lyra and Swap*; Kumara, S.T.; Kariyappa, R.; Dominique, M.; Berghmans, D.; et al.; Advances in Astronomy, 2012, pp. 1-5 (2012)





FACULTY OF SCIENCE  
DEPARTMENT OF MATHEMATICS  
CENTRE FOR MATHEMATICAL PLASMA-ASTROPHYSICS  
3, Circular Avenue  
B-1180 Uccle  
marie.dominique@oma.be

